SCUOLA INTERNAZIONALE SUPERIORE DI STUDI AVANZATI

DOCTORAL THESIS

Massive black holes from single and binary stars

Author:
Cristiano Ugolini

Supervisor:
Prof. Marco Limongi
Prof. Mario Spera

A thesis submitted in fulfillment of the requirements
for the degree of Doctor of Philosophy

in the

Astrophysics and Cosmology

December 2024

Declaration of Authorship

I, Cristiano Ugolini, declare that this thesis titled, “Massive black holes from single and binary stars” and the work presented in it are my own. I confirm that:

- This work was done wholly or mainly while in candidature for a research degree at this University.
- Where any part of this thesis has previously been submitted for a degree or any other qualification at this University or any other institution, this has been clearly stated.
- Where I have consulted the published work of others, this is always clearly attributed.
- Where I have quoted from the work of others, the source is always given. With the exception of such quotations, this thesis is entirely my own work.
- I have acknowledged all main sources of help.
- Where the thesis is based on work done by myself jointly with others, I have made clear exactly what was done by others and what I have contributed myself.

Signed:

Date:

"*With four parameters I can fit an elephant, and with five I can make him wiggle his trunk.*"

John von Neumann

Abstract

The first direct detection of gravitational waves in 2015 ushered in a new era for studying compact objects. Upcoming detectors like the Einstein Telescope are expected to contribute thousands of binary coalescence events to the existing data pool. However, uncertainties in the nature of stellar remnants from core-collapse supernovae and binary stellar evolution hinder our theoretical understanding of compact objects binaries. In the first part of my work, we examined the properties of stellar remnants using a grid of rotating and non-rotating massive stars at various metallicities from Limongi and Chieffi, 2018. We simulated supernova explosions of evolved progenitors with the HYdrodynamic Ppm Explosion with Radiation diffusION code (Limongi and Chieffi, 2020), calibrated to match SN1987A's properties. We found that the heaviest black holes are influenced by initial stellar rotation, metallicity, and the onset of pulsational pair-instability supernovae (PPISNe). Non-rotating progenitors at $\left[\mathrm{Fe/H}\right] = -3$ can form black holes up to $87\,\mathrm{M}_{\odot}$, within the theorized pair-instability mass gap, while rotating progenitors are limited to $41.6\,\mathrm{M}_{\odot}$ due to increased wind mass loss. We provided fitting formulas for compact remnant masses based on progenitor properties, suitable for rapid population synthesis codes. In the second part of my work, I studied binary black hole mass distributions using the rapid population synthesis code Stellar Evolution for N-body (SEVN) (Spera and Mapelli, 2017; Spera et al., 2019; Iorio et al., 2023). We focused on reproducing the observed primary black hole mass distribution from gravitational wave data, particularly the peak at $35\,\mathrm{M}_{\odot}$. Initially attributed to PPISNe (Abbott et al., 2021; Abbott et al., 2023), this peak arises from stable mass transfer in specific binary systems. (Hendriks et al., 2023; Briel, Stevance, and Eldridge, 2023). Additionally, we explored the roles of common envelope ejection efficiency and PPISNe in accumulating black holes in this mass range while examining the influence of varying the initial mass function on the primary black hole mass distribution.

Acknowledgements

This thesis marks the end of a journey. I must say, not an epic journey, but one I enjoyed doing. And as in all the good journeys I was not alone. I had mentors who guided me, comrades that shared with me the ups and downs, and even a vessel that took me in as I approached this journey.

Let me started by thanking the vessel itself, as none of this would have been possible without SISSA and its community. They welcomed me with open arms, providing me with the instruments to set sail and ride the waves, sometimes gravitational waves even. As one wise person - allegedly - said, "you were not made to live your lives as brutes, but to be followers of worth and knowledge". I thank SISSA and its community for making this possible.

However, without a guidance, all the instruments in the world are useless. I was, and am, particularly lucky because I found two person that complemented each other very well, and that helped me become the researcher that I am now (refer to them for complaints). I will mention them rigorously in chronological order.

I want to thank Marco Limongi. He taught me how to approach a new problem and never forget me, starting from the pandemic to these last days of my Ph.D. In him I found a person I can rely on and I like to talk to. Among our many conversation, however, I want to remember one that is distinguished from science. I will forever cherish the memory of that afternoon before the Conference League final, spent in the coffee room at the observatory, performing any sort of cabala rituals, trying to influence fate. I want to believe that we played a small part in that victory.

My second, but only in chronological order, supervisor is Mario Spera. He helped me broaden my interest and taught me the importance of interacting with other people to create bridges among supposedly different topics. He also spent with me countless hours perfecting papers, trying presentations and discussing about astrophysics, and many other topics. He brought me to my first conference, TUTT2022 at Otranto, and we raided together the delightful coffee breaks, while also meeting scientist from all over the world for the first time in my life as a researcher. But most importantly, Mario was always there for me, and for this I thank him.

I also want to Ugo, he arrived halfway through my PhD, but he provide an additional guidance that was precious to me. He will forever be my go-to-guy for applications, other than a person I am happy to call a friend. Thank you also to Franceso, my PISN-guy, Cecilia, without whom the second half-of this thesis wouldn't have been possible. Thank you also to the former and new addition to our SPERA group, in the end I didn't propose a better name, Mattia and Giovanni.

Finally, I want to thank all the APC group for welcoming me and all the events and opportunities to interact with fellow astrophysicist. I learned that being a researcher consist in running computer simulations as much as talking with other researchers. This is the reason why I must also thank all the people I met during my journey that are not in SISSA. I had the chance to interact with wonderful people, but I won't make a list, as I would surely forgot many important names, and I don't want to.

Now, most of the people reading these acknowledgments are be waiting for this part, where I will start mention all the friends unrelated to my research work. Let me start with a citation: "I don't know half of you half as well as I should like; and I like less than half of you half as well as you deserve." This means that you may not be named in the order you would prefer, and maybe what I will say about you will not reflect truly our relation, and for this I am sorry. I took already too much of your time, but let me postpone for another moment. These last few month, without many of my PhD-friends, and the last few years far from my Roma-friends (that before were just friends), taught me how valuable each of you are. This is why I will start with those that shared the beginning and the last few months of this journey.

Max and Mavi, thank you guys. You were the first friends I had in Trieste, when we were alone eating and drinking. I am happy to say that in these four years the only thing that changed is that we were not alone anymore, but surrounded with many other friends. I will never forget the Saturday Lunches, the Amaro Istriano and the laughs we shared.

About sharing, I want to thank the person I shared the most things during this PhD, Delpo. Starting from parenthesis, to training, passing through too many drunken walks. At some point we should start calling cabs. But no worries, in the 30 years we (i.e., **you**, according to the recent estimates) have left there will be plenty of occasions. Thank you also to Fabi, that was always happy to mock Delpo with me, who usually reacted very well. I will always remember the post-training sunset in Barcola.

Let me know mention the gym-bros. Thank you Jacopo, my favorite hyper-focused friend. Thank you Lorenzo, are you still in Paris? And thank you Davide, Giua, and Cristoforo (aka *Foro*), for the trainings but especially for the late night tennis lesson.

I am trying to follow some kind of logic path, in order not to put you guys in rankings, so let me thank now my other tennis friends, with whom I shared more tennis lessons, and matches, at better-thought times. Thank you FraGa and Valentina. And thank you Giulio, for the tennis, and for many other things.

Thank you to two out of three of the SISSA BOYS (Andrea and Giovanni), and Diego2, you never trained with me so you are here below, next time do some calisthenics with me. Nonetheless, I will miss you guys, maybe I will miss less the expensive outings we shared.

Now, since I ended-up in a cul-de-sac I will do a small leap of faith, to thank Daniele, my train-guy. Thank you also to Diego, who always sided with me when it was time to explain to Daniele why he was wrong, which happened quite often. Thank you also to Vania, we had many interesting discussion, I am inclined to believe that they started because you wanted to say the opposite of what I was saying, but it was funny and even sometimes even enlightening. Sorry if sometimes me and Delpo were unbearable, but you know him, he lacks common sense.

Thank you to my fourth office mate Francesco, your patience in helping me is precious and even though you left research for money (good idea), you will always be the saint that protects me against segmentation faults.

Finally, thank you to Massimo, you arrived in the final month and I will always regret that we had this little time together, but it was meaningful to me.

Thank you also to those that were with me even before of this journey. Thank you to those that were meant to be friends even before birth, and to those that became friends along the way.

Thank you to Sbouch, Gabbo, Lello, Pira and Tommi. I love you guys and with you we were able to create a new birthday for Lello, one that means actually something, since we were all together in Trieste, an event that take place once in a lifetime.

Thank you to Lorenzo, for being there for me, for the long talks and simply for being one of the best friend a person can ask for. And thank you for making it at my defense, I know it was not easy. I swear I will go back playing Age as soon as I finish this PhD.

Thank you to the Campeones, as a wise man with a big nose once said: "lontani forse, larghi mai".

Thank you to Buzzi and Laura, for the sushi, for the fun, but most importantly, for your friendship.

And thank you to the many friends I don't have the space to name, all of you gave me something.

Thanks to my family, by blood and by choice, who encouraged me to take this unusual but exiting journey, and who made it possible. Thank you to Marco and Monica, who made me feel welcomed, and who always treated me like a second son.

Thank to Mamma and Papà for you unwavering love and support, you always made me felt loved and smart and important, and part of this is yours. Thank you to my little makakini, my little twin brothers. Maybe we are far in space, but you are always close to my heart.

Thank you also to Nonna, who supported me from far away, but was always there, and to Nonno, who lighted the spark a long time ago.

And finally, I want to thank the most important person of my life, Flaminia. Probably I don't deserve you, but you made me better in uncountable ways. You were always there for me, supporting and encouraging me in my hardest time, and you were there to share my happiness in my best times, which wouldn't have been the same without you, not in the slightest. You showered me with love, and if I was able to give back a small amount of it, is probably more than many person experience in a lifetime. None of this would have been possible without you, this is why this work, and everything else, is dedicated to you.

Contents

List of Figures

List of Tables

Chapter 1

Introduction

On September 14, 2015 the LIGO interferometers captured a gravitational-wave (GW) signal from two merging black holes (BHs) with masses $\sim 36\,M_\odot$ and $\sim 29\,M_\odot$, respectively (see Abbott et al., 2016c; Abbott et al., 2016b; Abbott et al., 2016a). The event, named GW150914, was the first direct detection of GWs, and the proof that binary BHs (BBH) exist and can merge within a Hubble time. Furthermore, prior to GW150914, there were no unambiguous evidences for stellar BHs more massive than $\sim 25\,M_\odot$, which is the upper limit for the masses of BHs in known X-ray binaries (see Orosz, 2003; Özel et al., 2010; Miller-Jones et al., 2021). Thus, GW150914 also provides a robust evidence for the existence of heavy stellar BHs. To date, more than 90 BH-BH mergers have been reported by the LIGO-Virgo-KAGRA (LVK) collaboration, (Abbott et al., 2019; LIGO Scientific Collaboration and Virgo Collaboration et al., 2020; Abbott et al., 2023) and in about 70 of the events, at least one of the two BHs has mass $\gtrsim 25M_\odot$. Moreover, the number of detections is expected to significantly increase in the next years because of the recent O4 LVK observing run[1] and of the upcoming next-generation detectors (e.g., Einstein Telescope and Cosmic Explorer).

From the theoretical point of view, the formation and the evolutionary pathways of BHs and BBH are subject to significant uncertainties (see Mapelli, 2021; Spera, Trani, and Mencagli, 2022). Two main astrophysical formation channels have been proposed: the isolated binary evolution scenario and the dynamical formation pathway. In the former, the stellar progenitors evolve in complete isolation as a gravitationally bound pair and they eventually turn into compact objects and merge within a Hubble time (see van den Heuvel and De Loore, 1973; van den Heuvel, Portegies Zwart, and de Mink, 2017; Heggie, 1975; Tutukov and Yungelson, 1993; Brown, 1995; Bethe and Brown, 1998; Sandquist et al., 1998; Dewi, Podsiadlowski, and Sena, 2006; Justham, Podsiadlowski, and Han, 2011; Dominik et al., 2012; Dominik et al., 2015; Schneider et al., 2015; Belczynski et al., 2016; Belczynski et al., 2020; Marassi et al., 2019; Pavlovskii et al., 2017; Vigna-Gómez et al., 2018; Wysocki et al., 2018; Mapelli and Giacobbo, 2018; Neijssel et al., 2019; Graziani et al., 2020; Mandel and Fragos, 2020; Mandel and Farmer, 2022; van Son, Justham, and De Mink, 2021; van Son et al., 2022; Broekgaarden et al., 2021; Gallegos-Garcia et al., 2021; Marchant et al., 2021; Zevin et al., 2021). In the latter, a compact-object binary forms and shrinks after a series of gravitational few-body interactions in dense stellar environments (see Sigurdsson and Hernquist, 1993; Sigurdsson and Phinney, 1995; Moody and Sigurdsson, 2008; Banerjee, Baumgardt, and Kroupa, 2010; Banerjee, 2017; Banerjee, 2022; Downing et al., 2011; Mapelli et al., 2013; Mapelli, 2016; Ziosi et al., 2014; Rodriguez et al., 2015; Rodriguez, Chatterjee, and Rasio, 2016; Rodriguez et al., 2019; Di Carlo et al., 2019; Di Carlo et al., 2020a; Di Carlo et al., 2020b; Di Carlo et al., 2021; Rastello et al., 2019; Rastello et al., 2020; Rastello et al., 2021; Kremer et al., 2020; Wang, 2020; Wang et al., 2021; Wang, Tanikawa, and Fujii, 2022; Wang and Burrows, 2024; Ye et al., 2022).

However, both the isolated and the dynamical scenarios rely on many uncertain astrophysical processes, including the core-collapse supernova (ccSN) mechanism. Our knowledge

[1] See LIGO, Virgo AND KAGRA observing run plans.

of the SN engine is still limited, thus investigating the explosion mechanism, the stellar explodability, and the mass spectrum of stellar remnants is challenging.

Furthermore, from the LVK data, some peculiar distributions are emerging in some of the observed distributions of binary BHs (BBHs) observables. One particularly intriguing feature of the observed BBH population is the distribution of primary[2] BH masses. It presents accumulation regions and regions where there is a dearth of objects. Such features underlay that there must be some phenomenon in place, that combined with the initial conditions of the binaries, shapes the distribution of BH masses. The most robust statistical models (e.g., the POWER LAW + PEAK model, see Abbott et al., 2021; Abbott et al., 2023) foresee the presence of two peaks, one at $\sim 10\,M_\odot$ and one at $\sim 35\,M_\odot$. However, the origin of these feature is rather unclear, and many degenerate phenomena may be responsible for this, starting from the SN prescriptions to the evolution of a binary system and its initial conditions.

The interplay between uncertainties in the final fate of massive stars, their impact on binaries, and binary evolution processes remains an open problem. It requires to be tackled carefully, studying individually each component, in order to properly account for all the degenerate phenomena in place.

This is the purpose of this Thesis. In particular, I have investigated the BH mass spectrum obtained from the evolution of massive stars and their SN explosion. I also studied the implications of my results on the transition from directly collapsing massive star to stars that are unstable against pair-production, and on the BH mass distribution in the framework of isolated stars. Furthermore, I implemented my results in the population synthesis code SEVN, to study how different stellar and binary evolution prescriptions affect the final distribution of massive BHs, with a particular focus on the primary BH mass distribution.

In this Chapter, I will present the theoretical framework and the state-of-the-art knowledge on the evolution and final fate of massive stars (e.g. ccSN, but not only, see 1.1.4), on the binary stellar evolution processes, with a main focus on the isolated binary evolution scenario (see 1.2, as it is the framework we will treat in the following Chapters), and on the dynamical evolution scenario. In Chapter 2, I will present the numerical tool we used in our work, such as the HYPERION (HYdrodynamic Ppm Explosion with Radiation diffusION, see Section 2.1) code, I used for simulating the explosion of a ccSN. I will also describe the SEVN (Stellar Evolution for N-body, see Section 2.2) code, we used for simulating the evolution of population of binary systems.

In the following chapters, I will present the results of my work. Chapter 3 is devoted to discussing the results of the ccSNe simulations and their implications on the BH mass spectrum. We also provide some fitting formulas to predict the final remnant mass of a stellar progenitors on the basis of its properties at the presupernova stage. In Chapter 4, I will examine the outcome of the simulations of a large set of binary stars, performed with SEVN. I studied the effect of various initial conditions, of different prescriptions for the final fate of massive stars, including the results of Chapter 3, and of the binary stellar evolution processes on the BH mass distribution resulting from the evolution of isolated binaries.

Finally, Chapter 5 concludes the Thesis by summarizing the results and discussing potential future directions for this research.

1.1 Single star evolution

All stars with Zero-Age Main Sequence (ZAMS) mass $(M_{\rm ZAMS}) > 9\,M_\odot$ (see Limongi et al., 2023 for the precise value of this transition) are expected to end their life with a ccSN and form a compact object that can be either a BH or a neutron star (NS). However, the final

[2]The most massive BH of the binary. Hereinafter, with primary and secondary star/BH I will refer to the most and least massive object in the system, respectively.

remnant mass spectrum from single star evolution is still highly uncertain, as both stellar evolution and the final explosive processes are hampered by many uncertainties.

Furthermore, an alternative theory predicts that BHs can also form from gravitational collapse in the early Universe. Such objects are called *primordial BHs* (see Carr and Hawking, 1974; Carr, Kühnel, and Sandstad, 2016; Bird et al., 2016; Inomata et al., 2017). However, this Thesis focuses on stellar-mass BHs, and in this chapter, I will review the processes involved in their formation..

In this section, I will review the basics of the evolution of an isolated star and, as we are interested in the formation of massive BHs, the main mass-loss phenomena (e.g., stellar winds). Finally, I will summarize the state-of-the-art models predicting the final fate of massive stars.

1.1.1 Stellar evolution

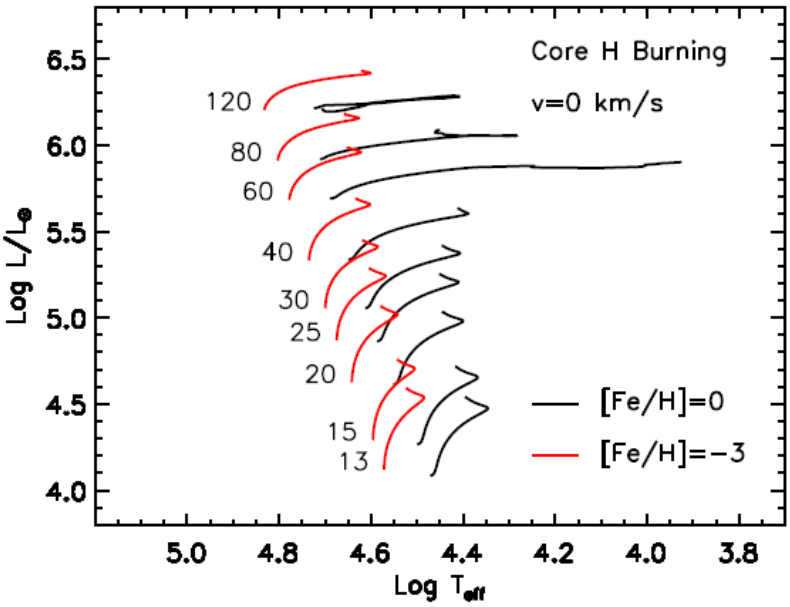

FIGURE 1.1: HR diagram of non-rotating stars during the MS for metallicity $\left[\mathrm{Fe/H}\right] = 0$ (black lines), and $\left[\mathrm{Fe/H}\right] = -3$ (red lines). This figure is taken from Limongi, 2017, and corresponds to Figure 2 in their paper.

Stars are self-gravitating objects composed of hot plasma that exist in a state of hydrostatic equilibrium. They achieve stability by balancing gravitational forces with outward pressure, a state known as hydrostatic equilibrium. They lose energy from their surface in the form of photons and/or from their core in the form of neutrinos. The equilibrium is maintained by the balance between the pressure gradient and gravitational forces. This pressure is provided by a combination of radiation, ideal gas, and partially or fully degenerate electrons. Since stars lose energy—either due to being hotter than their surroundings or because of neutrino losses—they simultaneously heat up and shrink, in accordance with the virial theorem. According to this theorem, a portion of the gravitational energy gained through contraction is converted into internal energy, while the remainder compensates for the energy lost. When the core temperature of a star reaches sufficiently high levels, thermonuclear fusion reactions occur, and nuclear energy replenishes the energy lost. This process temporarily halts gravitational contraction. As the available nuclear fuel becomes depleted, gravitational contraction and heating resume until the next source of nuclear fuel ignites. Consequently, the life of a star

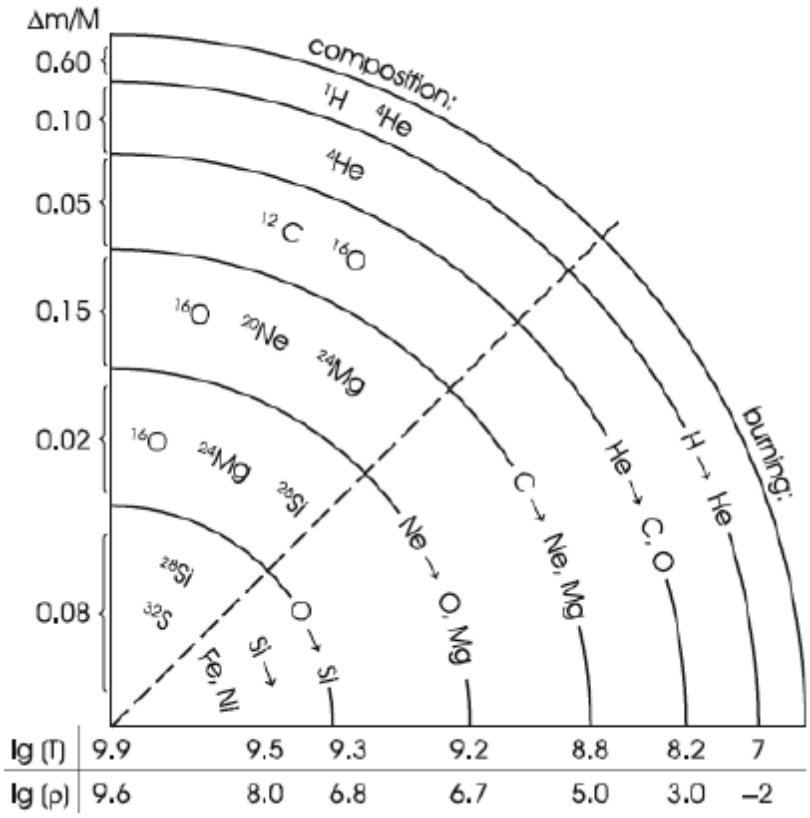

FIGURE 1.2: Stellar structure after all the central burning stages. Figure from Rudolf Kippenhahn, 2012.

can be understood as a continuous gravitational contraction of a self-gravitating ball of gas, occasionally interrupted by periods during which nuclear fusion provides the energy lost as radiation and/or neutrinos.

Upon its formation a massive star ignites into its core the thermonuclear fusion of hydrogen, defining the Zero Age Main Sequence (ZAMS). In massive stars, the core hydrogen burning phase is the longest-lasting nuclear burning stage and is primarily powered by the carbon-nitrogen-oxygen (CNO) cycle. Because of the high nuclear energy flux, stars that burn hydrogen via the CNO cycle will form a convective core that will progressively shrink, leaving behind a region of partially processes CNO materials. Furthermore, in rotating stars, these materials may be dredged up to the surface, providing observational constraints on angular mixing efficiency.

When the central hydrogen mass fraction drops below 10^{-7}, core H burning ceases, the convective core vanishes, and gravitational contraction begins. The H burning then shifts in shells.

The core H burning lasts between $10^6 - 10^7$ yr, for stars in the mass range $13 - 120\,M_\odot$. Furthermore, during the core-H burning (also known as Main sequence, MS) the star evolve towards increasingly higher luminosity and lower effective temperatures. This behavior outline a diagonal line in the Hertzsprung-Russell (HR) diagram, as outlined in Figure 1.1 (Figure 2 from Limongi, 2017).

During this phase mass loss is quite efficient and it scales directly with the mass (i.e. luminosity) and the metallicity (see Section 1.1.2 for further details) .

After the H-core depletion, the star starts the shell H-burning, and the burning shells move outwards in mass, as the He core mass increases.

During this phase the star evolves toward lower effective temperatures (i.e. the red side of the HR diagram) at constant luminosity, until the central He-burning is activated. The timescale for such a transition is highly correlated with the treatment of the chemical mixing on the edge of the He core, i.e., the criterion for the transition from radiative to convective energy transport (see Schwarzschild and Härm, 1958; Stothers, 1970; Langer, El Eid, and Fricke, 1985; Limongi, 2017). Once the He-core burning is activated, the evolution of the star depends on the metallicity and on the position on the HR diagram at the end of the core-H burning. This burning stage lasts for $10^6 - 10^5$ yr (i.e. roughly one order of magnitude less than the MS) and the evolution of the star is mainly driven by the He-core mass. At the end of the He-core burning stage, the star will be left with a core composed of different abundances of ^{12}C and ^{16}O. The relative abundances of these two elements, in combination with the CO core mass, will rule the evolution of the star from this moment onwards (see Chieffi and Limongi, 2020). From core helium exhaustion to the presupernova stage, massive stars undergo four major nuclear burning phases, named after their primary fuel: carbon, neon, oxygen, and silicon (see Limongi and Chieffi, 2008 for a detailed discussion of the nucleosynthesis occurring during each one of these nuclear burning). At the end of these burning stage, the star will present the characteristic *onion shell structure*, which is shown in Figure 1.2. The evolution of a massive star ends when its core is composed of iron-group elements (usually called "iron core"). This is because all the thermonuclear reactions until the formation of the iron core are *exothermal reactions*, thus they release energy, balancing the thermal energy that the stars loses via radiation, other than ensuring countering the self-gravity of the star. This behavior changes upon the formation of an iron core, as the energy per-nucleon decreases for elements heavier than $^{56}_{26}$Fe. Thus, forming such elements via thermonuclear reactions *requires* energy, instead of releasing it. This prevents the star from efficiently producing elements heavier than iron through core burning.

1.1.2 Stellar Winds

In the previous section, I discussed the evolutionary stages of massive stars. A key factor shaping their evolution is mass loss, which influences both their outer layers and internal structure.

In this section, I will briefly review the current formalism for stellar winds, as they are a crucial factor in determining both the evolution and the final fate of massive stars.

Wind mass loss arises from complex interactions between radiation and matter in stellar atmospheres, playing a crucial role in determining the final fate of massive stars. This phenomenon was firstly proposed by Saha, 1919, which suggested that the interplay between radiation and matter, in the outer layer of a star, could lead to inelastic impact of photons with the elements in the stellar surface. Thus, the matter would acquire a forward velocity and be expelled from the star.

As of now, we know that the strongly anisotropic and continuous component of photons from the innermost layers constantly exchanges energy and momentum with free electrons, ions, atoms and dust grains in stellar atmospheres. Projecting these interaction on the radial coordinate (i.e. assuming spherical symmetry), the momentum equation take the form:

$$v\frac{dv}{dr} = -\frac{GM}{r^2} - \frac{1}{\rho}\frac{dp}{dr} + g_{rad} \tag{1.1}$$

where M is the stellar mass, r is the radial coordinate, $v(r)$, $\rho(r)$, and $p(r)$ are the radial velocity, density and pressure profiles, respectively, and g_{rad} is the acceleration term due to radiation. Thus, the net effect of stellar winds is to add the g_{rad} term to the usual hydrostatic

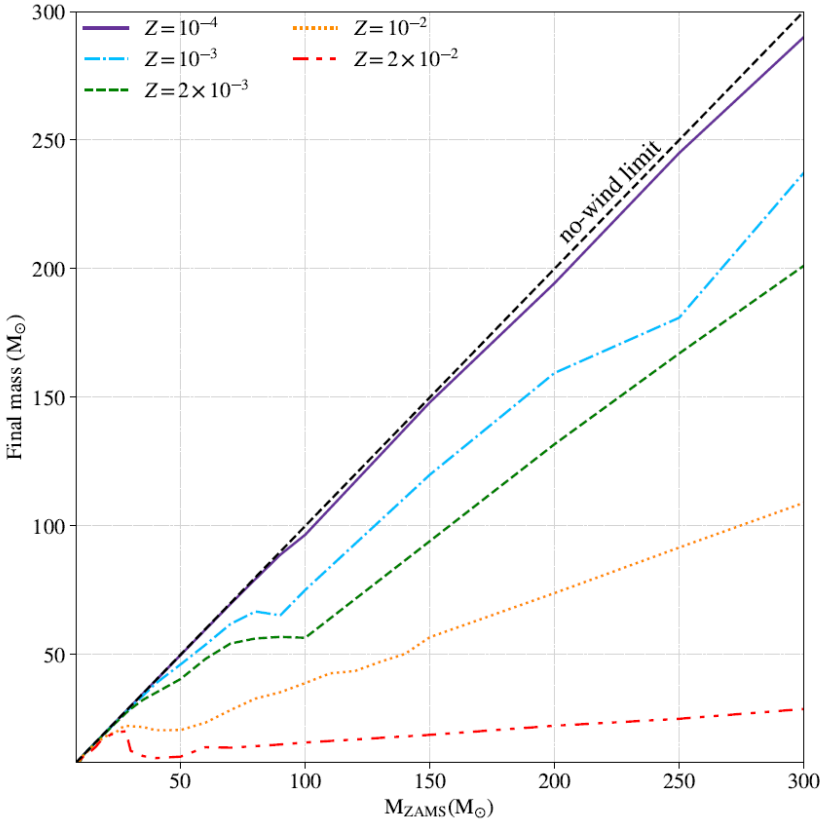

FIGURE 1.3: Final mass of massive stars as a function of their initial mass for various metallicities. The diagonal dashed-line correspond to the no-wind limit. This figure is taken from Spera, Trani, and Mencagli, 2022, and corresponds to Figure 2 in their paper.

equilibrium equation. This latter term can be described as

$$g_{rad} = g_{con} + g_{line} \tag{1.2}$$

where g_{con}, and g_{line} are the contribution to the radiative acceleration that are induced by electron scattering and spectral line opacity, respectively. Specifically, the term g_{line} means that there is a selection effect, which chooses only some precise lines, depending on the absorption frequency of the elements in the outer layers of the star. It is worth mentioning, that within this terms lay also the dust-driven winds, that are mainly efficient in cold ($T_{eff} \leq 10^4$) red super giants (RSGs, see also Loon et al., 2005).

One of the first model proposed to treat stellar winds considering the g_{line} term is the CAK model (see Castor, Abbott, and Klein, 1975, and named after the initials of the authors), that introduced a multiplier in the equation for stellar winds, that is:

$$v\frac{dv}{dr} = -\frac{GM}{r^2} - \frac{1}{\rho}\frac{dp}{dr} + g_{con}\Big[1 + M(\tau)\Big] \tag{1.3}$$

where τ is the optical depth of the stellar wind, and it depends on the opacity where the interaction take place, i.e. is evaluated case by case and *locally*. Furthermore, they also included the wind velocity gradient, as prescribed by Sobolev, 1960. From the work of Castor, Abbott, and Klein, 1975, it was apparent that all the spectral lines needed to be included $M(\tau)$, and that this term was $M(\tau) >> 1$, i.e. that stellar winds in hot massive stars are line driven.

This treatment, refined over time to include more spectral lines, revealed a strong metallicity dependence of stellar winds. In fact, in the UV (i.e. the peak frequency for hot massive

stars), hydrogen and helium present few spectral lines and the line-absorption mechanism is rather inefficient. On the other hand, metals have many line spectra in the UV band, which makes the line-absorption mechanisms very efficient in transferring energy to the matter, causing the onset of strong stellar winds, that are coupled with high mass loss efficiency throughout stellar evolution. In Figure 1.3, this effect is apparent, as stars with lower metal content retain much more mass than stars at high Z, that instead experience severe mass loss episodes during their life. This will influence the ability of massive stars to produce heavier BHs, depending on their initial metallicity and mass.

Abbott and Lucy, 1985 proposed a different approach, through Monte Carlo (MC) simulations. In this approach, photon packets are tracked on their journey from the photosphere to the outer wind. At each interaction, momentum and energy are transferred from the photons to the gas particles. This included also the possibility for multiple photon scatterings and pushed Vink, de Koter, and Lamers, 2001 to revise the $\dot{M} - Z$ relation for stellar winds, obtaining:

$$\dot{M} \propto L^{2.2} M^{-1.3} T_{eff} \left(\frac{v_\infty}{v_{esc}} \right)^{-1.3} \tag{1.4}$$

where the mass loss $\dot{M}$ is function of the star's luminosity L, its mass M and its effective temperature T_{eff}, with a factor proportional to the escape velocity v_{esc} and the terminal flow velocity v_∞. The main success of these models was that they were equally successful for relatively weak winds as they were for dense O-star winds. Vink, de Koter, and Lamers, 2001 found that the inner subsonic stellar winds for O-stars at high Z were caused by the iron-group elements. This is because, they are extremely efficient absorbers as their complex atomic structure allows for millions of different lines. On the other hand, for lower metallicities and outer regions of the stars, they found that the main contributor to stellar winds come from CNO elements. Prescriptions on stellar winds by Vink, de Koter, and Lamers, 2001 for massive stars and by Vink and Koter, 2005 are the ones currently adopted by most state-of-the-art stellar evolution codes.

Nonetheless, despite significant progress, several caveats remain in our understanding of stellar winds, which introduce substantial uncertainties into models of massive star evolution:

- CAK theory and MC approach work excellently for supersonic winds, while they struggle to reproduce subsonic winds (see Vink, 2022 for further details);
- Stars may approach Eddington luminosity limit during their life. This may cause enhanced mass loss, which may work independently on the metallicity (see Vink and de Koter, 2002; Yoon and Cantiello, 2010; Gräfener and Hamann, 2008; Gräfener et al., 2011; Chen et al., 2015; Tang et al., 2014);
- Homogeneity of stellar winds: observations seem to suggest that winds are clumpy, though the clumps' formation mechanism and evolution is still under debate (see Davies, Oudmaijer, and Vink, 2005; Puls et al., 2006. The properties of such clamps are highly uncertain as well, however, they significantly affects their impact on stellar winds (see Muijres et al., 2011).

When combining all these uncertainties the error associated to stellar winds they may induce even a factor of 2 uncertainty (typical for state-of-the-art models, e.g., Vink, 2022), that might have important consequences on the nature and mass spectrum of compact objects.

1.1.3 Stellar rotation

In this section, I will summarize the main effect that angular rotation induces in the evolution of a massive star. This section will largely be based on Meynet, Ekström, and Maeder, 2006; Chieffi and Limongi, 2013; Limongi and Chieffi, 2018; Roberti, Limongi, and Chieffi, 2024.

Stellar rotation is a phenomenon intrinsically difficult to model for state-of-the-art stellar evolution codes, as they are 1D codes working in spherical symmetry, while rotation is an effect inherently 2D (if not 3D). However, Kippenhahn and Thomas, 1970 and Endal and Sofia, 1976, showed that, with some assumption, it may be projected on 1D. The basic ideas are that one can evaluate the averaged mechanical and thermal effects induced by rotation, as prescribed by Kippenhahn and Thomas, 1970, with some assumptions:

- Cylindrical symmetry for angular velocity ω: this assumption is required to define equipotential surfaces. Furthermore, it allows to maintain the same form in the stellar structure equations, with the only addition of two *form factors*. They account for the mechanical and thermal distortions induced by angular rotation.

- $\omega =$ const on isobar surfaces.

This last assumption was further supported by the work of Zahn, 1992, showing that an assumption initially chosen for the sake of simplicity indeed captured the actual phenomenon. This approximation is currently called *stellular rotation*, and implies that the equipotential surfaces coincide with the isobars, an approximation already employed by Kippenhahn and Thomas, 1970, even if not under this definition.

However, this approximation allows only for the star to rotate as a solid body. This limitation has been surpassed thanks to the work of Meynet and Maeder, 1997, which demonstrated that even by relaxing the assumption of cylindrical symmetry—thus dropping the requirement for a conservative field, referred to hereafter as the *conservative case*—it was still possible to maintain the equations for stellar structure proposed by Kippenhahn and Thomas, 1970. However, this came with the price that the values of ρ and T, which were constant along the isobars in the cylindrical symmetry approximation, in the formalism proposed by Meynet and Maeder, 1997 have to be replaced with appropriate averages on each isobar. Nevertheless, from a formal point of view, the only variation is that the values of ρ and T need to be interpreted as constant along the isobars in the *conservative case*, while in the non-*conservative case* these two variables are averages along the isobars.

At this point the formalism is ready to be implemented in a stellar evolution code to simulate the effect of angular rotation on a star during its life. However, angular rotation is a phenomenon that should be considered on top of the other dynamical effects already in place in the internal structure of a massive star. Rotation introduces an important factor, whose net effect is to redistribute angular momentum and chemical species, and this affects significantly the traditional dynamical instabilities (usually determined on the basis of the Schwarzschild and/or Leydoux criteria) such as semiconvection in the H-burning, induced semiconvection in He-burning, and the possible occurrence of some overshooting. Furthermore, rotation also introduces other dynamical instabilities (e.g. meridional circulation and shear instability, see Chieffi and Limongi, 2013; Limongi and Chieffi, 2018; Roberti, Limongi, and Chieffi, 2024). To account for the effect of angular rotation on the stellar structure, one has to compute the transport of angular momentum and chemical species along the stellar evolution. For the former, there are various treatments, proposed by Chaboyer and Zahn, 1992; Talon and Zahn, 1997; Maeder, 2003; Mathis, Palacios, and Zahn, 2004. The latter is generally modeled along the formalism proposed by Chaboyer and Zahn, 1992; Zahn, 1992. In the asymptotic regime, the effect of rotation on the redistribution of chemical species can be described as a pure diffusive process.

The inclusion of some angular momentum changes many evolutionary properties of stars. The net effect of angular rotation can be summarized in two main effects:

- **Lowering of the effective gravity**: Centrifugal force and angular momentum transport, makes the stars expand, thus it evolves towards lower temperatures
- **Rotation driven mixing**: the interplay among convection, meridional circulation and turbulent shear determines both the angular momentum transport and the mixing of the chemicals. This latter result in longer central burning stages, i.e. stars with same $M_{\rm ZAMS}$ produce more massive cores than their non-rotating counterparts.

This two effects are generally in competition, since the former produces redder stars, while the latter result in brighter stars. For increased luminosity also the mass loss is more efficient, i.e. rotating stars are more prone to be stripped of their H-envelope, producing more WR stars.

Furthermore, it is worth noting that the effect of angular rotation have to be considered coupled with the other stellar parameters, e.g. $M_{\rm ZAMS}$ and Z, and one has to consider that the effects we discussed before for various masses and metallicities are even enhanced by stellar rotation.

However, from the point of view of the demography of massive BHs, the effects of angular rotation on a star can be summarized as two: *enhanced mass loss* and production of *more massive cores*, with respect to the non rotating counterparts.

Therefore, since the final fate of a massive star is ruled by its structure at the end of its life, from rotating stellar progenitors we generally will expect a population of compact WR stars at the pre-SN stage. Furthermore, these stars will have massive cores and very bounded structure. This will allow for the production of more massive BHs but also lower limits for the onset of pair-instabilities (see Section 1.1.4.2 and Section 3.3).

1.1.4 Final fate of a Massive star

1.1.4.1 Core-collapse Supernova

All stars with Zero-Age Main Sequence (ZAMS) mass $\left(M_{\rm ZAMS}\right) > 9.2\,{\rm M}_{\odot}$ (Limongi et al., 2023) are expected to end their life with a ccSN and form a compact object that can be either a BH or a neutron star (NS), depending on the mass of the stellar progenitor. These are the stars that are able to ignite hydrostatic Ne burning and form an iron-group core. However, once the Fe core is formed, the star is not sustained anymore by either the core's nuclear reactions or electron degeneracy pressure and it start collapsing. When the core's temperature reaches $\sim 10^{10}$ K, the photodisintegration of iron-group elements becomes the dominant interaction mechanism

$$^{56}{\rm Fe} + \gamma \rightarrow 13\,^{4}{\rm He} + 4{\rm n} \tag{1.5}$$

This process accelerate the collapse of the core, as it drains a significant amount of radiative energy ($\sim$ 2MeV per nucleon) from the star. Because of the accelerated core-collapse the core reaches temperature high enough that even α particles begin to be photodisintegrated

$$^{4}{\rm He} + \gamma \rightarrow 2{\rm p} + 2{\rm n} \tag{1.6}$$

Furthermore, at this stage even electron capture phenomena are efficient, because of the high electron kinetic energy, such that

$$p + e^{-} \rightarrow {\rm n} + \nu_e \tag{1.7}$$

This results in another energy-loss source, as neutrinos are able to free stream away, without interacting further with the stellar matter. Furthermore, this process also causes the an enrichment of neutrons, that will eventually halts the first stage of the core-collapse.

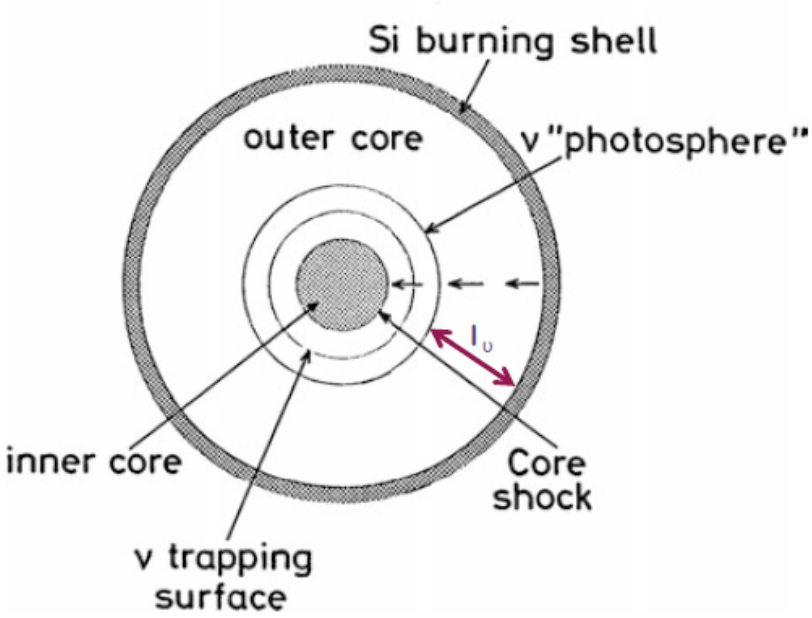

FIGURE 1.4: Cartoon of a core-collapsing star at the core-bounce. The central dashed region correspond to the proto-NS, and on its surface the shock-wave is forming. Moving outwards there is an infalling region, enclosed by the neutrino trapping region, which is so dense that neutrinos cannot free stream away. Finally, the last surface, above which the mean free path (l_ν) of neutrinos allow them to leave the star.

In fact, at this stage the core is already collapsing on the dynamical timescale, that at densities of $\sim 10^{10}\text{gcm}^{-3}$ means few milliseconds. As a consequence of the core-collapse, a very compact degenerate structure, mainly composed by neutrons (called proto neutron star, proto-NS), that can halt the collapse is formed, with a density $\sim 10^{14}\text{gcm}^{-3}$ and a typical binding energy of $\sim 10^{53}$ erg.

When a proto-compact object forms, the collapse ceases because it cannot accrete additional matter and it reaches a new stable state. In this state, the stellar matter is supported against its own gravitational pull by the internal pressure of the nucleon gas, which is highly incompressible due to the repulsive component of the nucleon-nucleon interaction potential (see Janka, 2017). However, the outward matter continues its collapse, overshooting this new equilibrium state, but because of the incompressible nature of the proto-NS the matter bounces back, generating a shock wave, that starts propagating outwards. This is the so called *bounce-shock mechanism*, firstly proposed by Colgate and White, 1966. If the shock was completely elastic and no dissipation mechanism was present this could have been sufficient in ejecting the matter above the shock, resulting in a successful SN explosion. However, the shock dissipates most of its energy while traveling outwards, through the infalling material, until it stalls at about hundreds of kilometers from the center, well within the Fe core, failing to produce a successful SN. This is because, the shock photodissociates iron elements as it moves through the core, and this process drains most of its energy.

At this stage, a new engine is required in order to produce a *successful* SN. The current reference model for ccSNe is based on the neutrino driven explosion, firstly proposed by Bethe and Wilson, 1985 (see also Burrows, Hayes, and Fryxell, 1995; Janka and Mueller, 1996; Janka, Melson, and Summa, 2016; Janka, 2017; Kotake, Sato, and Takahashi, 2006; Herant et al., 1994; Foglizzo, Scheck, and Janka, 2006; Burrows, Radice, and Vartanyan, 2019; Aguilera-Dena et al., 2022).

The basic idea is that at the central densities reached after the neutronization processes

neutrinos are essentially trapped in the core. Thus, they start a congestion that results in the stall of the neutronization process at $\sim 10^{12}\,\mathrm{g\,cm^{-3}}$, see Figure 1.4 for a schematic representation. The latter completes only seconds after the collapse, when most of the very high-energy neutrinos have had time to escape the core and to deposit part of their energy in the material behind the former shock wave. If sufficient energy is injected into the stalled shock by neutrino heating it can revive, initiating a successful SN explosion.

However, this process is inherently non-spherical, as 1D simulations of neutrino-driven explosions struggle to generate *successful SNe*, while higher dimension simulations (as first 2D and in recent years 3D) revealed that the region that receive energy injection via neutrino-heating experience non-radial instabilities. These latter have twofold effects: (i) they generate asymmetric explosions, and (ii) convert thermal energy into kinetic energy, further fueling the explosion, via the *convection-enhanced neutrino-driven mechanism* (see Burrows, Hayes, and Fryxell, 1995; Janka and Mueller, 1996).

State-of-the-art 3D simulations predict *successful SNe* for low mass stars ($M_{\mathrm{ZAMS}} \leq 30\,\mathrm{M_\odot}$), while struggle in predicting the outcome of more massive stars. Furthermore, such sophisticated simulations are subject to major uncertainties, especially on the progenitor star side, that are obtained from 1D stellar evolution codes and need to be projected on 3 dimensions, and are computationally intensive. Because of this, we struggle to follow the evolution of the explosion for more than a few seconds (Burrows et al., 2020; Bollig et al., 2021; Burrows et al., 2024; Wang and Burrows, 2024). However, the formation of massive BHs takes place on longer timescales, which are out of reach for state-of-the-art 3D models.

To overcome the computational limitations of detailed simulations, we resort to simplified models that artificially stimulate SN explosions by injecting some amount of kinetic energy (i.e., a kinetic bomb, see e.g. Limongi and Chieffi, 2003; Chieffi and Limongi, 2004) or thermal energy (i.e., a thermal bomb, see e.g. Thielemann, Nomoto, and Hashimoto, 1996) at an arbitrary mass coordinate location of the progenitor model. Alternatively, the inner edge of the exploding mantle is moved outward like a piston following the trajectory of a projectile launched with a specific velocity in a given potential (see Woosley and Weaver, 1995). Independently of the adopted techniques, the evolution of the shock is followed by means of 1D hydrodynamical simulations. The main advantage of this approach is that the computing cost is relatively small. Thus, it is possible to follow the evolution of the shock over longer timescales and to estimate the amount of fallback and the final remnant mass (see, e.g. O'Connor and Ott, 2011; Fryer et al., 2012; Ugliano et al., 2012; Ertl et al., 2016; Sukhbold et al., 2016; Sukhbold, Woosley, and Heger, 2018).

Furthermore, the 1D approach has been extensively used to study the SN explosion yields, especially in the context of explosive nucleosynthesis (see (Shigeyama and Nomoto, 1990; Thielemann, Hashimoto, and Nomoto, 1990; Thielemann, Nomoto, and Hashimoto, 1996; Nakamura et al., 2001; Nomoto et al., 2006; Umeda and Nomoto, 2002; Moriya et al., 2010; Chieffi and Limongi, 2013; Limongi and Chieffi, 2018)).

1.1.4.2 Pair-Instabilities

While for massive stars in the mass interval $M_{\mathrm{ZAMS}} \sim 9 - 80\,\mathrm{M_\odot}$, we have plenty of observations of spectacular transients, and a lack of robust theoretical models able to explain unambiguously these phenomena, for more massive stars is true the opposite.

We know that very massive stars ($M_{\mathrm{ZAMS}} \sim 80 - 200\,\mathrm{M_\odot}$) are radiation pressure dominated. Before running out of viable nuclear fuel, they can reach a thermodynamic state where electron-positron (e^+e^-) pair-production robs them of radiation support, triggering their collapse, hence the name pair-instability. This model is well known from the theoretical point of view (e.g. Fowler and Hoyle, 1964; Barkat, Rakavy, and Sack, 1967; Rakavy and Shaviv, 1967; Woosley, 2017) and there is general consensus among the astrophysical community. As a consequence

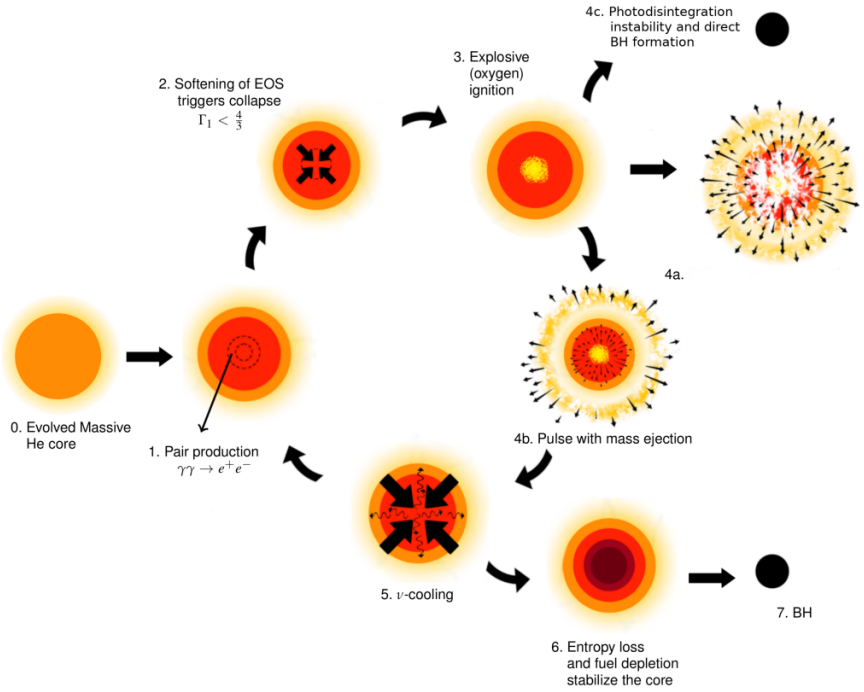

FIGURE 1.5: Cartoon representing the core evolution through (P)PISN. Step 3 represents when the evolution of the star takes different path depending on the binding energy of the star. 4a if the thermonuclear explosion energy surpasses the binding energy of the star, 4b if the thermonuclear episode unbound only part of the stellar structure (usually the H-envelope), and 4c when the energy lost via pair-instabilities triggers the direct collapse of the star (usually very massive stars). Figure from Renzo et al., 2020.

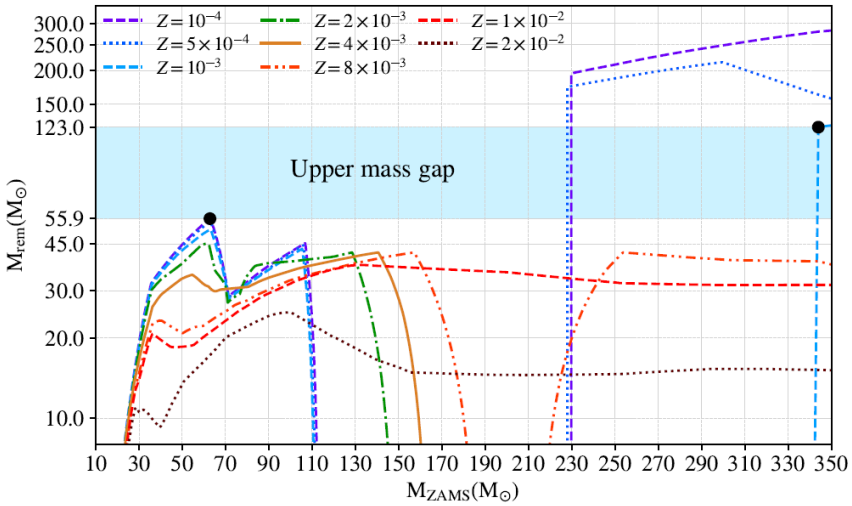

FIGURE 1.6: Mass of the BH as a function of the initial mass of its progenitor star, for different values of metallicity. The shaded cyan area shows the location of the upper mass gap. The two black points set the lower edge and the upper edge of the gap. Figure from Spera and Mapelli, 2017.

of the collapse induced by pair-instabilities, a thermonuclear fusion episode is triggered and it may be strong enough to power an explosion that completely destroys the star. However, while there is theoretical consensus, we are still lacking observational evidences (e.g. Briel et al., 2022; Gabrielli et al., 2024).

In this section, I will briefly present the theoretical model describing pair-instabilities

and their net effect on massive stars, especially from the point of view of the demography of massive BHs.

Stars that undergo pair-instabilities are those star that are massive enough that, during the nuclear burning stages, usually when the core is oxygen-dominated (see Fowler and Hoyle, 1964; Barkat, Rakavy, and Sack, 1967; Rakavy and Shaviv, 1967; Renzo and Smith, 2024), reach a central temperature of $T \sim 7 \times 10^8$ K. When this happens the following reaction take place:

$$\gamma\gamma \rightarrow e^+e^- \rightarrow \begin{cases} \nu_e^- \nu_e^+ \\ \gamma\gamma \end{cases} \tag{1.8}$$

Thus, a photon couple $\gamma\gamma$ produce an electron-positron pair e^+e^-. This latter then annihilates, producing either a neutrino-antineutrino pair $\nu_e^-\nu_e^+$, which stream out of the star carrying away their energy, or into a pair of photons $\gamma\gamma$, which on average have lower energy than the original photons. When this occurs in a star whose hydrostatic equilibrium depends on radiation pressure (e.g. a very massive star), it can lead to a catastrophic instability: the production of e^+e^- pairs effectively consumes radiation energy density. This softens the equation of state, causing a local thermal instability in the star. Figure 1.5 shows the evolution of a star undergoing pair-instabilities. Once the pair-production starts (step 1) and the EOS is softened, triggering the collapse (step 2) the thermonuclear explosive episode is initiated (step 3), and the final fate of the star depends on its core mass, and on the ratio between the energy released in the explosive burning and the binding energy of the star.

If the energy released in the explosion is enough to unbound the entire star, a pair-instability supernova (PISN) take place (step 4a). This is the phenomenon originally predicted by Fowler and Hoyle, 1964; Barkat, Rakavy, and Sack, 1967; Rakavy and Shaviv, 1967, which leads to full disruption of the star, leaving no remnant.

For slightly lower stellar masses, the central temperatures reached (and consequently, the nuclear burning rate) are lower: this results in less energetic explosions that fail to completely unbind the star. However, the explosion triggers one (or more) pulse that propagates through the star ejecting some material, depending on the strength of the pulse (see Barkat, Rakavy, and Sack, 1967; Chatzopoulos and Wheeler, 2012; Woosley, 2017; Woosley, 2019; Farmer et al., 2019; Marchant et al., 2019; Renzo et al., 2020; Farag et al., 2022). When these events occur, they may appear as bright transients that go under the name of pulsational pair-instability supernovae (PPISN). Even if the explosion is not strong enough to unbind and destroy the star, the thermonuclear explosion causes the core to expand. Thus, the core's temperature and density decrease, and the pair-production ceases. Afterwards, the star relaxes on the thermal timescale via neutrino cooling (see Barkat, Rakavy, and Sack, 1967; Fraley, 1968). Depending on the pulse efficiency, it may happen even that the density and temperature are driven to values low enough to shut off the neutrino cooling mechanism. If this latter is the case, the energy in the star resumes to be carried through photons and convection (see Woosley, 2017; Marchant et al., 2019; Renzo et al., 2020). After the relaxation time (spanning between few days to $\sim 10^5$ yrs, see Woosley, 2017; Renzo et al., 2020), pair-production may resume in the star's core, until it is eventually completely stable, either because of (i) the exhaustion of viable nuclear fuel, (ii) the mass loss due to pulses or (iii) the loss of energy during the cooling phase. Once the star is back to being stable the normal stellar evolution resumes, with the various central burning stages expected from a massive stars performed with what nuclear fuel is left after the pulsating phase. These stars will eventually produce an iron-group core and undergo a core-collapse. These stars are generally expected to directly collapse, through *failed SNe*, as the energy budget of the shockwave will not be enough to unbind the star (e.g. Woosley, 2017; Farmer et al., 2019; Costa et al., 2021; Hendriks et al., 2023).

Finally, stellar progenitors that are even more massive than the stars undergoing PISN

trigger a second kind of instability: the photodisintegration instability (see Bond, Arnett, and Carr, 1984; Fryer, Woosley, and Heger, 2001; Heger et al., 2003). In this stars, the energy released by the thermonuclear explosion instead of being employed to accelerate the matter, generating either a PISN or a PPISN, is used to photodisintegrate nuclei (C, O, Si, and the product of the thermonuclear explosion). Therefore, the explosion energy is not transformed into kinetic energy, canceling out the dynamical effect of pair-instability and causing the star to directly collapse into a massive BH ($\gtrsim 250\,M_\odot$).

However, while the physical phenomenon leading to the onset of pair-instabilities is theoretically well comprehended, the criterion for the transition from the different regimes is not fully understood. The processes triggering pair-instability are all taking place in the CO core of a massive star, thus the general approach is to use this latter as a proxy for the onset of pulsational-instabilities (see Spera and Mapelli, 2017; Woosley, 2017; Farmer et al., 2019; Costa et al., 2021). Such a metric is prone to some uncertainties, as recent works pointed out that several other factors play a role in the onset of (P)PISN, such as the chemical abundances in the CO core (that may be due to different $^{12}C(\alpha,\gamma)^{16}O$ reaction rates see Farmer et al., 2019; Chieffi and Limongi, 2020), or the role of angular rotation (see Chieffi and Limongi, 2013; Limongi and Chieffi, 2018; Costa et al., 2021), or the formalism for modeling dynamical instabilities in the star (see Renzo et al., 2020). Furthermore, one has also to consider that massive stars are often found in binaries, thus binary interaction may affect the property of the stars, and so the onset of pair-instabilities (see Vigna-Gómez et al., 2018; Marchant et al., 2019; Di Carlo et al., 2019; Di Carlo et al., 2020a; Renzo et al., 2020; Zapartas et al., 2021).

1.1.4.2.1 PPISN and PISN effect on the BH mass spectrum Even if there is no unanimous consensus on the criteria for the onset of the various pair-instability regime, their effect on the BH mass spectrum is well understood. PPISNe significantly enhance the mass loss of the stellar progenitor, while PISNe completely destroy it. Thus, they create a gap in the BH mass spectrum, referred to as the *upper-mass gap*. This gap ranges from $M_{\rm low} \sim 60-80\,M_\odot$ to $M_{\rm high} \sim 200-250\,M_\odot$. Figure 1.6 shows a typical BH mass spectrum with the *upper-mass gap*, obtained from a population of single stars, at various metallicities (the figure is taken from Spera and Mapelli, 2017).

This gap, especially its lower edge, is of great interest in the study of massive BHs, both from single stars and from binaries. In the former scenario, it will allow us to put further constrains on the details of the physical processes in place both during the stellar evolution and during ccSNe. This is because the lower edge of the mass gap will be the result of *failed SNe*, i.e. stars that directly collapse into BHs. In the latter scenario, is even more important to properly constrain the lower edge of the mass gap, as some of the progenitors of GW mergers had masses lying in the mass gap (e.g. LIGO Scientific Collaboration and Virgo Collaboration et al., 2020). As of now, to explain the formation of such massive BHs in the context of our current formalism for stellar evolution some complex phenomena are needed (e.g. hierarchical mergers, see Kimpson et al., 2016; Di Carlo et al., 2019; Di Carlo et al., 2020a, but also other channel have been proposed as in Roupas and Kazanas, 2019; Yang et al., 2019; Arca Sedda, 2020; Safarzadeh and Haiman, 2020; Liu and Bromm, 2020; Tanikawa et al., 2021; Farrell et al., 2021). However, future work that better details the transition from ccSNe to PPISNe is needed (for a review, see Renzo and Smith, 2024).

Ultimately, PPISNe are believed to have an additional impact on the black hole mass distribution from massive binary systems. Because of PPISNe, most stars with $60-80\,M_\odot \lesssim M_{\rm ZAMS} \lesssim 130\,M_\odot$, are expected to lose their hydrogen envelope and die as naked-He stars. As a consequence, the final BH masses of stars undergoing PPISN are expected to cluster in the $35-45\,M_\odot$ mass interval, on top of the BHs produced through ccSN from lighter stars, creating an accumulation of BHs in that particular mass-interval. This feature has been retrieved in the observed population of merging BBH detected by the LIGO-Virgo-KAGRA

(see Abbott et al., 2021; Abbott et al., 2023). However, many more effect may concur with the onset of PPISN in this accumulation of BHs, starting for the processes related to the evolution of a binary star system (see for further details Chapter 4), or the effect of dynamical interactions in a dense environment.

1.2 Isolated binary evolution

Many stars, especially the more massive ones, are born in binaries or higher multiple stellar systems. Moe and Stefano, 2017 showed that the multiplicity of stellar systems increases with the stellar mass. This suggests that NS and BH stellar progenitors are born not as single stars, but as binary members (and in a smaller part even of three or more stellar systems). Therefore, studying binary interactions between two massive stellar companions is crucial to understand the astrophysical evolution of many GW merger progenitors.

In this section, I will present the various binary processes that may affect binary stars.

1.2.1 Stellar Tides

In tightly bound stellar binaries, finite-size effects, such as tidal forces, become significant. Thus, the point mass approximation fails to adequately describe their motion. Eggleton, Kiseleva, and Hut, 1998 derived the equations of motion for a binary in such a state. The basic idea is that the star is deformed by its companion, generating a gravitational quadrupole moment. However, the response of the quadrupole moment is not instantaneous and the delay allows the coupling between rotational and orbital angular momenta, on top of the dissipation of orbital energy in the stellar interior because of the quadrupole momentum. The precise formulation of the tidal dissipation depends on the star's structure, as shown by Zahn, 1977 (see also Spera, Trani, and Mencagli, 2022).

Stellar tides introduce three main effects on the binary:

- Circularization of the orbit for eccentric binaries;
- Spinning-up of stars in close binaries: this effect synchronizes the rotation periods of the two stars to the orbital period, and it aligns the spin of the two stars with the angular momentum vector of the binary;
- Chemical homogeneous evolution (CHE): Tidal spin-up in a close binary introduces rotational mixing of the stellar interior, which tends to flatten its chemical composition gradient.

The first two effects are especially important in the context of GWs, as the tidal spin-up may change the original spins of the two compact objects. Thus, these parameters may help us distinguish the evolution pathway of the progenitor of GW merging systems. The CHE allow massive stars to retain their H-envelope post-MS and prevents the onset of a common envelope phase (CE, see Section 1.2.3), favoring the formation of high-mass BHs.

1.2.2 Mass Transfer

Section 1.1.2 presented the effects of stellar winds on the evolution of massive stars. However, when a star is in a binary system, stellar winds are not the only actor that changes a star's mass.

In this section, I will present the effect on a binary's orbit of mass variation of the two stars composing it, either through stellar wind mass loss or via mass transfer.

When a star is in a binary system, stellar winds leads not only to variation in the structure (mass, temperature, luminosity etc.) of the single star, but also in changes in the binary's orbit.

If they are isotropic (spherical symmetry, i.e. no change in the momentum of the system) and adiabatic (slow with respect to the orbital period), the semimajor axis of the orbit varies as:

$$\dot{a} = -a\frac{\dot{M}_1 + \dot{M}_1}{M_1 + M_2} \tag{1.9}$$

where $\dot{M}_{*,i}$ and M_i are the mass changes rate (negative since the star is losing mass via winds) and the mass of the i-th star, respectively. If the mass loss is slow the only effects of stellar winds is to widen the orbit, without varying the eccentricity (see Hadjidemetriou, 1963; Dosopoulou and Kalogera, 2016a).

However, it is possible that the mass loss by a star via stellar winds is accreted by its companion, introducing a positive value of $\dot{M}_i$. The accreted material may also carry momentum, both linear and angular, and this would further modify the orbit. The wind accretion rate can be calculated with the model developed by Bondi and Hoyle, 1944, but usually we refer to Hurley, Tout, and Pols, 2002 approximation:

$$\dot{M}_2 = \frac{1}{\sqrt{1-e^2}}\left(\frac{GM_2}{v_w^2}\right)^2 \frac{\alpha_w}{2a^2}\frac{|\dot{M}_1|}{\left[1+(v_{\rm circ}/v_w)^2\right]^{3/2}} \tag{1.10}$$

where e is the eccentricity of the binary, v_w the donor wind speed, $v_{\rm circ} = \sqrt{G(M_1+M_2)/a}$ is the mean orbital velocity, G is the gravitational constant and $\alpha_w \sim 1.5$ is an efficiency factor. Predict the answer of the binary system to stellar winds accretion is non-trivial, as it depends not only on the amount of mass transferred, but also on the efficiency of momentum transport. For a detailed treatment see Dosopoulou and Kalogera, 2016a; Dosopoulou and Kalogera, 2016b; Hamers and Dosopoulou, 2019.

Matter may be transferred from a star to its companion also via Roche lobe overflow (RLO), that is usually more efficient that wind accretion (see Mapelli, 2018). The Roche lobe (RL) of a star in a binary system is a teardrop-shaped equipotential surface surrounding the star. The RLs of the two members of the binary are connected at a single point, known as the Lagrangian L_1 point. The most common-used approximation for the RL has been proposed by Eggleton, 1983 an goes as follows:

$$R_L = a\frac{0.49q^{1/3}}{0.6q^{2/3} + \ln(1+q^{1/3})} \tag{1.11}$$

where q is the mass ratio of the system of each star with respect to its companion ($q = M_1/M_2$).

RLO take place when the radius of one star overfill its RL ($R_i < R_{L,i}$), and if this happens, the external layers of the star are forcefully stripped out by the gravitational pull of the stellar companion and the centrifugal force of the orbit. Part of this material will be accreted by the stellar companion, while some will be lost in the circumstellar medium. We will define the mass transfer as *conservative*, if all the matter is accreted by the stellar companion, and *non-conservative* otherwise. The lost matter will carry away also part of the angular momentum from the binary, shrinking it.

An estimate of the mass accretion rate has been proposed by Ge et al., 2010, under the assumption that the matter can be treated as an isentropic, adiabatic, and irrotational fluid, with velocity flow parallel to the axis connecting the two stars' centers. The mass accretion rate can be then estimated as:

$$\dot{M}_1 \simeq -\frac{M_1}{P_{orb}}\left(\frac{\Delta R}{R_{L,1}}\right)^{n+3/2} \tag{1.12}$$

where P_{orb} is the orbital period, $R_{L,1}$ is the RL of the donor star, $\Delta R = R_1 - R_{L,1}$ is the *RL filling factor*, and n and R_1 are the envelope's polytropic index and the donor star's radius, respectively.

However, RLO does not change only the binary's orbit, but also the structural properties of the two stars. Thus, modeling the response of the both the donor and the accretor star is crucial to predict the evolution of a stellar binary, other than the properties of the eventual remnants.

To evaluate the stability of the mass transfer one has to consider the typical timescales for stellar processes that are the *dynamical* timescale t_{dyn}(describing the time on which a star reacts to a perturbation to the hydrostatic equilibrium, also known as free-falling timescale), the *thermal* timescale t_{KH} (describing the maximumm allow variation rate in the thermal structure of a star, also known as Kelvin-Helmholtz timescale), and the *nuclear* timescale t_{nuc} (the time needed to exhaust the nuclear fuel). If the timescale over which a star loses mass because of a RLO episode is such that

$$t_{nuc} < \frac{M_1}{\dot{M}_1} << t_{KH} \tag{1.13}$$

the mass transfer is considered stable, as the mass transfer timescale is well above the thermal timescale, allowing the star to remain in thermal equilibrium. On the other hand, if is true that

$$t_{KH} < \frac{M_1}{\dot{M}_1} < t_{dyn} \tag{1.14}$$

this implies that mass transfer can disrupt a star's thermal equilibrium, inducing significant changes in luminosity and radius. Furthermore, in certain extreme cases, mass transfer may occur on a dynamical timescale, profoundly modifying the donor star's behavior.

To assess the stability of mass-transfer the most commonly used approach (see Portegies Zwart and Verbunt, 1996; Tout et al., 1997; Hurley, Tout, and Pols, 2002; Eggleton, 2006) is to assume that $R \propto m^{\zeta}$, and that the variation of the donor's star during RL is:

$$\frac{dR_1}{dt} = \frac{\partial R_1}{\partial t} + \zeta \frac{R_1}{M_1} \frac{dM_1}{dt} \tag{1.15}$$

where $\partial R_1 / \partial t$ is due to nuclear burning, while ζ represents the adiabatic/thermal response of the donor star to mass loss, and $dM_{*,1}/dt$ is the donor mass loss rate, i.e. is always negative. One has also to account for the RL variation during the mass transfer, computed as:

$$\frac{dR_{L,1}}{dt} = \frac{\partial R_{L,1}}{\partial t} + \zeta_L \frac{R_{L,1}}{M_1} \frac{dM_1}{dt} \tag{1.16}$$

where $\partial R_{L,1} / \partial t$ models the effects due to tides and GW radiation, and ζ_L describes the adiabatic response of the RL to mass loss, that can either expand or shrink. If $\zeta_L > \zeta$ the RL shrink faster than than the donor's radius the mass transfer is deemed unstable, otherwise it is stable.

The stability of mass transfer depends on the value of ζ. It can be unstable on the thermal timescale if ζ represents the thermal response of the donor and $\zeta < \zeta_L$, or on the dynamical timescale if ζ represents the adiabatic response of the donor and $\zeta < \zeta_L$. Should the mass transfer be dynamically unstable, or if both stars overfill their Roche lobes, the binary system will either merge—assuming there is no distinct core-envelope separation, i.e. a steep density gradient at the core-envelope boundary—or otherwise enter a common envelope (CE) phase (see Section 1.2.3).

1.2.3 Common Envelope

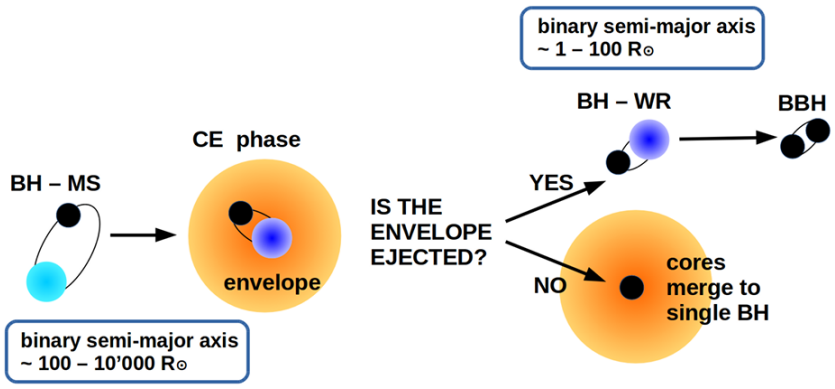

FIGURE 1.7: Schematic representation of the evolution of a BBH through CE. The companion of the BH (black circle) is initially in the main sequence (MS, light blue circle). Once the star evolve out of the MS, it overfills its RL and trigger a CE phase (if the mass transfer is not stable), where the star's core and the BH starts co-rotating. At this stage there are two possibilities: (i) the CE is ejected and we are left with a BH + naked-He star binary, whose semimajor axis is much smaller than the initial binary's; (ii) the CE is not ejected and the BBH and the He-core spiral in until they merge together, leaving a single BH. Figure from Mapelli, 2018.

Unstable mass transfer in binary systems can lead to a common envelope (CE) phase, during which one star becomes engulfed by the other's envelope. During this phase, the stars begin to spiral inward because of the gas drag from the envelope. This drag causes a loss of orbital energy, which, along with a portion of the orbital angular momentum, is transferred to the envelope, causing it to heat up and expand. At this stage, two outcomes are possible (summarized in Figure 1.7, from Mapelli, 2018): if the envelope is too tightly bound, the inspiral continues until the cores are tidally disrupted, resulting in a merger into a single star. On the other hand, if the envelope is ejected, a new short-period binary system is created.

The CE is a key factor in the formation of GW events from isolated binary stars, as it can shrink binary separations by a factor of hundreds, decreasing the coalescence time of compact-object binaries, and allowing them to merge within a Hubble time (see Dominik et al., 2015; Giacobbo and Mapelli, 2018; Mapelli and Giacobbo, 2018; Belczynski et al., 2020; Tanikawa et al., 2021; Zevin et al., 2021).

The most commonly used approach to model CE relies on analytical methods, as they are easier to implement and less numerically expensive than hydrodynamical simulations (see e.g. Sandquist et al., 1998; Ricker and Taam, 2012; Ivanova, Justham, and Podsiadlowski, 2015; Ivanova, 2018), and among them the most commonly adopted formalism is the $\alpha - \gamma$ model (see van den Heuvel and De Loore, 1973; Webbink, 1985; Nelemans et al., 2000), or energy formalism, as it is based on energy balance considerations.

The basic idea of this formalism is to compare the orbital energy pre-CE with the envelope's binding energy. By comparing these two energies, it is possible to estimate whether or not a binary will survive the CE phase, and, if it does, to estimate the final semimajor axis of the orbit.

The two parameters of the model, α, and γ, are used to parametrize the CE efficiency (i.e., which fraction of the removed orbital energy is transferred to the envelope) and the envelope

binding energy, respectively. The latter is estimated as proposed by de Kool, 1990 as:

$$E_{\rm env} = -\frac{GM_1 M_{1,env}}{\lambda R} \tag{1.17}$$

where R is the stellar radius, and $M_{1,env}$ is the mass of the stellar envelope. When both stars are giant stars with a well-formed core, both the envelopes are included in Eq. 1.17. The value of λ is usually obtained from polytropic fitting or from detailed 1D stellar evolution codes (see Hurley, Tout, and Pols, 2002; Dewi, Podsiadlowski, and Sena, 2006; Claeys et al., 2014; Kruckow et al., 2018).

Then, the fraction of the orbital energy of the cores, which goes into unbinding the envelope, can be expressed as

$$\Delta E_{orb} = \alpha(E_{orb,f} - E_{orb,i}) = \frac{GM_{1,c}M_{2,c}}{2}\left(\frac{1}{a_f} - \frac{1}{a_i}\right) \tag{1.18}$$

where $M_{1,c}$ and $M_{2,c}$ are the masses of the two cores, $E_{orb,i}$ ($E_{orb,i}$) and a_i (a_f) are the value of orbital energy and of the semimajor axis before (after) the CE phase, respectively. By equating Eq. 1.17 and Eq. 1.18 (i.e., assuming that all the variation of energy due to CE is employed to eject the CE), such that $\Delta E = E_{env}$, it is possible to estimate the final value of a_f.

For $\alpha = 1$, all the orbital energy due to the orbit's shrink is used to unbind the envelope, while for $\alpha < 1$, part of this energy is lost. Thus, the α parameter rules the efficiency of the CE inspiral. Population synthesis studies suggest that a larger value of α ($\alpha \gtrsim 3$) is required to match the binary NS (BNS) merger rates inferred by LVK collaboration (e.g., Giacobbo and Mapelli, 2018). This indicates that energy may be generated during the CE phase within this framework. Recent one-dimensional simulations propose alternative energy sources to binary contraction, such as the recombination energy released when hydrogen plasma recombines into atoms and molecules (Fragos et al., 2019).

However, the $\alpha - \lambda$ model, while numerically efficient, oversimplifies the complex physics of CE evolution by compressing it within two parameters. It presumes complete envelope ejection, despite hydrodynamic simulations indicating the possibility of partial ejection. It also assumes that the ejected envelope has zero kinetic energy at infinity, which may not be accurate. Moreover, the model overlooks critical factors like angular momentum transfer, tidal heating, and the recombination energy of the envelope material, all of which can significantly influence CE evolution outcomes (Ivanova et al., 2013).

1.3 Dynamical evolution

The dynamical scenario describes the formation of binary systems through gravitational interactions within stellar clusters, relatively dense groups of stars held together by gravitational forces. This process is an alternative method for forming merging compact-object binaries, considering that most stars, if not all, originate in stellar clusters.

In this section, I will briefly review the processes that interest binary systems (for a more detailed review of the processes in place in dense environments see Mapelli, 2018; Spera, Trani, and Mencagli, 2022), and the environment that host such processes.

1.3.1 Dense Stellar Environments

Star clusters are distinguished according to their age, density and mass.

The most massive and dense possible environments are nuclear star clusters (NSCs), which resides in the nuclei of galaxies, including our own (see Böker et al., 2002; Graham and

Spitler, 2009). In these clusters may also host a super-massive BH (SMBH) at their center, that plays an important role in the dynamical processes in place. The environment close to the BH can be a relevant formation site of GW progenitor systems. Furthermore, if the BH is accreting matter is called active galactic nucleus (AGN), and its accretion disk is a region that can trap BHs, thus it is a possible environment for GW mergers (see McKernan et al., 2012; McKernan et al., 2014; McKernan et al., 2018; McKernan et al., 2020; McKernan, Ford, and O'Shaughnessy, 2020; Bellovary et al., 2016; Bartos et al., 2017; Leigh et al., 2018; Secunda et al., 2019; Yang et al., 2019).

The globular clusters (GCs) are typically old systems ($\sim$ 12 Gyr, close to the Universe's age), that are very dense and massive ($\geq 10^4\,M_\odot$). Because of their age they are generally not star-forming, as they do not contain anymore gas or dust. Because of their high masses and central densities ($\rho_c \geq 10^4\,M_\odot pc^{-3}$), GCs are one of the most studied environment for the dynamical formation of GW-progenitor binaries (see Zwart and McMillan, 1999; Mapelli et al., 2005; Downing et al., 2011; Rodriguez et al., 2015; Antonini and Rasio, 2016; Askar et al., 2017; Arca Sedda, Askar, and Giersz, 2018; Rodriguez et al., 2019; Kremer et al., 2020).

Young dense star clusters (YDSCs) are relatively young (<100 Myr) systems, thought to be the most common birthplace of massive stars (see Lada and Lada, 2003; Portegies Zwart, McMillan, and Gieles, 2010). While they are generally smaller than GCs, their central densities may be comparable. YDSCs are thought to be close relatives of the ancient progenitors of GCs, as they have masses similar to those of GCs at the present day. However, as they experience stellar mass loss YDSCs are not massive enough to evolve into present-day GCs.

Finally, the smaller environments are open clusters (OCs) They are irregular systems composed of few stars (tens to few thousands) and are generally younger than GCs. Furthermore, they may still retain some gas from the primordial general cloud that originated them.

YDSCs and OCs are not long-lived as they eventually disintegrate within the tidal field of their host galaxy, losing mass in the process. Contributing to their disintegration are factors such as gas expulsion and stellar evaporation. Gas expulsion can occur in the early stages of gas-rich star clusters' lives. Stellar winds and SNe may remove the remaining gas from the cluster, weakening its gravitational pull and possibly leading to its disintegration, a phenomenon known as infant mortality.

1.3.2 Three body star encounters

In general, binaries have an energy reservoir, their internal energy:

$$E_{\rm int} = \frac{1}{2}\mu v^2 - \frac{GM_1M_2}{r} \tag{1.19}$$

where $\mu = M_1M_2/(M_1+M_2)$ is the reduced mass of the binary (whose components have mass M_1 and M_2), v is the relative velocity between the two members of the binary, and r is the distance between the two members of the binary. As shown by Kepler's laws, $E_{\rm int} = -E_b = -Gm_1m_2/(2a)$, where E_b is the binding energy of the binary system, a being its semi-major axis.

A binary can exchange its internal energy with the other stars only if it undergoes a close encounter with another star, which will perturb its orbital parameters. An encounter is defined a *close encounter* if the single star approaches the binary by few times the value of the orbital separation. If this is the case, we talk about a *three-body encounter*.

The frequency of such encounters scales with the local star densities, so this process has a non-negligible occurrence rate only in very dense environment, such as stellar clusters. As a consequence of a *three-body encounter*, a binary can either harden (increase its binding

energy, i.e., decrease its orbital separation), exchange objects (one of the two component of the binary is substituted by the third interacting object) or be ejected from the star cluster.

1.3.2.1 Hardening

When a binary system experiences multiple three-body encounters throughout its existence, it is expected that its semimajor axis will shrink due to such interactions, a phenomenon known as dynamical hardening.

According to Heggie, 1975, a binary can be labeled as hard (soft) if its binding energy is larger (smaller) than the average kinetic energy of stars in the same star cluster. It is worth noting that hardness is a property of the binary relative to its environment. Due to the higher velocity dispersion, the same binary in the core of a cluster might be soft, whereas in the halo it would be hard.

Heggie, 1975 showed that hard binaries tend to harden through *three-body encounters*, meaning that their semimajor axis will shrink. As BHs are among the most massive bodies in star clusters, they are expected to be in hard binaries, thus to harden as a consequence of dynamical interactions. Such a process may be efficient enough to reduce the semimajor axis enough to enter a regime where GW emission is efficient, producing merging BBH able to merge within a Hubble time. Heggie, 1975 predicts the hardening rate for hard binaries to be

$$\frac{d}{dt}\left(\frac{1}{a}\right) = 2\pi G\xi\frac{\rho}{\sigma} \tag{1.20}$$

where ξ is a the hardening parameter ($\xi \sim 0.1-10$, tuned through numerical experiments, see Hills, 1983; Quinlan, 1996), ρ is the local stellar mass density, and σ is the local velocity dispersion. If we couple Eq. 1.20 with Peters, 1964 equation for the GW emission:

$$\dot{a} = -\frac{64G^3M_1M_2(M_1+M_2)}{5c^5a^3(1-e^2)^{7/2}}\left(1+\frac{73}{24}e^2+\frac{37}{96}e^4\right) \tag{1.21}$$

One obtain the estimate of the evolution of a BBH binary affected by dynamical *three-body encounters* and GW emission:

$$\frac{da}{dt} = -2\pi\xi\frac{G\rho}{\sigma}a^2 - \frac{64}{5}\frac{G^3M_1M_2(M_1+M_2)}{c^5(1-e^2)^{7/2}}a^{-3} \tag{1.22}$$

that holds in the hard binary approximation. Furthermore, Eq. 1.22 holds under the assumption that the total mass of the binary is much larger than the average mass of a star in the cluster and that *three-body encounters* have a small impact parameter. The first term on the right hand side of Eq. 1.22 accounts for dynamical hardening and scales as $\propto a^2$, while the second term accounts for GW emission, scaling as $\propto a^{-3}$. Thus, the former is more efficient the larger is the binary, while the latter becomes efficient only for very close binaries.

1.3.2.2 Exchanges

Dynamical exchanges are three-body interactions where one member of a binary system is replaced by the third object. Such exchanges can result in the creation of new BBHs: for instance, if a binary consisting of a BH and a low-mass star is involved in an exchange with a single BH, a new BBH is formed. This is a crucial difference between BHs in isolated fields and those in star clusters: a BH that forms as an isolated object in the field is unlikely to join a binary system, whereas a single BH in the heart of a star cluster has a good chance of entering a binary through exchanges.

Exchanges are expected to result in the creation of more BBH than they can destroy. This is because the likelihood of an intruder replacing a member of a binary system is negligible if the intruder is less massive than both members of the binary. However, this probability increases significantly if the intruder is more massive than at least one of the binary members (see Hills and Fullerton, 1980). Therefore, BHs, that are among the most massive objects in a star cluster, are very efficient in acquiring companion via dynamical interactions, and exchanges are a crucial mechanism in forming BH binaries (see Ziosi et al., 2014).

BBH binaries formed via exchange have several distinguish features:

- Dynamically formed BBH are expected to be more massive than isolated BBH, as massive BHs are more likely to substitute lighter objects via exchanges or to acquire companions;
- Exchange BBH are more likely to have high eccentricities, as circularization effects associated to the binary evolution (see Section 1.2) are not in place. However, GW emission will later on reduce the orbit eccentricity;
- Dynamically formed BBHs are more likely to have misaligned spins, as they do not experience stellar tides (see Section 1.2.1). Furthermore, exchanges and other dynamical interactions lead to isotropically distributed spin directions, because dynamical interactions remove any memory of previous alignments.

It is worth mentioning that this latter effect, as of now, is one of the main properties that would allow us to distinguish the formation pathway of a merging BBH (see Farr et al., 2017; Farr, Holz, and Farr, 2018).

1.3.2.3 Ejection

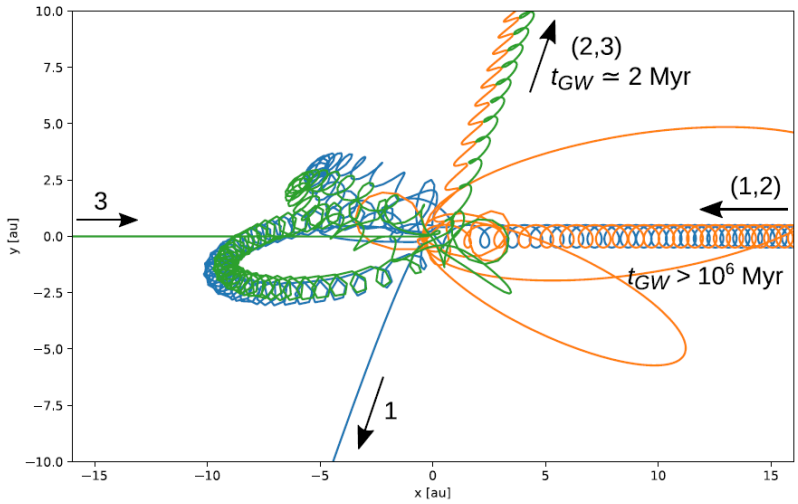

FIGURE 1.8: Trajectory evolution during a *three-body encounter* between a binary (1,2) and a single object (3). After a brief interaction an exchange take place, followed by the ejection of both the newly formed binary (2,3) and single (1). Because of the dynamical interaction the timescale for a GW merger is greatly reduced, from $t_{GW} > 10^6$ Myr, to few Myr. This dynamic interaction has been integrated with the few-body code TSUNAMI (see Trani, Fujii, and Spera, 2019; Trani and Spera, 2023), assuming that all the bodies are 50 $M_\odot$ BHs, the impact parameter is $b = 0.6$, and $v_\infty = 0.1\, km/s$. Figure from Spera, Trani, and Mencagli, 2022.

During three-body encounters, a portion of the internal energy of a hard binary is converted into the kinetic energy of the intruders and the binary's center of mass. Therefore, both the

binary and the intruder recoil, and both can be ejected from the parent star cluster, as shown in Figure 1.8 (Figure from Spera, Trani, and Mencagli, 2022). If this happens, they become field objects and will continue their evolution as isolated binaries, not participating in the cluster's life anymore.

Statistically speaking, most BNSs, BBHs and BH-NS systems are ejected before merging (see Zwart and McMillan, 1999; Downing et al., 2011; Ziosi et al., 2014; Rodriguez et al., 2015; Askar et al., 2017). This hampers the formation of massive BHs through hierarchical mergers, reducing the number of second-generation BHs, especially in an environment with low escape velocity. In fact, the denser is the environment the higher is the escape velocity value. Therefore, this effect introduces a selection effect based on the environmental properties, which affects the efficiency of hierarchical mergers. Recent work by Rodriguez et al., 2019 shows that hierarchical mergers occur only in massive stellar environments such as globular clusters, nuclear star clusters, and close to the central SMBH.

1.4 Hybrid scenarios

In this Chapter, I presented the evolution of isolated binary, and the various BSE processes, and the effect of stellar dynamic, which allows the formation of binaries in dense stellar environment.

However, distinguishing between the isolated binary channel and the dynamical channel might not be straightforward. This is because stellar evolution and stellar dynamics are processes that are active simultaneously.

Stellar binaries may evolve in complete isolation, if they are not in a dense environment, but they can be found in star clusters as well. If that is the case they may be affected by both dynamical processes and BSE processes at the same time. For instance, Di Carlo et al., 2020a showed that in YDSCs BBHs are formed via CE evolution of dynamically assembled main sequence binaries that, at some point of their life, are ejected from the cluster and merge in the field, appearing as if they had evolved in complete isolation. These systems contribute to the merger ratio more efficiently than dynamically assembled binaries. These are binaries that undergo at least a CE phase but also dynamical encounters, and the CE phase may also be triggered by these latter. Another example of the complex interplay between the isolated and the dynamical pathway is provided by Trani et al., 2021, as they show that binaries in YDSCs that are in the post-Ce phase, and are tidally spun up may merge with misaligned spins, because of *three-body encounters*.

Therefore, in such a hybrid scenario, a stellar binary may enter certain evolutionary stages that would not have been possible if it evolved as isolated binaries.

Chapter 2

Numerical Tools

In this Chapter, I will describe the numerical codes used throughout this thesis. In Section 2.1, I will describe the code that I used for the hydrodynamical simulation of ccSNe, HYdrodynamic Ppm Explosion with Radiation diffusION (HYPERION). In Section 2.2, I will present the rapid population synthesis code Stellar Evolution for N-body (SEVN).

2.1 HYPERION

This Thesis deals with CCSNe studied through 1D numerical simulations. The code used, called HYPERION (HYdrodynamic Ppm Explosion with Radiation diffusION, see Limongi and Chieffi, 2020), is capable of simultaneously simulating the ejection of the star's mantle and tracking Explosive Nucleosynthesis, solving the equations that describe the hydrodynamic state of the system and the variation of chemical species.

The equations describing the hydrodynamics of a system under the assumption that energy transport occurs via radiative diffusion are

$$\begin{cases} \dfrac{\partial \rho}{\partial t} &= -4\pi\rho^2 \dfrac{\partial r^2 v}{\partial m} \\ \dfrac{\partial v}{\partial t} &= -4\pi r^2 \dfrac{\partial P}{\partial m} - \dfrac{Gm}{r^2} \\ \dfrac{\partial E}{\partial t} &= -\dfrac{\partial}{\partial m}\left(4\pi r^2 v P + L\right) + \epsilon \end{cases} \tag{2.1}$$

where ρ is the density, r the radial coordinate, v is the velocity, m is the mass, P is the pressure, E is the energy per unit mass, which accounts for kinetic, gravitational, and thermal energy contributions, L is the luminosity associated with radiation, and ϵ represents other added or subtracted energy terms, for example, energy lost in the form of neutrinos or gained from nuclear burning reactions.
Assuming that the mean free path of photons is smaller than the characteristic dimensions of the stellar matter fluid, the luminosity due to photons is obtained in the diffusive limit as:

$$L = -(4\pi r^2)^2 \frac{\lambda a c}{3\kappa} \frac{\partial T^4}{\partial m} \tag{2.2}$$

where a is the radiation constant, c is the speed of light, κ is the Rosseland mean opacity, and λ is the flux limiter. This can be calculated as Levermore and Pomraning, 1981

$$\lambda = \frac{6 + 3R}{6 + 3R + R^2} \tag{2.3}$$

where

$$R = \frac{4\pi r^2}{kT^4}\left|\frac{\partial T^4}{\partial t}\right| \tag{2.4}$$

The Rosseland mean opacity is calculated according to the abundances of chemical species at solar metallicity $Z = Z_\odot = 1.345 \times 10^{-2}$.
It is then assumed that the variables P, E_{int}, ϵ, κ are treated according to the following scheme:

$$\begin{aligned} P &= P(\rho, T, X_i) \quad \textit{Equation of State} \\ E_{int} &= E_{int}(\rho, T, X_i) \quad \textit{Equation of State} \\ \epsilon &= \epsilon(\rho, T, X_i) \quad \textit{Cross Section Study} \\ \kappa &= \kappa(\rho, T, X_i) \quad \textit{Opacity Tables} \end{aligned}$$

Thus, P and E_{int} are described by equations of state Morozova et al., 2015, while ϵ is obtained from cross-section studies and κ using opacity tables Ferguson et al., 2005; Iglesias and Rogers, 1996.
Furthermore, since $E = E_{int} + E_{grav} + E_{kin}$ depends on v, ρ, T and r, and given that $\partial v/\partial t = r$, the system of Eq. 2.1, which describes the conservation equations for mass, momentum, and energy, is a system of 3 equations with 3 unknowns and can therefore, at least in principle, be solved.
Nucleosynthesis, on the other hand, is tracked by coupling the system of Eq. 2.1 with the set of equations

$$\begin{aligned} \left.\frac{\partial Y_i}{\partial t}\right|_{i=1,\dots N} = &\sum_j c_i(j)\Lambda_j Y_j + \sum_{j,k} c_i(j,k)\rho N_A \langle\sigma v\rangle_{j,k} Y_j Y_k + \\ &\sum_{j,k,l} c_i(j,k,l)\rho^2 N_A^2 \langle\sigma v\rangle_{j,k,l} Y_j Y_k Y_l \end{aligned} \tag{2.5}$$

Where N is the number of chemical species whose evolution is being followed, thus Eq. 2.5 represents a system of N equations.
The different terms represent, in order:

- β-decay, electron capture, and photo-dissociation processes;
- Two-body reactions;
- Three-body reactions.

The coefficients are obtained as

$$c_i(j) = \pm N_i \tag{2.6}$$

$$c_i(j,k) = \pm \frac{N_i}{(N_j)!(N_k)!} \tag{2.7}$$

$$c_i(j,k,l) = \pm \frac{N_i}{(N_j)!(N_k)!(N_l)!} \tag{2.8}$$

Where N_i represents the number of particles involved in the reaction, and $N_i!$ prevents double-counting of reactions involving identical particles. The sign $\pm$ is used if the i-th particle is created (+) or destroyed (-). Finally, the coefficient λ_i represents the rate of interaction via weak interaction or photodissociation, while $\langle\sigma\bar{v}\rangle$ refers to the cross section of the two- or three-body process.
The solution of the system of Eq. 2.1 is crucial because once it is solved for a time interval Δt, given a fixed chemical composition, the values obtained for T and ρ are used to solve the

system of Eq. 2.5.
The solution of the system of Eq. 2.1 is found numerically using the *finite volume method*. In the following, a brief summary of the method is provided before discussing its application to the specific problem studied in this thesis.

2.1.1 Finite Volume Method

The finite volume method is usually used to solve partial differential equations, such as those that make up the system of Eq. 2.1.
The idea is to solve the equations not using a grid of points but rather by employing a set of elementary finite volumes. Thus, in this case, a grid is used from which to derive the individual elementary volumes, or cells, establishing a grid of points x_i. Such points are identified by the centers of the cells, while their edges, or walls, are identified starting from the grid as

$$x_{i+1/2} = \frac{1}{2}(x_i + x_{i+1}) \tag{2.9}$$

These cells will serve as elementary volumes, where the conserved quantity q_i^n is assumed to be contained. Since the equations to be solved are conservation equations, this means that the only way to induce changes in the amount q_i^n is if some of it moves to adjacent cells. Similarly, q_i^n can only increase if a part of the conserved quantity is transported into the cell i.
Therefore, a change in q_i can be seen as a flux, outgoing or incoming, through adjacent cells. The flux $f_{i+1/2}$ can be defined at the interface between two cells, and the change between two adjacent cells can be defined as

$$\frac{q_i^{n+1} - q_i^n}{\Delta t} = -\frac{f_{i+1/2}^{n+1/2} - f_{i-1/2}^{n+1/2}}{\Delta x} \tag{2.10}$$

Or in explicit form

$$q_i^{n+1} = q_i^n - \frac{\Delta t}{\Delta x}\left(f_{i+1/2}^{n+1/2} - f_{i-1/2}^{n+1/2}\right) \tag{2.11}$$

The variable of this type of method is related to the spatial average of the unknowns within the cells, as shown in Figure 2.1.

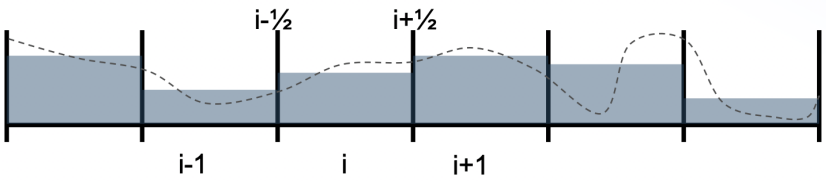

FIGURE 2.1: In each cell, the trend of the variable (dashed line) is reduced to its average defined by the shaded area.

In the case of an equation written in conservative form, such as

$$\frac{\partial U}{\partial t} = -\frac{\partial F}{\partial x} \tag{2.12}$$

The unknowns are obtained as

$$\langle U \rangle_i^n = \frac{1}{\Delta x}\int_{x_{i-1/2}}^{x-i+1/2} U(x, t^n)dx \tag{2.13}$$

where $x_{i\pm1/2}$ denote the edges of the single cell. The solution of a conservation equation can be written as

$$\langle U\rangle_i^{n+i} = \langle U\rangle_i^n - \frac{\Delta t}{\Delta x}\left(\tilde{F}_{i+1/2}^{n+1/2} - \tilde{F}_{i-1/2}^{n+1/2}\right) \tag{2.14}$$

In this way, the solution of the conservation equation must take into account the fluxes $\tilde{F}_{i\pm1/2}^{n+1/2}$ through the edges of the volume, calculated as

$$\tilde{F}_{i\pm1/2}^{n+1/2} = \frac{1}{\Delta t}\int_{t_n}^{t_{n+1}} F[U(x_{i\pm1/2},t)]dt \tag{2.15}$$

and obtained by calculating the time average within the cells of the variation of the conserved quantities, as in Figure 2.2.

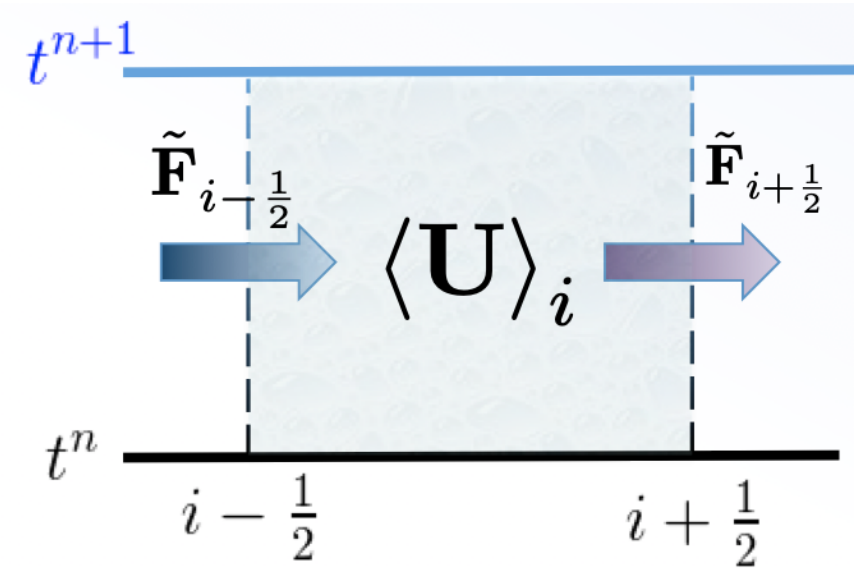

FIGURE 2.2: The conserved quantity $\langle U\rangle_i$ is modified by incoming and outgoing fluxes, respectively $\tilde{F}_{i-1/2}$ and $\tilde{F}_{i+1/2}$, noting that $\langle U\rangle_i$ is calculated at t_n.

The solution for $\langle U\rangle_i$ is known only at t_n, so an approximation is needed to evaluate the flux through the cell walls. Indeed, a variation of $\langle U\rangle$ is observed at the boundary between two cells, resulting in a sequence of local Riemann problems defined by the initial conditions as

$$U(x,0) = \begin{cases} U_L & \text{for} \quad x < x_{i+1/2} \\ U_R & \text{for} \quad x > x_{i+1/2} \end{cases} \quad \Longrightarrow U(x_{i+1/2},0) = ? \tag{2.16}$$

See Figure 2.3 and Figure 2.4 for a graphical representation of the situation at the boundary between two cells, respectively, before and after the solution of the local Riemann problem.

Thus, solving the Riemann problem yields the term $U(x_{i+1/2},0)$ to be inserted into Eq. 2.15, allowing $\langle U\rangle_i^{n+1}$ to be calculated.

2.1.2 Numerical Solution of the Equations

The integration of the system of Eq. 2.1 is performed using the Piecewise Parabolic Method (PPM) (see Colella and Woodward, 1984) and is broken down into three steps:

- Interpolation of the profile of the dependent variables ρ, v and P as a function of the mass coordinate using the interpolation algorithm described in Colella and Woodward, 1984;

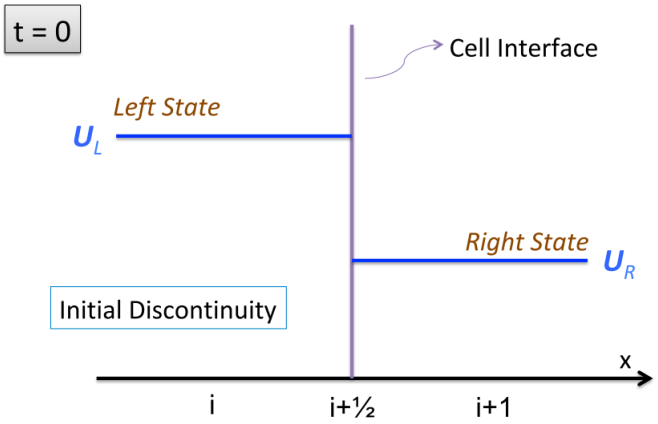

FIGURE 2.3: Visual representation of a discontinuity at the edge of two cells, before the solution of the Riemann problem.

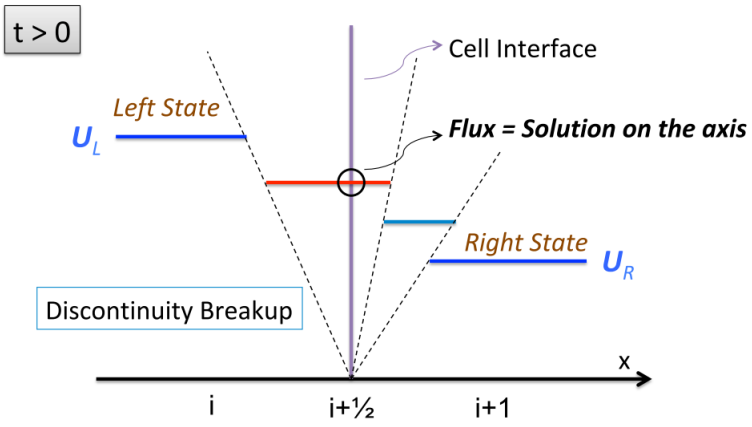

FIGURE 2.4: Visual representation of the implementation of the solution of the Riemann problem.

- Solution of local Riemann problems at the boundary between different cells in order to calculate time-averaged velocity and pressure values;
- Use of the obtained solutions to calculate the fluxes of conserved quantities.

To do this, Δm_j is defined as the mass contained in the j-th zone, and it is assumed that the conserved quantities are known, obtained as mass-weighted averages at time t_n, so that

$$U_j^n = \int_{m_{j-1/2}}^{m_{j+1/2}} U(m, t^n) dm \tag{2.17}$$

Where U is a vector representing the three unknowns of the system

$$U = \begin{pmatrix} \rho \\ v \\ P \end{pmatrix} \tag{2.18}$$

The goal is to calculate U_i^{n+1}, that is, the average of the conserved quantities calculated at $t^{n+1} = t^n + \Delta t$.

The first step, as mentioned, involves interpolating ρ, v, and P as functions of the mass coordinate using the interpolation algorithm described in Colella and Woodward, 1984.

In this specific case, the mass coordinate assumes the role of an independent variable in constructing a polynomial approximation function $a(m)$ such that

$$a_j^n = \frac{1}{\Delta m_j} \int_{m_{j-1/2}}^{m_{j+1/2}} a(m)dm \quad \text{with} \quad \Delta m_j = m_{j+1/2} - m_{j-1/2} \tag{2.19}$$

where a_j^n are $a_j^n = \rho_j^n,\ v_j^n,\ P_j^n$.

In the PPM scheme, a parabolic profile is used in each zone, obtained as

$$\begin{aligned} a(m) &= a_{L,j} + x\Big[\Delta a_j + a_{6,j}(1-x)\Big] \\ x &= \frac{m - m_{j-1/2}}{\Delta m_j} \end{aligned} \qquad \text{with} \qquad m_{j-1/2} < m < m_{j+1/2} \tag{2.20}$$

where

$$\Delta a_j = a_{R,J} - a_{L,j} \qquad a_{6,j} = 6\Big[a_j^n - \frac{1}{2}\big(a_{R,J} + a_{L,j}\big)\Big] \tag{2.21}$$

The coefficients a_R and a_L are obtained as in Colella and Woodward, 1984.

Using this parametrization, an interpolation is then performed, as in Figure 2.5, followed by integration, as shown in Figure 2.6, both taken from Colella and Woodward, 1984.

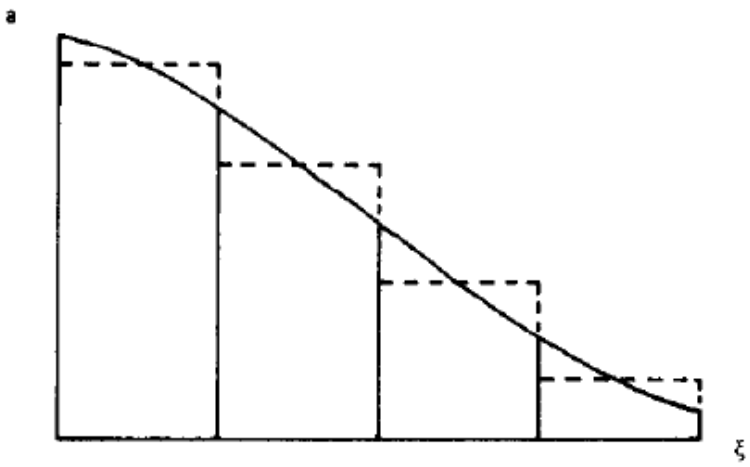

FIGURE 2.5: The Figure shows the interpolation carried out according to the PPM scheme for a generic transport equation. The initial data are given as mean values of a over the four regions shown, described by a generic coordinate ξ. The mean values are represented by dashed lines. From these data, interpolation is performed for the values of a at the cell edges using curves that account for the mean values in the four zones closest to the cell walls. The interpolating parabola between different cells, drawn with a solid line, connects the values at the edges. Moreover, if averaged over each region, it returns the initial mean value in that region. Figure from Colella and Woodward, 1984.

The second step involves obtaining $\bar{v}_{j+1/2}$ and $\bar{P}_{j+1/2}$, that are the time-averaged values of the velocity and pressure at the cell boundary. These are obtained by calculating the averages of the dependent variables over the regions of the spatial domain that can influence the boundary region, as in Figure 2.7.

The intersection between the spatially averaged states is calculated by solving the Riemann problem for $\bar{v}_{j+1/2}$ and $\bar{P}_{j+1/2}$, as in panel c of Figure 2.7.
For this purpose, $\rho^{\pm}_{j+1/2}$, $v^{\pm}_{j+1/2}$, and $P^{\pm}_{j+1/2}$ are defined, which are the average values of the variables over the regions between $m_{j+1/2}$ and the point where the $\pm$ characteristic profile intersects the line passing through $t = t^n$. This region for the j-th cell has a size $\rho_j^n \Delta V^n$, where

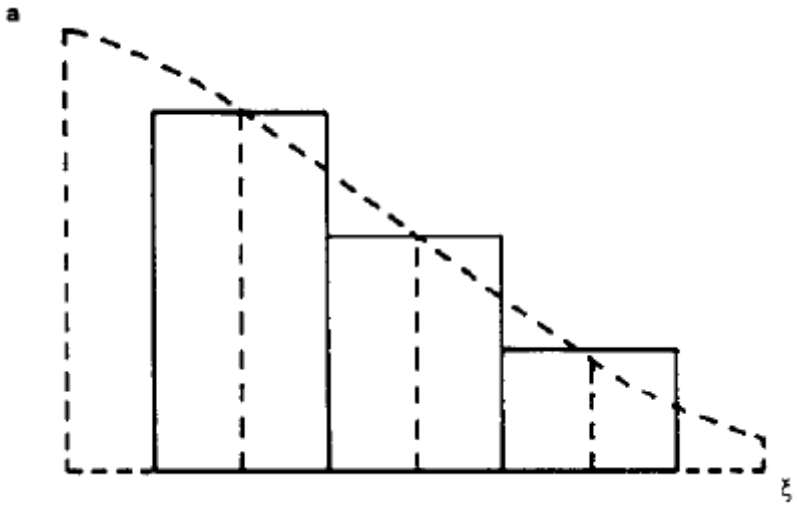

FIGURE 2.6: The integration carried out according to the PPM scheme is shown. The new means of the variable a are obtained by integrating the initial distribution shifted by a certain value $u\Delta t$. The shifted distribution is represented with a dashed line, while the result of the integration, that is, the new means over the new regions, is shown with a solid line. Figure from Colella and Woodward, 1984.

ΔV is the volume crossed by the wave in the time Δt in region j, calculated as

$$\Delta V = \langle S_j \rangle^n \Delta r^n \tag{2.22}$$

where Δr^n is the radial dimension of the region, and $\langle S_j \rangle^n \Delta$ is the average surface area of the region. The radial dimension is obtained as

$$\Delta r^n = c^n_{s,j} \Delta t \tag{2.23}$$

where $c^n_{s,j}$ is the speed of wave propagation in region j. The average surface area is obtained as

$$\langle S_j \rangle^n \Delta = \frac{\Delta V^n_j}{\Delta r^n_j} = \frac{4\pi}{3} \frac{\left(r^n_{j+1/2}\right)^3 - \left(r^n_{j-1/2}\right)^3}{r^n_{j+1/2} - r^n_{j-1/2}} \tag{2.24}$$

Since in general $\langle S \rangle = 4\pi \langle r \rangle^2$, we can define

$$\langle r_j \rangle^n = \frac{1}{3} \left[\frac{\left(r^n_{j+1/2}\right)^3 - \left(r^n_{j-1/2}\right)^3}{r^n_{j+1/2} - r^n_{j-1/2}} \right]^{1/2} \tag{2.25}$$

The size of the spatial domain capable of influencing the regions near the boundary of the j-th cell over the time interval Δt is thus obtained as

$$y_i = \rho^n_j \Delta V^n = \rho c^n_{s,j} \Delta t \langle S_j \rangle^n = \left(\gamma^n_j \rho^n_j P^n_j\right)^{1/2} \Delta t \langle S_j \rangle^n \tag{2.26}$$

where the relation $c_s = \sqrt{\gamma \frac{P}{\rho}}$ has been used, and where γ_i represents the adiabatic index in the j-th region.

Once the size of the regions over which the mean values $a^{\pm}_{j+1/2}$ are calculated is fixed, recalling the parabolic parameterisation of Eq. 2.20, they can be calculated as

$$a^{+}_{j+1/2} = \frac{1}{y_i}\int_{m_{j+1/2}-y_i}^{m_{j+1/2}} a(m)dm \tag{2.27}$$

$$a^{-}_{j+1/2} = \frac{1}{y_{i+1}}\int_{m_{j+1/2}}^{m_{j+1/2}+y_{i+1}} a(m)dm \tag{2.28}$$

from which we obtain

$$a^{+}_{j+1/2} = a_{R,j} - \frac{x}{2}\left[\Delta a_j - \left(1-\frac{2}{3}x\right)a_{6,j}\right] \quad \text{with} \quad x = \frac{y_j}{\Delta m_j} \tag{2.29}$$

$$a^{-}_{j+1/2} = a_{L,j+1} + \frac{x}{2}\left[\Delta a_{j+1} - \left(1-\frac{2}{3}x\right)a_{6,j+1}\right] \quad \text{with} \quad x = \frac{y_{j+1}}{\Delta m_{j+1}} \tag{2.30}$$

$$\tag{2.31}$$

where $a = \rho$, v, P. The values of $\bar{v}_{j+1/2}$ and $\bar{P}_{j+1/2}$ are then obtained by solving the local Riemann problem, in which $a_{j+1/2,L} = a^{+}_{j+1/2}$ and $a_{j+1/2,R} = a^{-}_{j+1/2}$.

However, before solving the Riemann problem it is necessary to make corrections compared to those obtained in Colella and Woodward, 1984, in order to take into account the effect of gravity.

Thus, we will have

$$P_{j+1/2,L} = P^{+}_{j+1/2} + \Delta t\left(\gamma^n_j \rho^{+}_{j+1/2} P^{+}_{j+1/2}\right)^{1/2} g^n_j \tag{2.32}$$

$$P_{j+1/2,R} = P^{-}_{j+1/2} - \Delta t\left(\gamma^n_j \rho^{-}_{j+1/2} P^{-}_{j+1/2}\right)^{1/2} g^n_{j+1} \tag{2.33}$$

$$v_{j+1/2,L} = v_{R,j} + \frac{A^{+}_{j+1/2} v^{+}_{j+1/2} - A_{j+1/2} v_{R,j}}{\frac{1}{2}\left(A^{+}_{j+1/2} + A_{j+1/2}\right)} \tag{2.34}$$

$$v_{j+1/2,R} = v_{L,j+1} + \frac{A^{-}_{j+1/2} v^{-}_{j+1/2} - A_{j+1/2} v_{L,j+1}}{\frac{1}{2}\left(A^{-}_{j+1/2} + A_{j+1/2}\right)} \tag{2.35}$$

where $g_j = Gm_j/r_j^2$. Instead, $A^{\pm}_{j+1/2}$ are the interpolation coefficients obtained from Eq. 2.28, calculated with $a^n_j = 4\pi(r^n_{j-1/2})^2$, $a_{L,j} = 4\pi(r^n_{j-1/2})^2$, $a_{R,j} = 4\pi(r^n_{j+1/2})^2$, and $A^n_j = \langle S_j \rangle^n$. The final values of $\bar{v}_{j+1/2}$ and $\bar{P}_{j+1/2}$ are then obtained by solving the following system of equations

$$\frac{\bar{P}_{j+1/2} - P_{j+1/2,L}}{W_L} + \left(\bar{v}_{j+1/2} - v_{j+1/2,L}\right) = 0 \tag{2.36}$$

$$\frac{\bar{P}_{j+1/2} - P_{j+1/2,R}}{W_R} + \left(\bar{v}_{j+1/2} - v_{j+1/2,R}\right) = 0 \tag{2.37}$$

$$W_L^2 = \left(\gamma_j \rho^{+}_j P^{+}_{j+1/2}\right)\left[1 + \frac{\gamma_j + 1}{2\gamma_j}\left(\frac{\bar{P}_{j+1/2}}{P_{j+1/2,L}} - 1\right)\right] \tag{2.38}$$

$$W_R^2 L = \left(\gamma_{j+1} \rho^{-}_j P^{-}_{j+1/2}\right)\left[1 + \frac{\gamma_{j+1} + 1}{2\gamma_{j+1}}\left(\frac{\bar{P}_{j+1/2}}{P_{j+1/2,R}} - 1\right)\right] \tag{2.39}$$

$$\tag{2.40}$$

This system is solved using Newton's method.

With $\bar{v}_{j+1/2}$ and $\bar{P}_{j+1/2}$ obtained, we proceed to the third and final step, which involves numerically solving the system of Eq. 2.1.

The radius of the interface $j+1/2$ is updated over the time interval $\Delta t = t^{n+1} - t^n$ as

$$r_{j+1/2}^{n+1} = r_{j+1/2}^{n} + \bar{v}_{j+1/2}\Delta t \tag{2.41}$$

Simultaneously, the average surface area of the wall at $j+1/2$ is also calculated as

$$\bar{A}_{j+1/2} = \frac{4\pi}{3}\frac{\left(r_{j+1/2}^{n+1}\right)^3 - \left(r_{j+1/2}^{n}\right)^3}{r_{j+1/2}^{n+1} - r_{j+1/2}^{n}} \tag{2.42}$$

The values in the j-th zone are then calculated for density and velocity as

$$\rho_j^{n+1} = \frac{3\Delta m_j}{4\pi\left(r_{j+1/2}^{n+1}\right)^3 - \left(r_{j-1/2}^{n+1}\right)^3} \tag{2.43}$$

$$v_j^{n+1} = v_j^n + \frac{1}{2}\left(\bar{A}_{j+1/2} + \bar{A}_{j-1/2}\right)\frac{\Delta t}{\Delta m_j}\left(\bar{P}_{j+1/2} - \bar{P}_{j-1/2}\right) + \frac{\Delta t}{2}\left(g_j^{n+1} + g_j^n\right) \tag{2.44}$$

The energy conservation equation is instead linearized as

$$\begin{aligned} E_j^{n+1} =& E_j^n - \frac{\Delta t}{\Delta m_j}\left(\bar{A}_{j+1/2}\bar{v}_{j+1/2}\bar{P}_{j+1/2} - \bar{A}_{j-1/2}\bar{v}_{j-1/2}\bar{P}_{j-1/2}\right) \\ & - \frac{\Delta t}{\Delta m_j}\left(L_{j+1/2}^{n+1} - L_{j-1/2}^{n+1}\right) + \epsilon_j^{n+1}\Delta t \end{aligned} \tag{2.45}$$

This cannot be solved directly since ϵ^{n+1} and L^{n+1} depend on T^{n+1}, which is still unknown at this stage of the integration. Using the fact that $E = E_{kin} + E_{int} + E_{grav}$, the previous equation can be rewritten as

$$\begin{aligned} E_j^{n+1} = & E_{int,j}^n + \left(E_{kin,j}^n + E_{grav,j}^n - E_{kin,j}^{n+1} - E_{grav,j}^{n+1}\right) + \epsilon_j^{n+1}\Delta t \\ & - \frac{\Delta t}{\Delta m_j}\left(\bar{A}_{j+1/2}\bar{v}_{j+1/2}\bar{P}_{j+1/2} - \bar{A}_{j-1/2}\bar{v}_{j-1/2}\bar{P}_{j-1/2}\right) \\ & - \frac{\Delta t}{\Delta m_j}\left(L_{j+1/2}^{n+1} - L_{j-1/2}^{n+1}\right) \end{aligned} \tag{2.46}$$

In this way, the first two terms do not depend on the temperature at time t^{n+1}; indeed, we have the term $E_{int,j}^n$, which does not depend on T^{n+1} since it was calculated at the previous integration step, as are $E_{kin,j}^n$ and $E_{grav,j}^n$. On the other hand, $E_{kin}^{n+1} = \frac{1}{2}(v_j^{n+1})^2$ and $E_{grav,j}^{n+1} = -Gm_j/r_j^{n+1}$ depend on values that have been already computed. Moreover, the third term is assumed to be composed of previously calculated terms, as ϵ^{n+1} primarily relies on ρ and T. Given that ρ_j^{n+1} has been computed, ϵ_j^{n+1} is then derived using ρ_j^{n+1} and T_j^n, with the assumption that the latter is constant.

Thus, we define

$$\begin{aligned} C_j =& E_{int,j}^n + \left(E_{kin,j}^n + E_{grav,j}^n - E_{kin,j}^{n+1} - E_{grav,j}^{n+1}\right) \\ & - \frac{\Delta t}{\Delta m_j}\left(\bar{A}_{j+1/2}\bar{v}_{j+1/2}\bar{P}_{j+1/2} - \bar{A}_{j-1/2}\bar{v}_{j-1/2}\bar{P}_{j-1/2}\right) \end{aligned} \tag{2.47}$$

We also define

$$G_j = C_j + \epsilon_{^{56}Ni,j}^{n+1}\Delta t \tag{2.48}$$

We can rewrite Eq. 2.46 as

$$E_{int,j}^{n+1} = G_j - \frac{\Delta t}{\Delta m_j}\left(L_{j+1/2}^{n+1} - L_{j-1/2}^{n+1}\right) \tag{2.49}$$

where G_j is defined at the center of the cell. Recalling Eq. 2.2 and Eq. 2.4, the luminosity can be linearized as:

$$L_{j+1/2}^{n+1} = -\bar{A}_{j+1/2}^2\left(\frac{1}{\kappa_{j+1/2}}\right)^{n+1}\frac{ac\lambda_{j+1/2}^{n+1}}{3}\frac{(T_{j+1}^{n+1})^4 - (T_j^{n+1})^4}{m_{j+1} - m_j} \tag{2.50}$$

It is also recalled that luminosity is defined at the boundary between two regions, while opacity κ is defined as a function of ρ and T, and thus at the center of a cell. For this reason, an approximation for κ is needed to interpolate its value $\kappa_{j+1/2}$. This can be obtained as

$$\left(\frac{1}{\kappa_{j+1/2}}\right)^{n+1} = \frac{(T_{j+1}^{n+1})^4/\kappa_{j+1}^{n+1} - (T_j^{n+1})^4/\kappa_j^{n+1}}{(T_{j+1}^{n+1})^4 - (T_j^{n+1})^4} \tag{2.51}$$

The flux limiter λ is calculated as

$$\lambda_{+1/2}^{n+1} = \frac{6 + 3R_{j+1/2}^{n+1}}{6 + 3R_{j+1/2}^{n+1} + (R_{j+1/2}^{n+1})^2} \tag{2.52}$$

where

$$R_{j+1/2}^{n+1} = \frac{2\bar{A}_{j+1/2}}{m_{j+1}m_j}\frac{\left|(T_{j+1}^{n+1})^4 - (T_j^{n+1})^4\right|}{(T_{j+1}^{n+1})^4 - (T_j^{n+1})^4}\left(\frac{1}{\kappa_{j+1/2}}\right)^{n+1} \tag{2.53}$$

Substituting Eq. 2.50, Eq. 2.51, Eq. 2.52, and Eq. 2.53 into Eq. 2.49 and recalling that $E_{int,j}^{n}$ depends only on ρ_j^{n+1} and T_j^{n+1}, it can be verified that $E_{int,j}^{n+1}$ is a function of only T_{j-1}^{n+1}, T_j^{n+1}, and T_{j+1}^{n+1}.

Assuming we have a number M of zones with boundary conditions

$$L_{1-1/2} = 0 \tag{2.54}$$

$$L_{M+1/2} = L_{M-1/2} \tag{2.55}$$

It follows that Eq. 2.49 is a system of M equations for the M unknowns T_j^{n+1} with $j = 1, ..., M$.

This system is solved using Newton's method, assuming a value T_j^{n+1} for the temperature, which implies solving the system

$$\begin{aligned}\frac{\partial E_{int,j}^{n+1}}{\partial T_j}\Delta T_j - \frac{\Delta t}{\Delta m_j}\left(\frac{\partial L_{j+1/2}^{n+1}}{\partial T_{j+1}}\Delta T_{j+1} + \frac{\partial L_{j+1/2}^{n+1}}{\partial T_j}\Delta T_j\right)\\ -\left(\frac{\partial L_{j-1/2}^{n+1}}{\partial T_j}\Delta T_j + \frac{\partial L_{j-1/2}^{n+1}}{\partial T_{j-1}}\Delta T_{j-1}\right) = -\delta_j\end{aligned} \tag{2.56}$$

where

$$\delta_j = E_{int,j}^{n+1} - G_j - \frac{\Delta t}{\Delta m_j}\left(L_{j+1/2}^{n+1} - L_{j-1/2}^{n+1}\right) \tag{2.57}$$

The derivative of the internal energy in Eq. 2.56 is obtained from the equation of state, while the derivatives of the luminosity are obtained using the value of L obtained from Eq. 2.50, ignoring the derivative of opacity with respect to temperature.

Thus, the coefficient matrix of the system is obtained, rewritten as

$$\frac{\Delta t}{\Delta m_j}\frac{\partial L^{n+1}_{j-1/2}}{\partial T_{j-1}}\Delta T_{j-1}+\left[\frac{\partial E^{n+1}_{int,j}}{\partial T_j}-\frac{\Delta t}{\Delta m_j}\left(\frac{\partial L^{n+1}_{j+1/2}}{\partial T_j}-\frac{\partial L^{n+1}_{j-1/2}}{\partial T_j}\right)\right]\Delta T_j-\frac{\Delta t}{\Delta m_j}\frac{\partial L^{n+1}_{j+1/2}}{\partial T_{j+1}}\Delta T_{j+1}=-\delta_j \tag{2.58}$$

with coefficient matrix

$$\begin{bmatrix} b_1 & c_1 & 0 & \dots & 0 \\ a_2 & b_2 & c_2 & & \vdots \\ 0 & \ddots & \ddots & \ddots & 0 \\ \vdots & & a_{M-1} & b_{M-1} & c_{M-1} \\ 0 & \dots & 0 & a_M & b_M \end{bmatrix} \tag{2.59}$$

where

$$a_j=\frac{\Delta t}{\Delta m_j}\frac{\partial L^{n+1}_{j-1/2}}{\partial T_{j-1}} \tag{2.60}$$

$$b_j=\frac{\partial E^{n+1}_{int,j}}{\partial T_j}-\frac{\Delta t}{\Delta m_j}\left(\frac{\partial L^{n+1}_{j+1/2}}{\partial T_j}-\frac{\partial L^{n+1}_{j-1/2}}{\partial T_j}\right) \tag{2.61}$$

$$c_j=-\frac{\partial L^{n+1}_{j+1/2}}{\partial T_j}\Delta T_j+\frac{\partial L^{n+1}_{j-1/2}}{\partial T_{j-1}} \tag{2.62}$$

This matrix is used by employing the SPARSEKIT2 package (Yousef Saad website).

After inversion, the initial value of T_j^{n+1} is updated to $T_j^{n+1} \longrightarrow T_j^{n+1}+\Delta T_{j+1}$, and the process is iterated until $\frac{\Delta T}{T}$ is within the chosen tolerance margin.

It remains to discuss the calculation of the term ϵ, which in general can be separated into $\epsilon=\epsilon_{nuc}+\epsilon_\nu$, with ϵ_{nuc} representing the energy generated by nuclear reactions while ϵ_ν is the energy lost due to neutrino production from thermal and weak interaction processes. In this version of the code, the only nuclear energy term considered is that associated with the radioactive decay $^{56}Ni \longrightarrow {}^{56}Co \longrightarrow {}^{56}Fe$, consequently $\epsilon_{nuc}=\epsilon_{^{56}Ni}$. This term is particularly relevant when calculating the light curves, allowing comparison with known SNe. It is calculated starting from the radiative transport equation

$$\frac{dI_\nu}{dz}=j_\nu-\alpha_\nu I_\nu \tag{2.63}$$

Where I_ν is the energy flowing per unit time, surface area, solid angle, and frequency along direction z, thus $\frac{dI_\nu}{dz}$ represents the variation of this energy along the propagation direction z. This variation is due to two different contributions:

- j_ν: energy produced per unit volume, time, solid angle, and frequency;
- $\alpha_\nu=n\sigma_\nu$ represents the absorption coefficient of the energy emitted along the propagation direction.

In the case of γ-rays produced along the z axis due to the decay of ^{56}Ni, Eq. 2.63 becomes

$$\frac{dI_\nu}{dz}=\eta-\kappa_\gamma\rho I \tag{2.64}$$

where the absorption coefficient is calculated as $\alpha = \kappa_\gamma \rho$, since the cross-section of the interactions between radiation and matter is given by the opacity to γ-rays. Similarly, the energy production term per unit volume j_ν is due solely to the energy released per unit volume by the decay of ^{56}Ni, obtained as

$$\eta = \frac{X_{Ni}\epsilon_{Ni}\rho}{4\pi} \tag{2.65}$$

Introducing the optical thickness $d\tau = -\kappa_\gamma \rho dz$ and defining

$$I' = \frac{4\pi\kappa_\gamma}{\epsilon_{Ni}} I \tag{2.66}$$

We obtain

$$\frac{dI'}{d\tau} = I' - X_{Ni} \tag{2.67}$$

We can now define

$$\mathbf{I} = I' e^{-\tau} \tag{2.68}$$

$$\mathbf{X}_{Ni} = X_{Ni} e^{-\tau} \tag{2.69}$$

Thus, the solution to the radiative transport equation becomes

$$\mathbf{I}(\tau_{j+1}) = \mathbf{I}(\tau_j) - \int_{\tau_j}^{\tau_{j+1}} \mathbf{X}_{Ni}(\tau) d\tau \tag{2.70}$$

Which, in terms of I' and X_{Ni}, assuming the latter is constant between j and $j+1$, becomes

$$I'(\tau_{j+1}) = I'(\tau_j) e^{-(\tau_j - \tau_{j+1})} + X_{Ni}\left[1 - e^{-(\tau_j - \tau_{j+1})}\right] \tag{2.71}$$

From Eq. 2.64, it is apparent that the energy deposited locally, in units of erg cm^{-3} s^{-1} sterad^{-1}, is $\kappa_\gamma \rho I$, which represents the energy absorbed by the medium and, when integrated over the entire solid angle of emission, provides the measure of the energy injected locally

$$E_{injected} = 4\pi\kappa_\gamma \rho J \tag{2.72}$$

where

$$J = \frac{1}{4\pi}\int_\Omega I(\Omega') d\Omega' \tag{2.73}$$

is the specific intensity integrated over the entire solid angle. Using the same change of variable as in Eq. 2.66, we obtain

$$J' = J = \frac{1}{4\pi}\int_\Omega I'(\Omega') d\Omega' = \frac{\kappa_\gamma}{\epsilon_{Ni}}\int_\Omega I(\Omega') d\Omega' = \frac{4\pi\kappa_\gamma}{\epsilon_{Ni}} J \tag{2.74}$$

Thus, Eq. 2.72 becomes

$$E_{injected} = 4\pi\kappa_\gamma\rho J = 4\pi\kappa_\gamma\rho\frac{\epsilon_{Ni}}{4\pi\kappa_\gamma}J' = \rho\epsilon_{Ni}J' = \rho\epsilon_{Ni}\frac{1}{4\pi}\int_\Omega I'(\Omega')d\Omega' \quad [erg\,cm^{-3}\,s^{-1}] \tag{2.75}$$

Dividing by ρ, we obtain the energy deposited locally per unit mass and time due to the decay of ^{56}Ni

$$\epsilon_{^{56}Ni} = \epsilon_{Ni}\frac{1}{4\pi}\int_\Omega I'(\Omega')d\Omega' \quad [erg\,g^{-1}\,s^{-1}] \tag{2.76}$$

which can be more compactly written by defining an energy deposition function

$$d = \frac{1}{4\pi}\int_{\Omega} I'(\Omega')d\Omega' \tag{2.77}$$

such that the energy deposited in each grid point per unit mass is defined as

$$\epsilon_{^{56}Ni} = \epsilon_{Ni}\, d \quad [\mathrm{erg\,g^{-1}\,s^{-1}}] \tag{2.78}$$

where the energy released per radioactive decay can be estimated as

$$\epsilon_{Ni} = 3.9\times10^{10}e^{-t/\tau_{Ni}} + 6.78\times10^{9}\left[e^{-t/\tau_{Co}} + e^{-t/\tau_{Ni}}\right] \quad [\mathrm{erg\,g^{-1}\,s^{-1}}] \tag{2.79}$$

with τ_{Ni} and τ_{Co} representing the mean lifetimes of ^{56}Ni and ^{56}Co, respectively.

Calculating $\epsilon_{^{56}Ni}$ in the *j-th* region requires knowledge of the deposition function d_j, obtained by integrating I'_j over the entire solid angle.

Finally, to complete the description of the integration algorithm for the system of Eq. 2.1, it is necessary to define the boundary conditions.

2.1.3 Boundary Conditions

The PPM method described thus far assumes the presence of six "ghost zones" in the computational domain. Consider, for example, the first region with $j = 7$. To perform the integration in this zone, it is necessary to calculate $\bar{v}_{6+1/2}$ and $\bar{P}_{6+1/2}$, and to do so, the states on the right and left must be defined, respectively $a^{+}_{6+1/2}$ and $a^{-}_{6+1/2}$, with $a = \rho,\ v,\ P$.

From Eq. 2.28, it is known that to calculate $a^{+}_{j+1/2}$, $a_{R,6}$, $\Delta a_{R,6}$, $a_{6,6}$ must be known, which are the polynomial interpolation in region $j = 6$. In general, to calculate $a_{L,j}$ and $a_{R,j}$, the two preceding and two following regions are needed. Specifically, to calculate $a_{L,j}$, the regions $j-1,\ j+1,\ j+2$ are required, while to calculate $a_{R,j}$, the regions $j-2,\ j-1,\ j+1$ are needed. Consequently, to calculate $j = 7$, three ghost regions are required, corresponding to $j = 4, 5, 6$.

In the scheme used, six "ghost zones" were assumed at the inner and outer edges of the integration domain. The inner boundary conditions are reflective, while the outer boundary is set to a zero gradient condition.

Specifically, it is assumed that at the outer boundary, all quantities remain constant and equal to the value in the last "physical" region, except for the pressure, which is set to $P =^{-24}$ dyne cm^{-2}. Thus, for any quantity a, we have

$$a_{7-j} = a_7 \qquad j = 1,\ldots,6 \tag{2.80}$$

The radius of these regions is obtained from ρ and dm.

On the other hand, at the inner surface due to the imposition of reflection,

$$a_{7-j} = \mathrm{sign}\cdot a_{7+j-1} \qquad j = 1,\ldots,6 \tag{2.81}$$

where

$$\mathrm{sign} = - \quad \text{if } a = v \tag{2.82}$$

$$\mathrm{sign} = + \quad \text{if } a \neq v \tag{2.83}$$

2.2 SEVN

SEVN is a rapid binary population synthesis code (Spera, Mapelli, and Bressan, 2015; Spera and Mapelli, 2017; Spera et al., 2019; Iorio et al., 2023). It can calculate simultaneously both single stellar evolution (SSE) and binary stellar evolution (BSE) processes. The former are simulated by interpolating pre-computed stellar tracks (in this Thesis I used the fiducial tracks, computed with the PARSEC stellar evolution code, see Bressan et al., 2012; Costa et al., 2019; Costa et al., 2021; Nguyen et al., 2022), which are included in the code in the form of look-up tables. The latter are implemented with analytical and semi-analytical prescriptions.

Such an implementation has the advantage of being very general and very flexible. One can easily vary the stellar evolution tracks (e.g., Mapelli et al., 2020 implemented also tracks from Limongi and Chieffi, 2018), i.e. the details of the stellar evolution, since they are not hard coded in SEVN. It is sufficient to change the uploaded look-up tables.

In the following, we will briefly present the treatment of SSE, and also the most relevant BSE processes.

2.2.1 Single star evolution

In the following sections, I will describe the main ingredients that SEVN employs to evolve a star from the ZAMS to the formation of the final compact remnants or to the binary's disruption.

2.2.1.1 Stellar evolution tables

SEVN employs pre-computed stellar evolution tables. Such tables are designed to contain the evolution of the properties of an ensemble of stellar tracks that are defined as function of their initial mass $M_{\rm ZAMS}$ and metallicity Z. Furthermore, two kinds of look-up tables are required to ensure the correct functioning of SEVN: one set of tables of stars that start their life at the ZAMS, i.e. on the hydrogen main sequence (MS), and one set of tables that follow the evolution of HE-naked stars (hereafter, pure-He stars), i.e. stars that have completely lost their H envelope. The latter are generated by evolving a set of tracks with PARSEC and removing the H-rich envelope at the beginning of the central He-burning phase (see Spera et al., 2019).

In Table 2.1, I summarize the tables available in the latest release of SEVN (see Iorio et al., 2023).

All the stellar evolution models include at least seven tables, which are grouped by metallicity. Each table contains different stellar properties, with at least seven mandatory tables (identified in Table 2.1 with an M in the Type column), that provide the main stellar properties, such as: the time, the stellar phase, mass, luminosity and radius and the star's HE and CO-core mass. In all the tables, each row represents a different star for the various values of $M_{\rm ZAMS}$ and Z. Each column provides the table's property value at the corresponding time (i.e. same row and column) in the time table. For instance, the first entry on each row in the mass table represents $M_{\rm ZAMS}$ of the star.

Furthermore, there are also optional tables for various other stellar properties. However, if such tables are not provided, SEVN is able to estimate these properties with various analytic approximations (see Appendix A1 in Iorio et al., 2023). It is worth mentioning, that such tables are not mandatory since many stellar evolution codes do not provide these properties. However, they are crucial to properly model several binary evolution processes (e.g. the nature of the convective envelope for the stability of the mass transfer).

TABLE 2.1: Summary of the stellar evolution tables used in SEVN. Column 1: property in the table; Column 2: table's units; Column 3: it specifies if a table is mandatory (M) or optional (O), as SEVN includes analytic recipes to replace the optional tables if they are not available; Column 4: Weights used by SEVN during the property interpolation: rational (R), linear (LIN), log (LOG) (see Section 2.2.1.3). Table rearranged on the basis of Table 1 by Iorio et al., 2023.

Table	**Units**	**Type**	**Interpolation**
Time	Myr	M	R
Phase[a]	Myr	M	R
Mass	$M_\odot$	M	LIN
Luminosity	$L_\odot$	M	LOG
Radius	$R_\odot$	M	LOG
He-core mass	$M_\odot$	M	LIN
CO-core mass	$M_\odot$	M	LIN
He-core radius	$R_\odot$	O	LOG
CO-core radius	$R_\odot$	O	LOG
Stellar inertia[b]	$M_\odot R_\odot^2$	O	LOG
Envelope binding energy[b]	$M_\odot R_\odot^{-1} (G^{-1})^*$	O	LOG
Surface abundances[b] (H, He, C, N, O)	Mass fraction	O	LIN
Convective envelope			
Mass	Normalized to star mass	O	LIN
Depth	Normalized to star radius	O	LIN
Turnover time	yr	O	LIN

[a]The phase table reports the starting time of each SEVN phase (Table 2).
[b]Not included in the stellar tracks used in this work (Section 3.1).
[*]The envelope binding energy is normalized over the gravitational constant G (assumed in solar units and years).

2.2.1.2 Stellar phases

In Spera et al., 2019, it was found that the interpolation from the look-up table is significantly more efficient if the percentage of life of a star is used instead of the absolute value of time. This is because, by imposing such a variable for the interpolation, it is ensured that the stars used for the interpolation are in the same evolutionary phase as the interpolated star.

In the current version of SEVN, the stellar evolution is divided in seven physically motivated phases, which are reported in Table 2.2.

Phase 0 represents the pre-MS (PMS), is the stellar phase from time $t = 0$ to the ignition of central hydrogen burning. Phase 1 is associated with MS, until the formation of an He-core(He-core mass >0). Once the He core is formed the star enters the Terminal-MS (TMS), which is identified with phase 2. Phase 3 starts when the central hydrogen core is exhausted and the star is burning the hydrogen in shells. This phase is called the shell hydrogen burning (SHB) phase and lasts until the ignition of the central He-burning (CHeB). This latter is the CHeB phase (or He-MS), with phase id=4, and it is followed, analogously at the H-MS, by the Terminal-CHeB (TCHe, with phase 5). This latter is distinguished by the beginning of the formation of a CO-core, with CO-core mass >0. It is followed by the shell He burning phase (SHeB) marked with phase=6. Such a phase lasts until the formation of the final compact remnant at the end of a star's life. This is also the last possible stellar phase, and it is identified with phase 7.

If a star is stripped by its H-envelope because of stellar winds or binary interactions (see

TABLE 2.2: Column 1: SEVN stellar evolutionary phases; Column 2: integer identifiers; Column 3: Remnant types. Table rearranged on the basis of Table 2 in Iorio et al., 2023

SEVN Phase	Phase ID	SEVN Remnant subphase	Remnant ID
Pre-main sequence (PMS)	0	–	0
Main sequence (MS)	1	–	0
Terminal-age main sequence (TAMS)	2	–	0
Shell H burning (SHB)	3	–	0
Core He burning (CHeB)	4	–	0
Terminal-age core He burning (TCHeB)	5	–	0
Shell He burning (SHeB)	6	–	0
Remnant	7	He white dwarf (HeWD)	1
		CO white dwarf (COWD)	2
		ONe white dwarf (ONeWD)	3
		neutron star (ECNS)	12
		neutron star (CCNS)	13
		black hole (BH)	14
		no compact remnant (Empty)	–

Section 2.2.2), it evolves as a pure-He star and its properties are interpolated on the basis of the pure-He look-up table. It is worth mentioning that in SEVN there are no particular phases associated with He-naked stars. Thus, the only difference from hydrogen-rich stars is that a pure-He star will skip phases 0-3 and start its life as a phase 4 star.

2.2.1.3 Interpolation

The properties of each star at any time-step are obtained by interpolating the between four similar tracks, i.e. the *interpolating tracks*. The current method implemented in SEVN is for the interpolation is the one proposed by Iorio et al., 2023. In this section, I will briefly summarize it.

Upon initialization of a star, SEVN assigns it with four *interpolating tracks* either for the hydrogen or pure-He look-up tables. The four tracks have two different metallicities (Z_1 and Z_2) and four different initial masses masses ($M_{\rm ZAMS,\,1}$, $M_{\rm ZAMS,\,2}$, $M_{\rm ZAMS,\,3}$, and $M_{\rm ZAMS,\,4}$, two per metallicity). The values of Z_i and $M_{\rm ZAMS,\,i}$ are chosen such that $Z_1 \leq Z < Z_2$, and $M_{\rm ZAMS,\,1/3} \leq M_{\rm ZAMS} < M_{\rm ZAMS,\,2/4}$, where Z, and $M_{\rm ZAMS}$ are the initial values for metallicity and mass of the stars, respectively, that is being interpolated. In the case $M_{\rm ZAMS}$ or Z are equal to the maximum values provided by the look-up tables the intervals are modified as: $Z_1 < Z \leq Z_2$, and $M_{\rm ZAMS,\,1/3} < M_{\rm ZAMS} \leq M_{\rm ZAMS,\,2/4}$.

Once the *interpolating tracks* have been chosen a given property P is computed as:

$$P = \frac{Z_2 - Z}{Z_2 - Z_1} P_{Z,1} + \frac{Z - Z_1}{Z_2 - Z_1} P_{Z,2} \tag{2.84}$$

with

$$P_{Z,1} = \beta_1 P_{\rm ZAMS,1} + \beta_2 P_{\rm ZAMS,2} \tag{2.85}$$

$$P_{Z,2} = \beta_3 P_{\rm ZAMS,3} + \beta_4 P_{\rm ZAMS,4} \tag{2.86}$$

where $P_{\rm ZAMS,i}$ is the property value of the i-th track at the ZAMS, and β_i are the interpolation weights.

In the current public version of SEVN are included three different interpolation weights:

(i) *Linear*,

$$\beta_{1/3} = \frac{M_{\rm ZAMS,2/4} - M_{\rm ZAMS}}{M_{\rm ZAMS,2/4} - M_{\rm ZAMS,1/3}}, \tag{2.87}$$

$$\beta_{2/4} = \frac{M_{\rm ZAMS} - M_{\rm ZAMS,1/3}}{M_{\rm ZAMS,2/4} - M_{\rm ZAMS,1/3}}; \tag{2.88}$$

(ii) *Logarithmic*,

$$\beta_{1/3} = \frac{\log M_{\rm ZAMS,2/4} - \log M_{\rm ZAMS}}{\log M_{\rm ZAMS,2/4} - \log M_{\rm ZAMS,1/3}}, \tag{2.89}$$

$$\beta_{2/4} = \frac{\log M_{\rm ZAMS} - \log M_{\rm ZAMS,1/3}}{\log M_{\rm ZAMS,2/4} - \log M_{\rm ZAMS,1/3}}; \tag{2.90}$$

(iii) *Rational*,

$$\beta_{1/3} = \frac{M_{\rm ZAMS,1/3}\left(M_{\rm ZAMS,2/4} - M_{\rm ZAMS}\right)}{M_{\rm ZAMS}\left(M_{\rm ZAMS,2/4} - M_{\rm ZAMS,1/3}\right)}, \tag{2.91}$$

$$\beta_{2/4} = \frac{M_{\rm ZAMS,2/4}\left(M_{\rm ZAMS} - M_{\rm ZAMS,1/3}\right)}{M_{\rm ZAMS}\left(M_{\rm ZAMS,2/4} - M_{\rm ZAMS,1/3}\right)}. \tag{2.92}$$

Logarithmic weights are used in SEVN for properties that are internally stored, such as radius and luminosity. *Rational weights* have been introduced in Spera et al., 2019, as they found that such weights improve significantly the interpolation for the starting time of the various stellar phases and the star's life estimate. For all the other quantities, SEVN uses the *linear weights*.

Upon initialization of a star, SEVN set the starting time of the stellar phases $t_{\rm start,p}$ by using Eq. 2.86 and Eq. 2.84, where $P_{\rm ZAMS,i}$ are the phase times from the phase table. The stellar lifetime is estimated in the same way, assuming that the last element per row in the SEVN time tables is the stellar lifetime of the *interpolating tracks*.

The other properties need to be estimated at a given time t, thus the corresponding value of $P_{\rm ZAMS,i}$ needs to be estimated at the same time. However, as previously mentioned, in SEVN P is estimated on the basis of the residual percentage of life in the stellar phase, rather than the absolute time value t. The percentage of life in a given phase is computed as:

$$\Theta_{\rm p} = \frac{t - t_{\rm start,p}}{t_{\rm start,p_{next}} - t_{\rm start,p}} \tag{2.93}$$

with $t_{\rm start,p}$ that indicates the starting time of the current phase, and $t_{\rm start,p_{next}}$ indicating the starting time of the following stellar phase $\rm p_{next}$ (cfr. Table 2.2). Once $\Theta_{\rm p}$ is computed, SEVN computes $P_{\rm ZAMS,i}$ at the time;

$$t_i = t_{\rm start,p_i} + \Theta_{\rm p}\Delta_{\rm p,i} \tag{2.94}$$

where $t_{\rm start,p_i}$ and $\Delta_{\rm p,i}$ are the starting time and the time duration of the current phase, respectively, for the i-th *interpolating track*.

Therefore, SEVN chose the various percentages of time in a given phase with Eq. 2.93, and then linearly interpolates over time to provide estimates for $P_{\rm ZAMS,i}$ for all *interpolating tracks*. Such an approach is strongly physically motivated, as it ensures that the *interpolating tracks* are in the same evolutionary stage. It also reduces the interpolation errors to a few percent (see Spera et al., 2019).

2.2.1.4 Final fate of massive stars

In this section, I will briefly present the various treatments included in SEVN for the final fate of massive stars, and their compact remnants.

Once in SEVN the time over which a star is evolved exceeds the stellar lifetime, it forms a compact remnant. The nature of the compact remnant (listed in Table 2.2) is determined on the basis of the final CO-core mass $M_{\rm CO}$ of a star at the end of its life:

- $M_{\rm CO} \leq 1.38\,{\rm M}_\odot$: the final remnant is a white dwarf (WD). Depending on $M_{\rm ZAMS}$ and on the final He-core mass $M_{\rm He}$ the WD can be either an helium WD (HeWD, if $M_{\rm ZAMS} \lesssim 2\,{\rm M}_\odot$) a carbon-oxygen WD (COWD, if the final value of the He-core mass is such that $M_{\rm He} \leq 1.6\,{\rm M}_\odot$) or an oxygen-neon WD (ONeWD).
- $1.38\,{\rm M}_\odot \leq {\rm M}_{\rm CO} < 1.44\,{\rm M}_\odot$: the final remnant is an electron-capture neutron star (ECNS), resulting from an electron-capture SN.
- $M_{\rm CO} \geq 1.44\,{\rm M}_\odot$: the final remnant is the result of a core-collapse SN. It can be either a NS or a BH, depending on the property of the stellar progenitor at the presupernova (preSN)-stage.

2.2.1.4.1 Core-collapse Supernovae SEVN includes different prescriptions for the ccSN processes, based on the work of Fryer et al., 2012, such as the *rapid* and *delayed* explosion mechanisms. The *rapid* model assumes that the supernova (SN) initiates within 250 ms of the stellar collapse, while the *delayed* model involves a longer timescale before shock formation. These models are based on neutrino-driven and convection-enhanced mechanisms for the onset of ccSN, the difference being that in the *rapid* scenario, the SN onset occurs within 250 ms from the collapse of the stellar progenitor, whereas in the *delayed* scenario, the shock wave that leads to the eventual SN forms over a longer timescale, exceeding 250 ms. The final remnant mass in both scenarios is calculated as the sum of the proto-compact object mass and the fallback material.

Specifically, we adopted the `rapid_Gauss` and `delayed_Gauss` routines present in SEVN, which are based on the *rapid* and *delayed* models from Fryer et al., 2012 but draw NS masses from a Gaussian distribution with mean $1.33\,{\rm M}_\odot$ and standard deviation $0.09\,{\rm M}_\odot$, following the fit presented in Özel et al., 2012; Özel et al., 2016. This addition was implemented to better match the observed properties of the NS population.

We also included the prediction for remnant masses based on the results of Ugolini et al., 2024. Specifically, we implemented the fitting formula we found in our work on the initial mass-remnant mass relation (see Chapter 3 for more details).

2.2.1.4.2 Pair-instability supernovae Furthermore, we were interested in the role played by pair instabilities (PIs) (see Fowler and Hoyle, 1964; Barkat, Rakavy, and Sack, 1967; Rakavy and Shaviv, 1967) in the final mass spectrum of primary BHs in binary black hole (BBH) systems that will eventually merge through gravitational-wave (GW) emission (see Chapter 4). Specifically, we investigated the pulsational pair instabilities (PPIs). The precise threshold for PPI onset depends on various factors, and different criteria are present in the literature (e.g., Woosley 2017; Woosley 2019; Farmer et al. 2019; Renzo et al. 2020; Ugolini et al. 2024). The effect of PIs depends largely on the properties of the stellar progenitor, especially the CO core mass. More refined criteria for PI onset have been proposed by Marchant et al., 2019; Renzo et al., 2020; Costa et al., 2021, but they require precise knowledge of the stellar structure, which is beyond SEVN current capabilities. If a star has a CO core massive enough to trigger PI, it can undergo one of three possible outcomes (for more details, see Renzo and Smith, 2024 for a review). For lower-core masses ($28-38\,{\rm M}_\odot \leq {\rm M}_{\rm CO} \leq 54-60\,{\rm M}_\odot$, with

the lower limit that depends on the chosen criterion), PIs trigger strong pulsational events, known as PPISNe, that significantly enhance mass loss. This leads to lighter BHs as the final compact objects. For CO core masses in the range $54-60\,M_\odot \leq M_{CO} \leq 110-120\,M_\odot$, the progenitor is completely destroyed in a PISN, leaving no remnant. Finally, if the CO core is $\geq 110-120\,M_\odot$, PI causes a dynamical instability that results in the direct collapse of the star into a massive BH.

To account for the uncertainties present in the literature regarding PI onset, we performed our simulations assuming four different prescriptions for PPI treatment: `noPPISN`, `M20`, `F19`, and `U24`. The `noPPISN` model disables the onset of PPIs, meaning no pulsational pair-instability supernovae occur, and all massive stars end their lives via ccSNe. The `M20` model, based on Mapelli et al., 2020, was implemented in the previous version of SEVN. This model uses the fit by Spera and Mapelli, 2017, which is based on the results of 1D hydrodynamical simulations of PPISNe by Woosley, 2017. In this scenario, a star is assumed to undergo PPI for $32\,M_\odot \leq M_{He} \leq 64\,M_\odot$. The final remnant mass is obtained by applying a corrective factor $\alpha \in [0,1]$ to the BH mass that would normally be formed through ccSN of the progenitor.

The `F19` model has been implemented in the current version of SEVN and is based on MESA simulations of pure-He stars by Farmer et al., 2019. The model uses the CO core mass as a proxy for PI onset, which occurs for $38\,M_\odot \leq M_{CO} \leq 60\,M_\odot$. The final remnant mass in SEVN is determined using:

$$M_{BH} = \min(M_{preSN}, M_{F19}) \tag{2.95}$$

where M_{preSN} is the mass of the progenitor at the pre-supernova stage, and M_{F19} is the remnant mass as determined by Farmer et al., 2019, which depends on both the final CO core mass and the initial metallicity.

The `U24` model is based on the FRANEC tracks presented in Limongi and Chieffi, 2018 and was introduced in Ugolini et al., 2024. We found that FRANEC stellar tracks are stable for CO core masses $\leq 33\,M_\odot$. We assumed a threshold for PPI onset of $M_{CO} = 35\,M_\odot$ to account for the possibility that PPI may not occur at slightly higher core masses. The compact remnant mass was estimated by assuming that all stars undergoing PPI lose their hydrogen envelope and then interpolating CO core masses to match the results obtained by Woosley, 2017 for naked-helium stars. For more details see Chapter 3.

2.2.1.5 Supernova kicks

Finally, in this section we will describe the treatment of natal kicks associated with the birth of a compact remnant after an ecSN or a ccSN.

In SEVN are included several treatment for natal kicks, here I will present the fiducial model that was employed in my work. Such a method is based on the work by Giacobbo and Mapelli, 2020, and the kick velocities are estimated:

$$V_{kick} = f_{H05}\frac{\langle M_{NS}\rangle}{M_{rem}}\frac{M_{ej}}{\langle M_{ej}\rangle} \tag{2.96}$$

with $\langle M_{NS}\rangle$, and $\langle M_{ej}\rangle$ are the average mass of the NS and of the ejecta from SSE, respectively. M_{rem} M_{ej} are the compact object mass and the ejecta mass, respectively. Finally, f_{H05} is a random number extract from a Maxwellian distribution, with mean 1 dimensional-root mean square $\sigma_{kick} = 265\,km/s$ (derived from linear fits, see Hobbs et al., 2005).

The values of $\langle M_{NS}\rangle$, and $\langle M_{ej}\rangle$ have been calibrated using the SSE function of SEVN, for a population of stars extracted according to a Kroupa initial mass function (IMF) with metallicity $Z = 0.02$.

The treatment of natal kicks is crucial in a code like SEVN, since natal kicks may change drastically the orbital properties of a stellar binary. They can modify the relative orbital velocity and the position of the center of mass, resulting in a tighter or looser binary. Furthermore, if the semimajor axis becomes <0 and/or the eccentricity of the binary becomes >1, the binary is considered disrupted as a consequence of the SN explosion. It is worth noting that such a phenomenon is usually associated to ccSNe, as ecSNe tend to born with weaker natal kicks, because of the lower amount of ejected material (see Tauris, Langer, and Podsiadlowski, 2015; Tauris et al., 2017).

2.2.2 Binary stellar evolution

Other than evolving the single stars by means of the interpolation algorithm, SEVN includes prescription to treat several BSE processes, such as: wind mass transfer, Roche-lobe overflow (RLOF), common envelope (CE), stellar tides, circularization at the RLO onset, collision at periastron, orbit decay by GW emission, and stellar mergers. In this section, I will focus on the processes most relevant to my work, presented in Chapter 4, thus the formalism behind the treatment of stable/unstable mass transfer and the mechanism for GW-emission. For further details on the other many processes treated in SEVN I refer the reader to Iorio et al., 2023 and reference therein.

2.2.2.1 Roche-lobe overflow

A Roche-lobe (RL) is defined as the region of space, around a star in a binary system, within which the orbiting material is graviationally bound to such star. Therefore, when a star expands during its life may overfill its RL and as a result parts of its envelope falls back onto the stellar companion. This process is called RLO. As a consequence of such a process, the parameters of a binary may vary significantly since it alters both the masses, and therefore the mass ratio, and both the radii of the two stars, and the semi-major axis of the orbit of the system.

In SEVN a RLO occurs each time the radius of one of the two stars becomes equal to the radius of the RL (or overcomes it). It is computed using the analytical expression provided by Eggleton, 1983 at each time-step as:

$$R_L = a\frac{0.49q^{1/3}}{0.6q^{2/3} + \ln(1+q^{1/3})} \tag{2.97}$$

where q is the mass ratio of the system of each star with respect to its companion.

Once the RLO is triggered there is a transfer of matter from the star overfilling the RL, called the *donor*, to its companion, the *accretor* that continue until is true for both the stars radii that $r < R_L$.

However, because of the mass transfer itself, during a RLO phase the mass ratio of the two stars changes, as well as the semimajor axis of the binary system. This triggers a shrink or and expansion of the RL. If it changes too rapidly or too slowly, the mass transfer may become unstable, because of the adiabatic response of the star to the mass-loss. Thus, the binary may trigger either a stellar merger, or a CE.

To asses the stability of mass loss, SEVN adopts a formalism common to many population synthesis codes, that is based on the mass ratio $q = M_d/M_a$, where M_d, and M_a are the donor and the accretor masses, respectively. The mass ratio computed in this way is then compared with some critical value q_c, that depends on the stellar evolution phases of the binary. As long as it is true that $q < q_c$, the mass transfer is considered stable, otherwise it is unstable on the dynamical timescale. In my work, I relied on the fiducial configuration presented by Iorio et al., 2023, summarized in Table 2.3 (designed on the basis of Table 3 from Iorio et al., 2023). Such configuration uses the same q_c as Hurley, Tout, and Pols, 2002, but the mass transfer

is assumed to be always stable for star in the MS or in the Hertzsprung-gap (HG), as they have radiative envelopes. Moreover, stars with deep convective envelopes have a particular treatment for q_c, that is modeled as:

$$q_c = 0.362 + \frac{1}{3\left(1 - \frac{M_{He,d}}{M_d}\right)} \tag{2.98}$$

where $M_{He,d}$ and M_d are respectively the He-core mass and the total mass of the donor star, respectively. Eq. 2.98 is based on the models by Webbink, 1988.

TABLE 2.3: Based on Table 3 from Iorio et al., 2023. Critical mass ratios as a function of the donor BSE stellar type for the fiducial q_c model implemented in SEVN. See Table 2 for further details on BSE types and their correspondence to SEVN phases. The word "stable" indicates that the mass transfer is always stable. Table rearranged from Table 3 in Iorio et al., 2023.

BSE type of the donor star	**QCRS**
0 (low mass MS)	0.695
1 (MS)	stable
2 (HG)	stable
3/5 (GB/EAGB)	Eq. 2.98
4 (CHeB)	3.0
7 (HeMS)	stable
8 (HeHG)	0.784
>10 (WD)	0.628

2.2.2.2 Stable Mass Transfer

If the mass transfer is deemed stable according to the q_c criterion, it is treated as follows. The donor mass loss rate in SEVN is computed, according to Hurley, Pols, and Tout, 2000, as:

$$\dot{M}_d = -F(M_d)\left(\ln\left(\frac{R_d}{R_{L,d}}\right)\right)^3 \quad \mathrm{M}_\odot\,\mathrm{yr}^{-1} \tag{2.99}$$

where $F(M_d)$ is a normalization function, R_d is the donor's radius and $R_{L,d}$ is the RL of the donor star. However, SEVN is designed in such a way that the mass transfer may be not conservative, i.e. the mass accreted by the accretor may me less than the mass lost by the donor, that is computed as:

$$\dot{M}_a = \begin{cases} min(\dot{M}_{Edd}, -f_{MT}\dot{M}_d) & \text{if the accretor is a compact object} \\ -f_{MT}\dot{M}_d & \text{otherwise} \end{cases} \tag{2.100}$$

where $\dot{M_{Edd}}$ is the accretion mass rate onto a compact object in the Eddington limit, and f_{MT} is the efficiency of the mass accretion. In our work, we kept it at the fiducial value of $f_{MT} = 0.5$ assumed in Iorio et al., 2023.

2.2.2.3 Unstable Mass transfer

When the mass transfer becomes unstable, it can trigger either a stellar merger or a common envelope (CE) phase, depending on the stellar phase of the donor star. Stars with a clear envelope/core separation (preMS, MS or HeMS) undergo a stellar merger. On the other hand,

if there is a clear separation between the envelope and the core, i.e. an He core has already been formed, the binary will undergo a CE phase. Finally, if the donor star is in the HG phase, it is unclear in the literature if it will trigger a CE (the optimistic scenario by Dominik et al. 2012 and in Vigna-Gómez et al. 2018 the binary system triggers a CE phase) or a stellar merger (pessimistic scenario in Dominik et al. 2012, Mapelli 2018). In SEVN the default option is that these cases will also lead to a CE phase.

2.2.2.4 CE evolution

If the binary system enters a CE phase both the stars are stripped of their H-envelope and they orbit each other in their now shared envelope. This introduce dragging forces in their equation of motion and as results the orbits shrinks, i.e. the semi-major axis is reduced. At this stage, the system has two possible evolutionary outcomes, either the CE is expelled or the two cores merge forming a compact object.

The CE phase is parametrized in SEVN following the α-formalism (see Webbink 1985; Tout et al. 1997) and to evaluate if the CE is eventually expelled we compute the envelope's binding energy at the beginning of the CE as:

$$E_{\mathrm{bind},i} = -G\Big(\frac{M_1 M_{\mathrm{env},1}}{\lambda_1 R_1} + \frac{M_2 M_{\mathrm{env},2}}{\lambda_2 R_2}\Big) \tag{2.101}$$

where $M_1\,(M_2)$ is the mass of the primary (secondary) star, $M_{\mathrm{env},1}$ $(M_{\mathrm{env},2})$ is the mass of the envelope of the primary (secondary) star, R_1 (R_2) is the radius of the primary (secondary) star. Finally, λ_i is a structural parameter that takes into account the binding energy of each star envelope and it is computed by following Claeys et al., 2014.

Then, the variation of binding energy of the system during the CE phase is computed as:

$$\Delta E_{\mathrm{orb}} = \frac{G M_{c,1} M_{c,2}}{2}\Big(a_{\mathrm{f}}^{-1} - a_{\mathrm{i}}^{-1}\Big) \tag{2.102}$$

where $M_{c,1}$ and $M_{c,2}$ are the cores of the two stars and a_{i} and a_{f} are the semi-major axis at beginning and at the end of the CE phase, respectively. Finally, the post-CE separation is found by imposing $E_{\mathrm{bind},i} = \alpha \Delta E_{\mathrm{orb}}$. The parameter α represents how efficiently the binding energy of the system is converted into kinetic energy, that eventually expels the CE. The original formulation accounted only for $\alpha \in [0,1]$, while in our work we have $0.5 \leq \alpha \leq 10$. This is because the α-formalism is a simplified model, and in this way we account also for the fact that the binding energy is not the only source of kinetic energy that take part into the ejection of the envelope (see Röpke and De Marco, 2023 and reference therein).

2.2.2.5 Stellar mergers

When the mass transfer becomes unstable for a donor star with unclear envelope/core separation, in SEVN a stellar merger takes place and from the two star of the binary a new single object is born. The new star is obtained by simply summing the CE cores, the He cores, and the total masses of the two progenitor stars. It also has the same phase and stellar phase of the most evolved of its progenitors.

In the case of a merger between a compact object and a star, it is assumed that the star is disrupted with the compact object, which does not accrete any matter.

the code sums the CO cores, the helium (He) cores and the envelopes and the resulting star on has the phase and the remaining percentage of life of the most evolved pre-merger star. Furthermore, a WD-WD merger provokes a SNIa, that leaves no remnant, and NS-NS merger results in a BH if the final mass if above $3\,\mathrm{M}_\odot$. However, with the exception of WD-WD

mergers, the final remnant of a merger between two compact object will always be a compact object with mass equal to the sum of the masses of its progenitors.

2.2.3 Gravitational waves emission

In SEVN it is implemented the formalism for the GW emission impact on a binary, computed as:

$$\dot{a} = -\frac{64G^3 M_1 M_2 (M_1 + M_2)}{5c^5 a^3 (1-e^2)^{7/2}} \left(1 + \frac{73}{24}e^2 + \frac{37}{96}e^4\right) \tag{2.103}$$

$$\dot{e} = -\frac{304G^3 M_1 M_2 (M_1 + M_2)}{15c^5 a^4 (1-e^2)^{5/2}} \left(1 + \frac{121}{304}e^2\right) e \tag{2.104}$$

accordingly to the formalism developed in Peters, 1964. Eq. 2.103 and Eq. 2.104 are used to provide an estimate of the GW-merger timescale, allowing to determine if a compact object binary will merge within a Hubble time.

2.2.4 The algorithm

In this section I will briefly present the algorithm flowchart, especially the decision-making interface.

2.2.4.1 The adaptive time-step

SEVN employs a prediction-correction method to chose the right time-step for accounting for the various processes in place during the evolution of a stellar binary. This is crucial to properly evolve both the individual properties of the two stars and the properties of the binary, whose timescale for variation ranges across multiple order of magnitudes, with processes that take place over minutes and processes that lasts tens or thousands of Myr.

Therefore, to chose the time-step, SEVN imposes that any property P, among the all properties of both the single stars and the binary, does not experience a drastic variation. It does that by choosing a *maximum amount* of relative variation δ_{max} such that

$$\max_{P \in \text{properties}} |\delta P| \leq \delta_{max} \tag{2.105}$$

where δP is the relative property variation. The default value of for the maximum variation is $\delta_{max} = 0.05$.

Then, SEVN computes the time-step as:

$$dt_{next} = \min_{P \in \text{properties}} \left(\delta_{max} \frac{dt_{last}}{|\delta P_{last}|}\right) \tag{2.106}$$

with $dt_{last}/|\delta P_{last}|$ that is the inverse of δP_{last} time derivative, as dt_{last} and δP_{last} are the previous time-step and the variation of the property P in such a time-step, respectively. If the value of dt_{next} is calculated with Eq. 2.106 satisfies the condition of Eq. 2.105 the evolution proceeds. Otherwise, SEVN predicts a smaller time-scale with Eq. 2.106 updating δP_{last} and dt_{last}, until Eq. 2.105 is satisfied or the newly computed time-step differs from the previous one by less than 20%.

Furthermore, once a star is close to a phase shift, to ensure that the stellar properties are correctly evaluated just before and just after the phase shift, SEVN implements an additional treatment. It reduces the time-step such that the next evolution step brings the star (or the binary) 10^{-10} Myr before the phase change. The subsequent step, is devised in such a way

that moves the star (binary) 10^{-10} Myr into the next phase. This allow to carefully account for sharp transitions, such as SNe and WD formation, as for this star the properties of the stellar progenitor immediately before the phase shift are crucial. Finally, several others controls are in place for the various time-steps, which guarantees that each stellar phase is correctly evaluated (at least 10 times per phase), that the interpolation algorithm does not skip more than two points in the look-up tables, and that the evolution time cannot exceed the simulation ending time.

By combining all the various control on the time-steps, it results that in SEVN, for a typical binary, the time-step may vary over 9 to 10 orders of magnitude.

2.2.4.2 Time evolution

In Figure 2.8 (Figure 3 by Iorio et al., 2023), it is summarized the temporal evolution scheme, its logic, and the various controls in place. At each time-step SEVN evolves the two star independently, and then it evolves the binary accounting for the property variations ΔP. After the integration of all the binary-evolution processes, SEVN compute the updated value of the given *binary* property P at the time t as:

$$P(t) = P(t_0) + \Delta P \tag{2.107}$$

where $P(t_0)$ are the properties at the initial stage of the evolution step and ΔP is the overall variation of the property P. For each stellar properties, Eq. 2.107 is slightly modified, and they are computed as:

$$P(t) = P_s(t) + \Delta P \tag{2.108}$$

where $P_s(t)$ is the expected value for the given property P after a time-step. Thus, in such a way also the individual properties of each star accounts for the BSE (e.g. mass accreted or lost during a RLO. Both SSE and BSE processes are repeated until the condition of Eq. 2.105 are satisfied.

Finally, in SEVN there are object whose properties do not vary with time. They are the compact remnants, that maintain their properties constant over time, and naked-CO stars, that are treated similarly to compact objects, until they end their life becoming compact objects.

The transition into compact object is modeled to take place at the beginning of a new time-step, thus in that time-interval also the natal kicks, when needed, will be applied to the binary. Therefore, during that particular time-step, the binary will take into account in its evolution also the effect of a possible SN.

Finally, if a RLO circularization, a stellar merger and/or a CE phase takes place, SEVN assumes an almost instantaneous process, with an arbitrary-small time-step $dt = 10^{-15}$ Myr. These processes are then computed during the arbitrary time-step.

Finally, at the beginning of each time-step, SEVN checks if a SNIa will take place or if it needs to change the *interpolating tracks*.

2.2.4.3 Jump to different tracks

Because of one of the may binary effects, a star may change significantly its properties. The property more prone to such a variation is the stellar mass, that may vary because of mass-loss/accretion (e.g., RLO, stellar mergers, CE). If this is the case, one (or more) of the *interpolating tracks* that SEVN chose at the ZAMS may not be the most indicated for the new star, and SEVN must find a stellar tracks that matches the new star's properties.

Depending on the phenomenon triggering the stellar variation, several criterion are in place in SEVN:

- **Stars without a core (MS ore pure-He MS stars)**: SEVN moves to a new track each time the total mass loss/accreted (because of binary processes) over time is more than 1% of the star's total mass;
- **Stars with a core (either an He or a CO-core)**: the core's properties dictates the stellar evolution, thus there is a change of *interpolating tracks* only if the core's mass varies;
- **Stellar merger**: when two stars merge there is always a change of *interpolating tracks*;
- **A H-rich star looses its envelope**: If a star with mass M and He-core mass M_{He} is such that $(M - M_{He})/M \lesssim 0.02$, the star becomes a Wolf-Rayet star, and it start evolving as a pure-He star (i.e. following a pure-He track).

In order to choose the new *interpolating track*, SEVN searches for the the stellar tracks with the same Z and in the same evolutionary phase of the current star, that have the mass (or core-mass, depending on the stellar phase) closer to the current star. SEVN searches such a track either among the H-rich stars for stars that have an hydrogen envelope or among the pure-He stars, either for a pure-He star or a star that has been stripped of its H-envelope in that time-step. For stellar mergers it searches the new *interpolating tracks* in the H-rich tables or in the pure-He tables, depending if one of two mergers stars had retained its H-envelope or not, respectively, at the pre-merger time-step.

For tracks without a formed core, SEVN employs the algorithm described in Spera et al., 2019.

Let's define the current mass of the star M and $M_{\rm p,i}$, $M_{\rm ZAMS,i}$ the values of the masses of the *interpolating tracks* currently and at the ZAMS. The new *interpolating track* is chosen assuming a linear relation between $M_{\rm p,i}$, and $M_{\rm ZAMS,i}$, such that:

$$M = \frac{M_{\rm p,2} - M_{\rm p,1}}{M_{\rm ZAMS,2} - M_{\rm ZAMS,1}}(M_{\rm ZAMS,new} - M_{\rm ZAMS,1}) + M_{\rm p,1}. \tag{2.109}$$

This is an iterative process, that starts by assuming $M_{\rm ZAMS,1} = M_{\rm ZAMS,\mathit{old}}$ and $M_{\rm ZAMS,1} = M_{\rm ZAMS,\mathit{old}} + 1.2\delta M$, where δM is the cumulative amount of mass lost/accreted in the binary processes. Such a process goes on until is true that:

$$\frac{M_{\rm p,new} - M}{M} < 0.005 \tag{2.110}$$

When this condition is not satisfied, Eq. 2.109 is iterated substituting $M_{\rm ZAMS,1}$ or $M_{\rm ZAMS,2}$ with $M_{\rm ZAMS,new}$. Such an iteration is repeated until Eq. 2.110 is satisfied, or after ten iterations or if $M_{\rm ZAMS,new}$ exceeds the possible values in the look-up tables. If SEVN does not find a value for $M_{\rm ZAMS,new}$ that satisfies Eq. 2.110 it chooses the $M_{\rm ZAMS,new}$ such that it minimize $M_{\rm p,new} - M/M < 0.005$.

For stars that have formed a core, SEVN looks for the best match in terms of $M_{\rm ZAMS,new}$ by looking at the core masses. It ranges in the interval $[\max(M_c, M_{\rm ZAMS,min}), M_{\rm ZAMS,max}]$, with the extremes of the interval that are the borders of the mass table, and employs the bisection method, as in Spera et al., 2019. Also in this case, SEVN performs at most 10 iterations. If Eq. 2.110 is satisfied within these iterations, a new value of $M_{\rm ZAMS,new}$ is found. Otherwise, it chooses for $M_{\rm ZAMS,new}$ the one that best matches the core mass.

Once SEVN establishes $M_{\rm ZAMS,new}$, it jumps on the new track. It applies the same method for all the four *interpolating tracks* and it updates all the stellar properties except the mass-properties (total mass, and He-core and CO-core masses).

To ensure the convergence of the track-finding algorithm, Spera et al., 2019 forced the masses of the stars and of the cores to evolve in such a way that:

$$M_{t_1} = M_{t_0}\,(1+\delta m), \quad \text{with} \quad \delta m = \frac{m_{t_1} - m_{t_0}}{m_{t_0}} \tag{2.111}$$

where M_{t_1}, and M_{t_0} are the masses computed at the time t_1 and t_0. Instead, m_{t_1}, and m_{t_0} are the masses obtained from the *interpolating tracks* at the same times t_1 and t_0.

Therefore, Eq. 2.111 forces the temporal evolution of the mass properties to perform only small changes per time-step.

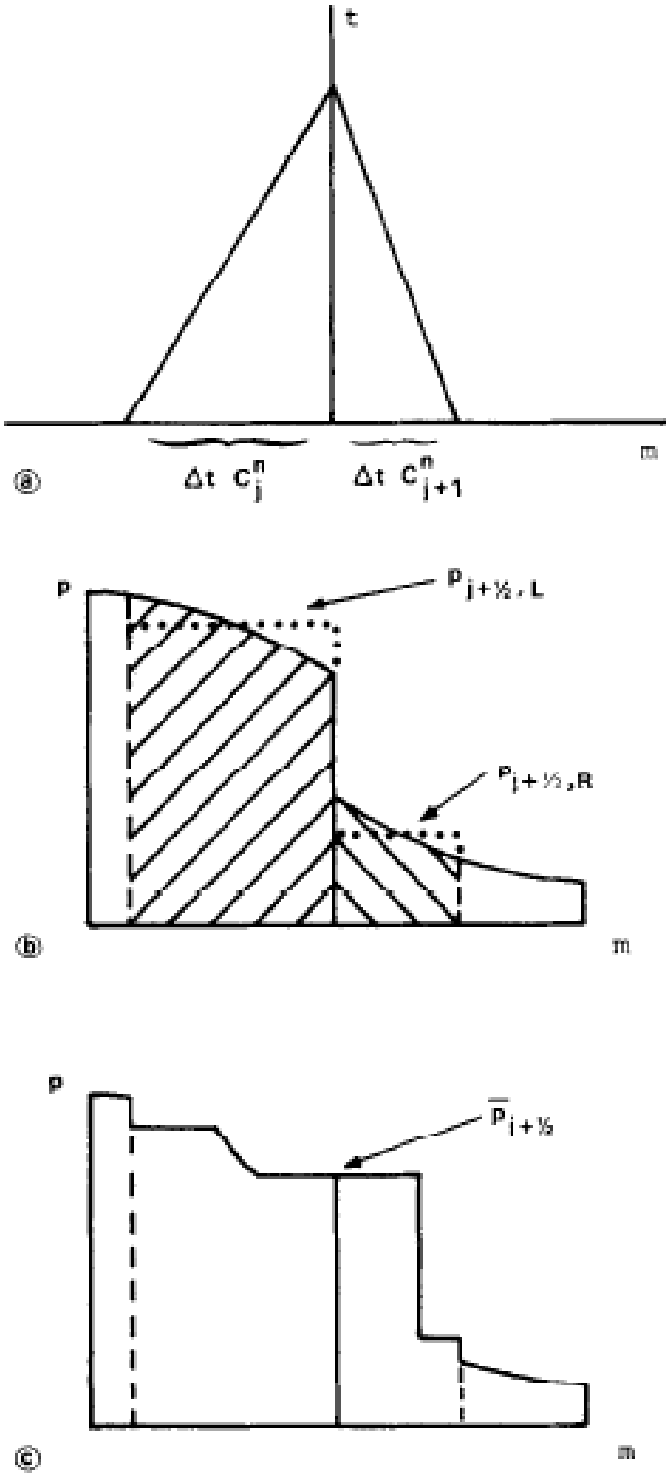

FIGURE 2.7: Figure from Colella and Woodward, 1984. The figure shows the computation of Lagrangian fluxes according to the PPM scheme. Panel *a*: The path of waves arriving at the boundary between two regions after a time interval is drawn. Panel *b*: The interpolation of each variable in the domain cells is replaced with a mass-weighted average. This facilitates computation in the case of nonlinear interaction between two cells. Panel *c*: The interaction between the two averaged states is described by the solution of the local Riemann problem at the boundary between the two cells, indicated in the figure as $\bar{P}_{j+1/2}$.

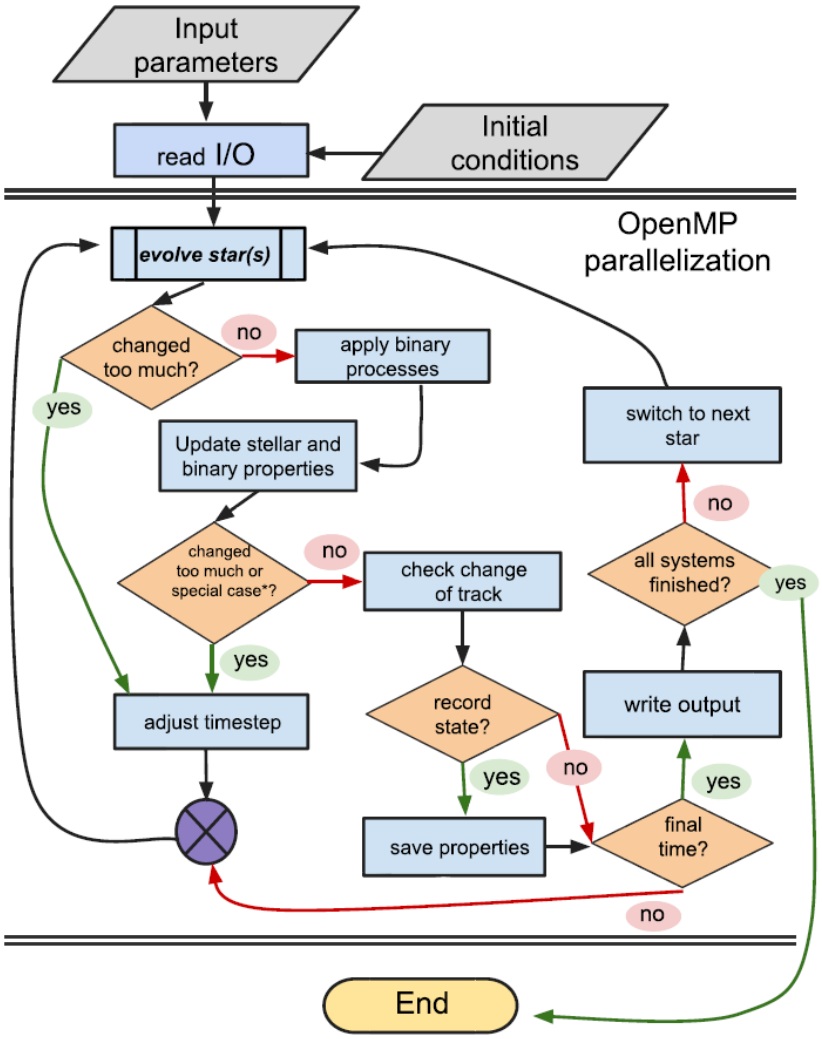

FIGURE 2.8: The schematic outlines the SEVN evolution algorithm. The 'changed too much' checks refers to Eq. 2.105, that accounts for variation in stellar and/or binary properties. If SEVN is evolving a single-star it omits the 'apply binary processes' and 'update stellar and binary properties' sections. The 'special case' check is for instances where SEVN reruns the evolution for specific binary processes, like common envelope (CE) or stellar mergers. This figure is taken from Iorio et al., 2023, and corresponds to Figure 3 in their paper.

Chapter 3

The initial mass- remnant mass relation from core-collapse supernovae

This Chapter is based on the paper Ugolini et al., 2024.

3.1 Introduction

Through 1D simulations, several authors have attempted to link the explodability of stellar progenitors to the structural properties of stars at the presupernova (pre-SN) stage (see O'Connor and Ott, 2011; Fryer et al., 2012; Horiuchi et al., 2014; Ertl et al., 2016; Sukhbold et al., 2016; Mandel and Fragos, 2020; Patton and Sukhbold, 2020; Patton, Sukhbold, and Eldridge, 2022). Such prescriptions for the explodability have been adopted in many population synthesis codes (e.g., Eldridge, Izzard, and Tout 2008; Spera, Mapelli, and Bressan 2015; Agrawal et al. 2020; Zapartas et al. 2021; Fragos et al. 2023), to predict the final fate of massive stars and the formation and evolution of compact-object binaries in different astrophysical environments. Such analytical relations for the explodability are usually applied to stellar progenitors that are different from those employed to compute the prescriptions, and therefore must be adopted with caution. In addition, we are still far from making any conclusive statement on the final fate of massive stars. Specifically, the role played by stellar rotation, metallicity, and different stellar evolutionary models of the progenitors is still mostly unexplored.

In this Chapter, we try to address some of these problems by studying the explosion of progenitor stars and the formation of compact remnants through the latest version of our hydrodynamic code HYPERION (HYdrodynamic Ppm Explosion with Radiation diffusION, see Limongi and Chieffi 2020), which includes a treatment of the radiation transport in the flux-limited diffusion approximation. We simulate the explosion of an up-to-date homogeneous set of both rotating and non-rotating progenitor stars provided by Limongi and Chieffi, 2018 (hereinafter, LC18). For the SN explosion, we adopt the thermal-bomb approach and we calibrate the parameters that describe the energy-injection process by comparison with SN1987A. We apply our methodology to investigate the distribution of remnant masses as a function of $M_{\rm ZAMS}$, focusing on the role played by different initial metallicities and different values of initial stellar rotation.

In Section 3.2, we present our methodology. In Section 3.3 we present the results of our simulations. In Section 3.4 we investigate the implications of our results, and Section 3.5 contains the conclusions.

3.2 Methods

We use the HYPERION code to simulate the explosion of a set of pre-SN models of massive stars presented in LC18. The details of the code are discussed in Chapter 2, Section 2.1.

To induce the explosion, we remove the innermost $0.8\,M_\odot$ of the pre-SN model, and artificially deposit at this mass coordinate a given amount of thermal energy ($E_{\rm inj}$). We assume that $E_{\rm inj}$ is diluted both in space, over a mass interval $dm_{\rm inj}$, and in time, over a time interval $dt_{\rm inj}$. Therefore, our numerical approach relies on the three free parameters $E_{\rm inj}$, $dm_{\rm inj}$, and $dt_{\rm inj}$, which need to be calibrated. The details of the calibration are presented in Sec. 3.2.1.

Once the energy is deposited into the pre-SN model, a shock wave forms. The shock wave starts to propagate outwards and eventually drives the explosion of the star. While the shock advances, it induces explosive nucleosynthesis and accelerates the shocked matter. After the initial energy injection, the innermost regions begin to fall back onto the proto-compact object, which progressively increases its mass. After the end of the fallback phase, we define the *mass cut* as the mass coordinate that divides the final remnant from the ejecta. Depending on the position of the mass cut, we can recognize two possible outcomes of our simulations: successful explosion, if a substantial fraction of the envelope is ejected during the explosion (the simulated physical time is of 1 yr, $\sim 3\times10^7\,s$, that is sufficient to follow also the homologous expansion of the ejected matter in the circumstellar medium and the formation of the light-curve), or failed explosion if essentially the whole star collapses to a black hole. The former case is presented in Sec. 3.3.1, while the latter is discussed in Sec. 3.3.2.

3.2.1 Calibration of the explosion

During the explosion, the innermost zones of the stellar mantle are heated up by the expanding shock wave to temperatures high enough to induce explosive nucleosynthesis. One of the main products of the nucleosynthesis is ^{56}Ni, which is synthesized by the explosive Si burning in the innermost regions of the mantle (see Thielemann, Nomoto, and Hashimoto, 1996; Woosley and Weaver, 1995; Arnett, 1996; Limongi, Straniero, and Chieffi, 2000. Therefore, the location of the mass cut is crucial to constrain the amount of ejected ^{56}Ni: in absence of mixing, the more external the mass cut, the lower the abundance of nickel in the ejecta. Another important outcome of our simulations is the final kinetic energy of the ejecta, which comes from the conversion of a fraction of the thermal energy initially injected into the progenitor star. The amount of ejected ^{56}Ni and the final kinetic energy of the ejecta depend on the explosion parameters, i.e. $E_{\rm inj}$, $dm_{\rm inj}$, and $dt_{\rm inj}$. We calibrate these parameters considering SN1987A, which is the most extensively studied ccSN to-date (Arnett et al., 1989; Woosley, 1988). Specifically, our goal is to find the combination of the explosion parameters that match both the ejected ^{56}Ni and the kinetic energy of the ejecta with the values estimated for the SN 1987A, i.e. $m_{^{56}\rm Ni}\sim0.07\,M_\odot$ and $\sim10^{51}$ erg $=1$ foe (see, e.g., Arnett et al. 1989; Shigeyama and Nomoto 1990; Utrobin 1993; Utrobin 2006; Blinnikov et al. 2000). To reach our goal, we simulate the explosions of the stellar progenitor of our grid that best match the helium core of the progenitor of SN 1987A (i.e., Sk — 69°202 e.g. Woosley 1988; Arnett et al. 1989; Arnett 1996 with $M_{\rm He}\sim6\,M_\odot$, e.g. Woosley 1988). We made this choice because$E_{\rm ejecta}$ and $m^{^{56}\rm Ni}$ do not depend on the structure of the hydrogen envelope of the star.

Therefore, we adopt a $15\,M_\odot$-progenitor model with initial solar composition ($\left[\mathrm{Fe/H}\right]=0$, i.e. the model 15a000 in the set of LC18) and, in each simulation, we adopt a different set of explosion parameters. Figure 3.1 shows the final kinetic energy of the ejecta and the corresponding amount of ejected ^{56}Ni obtained from our simulations using different explosion parameters, with $E_{\rm inj}\in[1.9;2.1]$ foe, $dm_{\rm inj}\in[0.05;0.4]\ M_\odot$, and $dt_{\rm inj}\in\left[10^{-9};1\right]$ s.

The combination of explosion parameters that best matches the values of SN1987A is: $dt_{\rm inj}=0.01\,s$, $dm_{\rm inj}=0.1\,M_\odot$, and $E_{\rm inj}=2.0$ foe. We adopt this combination of explosion parameters in all the simulations presented in this work. Using the calibrated values of $E_{\rm inj}$, $dm_{\rm inj}$, and $dt_{\rm inj}$, we compute the explosion of a subset of the pre-SN models presented in LC18.

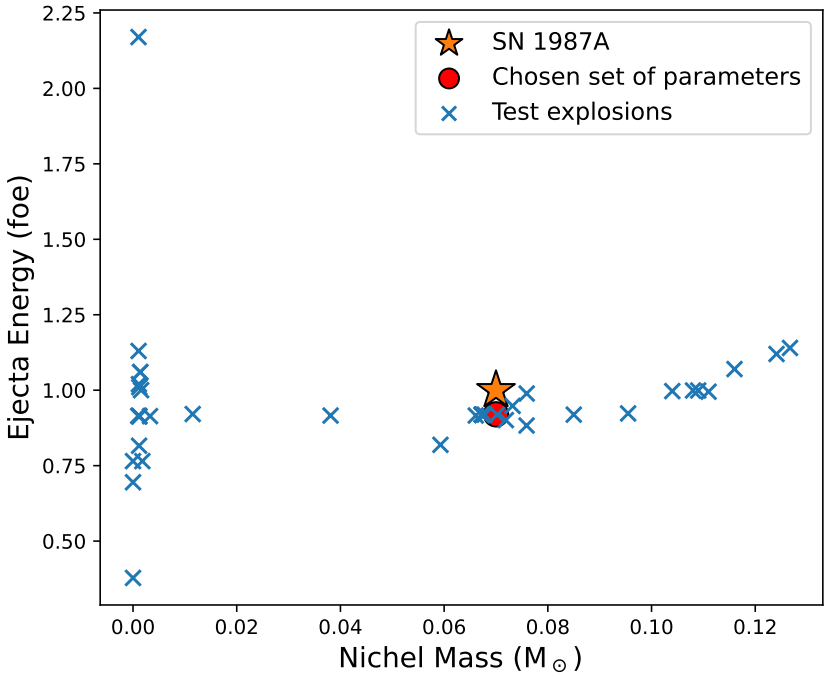

FIGURE 3.1: Final kinetic energy of the ejecta as a function of the ejected mass of ^{56}Ni obtained running various explosion tests (blue crosses) with different values of the initial explosion parameters, $E_{\rm inj}$, $dm_{\rm inj}$, and $dt_{\rm inj}$. The red dot refers to the simulation of the explosion that best matches the properties of SN1987A (orange star).

3.2.2 Progenitors unstable against pair production

Figure 3.2 shows the mass at the pre-SN stage $M_{\rm preSN}$ and the CO core mass $M_{\rm CO}$ of the stars of our simulations grid as a function of $M_{\rm ZAMS}$. The properties of the models for which we perform the explosions are also summarized in Table A.2 and Table A.3.

In our grid of non-rotating stellar models, we find that at subsolar metallicities the non-rotating stellar progenitors with $M_{\rm ZAMS} = 80\,{\rm M}_\odot$ end their life as ccSNe with CO core masses of $\sim 30\,{\rm M}_\odot$, while the $120\,{\rm M}_\odot$-progenitors become unstable (i.e., the adiabatic index Γ_1 approaches the critical value of $4/3$ in a substantial fraction of the core) and start entering the pair-instability phase (Fowler and Hoyle 1964; Barkat, Rakavy, and Sack 1967; Rakavy and Shaviv 1967). Thus, the progenitors unstable against pair production start to evolve on the hydrodynamical timescale and the FRANEC code cannot follow the evolution of the stellar structure anymore. Furthermore, pulsational pair-instability supernovae (PPISNe) are very different from the ccSNe HYPERION is designed to deal with, thereby we cannot simulate the final stages of massive stars that develop pair instabilities.

Finally, the mass resolution of the pre-SN simulated grid does not allow us to determine the mass threshold for the onset of the PPISNe; from our data, the only thing we know is that $120\,{\rm M}_\odot$ progenitors at sub-solar metallicity are unstable against pair production, while the $80\,{\rm M}_\odot$ progenitors are not. In order to determine which is the minimum mass of the CO core that enters the PPISNe regime ($\rm M_{CO}^{PPISN}$) and the minimum one that enters the PISNe ($\rm M_{CO}^{PISN}$), we can refer to the values provided by Heger and Woosley, 2002 (hereinafter HW02) and Woosley, 2017 (hereinafter W17), i.e. $\rm M_{CO,HW02}^{PPISN} = 33\,M_\odot$ and $\rm M_{CO,W17}^{PPISN} = 28\,M_\odot$, respectively. These two values are in a good agreement with the LC18 models ($\rm M_{CO,LC18}^{PPISN} > 33\,M_\odot$), within the theoretical uncertainties. Additionally, it should be noted that, in W17, the pulses associated with a CO core mass of $M_{\rm CO} = 28 - 31\,{\rm M}_\odot$ are quite weak, and the

first significant pulse occurs at a CO core mass of approximately 33 $M_\odot$. Hence, we adopt $M^{PPISN}_{CO,W17} = 33\,M_\odot$ as the minimum CO core mass that enters the PPISN. Furthermore, since the liming masses obtained in both cases (i.e. HW02 and W17) are compatible with the results of LC18, in the following we will refer, and use, the results provided by W17. Finally, following W17, stars with CO core mass $\geq 54\,M_\odot$ are completely disrupted by PISNe. This value corresponds to an initial mass which is larger than the maximum mass considered in our SN grid.

Independently of the rotation rate and metallicity, Figure 3.2 shows that M_{preSN} and M_{CO} scale linearly with M_{ZAMS}.

Therefore, to find the values of M_{ZAMS} and M_{preSN} of the first progenitor unstable against pair instabilities we assume:

$$M^{PPISN}_{ZAMS} = \left(M^{PPISN}_{CO} - q_1\right)/k_1 \tag{3.1}$$

$$\begin{aligned} M^{PPISN}_{preSN} &= k_2 M^{PPISN}_{ZAMS} + q_2 \\ &= \frac{k_2}{k_1}\left(M^{PPISN}_{CO} - q_1\right) + q_2 \end{aligned} \tag{3.2}$$

where k_1 and q_1 (k_2 and q_2) are the slope and intercept of the line M_{CO} vs M_{ZAMS} (M_{preSN} vs M_{ZAMS}).

Therefore, according to both W17 we find M^{PPISN}_{ZAMS} for the various metallicities and rotation velocities that are reported in Table A.1. Specifically, in Table A.1 we report, for all the initial values of metallicity and angular rotation, the values of M^{PPISN}_{ZAMS} and M^{PPISN}_{preSN} that we obtain for the last progenitors stable against pair-instabilities. When the heaviest stars of our pre-SN grid are stable against pair-production we cannot predict for which values of M_{ZAMS} they will become unstable against pair-instability (i.e. which stellar progenitors will explode as PPISNe or PISNe), thus M^{PPISN}_{ZAMS} and M^{PPISN}_{preSN} are labeled as Not Available (N.A.) in Table A.1.

3.3 Results

In this section, we present the results of the simulations performed in the pre-SN models described in Figure 2 and Tables 2 and 3 (see also LC18).

We simulate the explosions for all the models with pre-SN CO core masses $\leq 33\,M_\odot$ because these models are considered stable against pair production, as in LC18 (see Section 3.2.2). The results of the simulations are also summarized in Tables A.2 and A.3.

3.3.1 Successful explosions

To illustrate the properties of a typical successful explosion in our simulations, we consider a typical successful explosion looks like in our simulations, we consider a non-rotating 25 $M_\odot$ star with metallicity $[Fe/H] = -2$. Figure 3.3 shows the chemical structure of the model which is characterized by an extended H-rich envelope, with a He core mass of 9.87 $M_\odot$ and a CO core mass of 5.95 $M_\odot$. The ONe shell extends from mass coordinate 1.73 $M_\odot$ to 5.17 $M_\odot$, while the Si shell, which is enriched by the products of the O-shell burning, is in the range 1.43 $M_\odot$ — 1.73 $M_\odot$. The mass of the iron core is therefore 1.43$M_\odot$.

Figure 3.4 shows the temperature and density profiles of the star at the pre-SN stage. During the pre-SN evolution, the progenitor loses a negligible amount of mass because of its initial low metallicity and has a low effective temperature of $\sim 4.7 \times 10^3$ K. Thus, it ends its life as a Red Super Giant (RSG, Limongi and Chieffi 2018).

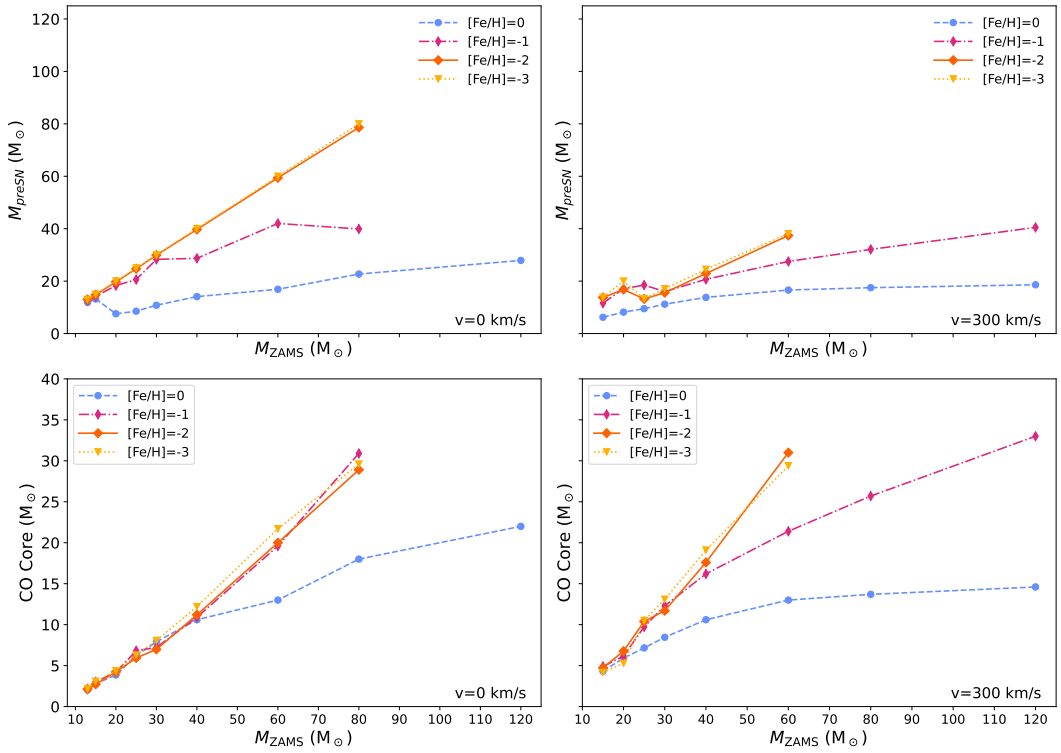

FIGURE 3.2: Mass at the pre-SN stage (top-row panels) and CO core mass (bottom-row panels) as a function of M_{ZAMS} for the non-rotating progenitors (left panels) and progenitors rotating with an initial velocity of 300 km/s (right panels). Different colors represent different initial metallicities: $[\mathrm{Fe/H}] = 0$ (dashed light blue line), $[\mathrm{Fe/H}] = -1$ (dash-dotted violet line), $[\mathrm{Fe/H}] = -2$ (orange solid line), and $[\mathrm{Fe/H}] = -3$ (dotted yellow line).

The density profile (see Figure 3.4) shows gradients at mass coordinates which correspond to boundaries between shells of different chemical composition. The most prominent density gradient is at the mass coordinate of $\sim 10\,\mathrm{M}_\odot$ and it corresponds to the interface between the He core and the H envelope. The injection of thermal energy into the iron core results in the formation of a shock wave that moves outward in mass and compresses, heats up, and accelerates the overlying layers. Once the shock emerges from the iron core, it propagates through the outer layers, where it triggers the explosive nucleosynthesis. Figure 3.5 shows the evolution of the velocity profile of the shock wave at different times after the onset of the explosion. After ~ 0.7 s, the shock wave reaches the mass coordinate of $\sim 2.7\,\mathrm{M}_\odot$, where the peak temperature of the shock becomes too low to trigger any other additional burning. Therefore, from this mass coordinate outward, the chemical structure sculpted by the hydrostatic evolution will be unaffected by the passage of the shock wave.

After 15.5 s from the beginning of the explosion, while the shock is still moving through the CO core, some of the innermost layers (i.e. the inner $\sim 2\,\mathrm{M}_\odot$) revert their motion because their velocity is lower than the local escape speed (see the negative values of the orange line in Figure 3.5).

At ~ 100 s, the shock reaches the He/H interface at a mass coordinate of $\sim 10\,\mathrm{M}_\odot$, where a strong density gradient (see Figure 3.4) causes the formation of a reverse shock (see Woosley and Weaver, 1995). From this time onward, the explosion is characterized by a shock wave moving outward in mass and by a reverse shock, which propagates inward in mass, slowing down the previously accelerated material. This effect is apparent from the behavior of the velocity of the shock 1000 s after the onset of the explosion (red dashed line in Figure 3.5),

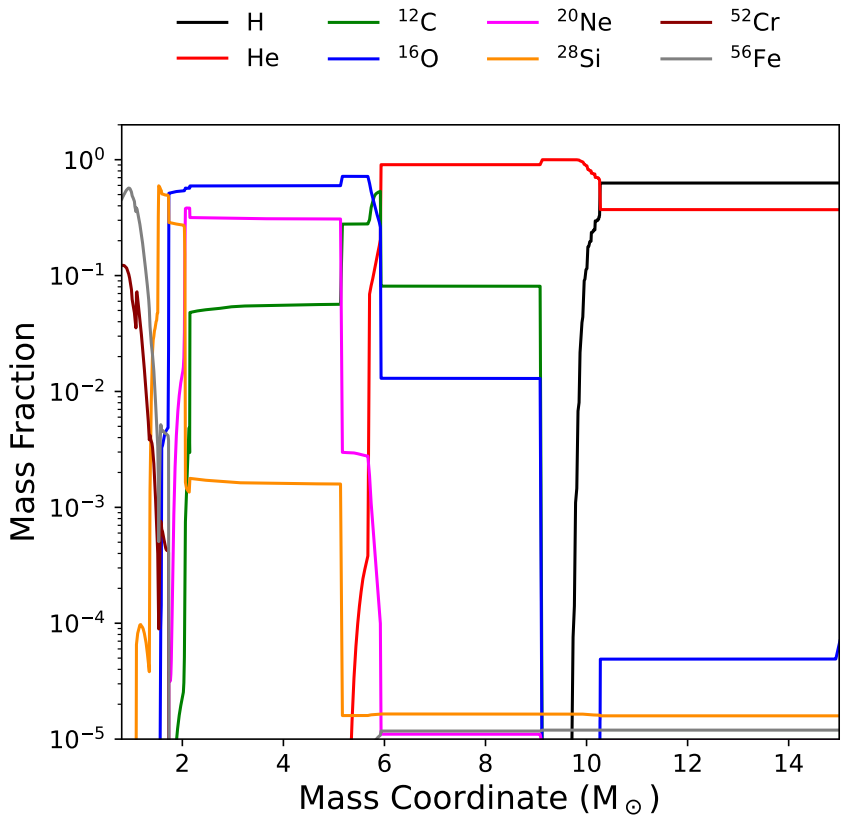

FIGURE 3.3: Chemical composition as a function of the interior mass coordinate of a non-rotating model with $M_{\rm ZAMS} = 25\,{\rm M}_{\odot}$ and $\left[{\rm Fe/H}\right] = -2$ at the pre-SN stage. We show the chemical composition up to the mass coordinate of $15\,{\rm M}_{\odot}$. We report the abundances of H (black line), He (red line), ^{12}C (green line), ^{16}O (blue line), ^{20}Ne (magenta line), ^{28}Si (orange line), ^{52}Cr (dark red line) and ^{56}Fe (gray line).

for which we find that the velocity of the outer regions of the shock is smaller than that of the innermost regions of the shock wave. This happens because the latter have not yet been affected by the reverse shock at this stage of the explosion.

Furthermore, Figure 3.5 shows also that when the shock reaches the He/H interface, the compact remnant increases its mass up to $\sim 2\,{\rm M}_{\odot}$, since the layers which had negative velocity when the shock has reached the CO core have now reached zero velocity.

The fallback process eventually ends $\sim 3 \times 10^4$ s after the onset of the explosion, leaving a compact remnant with a final mass of $5.77\,{\rm M}_{\odot}$ (the purple shaded area in Figure 3.5). It is worth noting that such a heavy compact remnant includes also the layers where the explosive nucleosynthesis happened ($\lesssim 2.7\,{\rm M}_{\odot}$, i.e. the Si and ONe shells, see Figure 3.3), preventing their ejection into the interstellar medium unless some mixing of material from the innermost zones to the outer layers is occurring during the explosion. Finally, $\sim 1.5 \times 10^5$ s (i.e. ~ 1.7 days) after the beginning of the explosion, the forward shock reaches the surface of the star (shock breakout).

Figure 3.6 shows the kinetic energy, the sum of internal and gravitational energy, and the total energy of the star as a function of the mass coordinate, at times > 15 seconds after the onset of the explosion. From this Figure it is apparent that, at each time, some regions are falling back onto the proto-compact object (i.e. those with negative total energy) and some are being expelled by the shock wave (i.e. those with positive total energy). The last region with negative total energy corresponds to the boundary of the final remnant, that is represented in

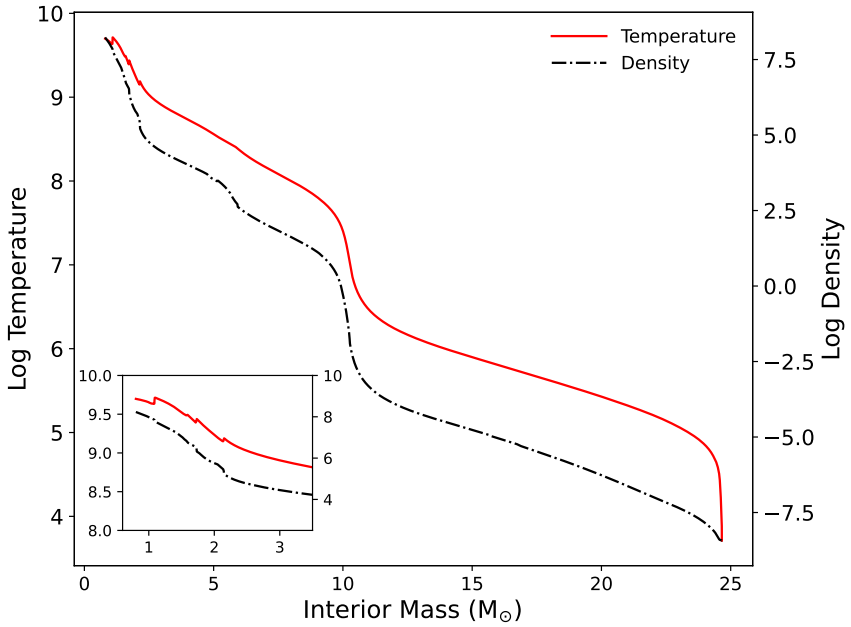

FIGURE 3.4: Temperature profile (solid red line) and mass density profile (dash-dotted black line) of the stellar progenitor at the pre-SN stage as a function of the mass coordinate. **A zoom-in on the innermost region of the core, up to** $5\,M_\odot$**, is highlighted in the lower right box.**

Figure 3.6 with a purple shaded area.

We present the whole process in Figure 3.7, which shows the evolution of the radius of various mass shells (grey, in step of $1M_\odot$, and dotted red lines, in step of $3M_\odot$) inside the stellar progenitor as a function of time. From this Figure we can distinguish the layers of the star that fall back onto the compact object, i.e., those that form the final remnant (represented by the dashed yellow line), and those that are successfully ejected at the shock breakout. Roughly at $\sim 10\,s$ we find that the radius of the mass shells corresponding to the most internal $2\,M_\odot$ of the star (the first two grey lines) revert their trajectory, start to fall back onto the proto-compact object, and they reach the latter $\sim 100\,s$ after the onset of the explosion.

Figure 3.7 also shows when the fallback ends. The last shell that falls back onto the compact object reverts its trajectory roughly $\sim 10^4$ s after the onset of the explosion and it reaches the compact remnant at $t = 3\times10^4$ s (consistent with our results reported in Figure 3.5 and in the bottom left panel of Figure 3.6). For $t \geq 3\times10^4$ s, such mass shell has zero velocity forming the final remnant with mass $5.77\,M_\odot$. In Figure 3.7 all the layers that eventually form the final remnant are shown to instantaneously drop onto the compact remnant but this is only a numerical effect, since once they revert their trajectory, falling back onto the BH, we do not follow their evolution anymore, i.e. we do not observe the free fall trajectories.

In contrast, the outer region is eventually ejected by the shock wave at the shock breakout, and it keeps moving outward in the interstellar medium with a radial velocity that grows linearly with time.

3.3.2 Direct collapse

The progenitor model we adopt to describe a typical failed explosion which undergoes a direct collapse (DC) to BH in our simulations is a non-rotating $80\,M_\odot$-star with metallicity $[Fe/H] = -2$. Figure 3.8 shows the chemical structure of the star at the pre-SN stage. The structure is characterized by an extended H-rich envelope, a He core mass of $38.3\,M_\odot$ and a CO core mass of $28.9\,M_\odot$. The ONe shell extends between mass coordinate $4.33\,M_\odot$ and

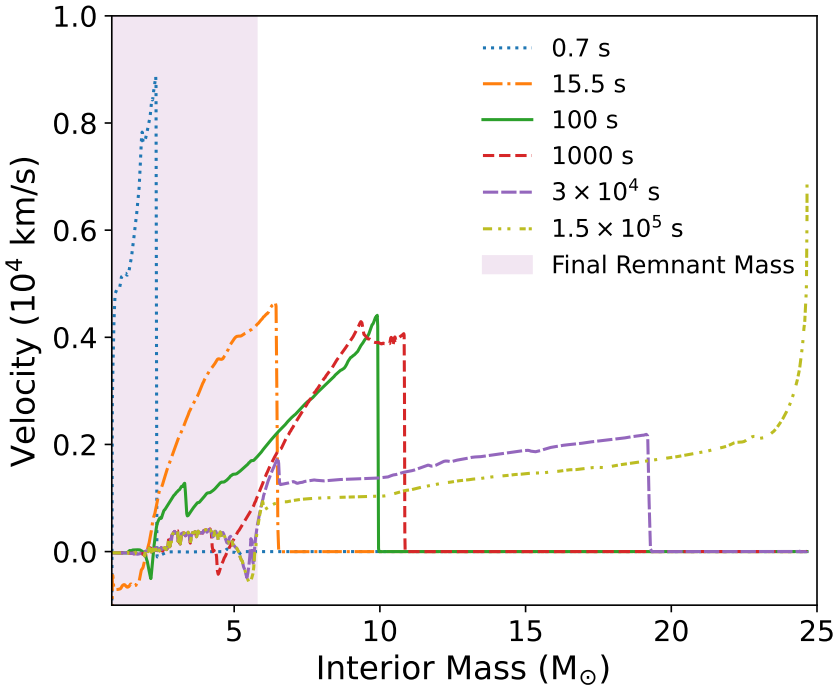

FIGURE 3.5: Velocity of the shock wave as a function of the mass coordinate at different times after the onset of the explosion: the end of the explosive nucleosynthesis (dotted blue line), the shock wave enters the CO core (dash-dotted orange line), the shock wave reaches the He/H interface (solid green line), 1000 s after the onset of the explosion (dashed red line), the formation of the compact remnant (long dashed purple line), and the shock breakout (short dot-dashed light green line). The shaded purple area represents the extension of the final compact remnant.

14.9 $M_\odot$ while the Si shell extends from 1.76 $M_\odot$ to 4.33 $M_\odot$. The mass of the iron core is 1.76$M_\odot$.

Figure 3.9 shows the temperature and the density profile of the progenitor as function of the mass coordinate. From this Figure it is apparent that the density profile presents various steep density gradients, each one corresponding to the boundaries between shells of different chemical composition. As in the previous case of a successful explosion, this star loses a negligible amount of mass during its life because of its initial low metallicity and it reaches the pre-SN phase as a RSG, having an effective temperature of 6.3×10^3 K.

In Figure 3.10, we show the velocity profile of the explosion as a function of the mass coordinate at different times after the onset of the explosion. Figure 3.10 shows that the velocity of the shock progressively decreases with time. The regions behind the shock wave begin reverting their trajectory $\sim$ 1.5 s after the onset of the explosion, since they have exhausted their initial kinetic energy. Thus, they start falling back onto the proto-compact object with negative radial velocity. As the shock moves at larger mass coordinates, more and more internal layers exhaust their kinetic energy, and fall back onto the core, until the velocity of the shock becomes almost zero at $\sim$ 36 s after the onset of the explosion. Therefore, in this case, the shock wave does not have enough energy to eject the mantle of the star.

Figure 3.11 shows the dynamics of the innermost layers of the stellar progenitor. Such layers undergo a brief acceleration phase when the shock wave reaches them. However, such acceleration is not sufficient to unbound these regions from the star. In Figure 3.11 we notice the same behaviour we presented in Figure 3.10: already $\sim$ 1.5 s after the onset of the explosion, the innermost layers of the star revert their trajectory, falling back onto the proto-compact object, reaching the latter only a few seconds later, and becoming part of the

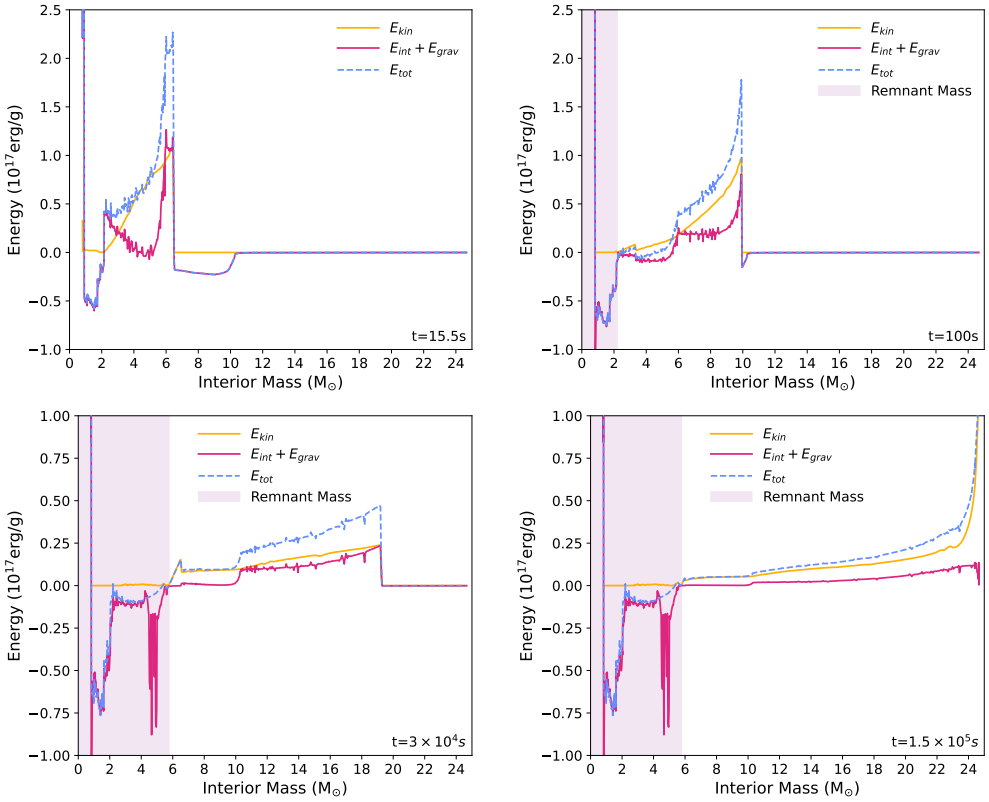

FIGURE 3.6: Interior profiles of the kinetic energy (yellow line), the internal energy plus the gravitational energy (purple line), and the total energy (dashed light blue line) at various times during the explosion for a non-rotating stellar progenitor with $M_{\rm ZAMS} = 25\,{\rm M}_\odot$ with metallicity $\left[{\rm Fe/H}\right] = -2$. The shaded purple area in the panels represents the region of the star forming the compact remnant at each time. It is completely formed at $t = 3\times10^4$s.

final remnant at ~ 5 s. Furthermore, the acceleration decreases in the outer layers, which start to collapse again immediately after the passage of the shock wave. Therefore, the latter cannot reach the surface of the star and the entire progenitor directly collapses into a heavy BH.

3.3.3 Remnants BHs from non-rotating progenitors

Figure 3.12 shows the remnant masses as a function of $M_{\rm ZAMS}$, for non-rotating progenitors and for various initial metallicities. From Figure 3.12 it is apparent that the remnant mass increases as a function of $M_{\rm ZAMS}$ for all the considered metallicities. Furthermore, the remnant mass is larger for progenitors at lower metallicities, and does not depend significantly on metallicity for progenitors with $M_{\rm ZAMS} \lesssim 25\,{\rm M}_\odot$. The remnant mass curves follow closely the behavior of the CO core mass (see the bottom-left panel of Figure 3.2).

This happens because the remnant mass depends on the binding energy of the star at the pre-SN stage, and that comes mainly from the CO core. Moreover, larger CO core masses imply lower ^{12}C mass fractions at core-He depletion, i.e. a less efficient C-shell burning, which, in turn, causes a higher contraction of the CO core resulting in a more bound structure. Figure 3.13 shows the mass of the progenitor star at the pre-SN stage and the mass of the compact remnant as a function of the initial mass of the star, for various metallicities. In our simulations, we assume that DC occurs if the fraction of the progenitor's envelope ejected by the shock wave is less than 10% of the pre-SN mass. For example, the progenitor at solar metallicity with $M_{\rm ZAMS} = 60\,{\rm M}_\odot$ has a pre-SN mass of $16.9\,{\rm M}_\odot$ and forms a remnant of $16.2\,{\rm M}_\odot$, ejecting only $0.7\,{\rm M}_\odot$ of H envelope, thus we consider it a DC. Following this approach, we find

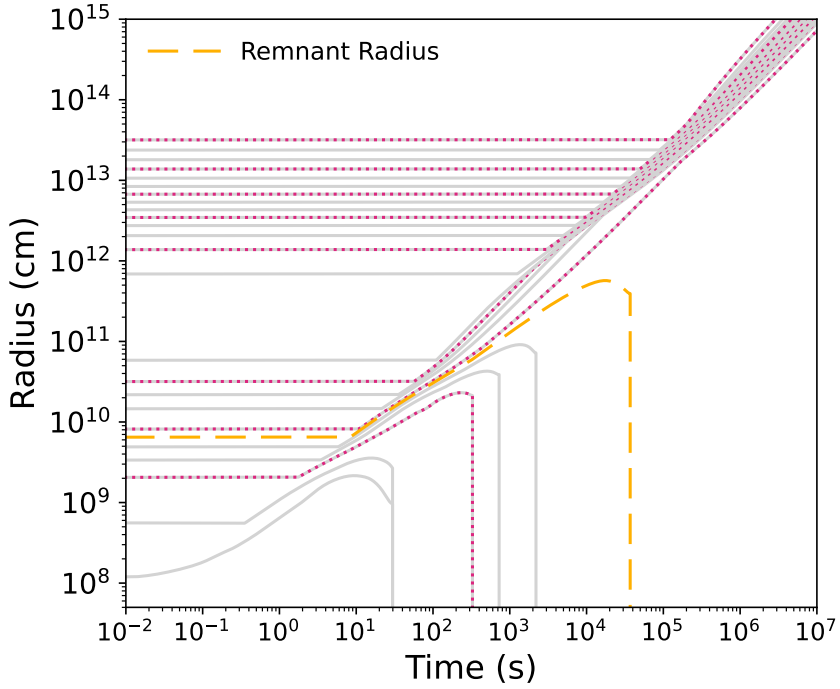

FIGURE 3.7: Evolution of the radius of various shells (grey and dotted purple lines) inside the stellar progenitor as a function of time. Each grey (dotted purple) line on top encloses 1 $M_\odot$ (3 $M_\odot$) more than the grey (dotted purple) line immediately below. We also show the evolution of the radius of the final compact remnant (yellow dashed line).

that stars with $M_{\rm ZAMS} \gtrsim 60\,M_\odot$ do not explode and collapse directly to a BH for the initial metallicities $[{\rm Fe/H}] = 0$, $[{\rm Fe/H}] = -2$, $[{\rm Fe/H}] = -3$. For $[{\rm Fe/H}] = -1$, the threshold for DC is $M_{\rm ZAMS} = 80\,{\rm M}_\odot$. This happens because the progenitor with $M_{\rm ZAMS} = 60\,{\rm M}_\odot$ ends its life as a RSG. Thus, the shock wave ejects part of the H envelope since this is very loosely bound to the star. This happens only for this value of metallicity, because at $[{\rm Fe/H}] = 0$ the star with $M_{\rm ZAMS} = 60\,{\rm M}_\odot$ has already lost all its H envelope at the pre-SN stage, while at $[{\rm Fe/H}] = -2$ and $[{\rm Fe/H}] = -3$ stellar winds are quenched, i.e. all the H envelope is retained and the star is much more compact.

The BH masses at the threshold for DC depend on the final mass of the progenitor stars at the pre-SN stage that, in turn, depends on the mass-loss history during the pre-SN evolution. The mass-loss rate decreases significantly at low metallicity, where stellar winds are quenched. Therefore, the models with initial metallicity lower than $[{\rm Fe/H}] = -1$ evolve approximately at constant mass. As a consequence, the BH masses correspond to the threshold in $M_{\rm ZAMS}$ for DC (see Table A.1) . Above $M_{\rm ZAMS}^{\rm PPISN}$ we compute the remnant masses taking into account the results of W17 (see, e.g., its Table 1) by interpolating on the CO core mass. The results are reported in Figure 3.13 as yellow diamond points and are connected through the dashed green yellow lines. From this Figure it is apparent that at $[{\rm Fe/H}] = -1$ the onset of PPISNe does not affect significantly the maximum BH mass that forms. This happens because - at the pre-SN stage - stars have already lost a significant part of their H envelope, thus the mass loss caused by PPISNe does not affect significantly the final BH mass. In contrast, for $[{\rm Fe/H}] = -2, -3$, stars evolve at almost constant mass and end their life with heavy H envelopes. Therefore, the expulsion of the latter at the onset of PPISN significantly affects the final BH mass. This effect is apparent in the bottom-row panels of Figure 3.13, where we see a steep variation of the final remnant mass at the onset of PPISNe.

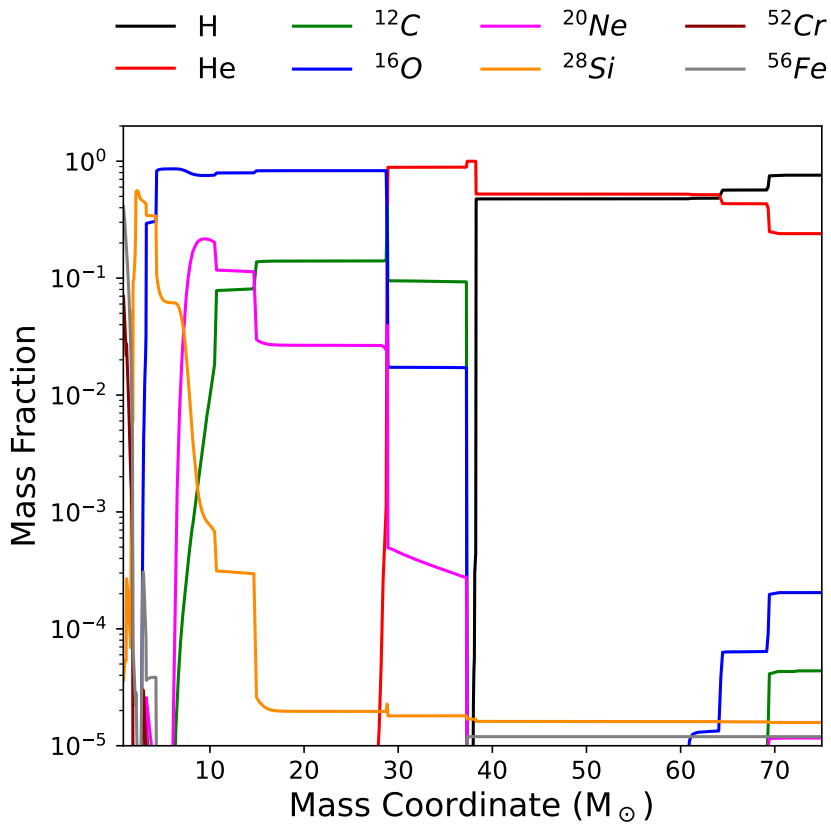

FIGURE 3.8: Chemical composition as a function of the interior mass coordinate of a non-rotating model with $M_{\rm ZAMS} = 80\,{\rm M}_\odot$ and $\left[{\rm Fe/H}\right] = -2$ at the pre-SN stage. We report the abundances of H (long dash-double dotted black line), He (double dash-dotted red line), ^{12}C (long dashed green line), ^{16}O (short dashed blue line), ^{20}Ne (dashed magenta line), ^{28}Si (short dash-double dotted orange line), ^{52}Cr (solid dark red line) and ^{56}Fe (long dash-dotted gray line).

3.3.4 Remnants BHs from rotating progenitors

Figure 3.14 shows the remnant masses as a function of $M_{\rm ZAMS}$, for rotating progenitors and for various initial metallicities. From Figure 3.14 it is apparent that, at solar metallicity, the remnant mass does not increase significantly with the initial progenitor mass. In contrast, for $\left[{\rm Fe/H}\right] = -1,\,-2,\,-3$, the remnant mass curve has a local minimum at $25\,{\rm M}_\odot$, which occurs when the stellar winds are strong enough to completely remove the H envelope. Furthermore, as in the case of the non-rotating progenitors, for $M_{\rm ZAMS} \gtrsim 25\,{\rm M}_\odot$ the remnant masses are larger at lower metallicities, and follow the behavior of the CO core mass at the pre-SN stage (see also Section 3.3.3).

Figure 3.15 shows how the remnant mass and the mass of the star in the pre-SN phase depend on $M_{\rm ZAMS}$, for rotating models with different initial metallicities. We find that most of the rotating progenitors directly collapse to BHs. This happens because rotating stars end their life as He-stars, i.e. they end their life with more bound structures at the pre-SN stage with respect to non-rotating progenitors, thus they are more prone to failed SN explosions and to form more massive BHs. Specifically, stars with $M_{\rm ZAMS} \gtrsim 30\,{\rm M}_\odot$ collapse directly to a BH, whereas the fate of stars with $M_{\rm ZAMS} \lesssim 30\,{\rm M}_\odot$ depends on the initial metallicity.

At solar metallicity, the threshold value of $M_{\rm ZAMS}$ for the DC decreases down to $\sim 20\,{\rm M}_\odot$, since only the progenitor with $M_{\rm ZAMS} = 15\,{\rm M}_\odot$ evolves through a successful SN explosion. At $\left[{\rm Fe/H}\right] = -1$, the only exploding progenitor is the one with $M_{\rm ZAMS} = 25\,{\rm M}_\odot$, and it ejects all its H envelope, while the less massive progenitors directly collapse to BHs. Although this

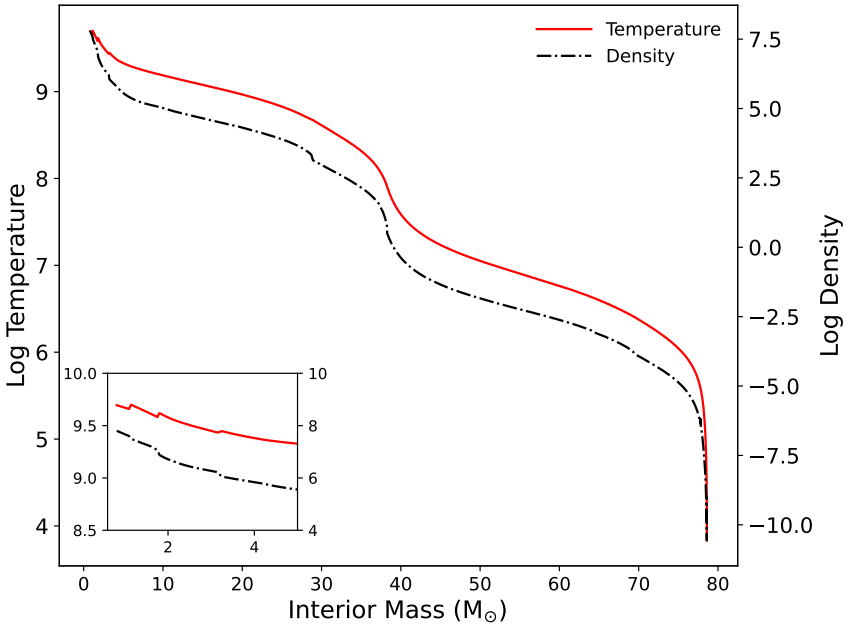

FIGURE 3.9: Temperature profile (red line) and density profile (dash-dotted black line) at the pre-SN stage as function of the mass coordinate of a non-rotating stellar progenitor with $M_{\rm ZAMS} = 80\,{\rm M}_{\odot}$ and $\left[{\rm Fe/H}\right] = -2$. A zoom-in on the innermost region of the core, up to $5\,{\rm M}_{\odot}$, is highlighted in the lower right box .

occurs only for one progenitor in the simulation set, the non-monotonic behaviour for the explodability is not apparent for non-rotating progenitors (see Figure 3.13). At $\left[{\rm Fe/H}\right] = -2$, all the progenitors evolve through DC. The progenitor with $M_{\rm ZAMS} = 20\,{\rm M}_{\odot}$ ejects some material but it is still consistent with our definition of DC, thus the threshold value of $M_{\rm ZAMS}$ for the DC is $\sim 15\,{\rm M}_{\odot}$. The stars at $\left[{\rm Fe/H}\right] = -3$ behave similarly to solar metallicity models, and the only exploding progenitor is the one with $M_{\rm ZAMS} = 15\,{\rm M}_{\odot}$, thus the threshold of $M_{\rm ZAMS}$ for the DC is at $\sim 20\,{\rm M}_{\odot}$.

For rotating progenitors, mass loss is enhanced because rotation forces the models to become red giants and therefore to approach their Eddington luminosity during their redward excursion in the HR diagram (see LC18). When this happens, a substantial amount of mass is lost and most of the stellar models loose all their H rich envelope and become Wolf-Rayet stars. Therefore, progenitors with the same $M_{\rm ZAMS}$ and metallicity retain less mass at the pre-SN stage than non-rotating stars. This is apparent especially at lower metallicities, where stellar winds for non-rotating progenitors are quenched. This effect is not significant for progenitors with $M_{\rm ZAMS} \leq 30\,{\rm M}_{\odot}$, since such stars have weak stellar winds. As a consequence, we obtain less massive BHs from rotating stellar progenitors than from non-rotating ones.

The BH masses corresponding to the threshold in $M_{\rm ZAMS}$ for the DC are $\sim 8\,{\rm M}_{\odot}$, $\sim 16\,{\rm M}_{\odot}$, $\sim 14\,{\rm M}_{\odot}$ and $\sim 20\,{\rm M}_{\odot}$ for metallicities $\left[{\rm Fe/H}\right] = 0$, $\left[{\rm Fe/H}\right] = -1$, $\left[{\rm Fe/H}\right] = -2$, $\left[{\rm Fe/H}\right] = -3$, respectively. The threshold CO core mass for PPISNe, $\mathrm{M}_{\rm CO}^{\rm PPISN} \sim 33\,{\rm M}_{\odot}$ are reported in Table A.1. To estimate the remnant masses of the models with $M_{\rm ZAMS} \geq M_{\rm ZAMS}^{\rm PPISN}$ we apply the results of W17, as described in Section 3.3.3. The results of such interpolations are the diamond yellow points, which are connected through the dashed yellow lines. From Figure 3.15, it is apparent that, for rotating stellar progenitors, there is no major change in the BH mass due to the onset of PPISNe. This happens because the rotating stars end their life as naked He stars, thus they have lost their H envelope. Therefore, the rotating stars only lose a small fraction of their He core at the onset of the PPISNe, because of the pulsational phase, and then collapse to to BHs.

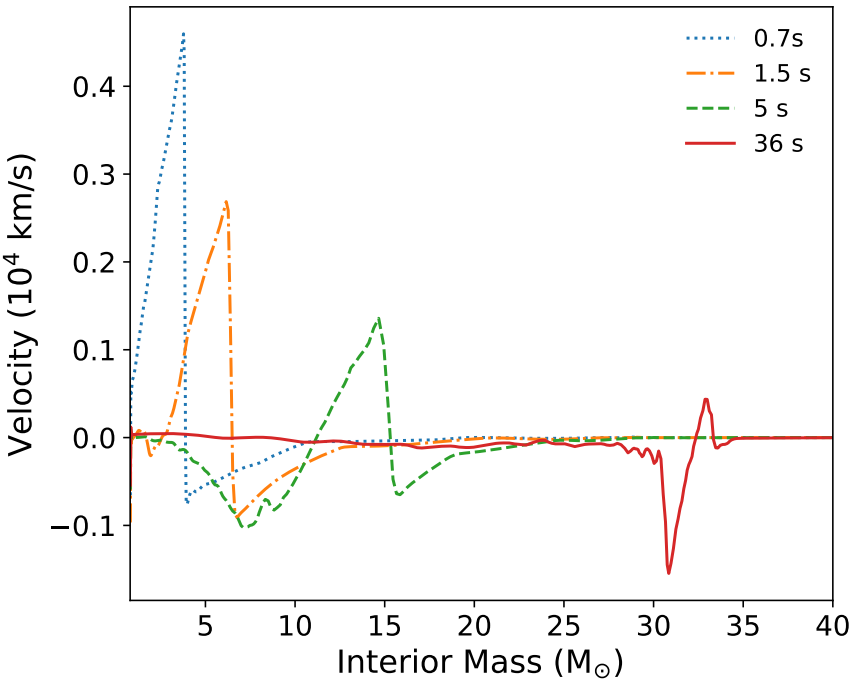

FIGURE 3.10: Same of Figure 3.5 but for a directly collapsing progenitor. The velocity profile is reported at different crucial times during the explosion: when the explosive nucleosynthesis stops (dotted blue line), when the layers behind the shock start to fallback onto the compact remnant (dash-dotted orange line), when the shock enters the CO core (dashed green line) and when the velocity of the shock becomes negligible (solid red line).

3.4 Discussion

3.4.1 The maximum BH mass

Figure 3.16 shows the maximum BH mass resulting from our simulations as a function of the initial stellar metallicity, and assuming rotating and non rotating **single star** models. It illustrates the impact of the initial metallicity and angular rotation of the stellar progenitor on the final remnant mass we obtain from single stellar evolution.

For $[\mathrm{Fe/H}] = 0$ and $[\mathrm{Fe/H}] = -1$, stellar winds play a crucial role as they remove a significant fraction of mass of the progenitor stars before they DC to BHs. From our simulations we find that the maximum BH mass we form is $\sim 27.9\,\mathrm{M}_\odot$ and $\sim 41.9\,\mathrm{M}_\odot$, for $[\mathrm{Fe/H}] = 0$ and $[\mathrm{Fe/H}] = -1$ in the non-rotating case, and $\sim 18.6\,\mathrm{M}_\odot$ and $\sim 40.5\,\mathrm{M}_\odot$, for $[\mathrm{Fe/H}] = 0$ and $[\mathrm{Fe/H}] = -1$ in the rotating case. All these BHs come from the collapse of stellar progenitors with $M_{\mathrm{ZAMS}} = 120\,\mathrm{M}_\odot$. Therefore, we find that angular rotation slightly enhances the effects of stellar winds at solar metallicity, while at $[\mathrm{Fe/H}] = -1$ the effect of rotation on the final remnant masses is negligible. For the cases $[\mathrm{Fe/H}] = -2, -3$ the heaviest BHs from non-rotating stellar progenitors have mass $\sim 83.3\,\mathrm{M}_\odot$ and $\sim 87.0\,\mathrm{M}_\odot$ respectively, and they both correspond to stellar progenitors with $M_{\mathrm{ZAMS}} \simeq 87\,\mathrm{M}_\odot$ (as reported in Table A.1). In the rotating case, the maximum BH mass is $\sim 39.9\,\mathrm{M}_\odot$ and $\sim 41.6\,\mathrm{M}_\odot$ for $[\mathrm{Fe/H}] = -2$ and $[\mathrm{Fe/H}] = -3$, respectively, and they correspond to stellar progenitors with $M_{\mathrm{ZAMS}} \simeq 65\,\mathrm{M}_\odot$ (see Table A.1). Therefore, in the rotating scenario, the initial angular rotation enhances mass loss and induces the formation of larger convective regions and therefore larger CO cores (see LC18, Marassi et al. 2019, and Mapelli et al. 2020). As a consequence, stars are less massive at the pre-SN stage and enter the PPISNe regime at lower

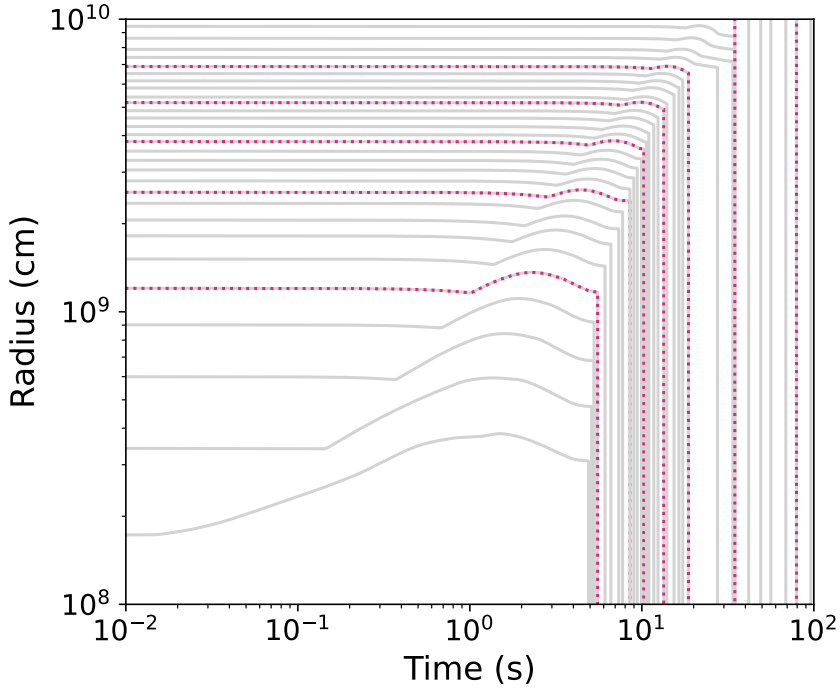

FIGURE 3.11: Same of Figure 3.7 but for the most central region of the progenitor with $M_{\rm ZAMS} = 80\,{\rm M}_{\odot}$ and $\left[{\rm Fe/H}\right] = -2$, where we can better appreciate the fallback of the layers right after being accelerated by the shock wave. We show the behavior of the shell enclosing different values of mass, of $1\,{\rm M}_{\odot}$ (each solid light grey lines) and $5\,{\rm M}_{\odot}$ (each dotted purple line), respectively.

initial masses compared to non-rotating progenitors. Such a combination of effects limits significantly the value of the maximum BH mass.

3.4.2 Implications for the PI mass gap

Figure 3.16 shows that we can form heavy BHs that lie in the upper mass gap predicted by PISN models, i.e. a dearth of BHs with masses in the range $60-120{\rm M}_{\odot}$ (e.g., Woosley 2017; Spera and Mapelli 2017). This is because we can form BHs in the upper mass gap because the FRANEC progenitors enter the pair-instability at different initial progenitor masses than those of other authors (e.g. Woosley 2017; Spera and Mapelli 2017; Farmer et al. 2019; Costa et al. 2021).

Given our choice of the minimum CO core pass for the onset of PPISN of $33\,{\rm M}_{\odot}$ (see Section 3.2.2), we find that, for the non-rotating models at $\left[{\rm Fe/H}\right] = -3$, the $M_{\rm ZAMS} = 80\,{\rm M}_{\odot}$ progenitor which ends its life with a CO core mass of $30\,{\rm M}_{\odot}$ is stable against pair production. Conversely, the $M_{\rm ZAMS} = 120\,{\rm M}_{\odot}$ has a CO core of $\sim 50\,{\rm M}_{\odot}$ and develops dynamical instabilities. To pin down the uncertainty on the maximum BH mass formed we would need to increase the resolution of our grid of progenitors between $M_{\rm ZAMS} = 80\,{\rm M}_{\odot}$ and $M_{\rm ZAMS} = 120\,{\rm M}_{\odot}$.

To compare our results with other studies, we show in Figure 3.17 the BH mass as a function of the pre-SN CO core mass of the progenitor star as obtained in this work (LC18 non-rotating progenitors at $\left[{\rm Fe/H}\right] = -3$), W17 (set D of its Table 2, a set of tracks evolved from the ZAMS with metallicity of $Z = 0.1\,{\rm Z}_{\odot}$ taking into account also the hydrogen envelope and for which they assume zero mass loss), Spera and Mapelli, 2017 (hereinafter S17) for metallicity of $Z = 1.3\times10^{-2}\,{\rm Z}_{\odot}$.

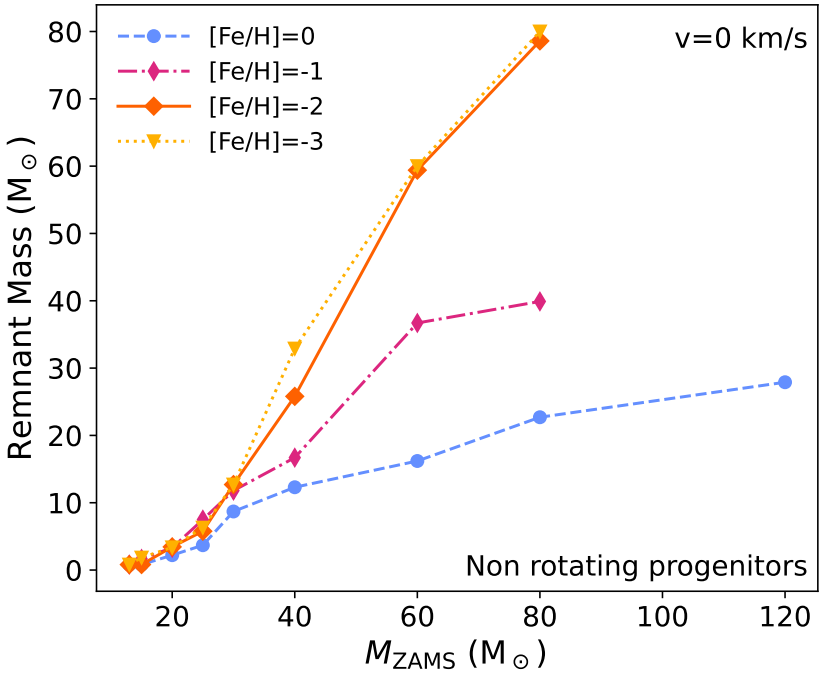

FIGURE 3.12: Remnant masses as a function of $M_{\rm ZAMS}$ for the progenitors with initial metallicity $\left[\mathrm{Fe/H}\right] = 0$ (dashed light blue line), $\left[\mathrm{Fe/H}\right] = -1$ (dash-dotted violet line), $\left[\mathrm{Fe/H}\right] = -2$ (orange solid line), and $\left[\mathrm{Fe/H}\right] = -3$ (dotted yellow line). We do not simulate the explosion of the stellar progenitors with $M_{\rm ZAMS} = 120\,\mathrm{M}_\odot$ at subsolar metallicities, since they are unstable against pair production.

To compare the BH mass spectra, we choose the stellar tracks with zero initial angular velocities, to exclude the effects of chemical mixing and mass loss enhancement, and with the lowest initial metallicities, to exclude degeneracies caused by different stellar-wind models.

Figure 3.17 shows that the first progenitors that evolve through the pulsational pair-instability phase (marked with crosses) are those of S17, with a CO core mass of $\sim 24\,\mathrm{M}_\odot$. This happens because, to enter the PPISNe regime, S17 adopted the He core mass criterion proposed in W17 (He core mass of $\sim 32\,\mathrm{M}_\odot$), which corresponds to CO core masses of $\sim 24\,\mathrm{M}_\odot$ when used in combination with the S17 stellar evolution tracks from the PARSEC code (Bressan et al. 2012).

The tracks of W17 enter the PPISNe regime when the CO core mass is $\sim 28\,\mathrm{M}_\odot$. It is important to note that these stellar tracks were evolved suppressing the mass loss phenomena of a set of stars with initial metallicity of $Z = 0.1\,\mathrm{Z}_\odot$, and that they were evolved from the ZAMS to the end of the PPISN regime. Thus, they represent a distinct set from the naked helium cores we used in Section 3.3.3 and 3.3.4 to infer the final remnant masses of the stars undergoing PPISNe.

Finally, our stellar progenitors become unstable against pair-instability when the CO core mass is $\gtrsim 33\,\mathrm{M}_\odot$. From Figure 3.17 it is apparent that the BH maximum mass ranges from $\sim 87\,\mathrm{M}_\odot$ (this work) to the minimum value of $\sim 53\,\mathrm{M}_\odot$ (S17), resulting in a discrepancy of $\sim 38\,\mathrm{M}_\odot$ in the maximum mass of the BHs obtained by different authors from the evolution of an isolated massive star. The discrepancy exists because different authors have different thresholds in the CO core mass for entering the PPISNe regime (see also Farmer et al., 2019, hereinafter F19). For instance, if we had used the value of $\mathrm{M}_{\rm CO}^{\rm PPISN}$ from F19 (e.g., $\mathrm{M}_{\rm CO,F19}^{\rm PPISN} = 41\,\mathrm{M}_\odot$) we would have ended up with BHs more massive than $\sim 100\,\mathrm{M}_\odot$, i.e. in the regime of intermediate-mass BHs.

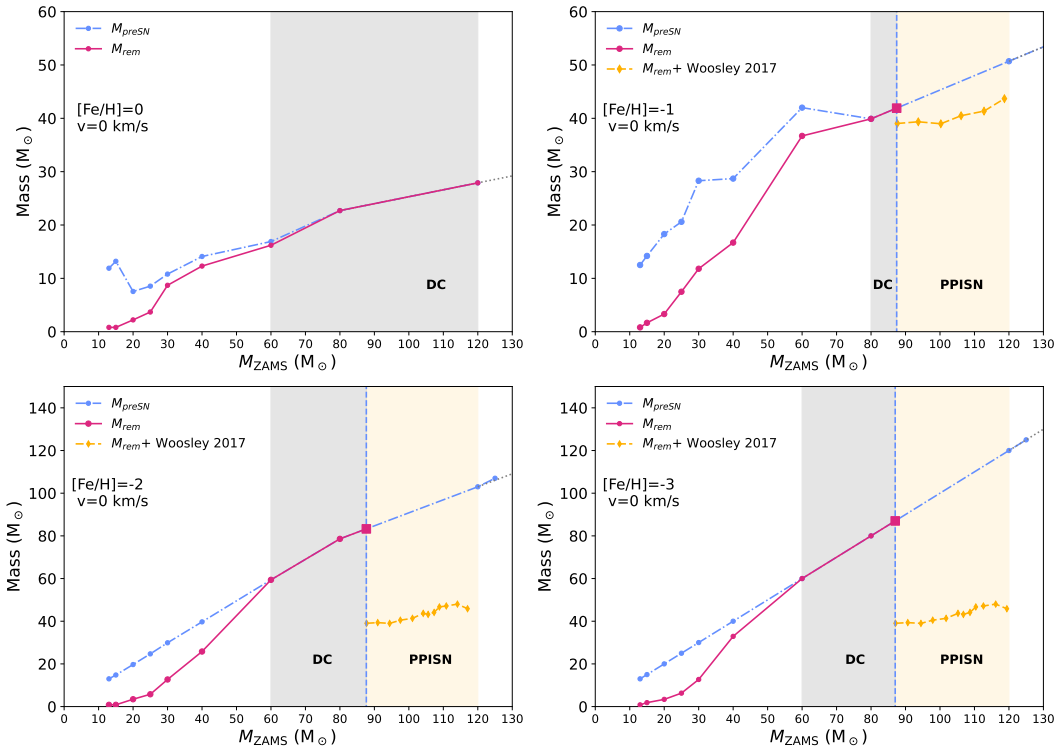

FIGURE 3.13: Pre-SN mass (dash-dotted light blue line), pre-SN mass extrapolated for $M_{\rm ZAMS} > 120 M_\odot$ (dotted grey line), remnant mass (solid violet line), and the remnant mass for the stars which develop pair instabilities (dashed yellow line), as a function of $M_{\rm ZAMS}$. The red points represent the stellar progenitors of the FRANEC grid, while the larger red squares correspond to the last progenitor stable against pair production, which has been obtained through interpolation (see Section 3.2.2 and Table A.1). The shaded grey area represents the region of DC, the shaded yellow area shows where stars undergo PPISNe. The vertical dashed lines represent the threshold values above which stars enter the PI regions.

Figure 3.18 shows the BH mass spectrum of this work and the results we would obtain by applying the W17 and F19 criteria for the onset of PPISNe to the S17 stellar evolution tracks. It shows that even the progenitors from S17, which have the lowest PPISNe entry point ($M_{\rm CO}^{\rm PPISN} = 24\,M_\odot$), can form BHs as massive as $\sim 70\,M_\odot$ adopting the W17 threshold for the CO core mass ($M_{\rm CO}^{\rm PPISN} = 28\,M_\odot$) instead of the He core mass criterion. Furthermore, S17 can form BH as massive as $\sim 90\,M_\odot$ adopting the F19 threshold ($M_{\rm CO}^{\rm PPISN} = 41\,M_\odot$), without changing the C/O ratio at the He core depletion, which is one of the key parameters to determine the onset of PPISNe (as shown in F19).

Therefore, adopting a self-consistent criterion to enter the PPISNe regime is crucial to investigate the BH mass spectrum and to constrain the lower edge of the upper mass gap. It is worth noting that the value of $M_{\rm CO}^{\rm PPI}$ is not the only property that affects the position of the lower edge of the upper mass gap. Besides the roles of DC, stellar winds, and rotation (cf. Sec. 3.3), the convective core overshooting parameter ($\alpha_{\rm ov}$) also has a central role in the formation of heavy stellar BHs. This is because overshooting dredges extra H from the envelope into the core during the central H burning, thus it governs the mass of the He core, and - in turn - the mass of the CO core. Vink et al., 2021 showed that a small value of overshooting ($\alpha_{\rm ov} \lesssim 0.1$) is associated with smaller cores and stars likely end their life as Blue Super Giants (BSGs). Such stars are very compact, they tend to avoid the PPISNe regime, because they form smaller CO cores and they experience negligible mass loss during their life. As a consequence, such stars are likely to form very heavy BHs in the range 74—87 $M_\odot$. In contrast, stars with

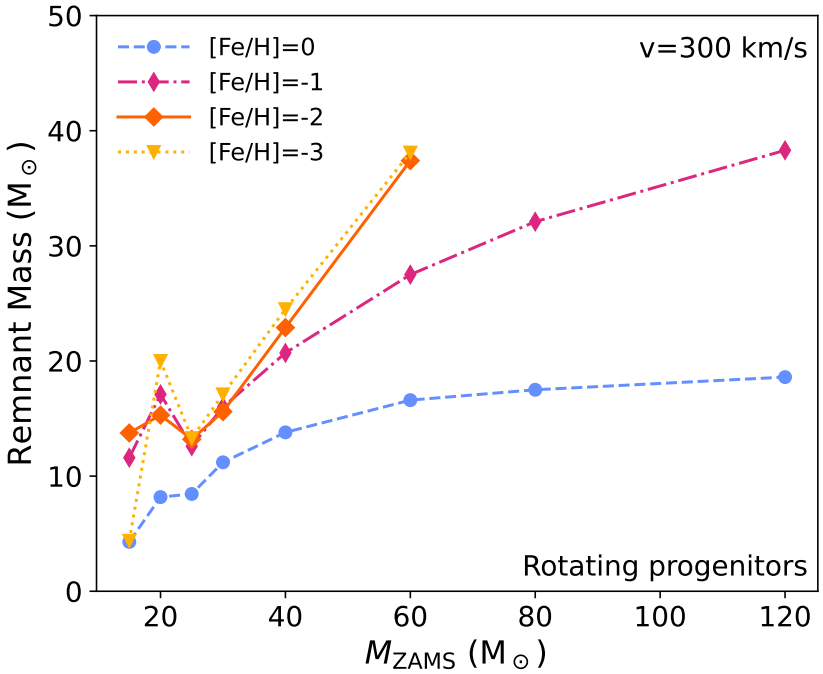

FIGURE 3.14: Same of Figure 3.12 but for rotating progenitors. We do not simulate the explosion of the stellar progenitors with $M_{\rm ZAMS} = 80\,{\rm M}_\odot$ and $120\,{\rm M}_\odot$ at $[{\rm Fe/H}] = -2, -3$, since they are unstable against pair production.

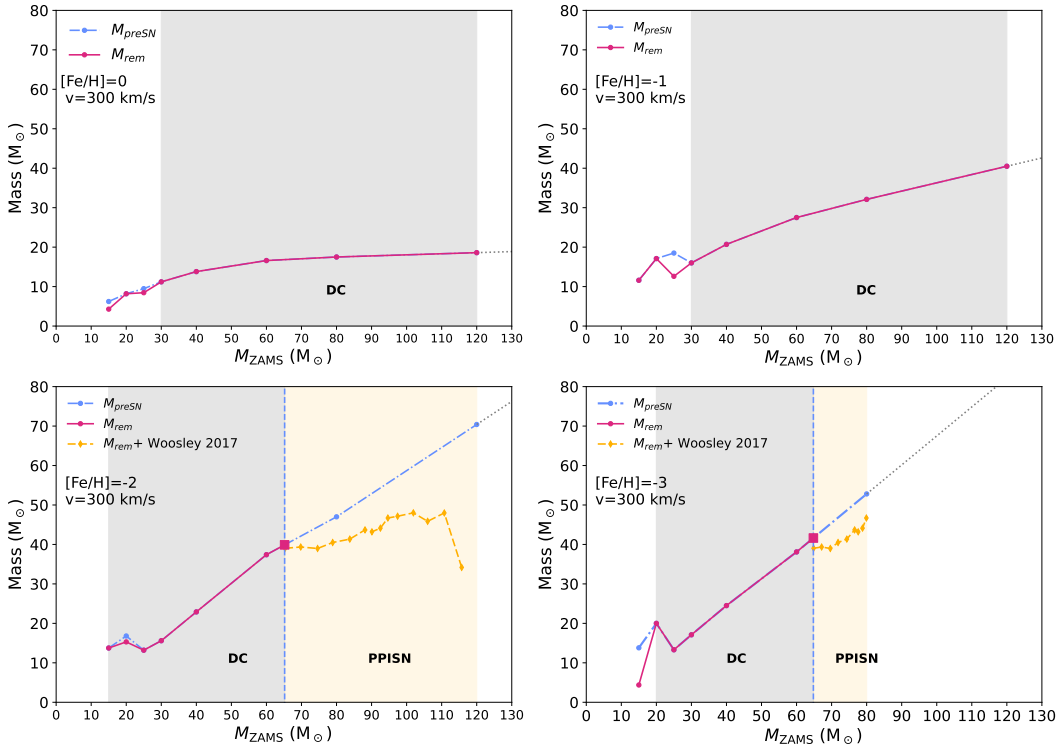

FIGURE 3.15: Same as Figure 3.13 but for rotating progenitors.

higher values of $\alpha_{\rm ov}$ exhibit more massive cores and likely evolve through the RSG phase, experiencing significant mass-loss episode. Hence, the stars enter the PPISNe with smaller

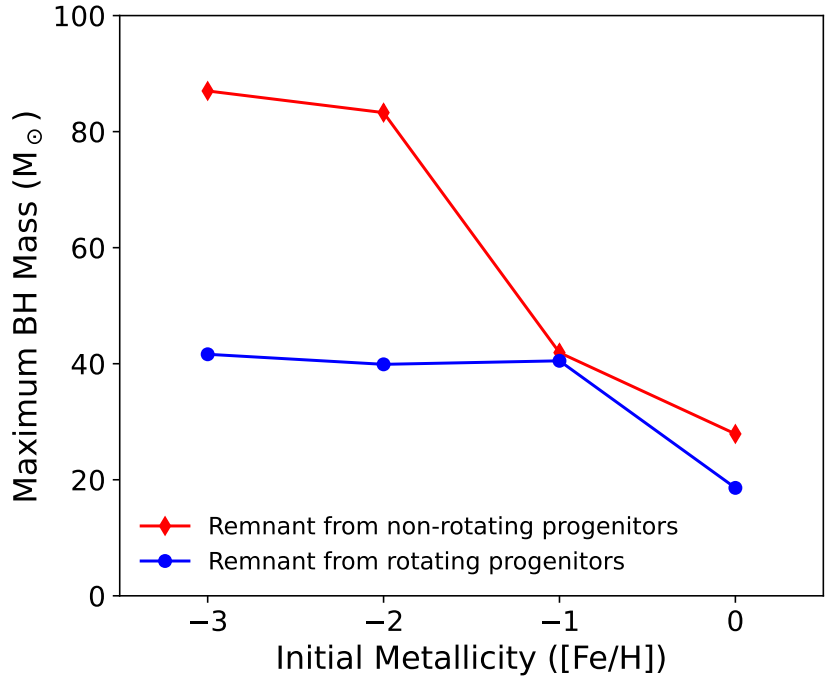

FIGURE 3.16: Maximum BH mass as a function of the initial metallicity for the non-rotating stellar progenitors (red line) and the rotating stellar progenitors (blue line) for the non-rotating progenitors.

pre-SN mass, forming less massive BHs.

We do not have conclusive evidences on the value of the core overshooting parameter yet, with observations providing evidence for higher possible values of the overshooting parameter than the one used in Vink et al., 2021 (e.g. Vink et al. 2010; Brott et al. 2011; Higgins and Vink 2019; Bowman 2020; Sabhahit et al. 2023; Winch et al. 2024). Furthermore, other authors such as Takahashi, 2018; Farmer et al., 2019; Farag et al., 2022; Mehta et al., 2022; Shen et al., 2023 show that the variation in the C/O ratio at the He core depletion plays a role in the onset of the PPISNe.

The parameter space of the factors ruling the final fate of massive stars is still mostly unexplored, and from this analysis it is apparent that there is still room for many future improvements. We will explore the impact of these different effects on the onset of PPISNe in a follow-up work.

3.4.3 Remnants mass distribution

Figure 3.19 and 3.20 show the remnants mass distribution we obtain by evolving a population of 10^6 isolated single stars with an initial-mass function (IMF) $dN/dM_{\rm ZAMS} \propto M_{\rm ZAMS}^{-2.35}$ (Kroupa 2001) and $M_{\rm ZAMS} \in [15\,{\rm M}_\odot; 150\,{\rm M}_\odot]$ for non-rotating and rotating progenitors, respectively. The mass of the remnant formed for each values of $[{\rm Fe/H}]$ and $M_{\rm ZAMS}$ is estimated by interpolating the $M_{\rm BH}$–$M_{\rm ZAMS}$ curve we find in Sec. 3.3.3, 3.3.4.

The panels of Figure 3.19 show several peaks in the remnants mass distribution. The most apparent peak of the remnants mass distributions is the one that corresponds to compact objects with mass 0.8—2 $\rm M_\odot$. This peak is a feature of the IMF and it shows up for all the considered metallicities for the non-rotating stars. It emerges because the majority of stellar progenitors extracted from the Kroupa IMF lie in the low-mass end with $M_{\rm ZAMS} \in [15\,{\rm M}_\odot; 20\,{\rm M}_\odot]$, and they are expected to form NSs, as result of successful ccSNe.

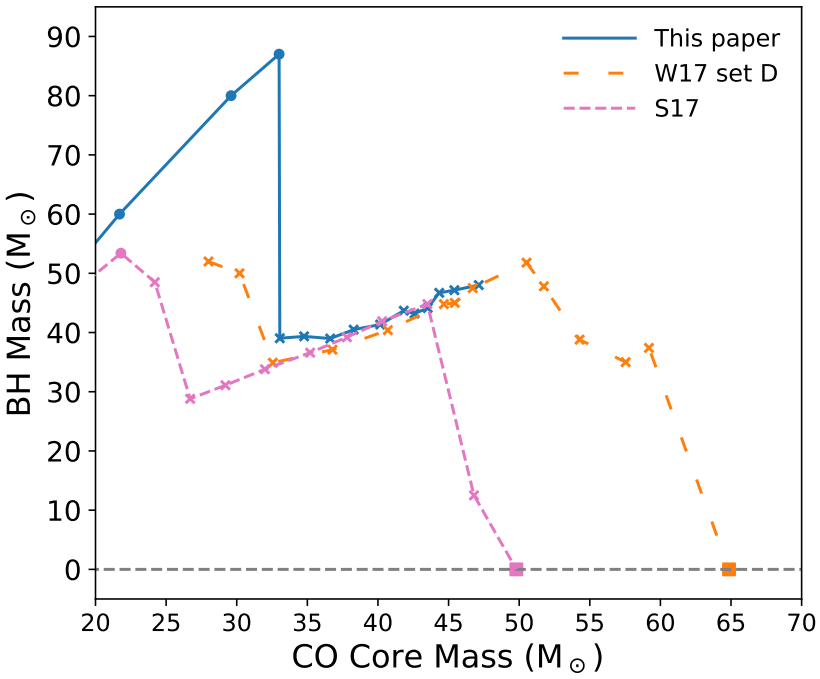

FIGURE 3.17: BH mass spectrum as a function of the CO core mass from various authors. Solid blue line: this work, non-rotating progenitors at $[\mathrm{Fe/H}] = -3$; long dashed orange line: set D of W17 (note that these models are obtained from stellar tracks computed at $Z = 0.1\,Z_\odot$ for which the mass loss has been inhibited, making these models distinct from those we used to compute the final remnant masses.); dashed pink line: models from Spera and Mapelli, 2017 with $Z = 1.3 \times 10^{-2}\,Z_\odot$ (S17). Circles (crosses) represent the models that are stable (unstable) against pair production, and squares are the stars disrupted by PISNe.

At $[\mathrm{Fe/H}] = 0$ (the top right panel of Figure 3.19), we find two other peaks in the remnant mass distribution, at BH masses of ~ 9—$13\,M_\odot$ and $\sim 23\,M_\odot$. The first one shows up because the $M_{\rm BH}$–$M_{\rm ZAMS}$ curve flattens out for $M_{\rm ZAMS} \in [30; 40]$ causing an accumulation of BHs at $\sim 13\,M_\odot$ (see the top left panel of Figure 3.13). The peak at $\sim 23\,M_\odot$ occurs at the transition from successfully-exploding progenitors to those that directly collapse to BHs. The heaviest BHs we obtain have masses $\simeq 28\,M_\odot$, consistent with the results presented in Sec. 3.3.3. At $[\mathrm{Fe/H}] = -1$ (top right panel of Figure 3.19) we find two peaks in the remnants mass distribution at $\sim 13\,M_\odot$ and $\sim 37 - 43\,M_\odot$. The former corresponds to a local flattening of the $M_{\rm BH}$–$M_{\rm ZAMS}$ curve in the region of progenitors with $M_{\rm ZAMS} = 30 - 40\,M_\odot$, and the latter is a degenerate effect due to the combination of the local flattening of the $M_{\rm BH}$–$M_{\rm ZAMS}$ curve and to the effect of the onset of the PPISNe, which causes significant mass loss and produce BHs with mass $\sim 37 - 48\,M_\odot$. Furthermore, at this value of metallicity the heaviest BH that forms has a mass $\sim 44\,M_\odot$, in agreement with the results presented in Sec. 3.2.2, 3.3.3.

At $[\mathrm{Fe/H}] = -2$ (bottom left panel of Figure 3.19), we find two peaks in the distribution for BHs with masses of $\sim 40\,M_\odot$, which again corresponds to the piling-up of BHs we obtain from the PPISNe, and of $\sim 78 - 84\,M_\odot$. This latter is the result of the piling-up of BHs from the stellar progenitors with $M_{\rm ZAMS}$ between $80\,M_\odot$ and $87\,M_\odot$ where the slope of the $M_{\rm BH}$–$M_{\rm ZAMS}$ curve decreases. Furthermore, the heaviest BHs that form have mass $\sim 83\,M_\odot$.

As in the case $[\mathrm{Fe/H}] = -2$, at $[\mathrm{Fe/H}] = -3$ (bottom right panel of Figure 3.19) we find that BHs pile up at masses $\sim 40 - 43\,M_\odot$ because of PPISNe. We find that above the threshold for DC, the BH mass distribution follows the IMF distribution, since stellar winds are quenched and stars directly collapse to BHs with mass equal to $M_{\rm ZAMS}$.

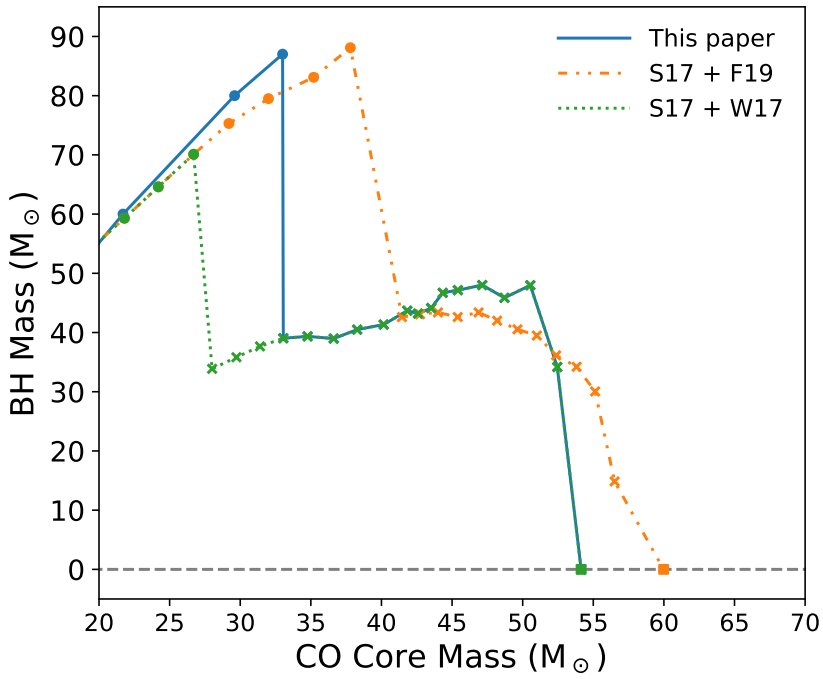

FIGURE 3.18: BH mass spectrum as a function of the CO core mass for different PPISN prescriptions. Solid blue line: this work, non-rotating progenitors at $[\mathrm{Fe/H}] = -3$; dash-dotted orange line: F19 PPISN threshold ($M_{\mathrm{CO}}^{\mathrm{PPISN}} = 41\,M_{\odot}$) applied to the S17 pre-SN progenitors; dotted green line: W17 PPISN threshold ($M_{\mathrm{CO}}^{\mathrm{PPISN}} = 28\,M_{\odot}$) applied to the S17 pre-SN progenitors. Circles (crosses) represent the models that are stable (unstable) against pair production, and squares represent the first star exploding as PISNe.

In summary, the features emerging from the BH mass distribution significantly depend on the adopted model, including the prescriptions for the pulsational pair-instability, and the details of the SN explosion. Furthermore, we find that the peak in the probability distribution corresponding to the transition between ccSNe and DC overlaps with the peak due to the PPISNe for some metallicities (e.g. $[\mathrm{Fe/H}] = -1$). Such peaks in the remnants mass distribution are not only uncertain and model dependent, but also degenerate with the details of the SN explosion mechanism.

From Figure 3.20 it is apparent that stellar rotation significantly affects the remnants mass distribution. The peak corresponding to stellar progenitors extracted from the low-mass end of the Kroupa IMF is now shifted to BH with masses $\sim 4\,M_{\odot}$ for $[\mathrm{Fe/H}] = 0, -3$ (upper left panel and bottom right panel of Figure 3.20, respectively) and $\sim 12\,M_{\odot}$ for $[\mathrm{Fe/H}] = -1, -2$ (upper right panel and bottom left panel of Figure 3.20, respectively). This effect is a degenerate feature of the abundance of stars with $M_{\mathrm{ZAMS}} = 15$—$20\,M_{\odot}$ and the outcome of the SN explosions at different initial metallicities for these stellar progenitors (see Section 3.3.4). Thus, we find that rotating stellar progenitors cannot produce NSs. At $[\mathrm{Fe/H}] = 0$, we find that the distribution has a peak corresponding to $\sim 8\,M_{\odot}$, which is due to the local flattening of the M_{BH}–M_{ZAMS} curve in the interval of M_{ZAMS} between $20\,M_{\odot}$ and $25\,M_{\odot}$. The heaviest BH we form at solar metallicity has mass $\sim 19\,M_{\odot}$.

At $[\mathrm{Fe/H}] = -2$ we find a peak in the remnants mass distribution corresponding to BHs masses of $\sim 40\,M_{\odot}$. This peak comes from the onset of the PPISNe. Such feature is independent of the details of the SN explosion and depends only on the prescription for the results of the PPISNe (combination of LC18 and W17 in this work). At $[\mathrm{Fe/H}] = -3$, we find a peak in the remnants mass distribution, which corresponds to BH masses of

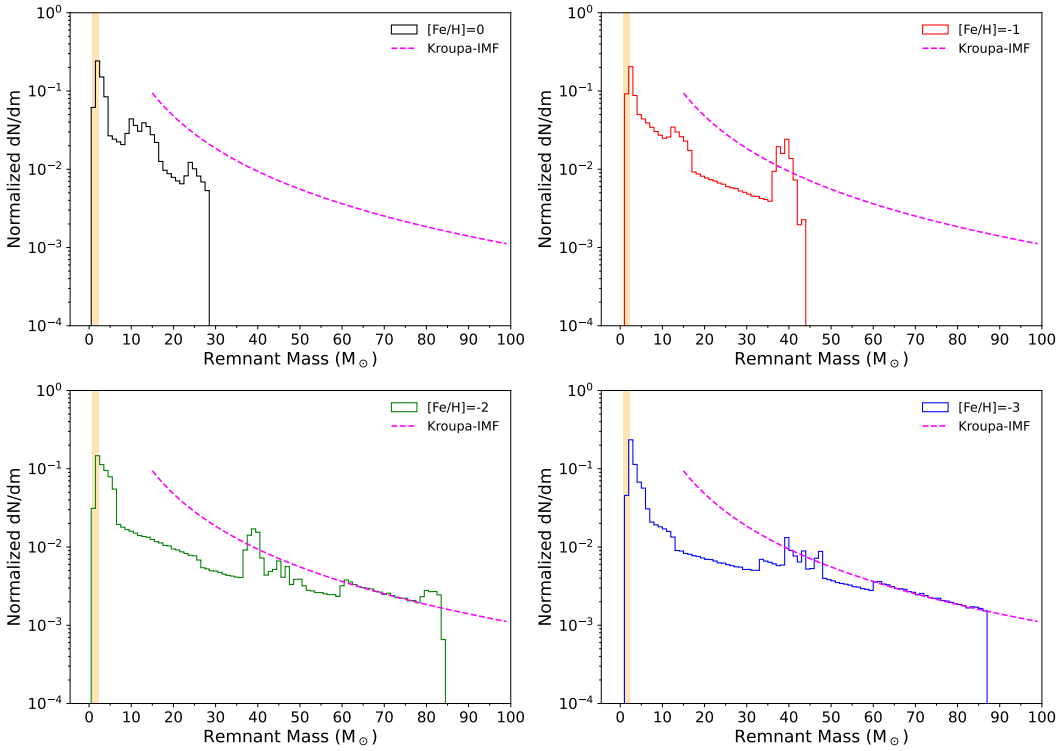

FIGURE 3.19: Normalized probability distribution of BH masses we obtain from a population of 10^6 stars whose mass follows a Kroupa, 2001 mass function ($dN/dM_{\rm ZAMS} \propto M_{\rm ZAMS}^{-2.35}$, dashed magenta line in all the panels) in the range $M_{\rm ZAMS} \in [15\,{\rm M}_\odot; 150\,{\rm M}_\odot]$ for non-rotating stellar progenitors. The yellow shaded area represents the mass interval of NSs assuming $M_{\rm NS} \in [0.8\,{\rm M}_\odot; 2.2\,{\rm M}_\odot]$. The Figure shows the remnant mass distribution we obtain for $[{\rm Fe/H}] = 0$ (upper left panel), $[{\rm Fe/H}] = -1$ (upper right panel), $[{\rm Fe/H}] = -2$ (lower left panel), and $[{\rm Fe/H}] = -3$ (lower right panel).

$\sim 13-20\,{\rm M}_\odot$. The piling-up of BHs in this mass region is due to the particular shape of the $M_{\rm BH}$–$M_{\rm ZAMS}$ curve in the region of $M_{\rm ZAMS}$ between $15\,{\rm M}_\odot$ and $\sim 30-40\,{\rm M}_\odot$. In such region, the $M_{\rm BH}$–$M_{\rm ZAMS}$ curve has a local minimum at $M_{\rm ZAMS} = 25\,{\rm M}_\odot$, which produce a BH with mass $\sim 13\,{\rm M}_\odot$. Thus, a wide interval of progenitors piles-up BHs with mass in the interval $\sim 13-20\,{\rm M}_\odot$ (see also Figure 3.15). Furthermore, we find peaks in the remnant mass distribution corresponding to BH masses of $\sim 40\,{\rm M}_\odot$ $\sim 43\,{\rm M}_\odot$ and $\sim 47\,{\rm M}_\odot$. The first peak is a degenerate feature from both the SN explosion details and the prescriptions for the PPISNe. The latter two depend only on the $M_{\rm ZAMS}$—M_{rem} curve we assume for the PPISNe. Finally, it is worth stressing that our results are based only on isolated single stars. Thus, considering binary stellar systems may significantly affects the results one can found about the BH mass spectrum.

3.4.4 Prescriptions for Population Synthesis Codes

In this section, we present a set of analytic prescriptions derived from our results. Such fitting formulae can be implemented in population-synthesis models to calculate the mass of the remnants, given the physical properties of the progenitor at the pre-SN stage.

The main value that our prescriptions provide is the fraction of mass that falls back onto the compact remnant during the explosion dM/M, that is:

$$\frac{dM}{M} = \frac{M_{\rm rem}}{M_{\rm preSN}} \tag{3.3}$$

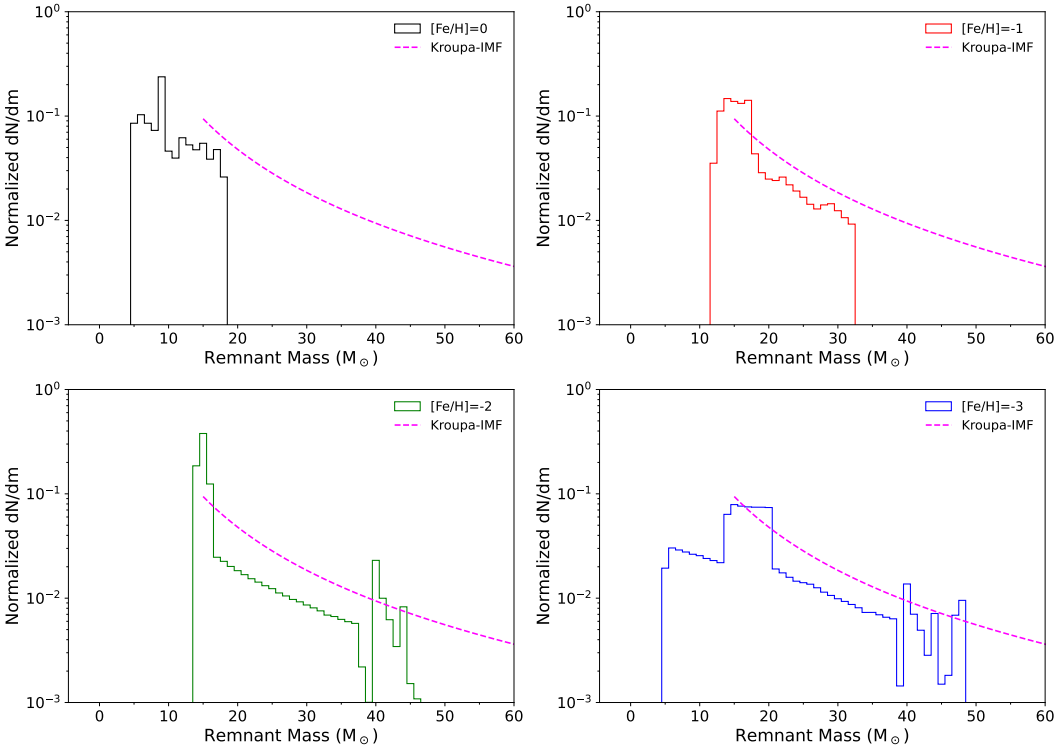

FIGURE 3.20: Same as Figure 3.19 but for rotating progenitors.

with $M_{\rm rem}$ that is the final remnant mass we obtain from the explosion.

The fraction of ejected mass is parametrized as a function of either the absolute value of the total energy, the binding energy of the stellar progenitor, or the CO core mass at the pre-SN stage. The total energy is computed as:

$$E_{tot} = E_{bind} + E_{int} + E_{kin} \tag{3.4}$$

where E_{bind} is the binding energy of the whole progenitor, E_{int} is the internal energy and E_{kin} is the kinetic energy of the stellar matter, over the whole progenitor.

The panels of Figure 3.21 show the linear fit we obtain for the non-rotating (left panels) and the rotating progenitors (right panels), as a function of the absolute value of the total energy (top), binding energy (middle), and CO core mass (bottom). For such analysis we study the fate of the explosion independently of the initial metallicity, thus in each panel we have all the models with $[\mathrm{Fe/H}] = 0 - 1, -2, -3$.

We first consider non rotating progenitor models. We find that we can fit the relation between dM/M and the absolute value of the total energy as:

$$dM/M = \begin{cases} a_{\rm SN}\,|E_{\rm tot}| + b_{\rm SN}, & |E_{\rm tot}| < |E_{\rm tot}|_{\rm DC} \\ 0, & |E_{\rm tot}| \geq |E_{\rm tot}|_{\rm DC} \end{cases} \tag{3.5}$$

with $a_{\rm SN} = 0.26\,\mathrm{foe}^{-1}$, and $b_{\rm SN} = -0.11$, and $|E_{\rm tot}|_{\rm DC} = 4.17$ foe. The latter is the value of $|E_{tot}|$ for which $dM/M = 0$, i.e. for the DC.

From the top-left panel of Figure 3.21 it is apparent that two progenitors deviate significantly from our best fit. We find one stellar progenitor that directly collapses to BH despite having $|E_{\rm tot}| < |E_{\rm tot}|_{\rm DC}$, and one progenitor that explodes with $|E_{\rm tot}| > |E_{\rm tot}|_{\rm DC}$. The former star has $M_{\rm ZAMS} = 60\,\mathrm{M}_\odot$ and $[\mathrm{Fe/H}] = 0$ and ends its life as a He-star, while the latter has

$M_{\rm ZAMS} = 60\,{\rm M}_\odot$ and $\left[{\rm Fe/H}\right] = -1$, and ends its life as a RSG, and therefore its H envelope is very loosely bound despite the high absolute value of the total energy. The relation between dM/M and the binding energy $E_{\rm bind}$ can be fit as:

$$dM/M = \begin{cases} c_{\rm SN} E_{\rm bind} + d_{\rm SN}, & E_{\rm bind} < E_{\rm bind,DC} \\ 0, & E_{\rm bind} \geq E_{\rm bind,DC} \end{cases} \tag{3.6}$$

With $c_{\rm SN} = 0.06\,{\rm foe}^{-1}$, and $d_{\rm SN} = 0.04$, and $E_{\rm bind,DC} = 15.9$ foe.

From the central-left panel of Figure 3.21 it is apparent that one progenitor deviates significantly from the best fit. This is again the model with $\left[{\rm Fe/H}\right] = -1$ and $M_{\rm ZAMS} = 60\,{\rm M}_\odot$, which explode as a SN with a binding energy of $E_{bind} = 19.5$ foe. If we did not consider this stellar progenitor, we would find a threshold value of ~ 10.0 foe for the binding energy above which the stars DC to BHs.

Finally, the relation between dM/M and the CO core mass $M_{\rm CO}$ can be fit as:

$$dM/M = \begin{cases} e_{\rm SN} M_{\rm CO} + f_{\rm SN}, & M_{\rm CO} < M_{\rm CO,DC} \\ 0, & M_{\rm CO} \geq M_{\rm CO,DC} \end{cases} \tag{3.7}$$

With $e_{\rm SN} = 0.06\,{\rm M}_\odot^{-1}$, and $f_{\rm SN} = -0.03$, and $M_{\rm CO}^{\rm DC} = 17.2\,{\rm M}_\odot$, where again we find that only the two progenitor stars with $M_{\rm ZAMS} = 60\,{\rm M}_\odot$, $\left[{\rm Fe/H}\right] = -1$ (that explodes as a SN despite having $M_{\rm CO} = 21.4\,{\rm M}_\odot > {\rm M_{CO,DC}}$), and with $M_{\rm ZAMS} = 60\,{\rm M}_\odot$, $\left[{\rm Fe/H}\right] = 0$ (the He-star with $M_{\rm CO} = 16.6\,{\rm M}_\odot < {\rm M_{CO,DC}}$ that directly collapses into a BH) deviate from the global trend.

In contrast, the right panels of Figure 3.21 show that rotating progenitors do not follow a linear relation between dM/M and $|E_{\rm tot}|$, $E_{\rm bind}$, or $M_{\rm CO}$, and that there are no threshold values of any of these quantities that clearly separate stars which explode as SNe from stars which DC to BHs. Therefore, we cannot find any linear relation between the properties of rotating stars at the pre-SN stage and the final-remnant mass.

It is important to stress that - even in the case of non-rotating stellar progenitors - we can only provide a rough estimate of the thresholds for the transition from stars that successfully explode as ccSNe and stars that directly collapse to BH. From the left panels of Figure 3.21, it is apparent that a linear relation is in place below the threshold for the DC, but that some stars deviate from the expected trends, indicating that this approach fails to fully capture the complexity of a SN explosion. Our analysis shows that the fate of the collapse of each stellar progenitor is ruled only by the dynamics of the shock wave, i.e. the micro-physics effects taking place during the explosion are crucial in determining its outcome.

3.5 Summary and Conclusion

In this Chapter, we studied the explosion of a subset of pre-SN models of massive stars presented in Limongi and Chieffi, 2018. The subset contains massive stars with masses in the range $13 - 120\,{\rm M}_\odot$, initial metallicities $\left[{\rm Fe/H}\right] = 0, -1, -2, -3$, and initial rotation velocities $v = 0\,{\rm km\,s^{-1}}$, $300\,{\rm km\,s^{-1}}$. Using the HYPERION code (Limongi and Chieffi, 2020), we simulate the explosion by removing the inner 0.8 ${\rm M}_\odot$ of the iron core, and injecting a given amount of thermal energy at the edge of this zone. Such approach required a set of free parameters to model the injection of energy. To fix these parameters, we have performed several calibration runs of a stellar progenitor similar to the progenitor of SN 1987A (Sk — 69°202), aimed at reproducing the observed kinetic energy of the ejecta (~ 1.0 foe) and ^{56}Ni mass ($\sim 0.07\,{\rm M}_\odot$) (Arnett et al., 1989; Utrobin, 1993; Utrobin, 2006; Utrobin, Immler, and Weiler, 2007; Blinnikov et al., 2000; Shigeyama and Nomoto, 1990).

Once we have chosen the explosion parameters, we have adopted this combination for the explosion of all the models of our grid of stellar progenitor, obtaining both successful and failed explosions (DC to BHs), depending on the initial stellar parameters, i.e. mass, metallicity and rotation velocity.

We find that:

- The metallicity plays a crucial role in the pre-SN evolution of a star, since it is strongly connected with the efficiency of stellar winds. For non rotating models, progenitors with $\left[\mathrm{Fe/H}\right] = -2$ and $\left[\mathrm{Fe/H}\right] = -3$ evolve at roughly constant mass during their life, while for $\left[\mathrm{Fe/H}\right] = 0$ and $\left[\mathrm{Fe/H}\right] = -1$ the stellar winds remove a significant fraction of mass from the stellar progenitor. For these models we find that the threshold masses above which the stars undergo a DC to BH are $M_{\mathrm{ZAMS}} \simeq 60\,\mathrm{M}_{\odot}$ for $\left[\mathrm{Fe/H}\right] = 0,\ -2,\ -3$ and $M_{\mathrm{ZAMS}} \simeq 80\,\mathrm{M}_{\odot}$ for $\left[\mathrm{Fe/H}\right] = -1$. The most massive BH has mass of $\simeq 91\,\mathrm{M}_{\odot}$, and comes from the DC of the most massive star at $\left[\mathrm{Fe/H}\right] = -3$ not undergoing PPISNe (assuming that $\mathrm{M}_{\mathrm{CO}}^{\mathrm{PPISN}} = 33\mathrm{M}_{\odot}$, see below).

- The presence of an initial angular rotation enhances the mass loss, and induces the formation of larger convective regions, and therefore larger CO cores, i.e. more bound structures. Thus, we find that for rotating stellar progenitors, the transition from a successful SN explosion to a DC to BHs occurs at lower M_{ZAMS} values ($\sim 20\,\mathrm{M}_{\odot}$, $\sim 30\,\mathrm{M}_{\odot}$, $\sim 15\,\mathrm{M}_{\odot}$, and $\sim 20\,\mathrm{M}_{\odot}$, for $\left[\mathrm{Fe/H}\right] = 0$, $\left[\mathrm{Fe/H}\right] = -1$, $\left[\mathrm{Fe/H}\right] = -2$, and $\left[\mathrm{Fe/H}\right] = -3$, respectively) than for the non-rotating progenitors. In contrast, because of the enhanced mass loss driven by rotation, even if more stars DC to BHs, the maximum BH masses formed are lower than for non-rotating stars. In addition, the chemical mixing induces the onset of the PPISNe at lower values of M_{ZAMS} with respect to the non-rotating progenitors. As a result, the maximum BH mass formed by rotating progenitors is $\sim 41\,\mathrm{M}_{\odot}$, which comes from the DC of a stellar progenitors undergoing PPISNe, that we model according to the results of W17 (assuming that $\mathrm{M}_{\mathrm{CO}}^{\mathrm{PPISN}} = 33\,\mathrm{M}_{\odot}$, see below).

- The maximum BH mass formed is very sensitive to the adopted criterium for the onset of PPISNe, which can be expressed in terms of the maximum CO core mass above which stars enter the PPISN regime, $\mathrm{M}_{\mathrm{CO}}^{\mathrm{PPISN}}$. From our simulated grid we find that $30M_{\odot} < M_{\mathrm{CO}}^{\mathrm{PPISN}} < 50M_{\odot}$, which is consistent with most of the published results. However, these vary considerably, from the lowest value adopted by S17, $\mathrm{M}_{\mathrm{CO}}^{\mathrm{PPISN}} = 24\,\mathrm{M}_{\odot}$, to the highest value adopted by F19, $M_{\mathrm{CO}}^{\mathrm{PPISN}} = 41\,\mathrm{M}_{\odot}$. Such a discrepancy results in a significant uncertainty on the maximum BH mass, which can be as low as $\sim 53\,\mathrm{M}_{\odot}$ in the case of S17, or even as high as $\sim 87\,\mathrm{M}_{\odot}$, which is the case of this paper.

- We have applied the results of our simulations to a populations of 10^6 stars whose masses are distributed accordingly to a Kroupa-IMF. The resulting BH probability distribution depends on the initial stellar metallicity and rotation rate, and encode information on the progenitor mass - BH mass relation. We showed that the features emerging in the BH mass distribution depend significantly on the adopted stellar models and show significant degeneracies.

- We provide linear relationships between the mass ejected during the explosion dM/M and the structural properties of the stellar progenitors at the pre-SN stage, such as the binding energy, the CO core mass and the absolute value of the total energy. Such relationships have been found only in the case of non-rotating stellar progenitors, even if some stars deviates from the linear fit. In contrast, we do not find any monotonic

relationship between dM/M and the progenitor's properties in the case of rotating stellar progenitors. We showed that, despite the relations can be adopted for fast population-synthesis studies, they fail to capture the details of the link between progenitor stars and their compact remnants.

It is worth mentioning that in this work we calibrate the explosions on the observational properties of SN1987A (i.e. the kinetic energy of the ejecta, and the mass of ^{56}Ni ejected into the interstellar medium). In a follow-up study we will a possible improvement will be to broaden the set of SNe used for the calibration process.

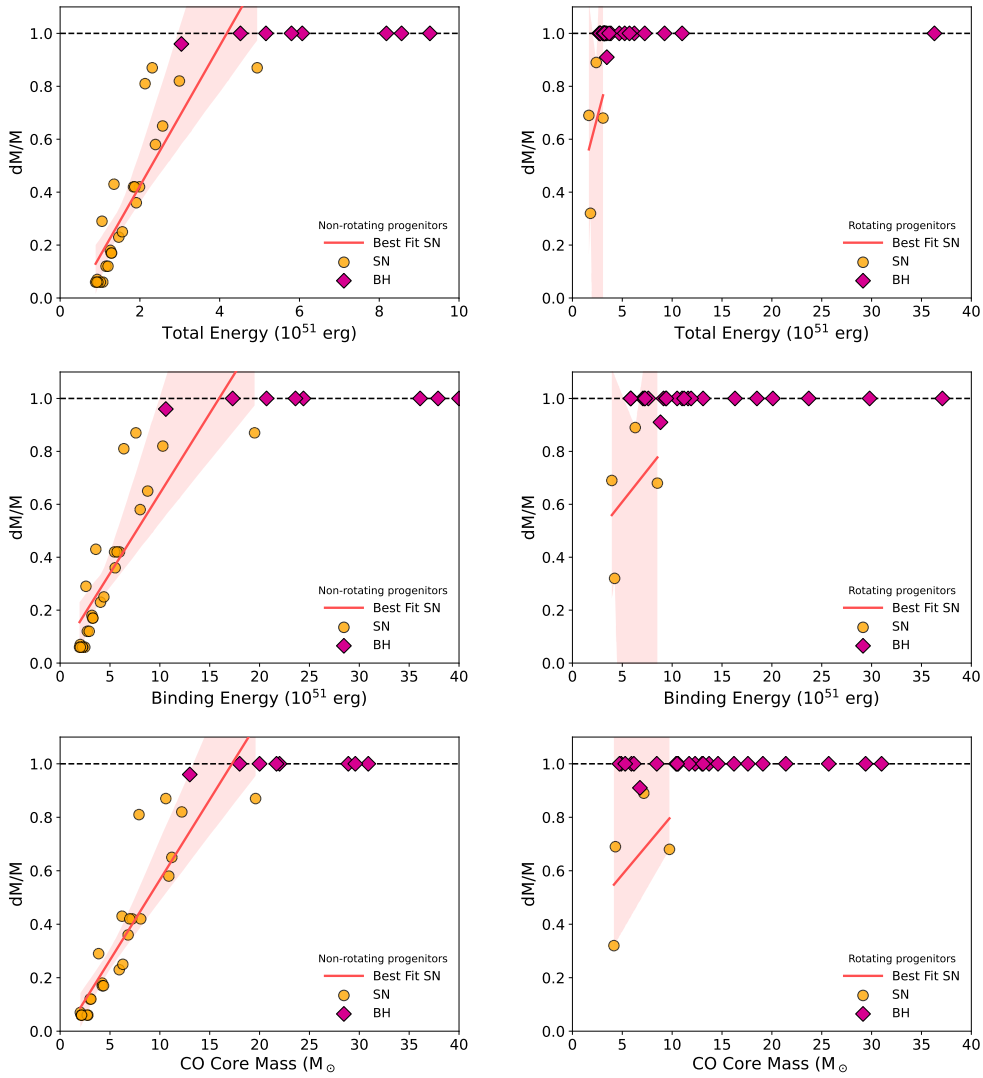

FIGURE 3.21: Linear relation between the mass that falls back after the explosions and some structural properties of the stellar progenitors at the pre-SN stage, such as the absolute value of the total energy (top panels), the binding energy (central panels) and the CO core mass (bottom panels). We have performed such analysis both for the non-rotating (left panels) and for the rotating stellar progenitors (right panels). We study the fate of the explosion independently of the initial metallicity, thus in each panel we have all the models with $[\mathrm{Fe/H}] = 0 - 1, -2, -3$. In each panel the circular orange points are the stellar progenitors undergoing successful SN explosions and the best fit for dM/M is the solid red line, while the diamond purple points represents the progenitors which DC to BHs. The black dashed line corresponds to $dM/M = 1$ i.e., the value of dM/M for the DC. The red shaded area is the 95% confidency interval for the SN linear regression.

Chapter 4

Constraining the features of the BBH mass distribution through population synthesis simulation

This Chapter is based on Ugolini et al., in prep.

4.1 Introduction

In this Chapter, we aim to reproduce a well-known feature of the black hole (BH) mass spectrum obtained from gravitational wave (GW) detections, the so-called *PPISN-peak* at approximately 34 $M_\odot$ in the distribution of the mass of the primary BHs (Stevenson et al., 2019; Abbott et al., 2021; Abbott et al., 2023; Karathanasis, Mukherjee, and Mastrogiovanni, 2023).

Our goal is to study the astrophysical processes behind this accumulation of massive objects at this particular mass, and we addressed this problem in the scenario of isolated binaries, assuming that all merging BBH binaries originate from massive stars born in binaries that remain gravitationally bound from their formation until merger.

4.2 Methods

We used catalogs of isolated binaries simulated with the state-of-the-art population synthesis code SEVN (see Section 2.2 for further details). SEVN is a highly flexible tool for population synthesis, utilizing on-the-fly interpolation of pre-computed stellar evolution tracks, making it both efficient and adaptable for different evolutionary scenarios. In this work we adopted the standard tracks computed with the PARSEC code (see for more details Bressan et al., 2012; Costa et al., 2021). We use the latest version of SEVN (Spera and Mapelli, 2017; Spera et al., 2019; Iorio et al., 2023), described in Iorio et al., 2023.

The code is presented in Section 2.2, in this section I will discuss the initial condition for the various simulations we performed.

4.2.1 Initial conditions for the simulations

We sample the masses of the primary stars from a Kroupa initial mass function (IMF, Kroupa, 2001), therefore their mass is distributed as:

$$\mathrm{pdf}(M_{\mathrm{ZAMS},1}) \propto M_{\mathrm{ZAMS},1}^{-2.3} \quad \text{with} \quad M_{\mathrm{ZAMS},1} \in [8, 150] \tag{4.1}$$

The mass ratio is drawn from the distribution found by Sana et al., 2012, based on the observation of massive stars in young clusters. Thus, we have:

$$\mathrm{pdf}(q) \propto q^{-0.1} \quad \text{with} \quad q = \frac{M_{\mathrm{ZAMS},2}}{M_{\mathrm{ZAMS},1}} \in [q_{min}, 1.0] \tag{4.2}$$

$$q_{min} = \max\left(\frac{5.0}{M_{\mathrm{ZAMS},1}}, 0.1\right) \tag{4.3}$$

The masses of the secondary stars is determined simply as:

$$M_{\mathrm{ZAMS},1} = qM_{\mathrm{ZAMS},2}. \tag{4.4}$$

The lower cutoff for the primary (secondary) distribution, set at $8.0, \mathrm{M}_\odot$ ($5.0, \mathrm{M}_\odot$), is slightly higher than the fiducial values used in Iorio et al., 2023. This adjustment is due to our focus on BBH (binary black hole) systems, particularly their high-mass end. Finally, also the initial orbital periods P and eccentricities e are sampled according to Sana et al., 2012 as:

$$\mathrm{pdf}(\mathcal{P}) \propto \mathcal{P}^{-0.55}, \quad \text{with } \mathcal{P} = \log(P/\mathrm{day}) \in [0.15, 5.5] \tag{4.5}$$

and:

$$\mathrm{pdf}(e) \propto e^{-0.42}, \quad \text{with } e \in [0, 0.9] \tag{4.6}$$

We generated 10^7 binaries and we used them as initial conditions for all our simulations (varying the initial metallicity and the combination of the other parameters). The total mass of the simulated binaries is$3.9 \times 10^8\ \mathrm{M}_\odot$, with a correction factor that takes into account for incomplete IMF sampling due to the mass cuts of $f_{\mathrm{cut}} = 0.185$.

For each combination of the SSE and BSE parameters, we performed 60 set of simulations, combining 15 different metallicities and 5 values of α for a total of 900 possible configurations (see Table 4.1, for all the other processes, we kept the fiducial assumptions of the `SEVN` code, see Iorio et al. 2023) of metallicity Z, CE efficiency α, ccSN and PPISN prescriptions. Furthermore, we simulated also a scenario where the mass transfer was assumed to be stable (assuming the `delayed_Gauss` and `M20` models for ccSNe and PPISNe, respectively). Finally, we investigated the impact of a top-heavy IMF (for further details see Section 4.4.4) on the results of the simulations. Thus, for $\alpha = 3,\ 5,\ 10$ we simulated the evolution of a population generated according to a Larson IMF (see Larson 1998).

In total, we studied the evolution of 9.6×10^9 binary systems.

TABLE 4.1: List of all the parameters describing the SSE and the BSE of our systems. See 2 for details on the ccSN and PPISNe treatment.

Parameters	Values
α **CE**	0.5, 1.0, 3.0, 5.0, 10, MT stable
ccSN treatment	`delayed_Gauss`, `rapid_Gauss`, `U24`.
PPISN treatment	`noPPISN`, `F19`, `M20`, `U24`.
Metallicity	2×10^{-4}, 3×10^{-4}, 4×10^{-4}, 5×10^{-4}, 7×10^{-4}, 1×10^{-3}, 1.4×10^{-3}, 2×10^{-3}, 3×10^{-3}, 4×10^{-3}, 5×10^{-3}, 7×10^{-3}, 1×10^{-2}, 1.4×10^{-2}, 2×10^{-2}.

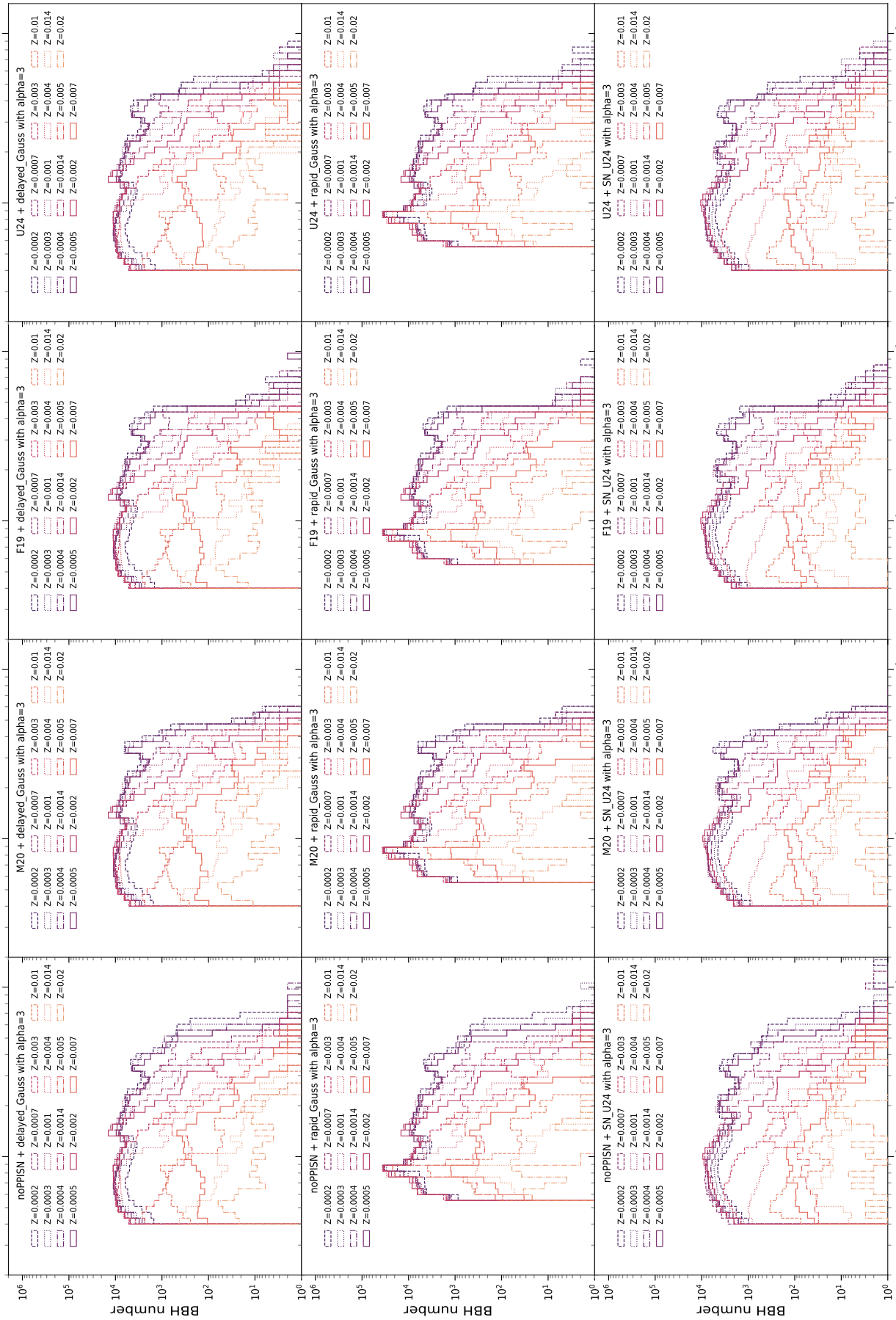

FIGURE 4.1: Primary BH mass distribution of BBH merging system in our simulation. From left to right: each row shows a different prescription for ccSNe (`delayed_Gauss` on the top row, `rapid_Gauss` on the central row, and `SN_U24`) on the bottom row), while each column shows a different treatment PPISNe (`noPPISN` on the first column, `M20` on the second column, `F19` on the third column, and `U24` on the fourth column). The color map refers to the metallicity of the progenitors ($Z = 2 \times 10^{-4}$, 3×10^{-4}, 4×10^{-4}, 5×10^{-4}, 7×10^{-4}, 1×10^{-3}, 1.4×10^{-3}, 2×10^{-3}, 3×10^{-3}, 4×10^{-3}, 5×10^{-3}, 7×10^{-3}, 1×10^{-2}, 1.4×10^{-2}, 2×10^{-2}). In Appendix B we show the alternative versions of this plot, for all the α values.

4.3 Results

4.3.1 Effect of SSE prescriptions

In this work, we focus on BBH systems that merge within a Hubble time. Figure 4.1 illustrates the mass distribution of the primary black holes (BHs) of these merging systems, specifically for a fiducial value of common envelope (CE) efficiency, $\alpha = 3$. Each row in Figure 4.1 represents a different prescription for core-collapse supernovae (ccSNe): `delayed_Gauss` (top row), `rapid_Gauss` (central row), and `SN_U24` (bottom row). Correspondingly, each column shows different criteria for the onset of PPISNe: `noPPISN` (first column), `M20` (second column), `F19` (third column), and `U24` (fourth column), as outlined in Table 4.1. The color variations in each panel reflect different progenitor metallicities.

From the top row of Figure 4.1, it is evident that the `delayed_Gauss` prescription yields an increased production of low-mass BHs ($\leq 5\,M_\odot$), accompanied by a notable peak in the range $15-22\,M_\odot$. Additionally, there is a pronounced tail of fewer but more massive BHs ($M_{BH} \geq 60\,M_\odot$). This distribution pattern indicates that delayed explosions are conducive to the formation of lower-mass black holes due to increased fallback during the supernova process. In contrast, the central row shows the `rapid_Gauss` prescription, which results in a significant reduction of low-mass BHs. In this scenario, BHs with masses less than $5\,M_\odot$ are rare, while a more prominent pile-up occurs around $10\,M_\odot$. The higher-mass tail is also less pronounced compared to the `delayed_Gauss` prescription. These results align with the known characteristics of the rapid explosion model, where the lack of fallback reduces the formation of lower-mass black holes (see Fryer et al. 2012).

The bottom row displays the mass distribution for the `SN_U24` prescription. At lower masses, this prescription produces results similar to `delayed_Gauss`, but with generally higher-mass BHs, where the peak shifts slightly upward ($\sim 20\,M_\odot$). The tail towards higher masses is also more populated compared to both the delayed and rapid scenarios. This suggests that the `SN_U24` model retains more mass during the collapse, leading to a preference for slightly heavier remnants.

The different PPISNe prescriptions across columns also significantly impact the primary BH mass distribution. In the first column (`noPPISN`), we observe an extended high-mass tail, with BH masses reaching beyond $\sim 100\,M_\odot$. This absence of PPISNe effects allows massive progenitors to retain more mass, ultimately collapsing into heavier BHs. For the `M20` prescription, the primary effect is a sharp upper cutoff in BH mass, with a maximum at approximately $50-60\,M_\odot$. In contrast, both the `F19` and `U24` models (third and fourth columns, respectively) allow for a tail of BHs with masses extending to $\sim 90\,M_\odot$. The differences between these models stem from the varying CO core mass thresholds at which pulsational pair-instabilities are triggered, with `U24` and `F19` permitting slightly higher thresholds ($M_{\rm CO} = 35\,M_\odot$ and $M_{\rm CO} = 38\,M_\odot$, respectively) compared to `M20` ($M_{\rm CO} = 28\,M_\odot$).

From Figure 4.4.2, we can also find broader patterns related to progenitor metallicity. The contribution to BH masses above $\sim 30\,M_\odot$ primarily originates from low-metallicity progenitors ($Z \leq 5 \times 10^{-4}$). This behavior is consistent across all SSE and PPISNe prescriptions, as lower metallicities reduce the impact of stellar winds, allowing more massive stars to form. In contrast, BHs with masses below $10\,M_\odot$ are produced even at higher metallicities, indicating that these lighter BHs are less sensitive to metallicity-driven mass loss. Interestingly, the peak at $\sim 35\,M_\odot$ appears consistently across different prescriptions, with only minor variations depending on whether PPISNe are included. This suggests a robust astrophysical mechanism behind the accumulation of BHs at this mass, which we will explore further in Section 4.4.

Overall, the choice of SSE prescription significantly shapes the primary BH mass distribution, particularly at the lower and upper ends of the mass spectrum. The `delayed_Gauss` prescriptions favor lower-mass BHs, while the `rapid_Gauss` treatment produces a dearth of

BHs below 5 $M_\odot$. The `SN_U24` model tends to yield heavier remnants, which is reflected in both the peak mass and the extended high-mass tail.

We show all the distributions for the different values of α in Appendix B.

4.3.2 Effect of BSE prescriptions

In the previous section, we showed the effect of different SSE prescriptions on the primary BH mass distribution of the merging BBH systems. In this section, we focus on the impact of BSE processes, particularly the efficiency of the CE phase, on the primary BH mass distribution of BBHH systems that merge within a Hubble time.

Figure 4.2 presents the mass distribution of primary BHs for merging BBH systems under different CE efficiencies. We consider a range of values $\alpha = 0.5$, 1, 3, 5, 10, along with a scenario where mass transfer (MT) is assumed to be always stable. In the Figure, we fixed the combination of SSE parameters choosing as treatment for the ccSNe and the PPISNe `delayed_Gauss` and `M20`, respectively. Henceforth, we will refer to this configuration as "fiducial" model.

In the upper-left panel, we show the primary BH mass distribution distribution of the merging BBHs as function of metallicity, assuming a CE efficiency $\alpha = 0.5$. This low efficiency results in many systems undergoing a CE phase merging before they can successfully eject the envelope, thereby reducing the number of BBH systems that will merge through gravitational-wave (GW) emission within a Hubble time. However, for those systems that do successfully eject the CE, the orbit experiences significant shrinking, which increases the likelihood of a future merger. In this scenario we notice that the least massive BHs, i.e. $M_{BH} \lesssim 10\,M_\odot$ are predominantly produced in more metal-rich environments ($Z \gtrsim 0.0014 = 0.1\,Z_\odot$). On the other hand, the most massive BHs are produced mainlyfrom metal-poor progenitors ($Z \leq 7\times10^{-4} \sim 0.05\,Z_\odot$).

In the upper middle panel, we show the primary BH mass distribution for $\alpha = 1$. This choice assumes that all the binding energy lost by the system due to the orbit shrinking is then transferred to the envelope, to fuel its ejection mechanism. With this efficiency, we observe an increased number of BBH mergers compared to $\alpha = 0.5$. The higher masses in the BH mass distribution continue to be predominantly formed in metal-poor systems, whereas less massive BHs ($10 \lesssim M_{BH} \lesssim 20\,M_\odot$) are produced by a mix of metal-rich and metal-poor progenitors. Finally, low-mass BHs are produced mainly by metal-rich progenitors.

The upper-right panel shows the mass distribution for $\alpha = 3$. In this scenario (and in the following ones, $\alpha = 5$, 10), the energy injected into the CE is three times the amount produced by the shrinking binary orbit. This increased efficiency allows more systems to successfully eject the CE, but also implies that there is an additional source of energy that contributes to the ejection mechanism. In this scenario, we find a more even distribution of low-mass BHs ($3\,M_\odot \lesssim M_{BH} \lesssim 10\,M_\odot$) across all metallicities. BHs in the mass range $10-20\,M_\odot$ are produced mainly from metallicities $\lesssim 2\times10^{-3} \sim 0.15\,Z_\odot$, whereas the higher-mass BHs ($\geq 20\,M_\odot$) are primarily produced by metal-poor ($7\times10^{-4} \sim 0.05\,Z_\odot$) systems.

For $\alpha = 5$, illustrated in the lower-left panel of Figure 4.2, we find that the trend is similar to that seen with $\alpha = 3$. The low-mass BHs are produced across a range of metallicities and high-mass BHs predominantly formed from low-metallicity progenitors.

In contrast, for $\alpha = 10$ the CE is ejected so efficiently that this phase does not last long enough to significantly shrink the binary orbit, resulting in fewer systems merging within a Hubble time, particularly at higher metallicities. This last result is due to the effect of stellar winds in loosening the orbit, that, on turn, reduces the BBH merger efficiency. Consequently, the primary BH mass distribution is dominated by metal-poor systems, since for them the stellar winds are quenched. The lower-right panel presents the scenario where mass transfer is assumed to be always stable. In this case, the CE phase is largely suppressed, though it can

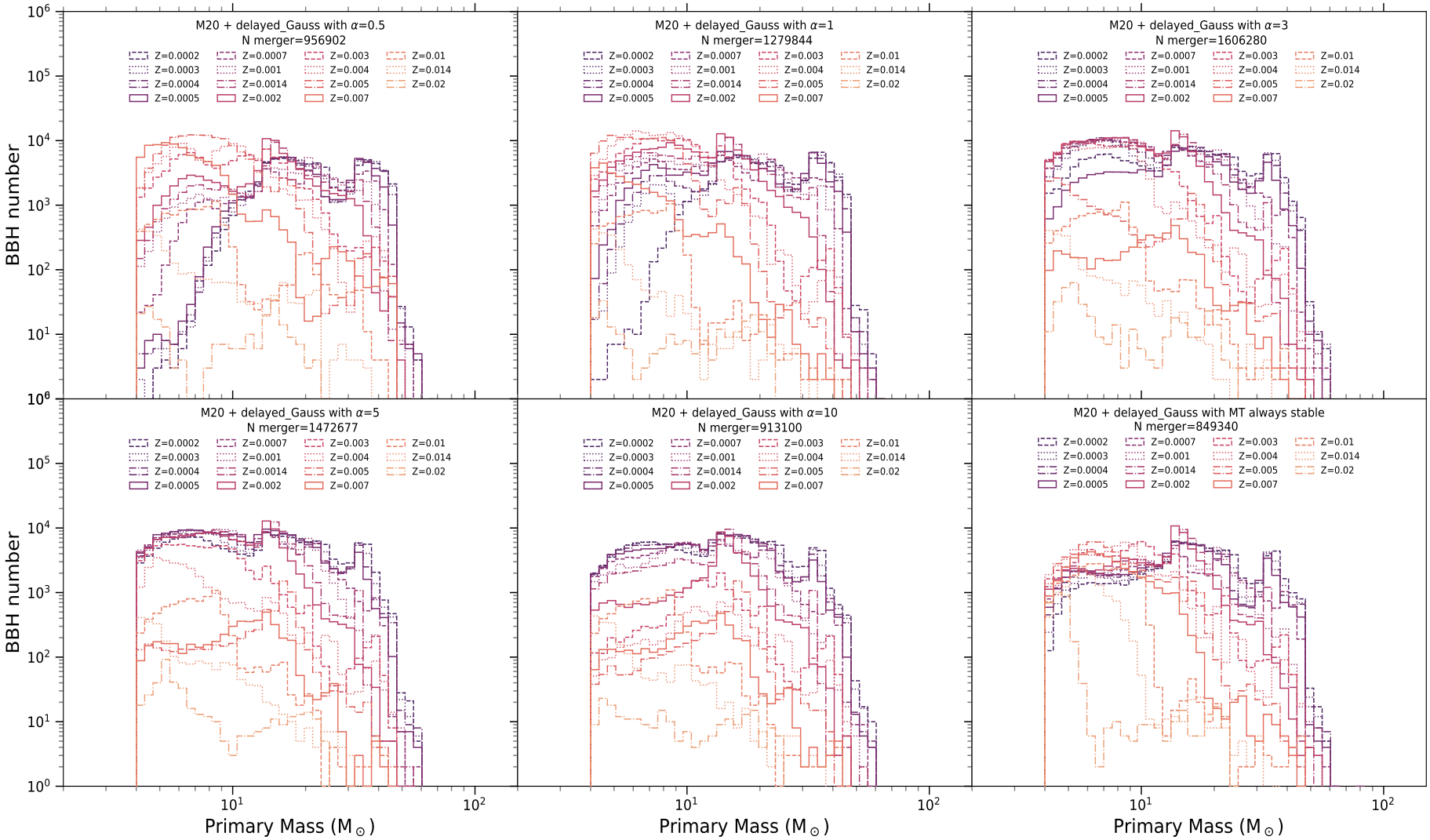

FIGURE 4.2: Primary BH mass distribution of BBH merging system in our simulation. Each plot shows the results we obtain for a different CE efficiency α. Upper panels, from left to right: $\alpha = 0.5,\ 1,\ 3$. Lower panels, from left to right: $\alpha = 5,\ 10$, and the scenario in which the mass transfer is assumed as always stable (worth noting, this doesn't mean we are completely disabling the possibility of entering a CE phase during the binary evolution, since there are still cases that triggers a CE). The colour map refers to the metallicity of the progenitors ($Z = 2\times10^{-4}, 3\times10^{-4}, 4\times10^{-4}, 5\times10^{-4}, 7\times10^{-4}, 1\times10^{-3}, 1.4\times10^{-3}, 2\times10^{-3}, 3\times10^{-3}, 4\times10^{-3}, 5\times10^{-3}, 7\times10^{-3}, 1\times10^{-2}, 1.4\times10^{-2}, 2\times10^{-2}$).

still occur when both stars overfill their RL (see Iorio et al., 2023). When it does occur, the CE is treated with the fiducial efficiency $\alpha = 3$. However, for such a choice of the BSE treatment, we find that rather few low-mass primary BHs are produced. This is because such BHs are mainly the result of binaries that evolve through a CE phase (see 4.3.2 for further details). When produced, such BHs are mainly the result of the evolution of metal rich systems, that dominates the production of primary BHs up to $M_{BH} \sim 10\,M_\odot$. Instead, more massive primary BHs are mainly produced by metal-poor stars, with $Z \leq 7 \times 10^{-4}$.

Furthermore, in the various panels of Figure 4.2 we show also the number of BBH mergers we obtain from the total population. We find that this number is significantly affected by the efficiency of the CE, growing with α up to $\alpha = 3$, for which we have the maximum number of mergers, that then starts decreasing for higher CE efficiencies.

For $\alpha = 0.5$ we find $\sim 9.5 \times 10^5$ BBH merging through GW emission. Thus, this choice of α implies that we have a substantial number of stellar mergers during the CE phase, as confirmed also in other works (e.g. Iorio et al. 2023). At a slightly higher efficiency $\alpha = 1$, the total number of BBH mergers is 1280657. Thus, we find $\sim 33\%$ more mergers than the scenario with $\alpha = 0.5$. This is because the CE phase is shorter and we have less stellar merger because of the orbital shrinking.

At $\alpha = 3$, we have the maximum number of BBH merger, $\sim 1.7 \times 10^6$ events. This is the optimal value for the CE efficiency when it comes to producing merging BBHs. This is because, such an efficiency is strong enough to successfully eject the CE but also not high enough to prevents the binary from shrinking.

For higher values of the CE efficiency, $\alpha = 5, 10$ we find that the number of mergers increasingly decreases. We obtain $\sim 1.4 \times 10^6$ and 9.1×10^5 mergers, respectively. This is because such high level of efficiency of the CE phase means that it does not last enough to effectively shrink the orbit of the binary systems. Therefore, many of the system that were shrunk through the CE phase at lower values of α, now remain too loose to merge within a Hubble time. Finally, in the scenario where we assume the mass transfer to be always stable, we find $\sim 8.5 \times 10^5$ BBH mergers. This represents the smallest number of BBH mergers among the various BSE simulations and it is due to the inefficiency of the binary shrinking mechanism: fewer systems experience a common-envelope (CE) phase compared to other scenarios, while most depend on stable mass transfer (SMT) to decrease the binary's orbit and enable a BBH merger.

Overall, the efficiency of the CE phase plays a critical role in shaping the primary BH mass distribution of merging BBH systems. Lower values of α lead to fewer successful CE ejections and thus fewer BBH mergers, whereas higher values increase the number of successful ejections but may reduce the orbital shrinking needed for eventual mergers, especially at higher metallicities. The scenario with the MS assumed as always stable shows that even without a dominant CE phase, BBH mergers can still occur, though the resulting mass distribution differs significantly from those scenarios with frequent CE events.

4.4 Discussion

4.4.1 PPISN contribution to the $35\,M_\odot$ peak

After the release of GWTC-2, and even more clearly after GWTC-3, it became evident from the inferred primary BH mass distribution that there is a peak. As a result, the POWER LAW + PEAK fitting model has become the most commonly used approach for statistical analyses based on the gravitational wave (GW) signals we recover from BBH mergers (Abbott et al., 2021; Abbott et al., 2023). This peak appears at primary BH masses of approximately $34\,M_\odot$. However, the exact value of M_{BH} for this peak is highly dependent on the Bayesian analysis used, leading to several different proposed values (see Abbott et al., 2021; Abbott et al., 2023;

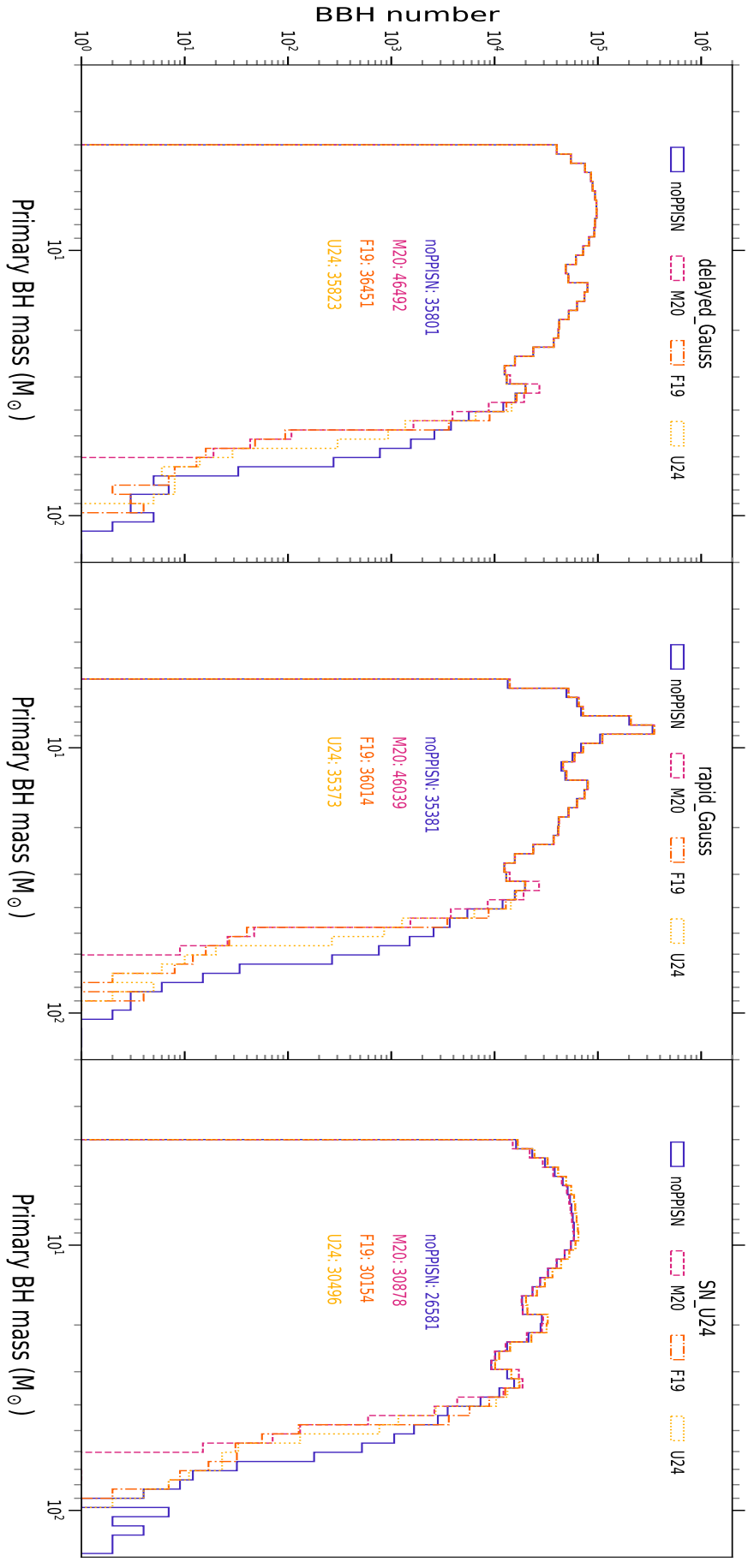

FIGURE 4.3: Primary BH mass distribution for different ccSNe prescriptions: `delayed_Gauss` (left panel), `rapid_Gauss` (central panel), and `SN_U24` (right panel). In each panel, the different histograms represent different PPISNe prescriptions: `noPPISNe` (blue solid line), `M20` (purple dashed line), `F19` (orange dot-dashed line), and `U24` (yellow dotted line). With the same color-lines are also displayed the number of BHs in the mass interval $32 - 37\,M_{\odot}$ for all the different PPISNe models. All the primary BH mass distributions shown in the various panels are obtained by fixing the value of the CE efficiency at the fiducial value $\alpha = 3$.

Sadiq, Dent, and Wysocki, 2022; Callister and Farr, 2023; Farah, Fishbach, and Holz, 2024, both from parametric and non-parametric models). Despite these differences, all proposed values consistently place it within the 32–37 $M_\odot$ mass interval.

Initially, the astrophysical explanation for the accumulation of BHs at this mass was attributed to the onset of pulsational pair-instability supernovae (PPISNe) in the primary star (see Talbot and Thrane, 2018; Stevenson et al., 2019; Belczynski et al., 2020; Karathanasis, Mukherjee, and Mastrogiovanni, 2023; Iorio et al., 2023). This phenomenon significantly affects the BH mass spectrum of massive stars, as it imposes an upper limit on mass and provides an additional mechanism for producing BHs in the mass range of 30–40 $M_\odot$. This degeneracy was believed to be the primary cause of the peak observed in GW data.

However, recent literature (see, e.g., van Son, Justham, and De Mink 2021; van Son et al. 2022; Briel, Stevance, and Eldridge 2023; Hendriks et al. 2023; Farrah et al. 2023; Farah, Fishbach, and Holz 2024) has highlighted other possible contributing factors to this peak. We will further discuss the role of these additional contributions in Section 4.4.2. In this section, we focus specifically on the contribution of PPISNe to the peak in the primary BH mass distribution.

In Figure 4.3 we show the primary BH mass distribution, obtained by aggregating all the simulated metallicities, for all the different SSE prescriptions and the fiducial value of the CE efficiency $\alpha = 3$.

The left panel shows the mass distribution for the `delayed_Gauss` model for core-collapse supernovae (ccSNe). The central panel displays results for the `rapid_Gauss` model, while the right panel presents the `SN_U24` model. Each panel includes the results for different PPISNe prescriptions: `noPPISN` (solid blue line), `M20` (dashed purple line), `F19` (dot-dashed orange line), and `U24` (dotted yellow line). Additionally, we show the number of merging BBH systems with primary masses in the range 32 – 37 $M_\odot$, using the corresponding colors for each PPISNe prescription.

In all panels, it is clear that the lower end of the BH mass spectrum is mainly influenced by the chosen ccSN model, as BHs with masses $\lesssim 30\,M_\odot$ form primarily through ccSNe. The left and middle panels highlight the differences between the two Fryer et al., 2012 prescriptions. In the `delayed_Gauss` scenario, we observe the formation of BHs slightly above the upper limit of the NS ($\sim 3\,M_\odot$). In contrast, in the `rapid_Gauss` model, we see a characteristic gap in the mass range 3–5 $M_\odot$, followed by a distinct peak at $\sim 10\,M_\odot$, consistent with the predictions of Fryer et al., 2012. In the right panel, for the `SN_U24` model, we find that fewer merging BBH systems are produced overall, but the distribution is otherwise similar to that obtained from the `delayed_Gauss` model. Furthermore, it is apparent that the impact of different PPISNe prescriptions becomes significant only for BH masses $M_{\rm BH} \gtrsim 30\,M_\odot$, and this influence is largely independent of the ccSN prescription. This is because PPISNe remnants are expected to directly collapse into BHs, with the final remnant mass depending only on the criteria for the onset of PPISNe and the mass loss due to pulsations.

In all panels of Figure 4.3, as discussed in Section 4.3.1, we find that the suppression of PPISNe (in the `noPPISN` scenario) results in a significant tail of massive BHs. In this scenario, BHs as massive as $\sim 80\,M_\odot$ are consistently produced, with some outliers exceeding $100\,M_\odot$. On the other hand, all PPISNe prescriptions introduce a sharp cut-off around $40\,M_\odot$, resulting in fewer than 0.5% of primary BHs in merging systems having masses above this threshold. Furthermore, in the mass range 32–37 $M_\odot$, an overabundance of BHs is consistently observed, regardless of the PPISNe prescription used. This peak is most pronounced in the `M20` model, which assumes a sharp transition at $M_{\rm HE} \geq 32\,M_\odot$, leading to additional BH accumulation. However, even in this case, PPISNe contribute only about 30% of BHs in the 32–37 $M_\odot$ mass range. Additionally, we observe roughly twice as many BHs in this range compared to the adjacent mass intervals (28–32 $M_\odot$ and 37–42 $M_\odot$). Therefore, there must be an additional

channel contributing to the formation of BHs in this specific mass range, which we will discuss in detail in the following section.

4.4.2 Formation channel of BBH in the peak

In the previous section, we discussed the role played by the various SSE prescriptions, focusing on the influence of the PPISN model on the primary BH mass distribution. We found that while different PPISNe prescriptions can lead to an accumulation of BHs in the peak-mass region (i.e. $32-37\,M_\odot$), this effect remains secondary.

In this section, we study the role that BSE processes play in shaping the BH mass spectrum.

In Figure 4.4, we show the contributions of the two main evolutionary channels for massive binary systems — binaries undergoing a CE event (purple lines) and binaries that evolve only through SMT (blue lines) — to the overall population of merging binaries (black lines). The Figure also illustrates the contribution of all metallicities in the catalog (solid lines) and the metal-poor population (dashed lines), defined as stars with $Z \leq 5\times10^{-4} \sim 0.03\,Z_\odot$. All panels represent simulations with the fiducial CE efficiency of $\alpha = 3$.

Each panel of Figure 4.4 present a different combination of SSE models for ccSNe and PPISNe. As discussed in Section 4.3.1, these combinations affect the BH mass distribution, and Figure 4.4 shows that the CE and SMT channels contribute differently to the primary BH mass distribution across the different models. The CE channel is particularly effective in producing the low-mass BHs, especially with $M_{\rm BH} \lesssim 15\,M_\odot$, and its contribution is relatively independent of metallicity for these lower masses. On the other hand, the SMT channel becomes significant only for $M_{\rm BH} \gtrsim 10\,M_\odot$, and it surpasses the CE channel for $M_{\rm BH} \gtrsim 20\,M_\odot$, becoming the main contributor to the more massive BH population.

A distinct behavior emerges for $M_{\rm BH} > 30\,M_\odot$. The CE channel produces BHs more evenly distributed across the mass spectrum, except in the case of the `M20` PPISNe model, as discussed in Section 4.3.1. On the other hand, the SMT channel shows a valley below $\sim 30\,M_\odot$, followed by a bump in the 32–37 $M_\odot$ range. This is suggesting a preference for forming BHs in this specific mass interval. Such a finding aligns well with the recent work by van Son et al., 2022; Briel, Stevance, and Eldridge, 2023. We also investigated the effect of CE efficiency on the primary BH mass distribution. In Figure 4.5, we present the primary BH mass distribution for the fiducial treatment of ccSNe and PPISNe (`delayed_Gauss` + `M20`) for $\alpha = 0.5, 1, 3, 5, 10$, as well as for the scenario in which MT is assumed to be always stable. Note that in this latter scenario, the CE onset is strongly suppressed, although a CE phase may still be triggered if both stars overfill their RL, in which case the CE efficiency is set to $\alpha = 3$.

Figure 4.5 shows both CE and SMT channels (purple and blue lines, respectively) for all simulated metallicities (solid lines) and metal-poor stars (dashed lines). The total primary BH mass distribution is also represented (black solid line).

In the upper left panel, we show the results for $\alpha = 0.5$. In this scenario the CE ejection is not very efficient (see Sec. 4.3.2, resulting in a lower number of BBH mergers. However, the CE phase is very efficient at shrinking the binary's orbit, making the CE channel the dominant mechanism for BBH mergers, and shaping the primary BH mass distribution. Almost all the primary BHs with $M_{\rm BH} \leq 10\,M_\odot$ are formed in systems that undergo at least one CE phase. Such systems are mainly produced by the binaries with $Z \geq 5\times10^{-4}$. Furthermore, the CE channel is also the main contributor to the bump at $32-37\,M_\odot$, though only slightly, as $\sim 53\%$ of the primary BHs contributing to the peak come from binaries with at least one CE event. It also apparent from Figure 4.5 that the two channels are degenerate in the mass interval $32-34.5\,M_\odot$, while the CE channel produces significantly more BHs with masses $35-37\,M_\odot$. On the other hand, SMT produces an accumulation of BHs in the interval between $\sim 13\,M_\odot$ and $\sim 22\,M_\odot$, accounting for $\sim 65\%$ of the merging primary BHs formed through SMT. Furthermore, it is apparent from Figure 4.5 that the $32-37\,M_\odot$ mass interval is

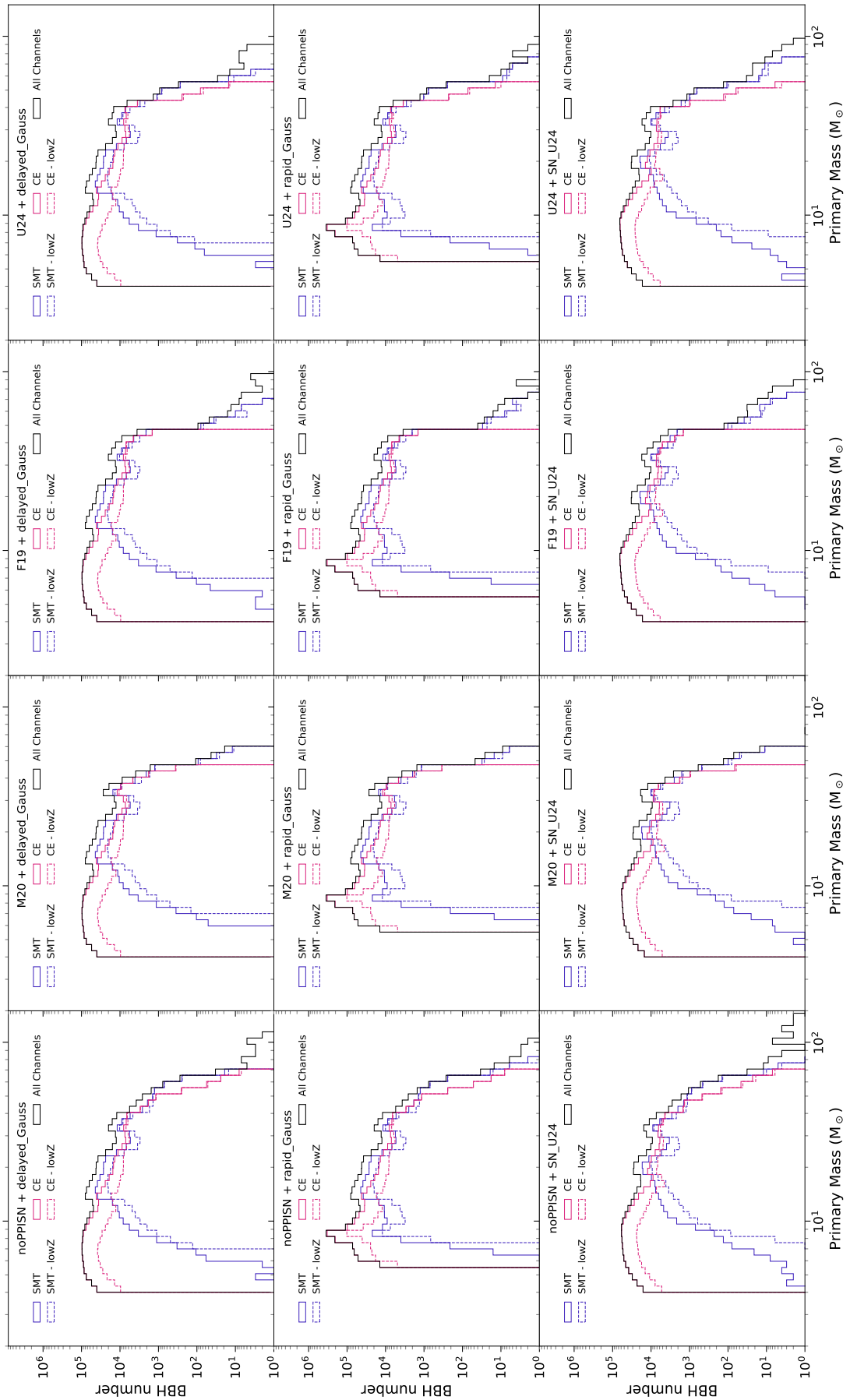

FIGURE 4.4: Primary BH mass distribution of BBH merging system in our simulation. From left to right: each row shows a different prescription for ccSNe (`delayed_Gauss` on the top row, `rapid_Gauss` on the central row, and `SN_U24`) on the bottom row), while each column shows a different treatment PPISNe (`noPPISN` on the first column, `M20` on the second column, `F19` on the third column, and `U24` on the fourth column). In each panel are shown the primary BH masses for the different evolutionary channels. We show the primary BH mass of the systems undergoing at least a CE phase (purple lines), both for metal-poor stars (i.e. $Z \leq 0.0005 \sim 0.03Z_{\odot}$, purple dashed line) and among all the simulated metallicities (see Table 4.1, solid purple line). We also show the primary BH masses of the systems that never enter a CE phase, i.e. those system that experience only SMT during their evolution as a binary, both for metal poor (blue dashed line) and the total simulated population (blue solid line). Finally, we show also the primary BH mass distribution for the whole simulated population (black solid line).

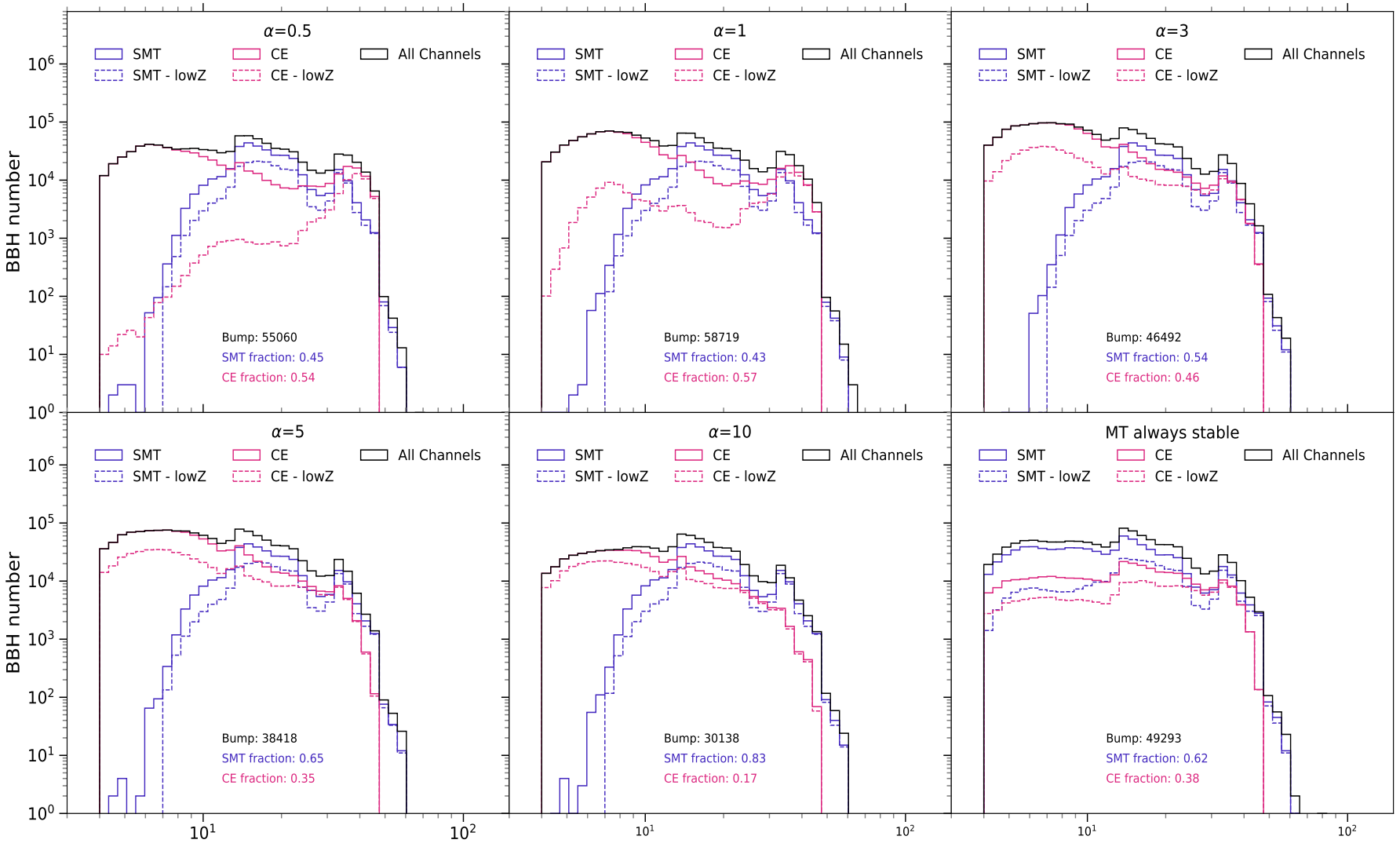

FIGURE 4.5: Primary BH mass distribution of BBH merging system in our simulation. Each plot shows the results we obtain for a different CE efficiency α. Upper panels, from left to right: $\alpha = 0.5,\ 1,\ 3$. Lower panels, from left to right: $\alpha = 5,\ 10$, and the scenario in which the mass transfer is assumed as always stable. In each panel, we show the primary BH mass distribution depending on the evolutionary channel leading to the BBH merger such as the SMT (blu lines) and the CE (purple lines). We also display the results for the metal-poor binaries (dashed lines) and for the total population (solid lines). Finally, we show also the total primary BH mass distribution, built considering all the possible BSE processes.

a region where primary BHs, that went through SMT during their life in the binary, tends to accumulate. In the 32–37 $M_\odot$ range, around 7% of BHs are formed, while the neighboring intervals (27–32 $M_\odot$ and 37–42 $M_\odot$) contribute around 3% and 2%, respectively.

In the upper middle panel, we show the results we obtain for $\alpha = 1$. In this scenario, the CE phase is slightly less efficient in shrinking the binaries compared to $\alpha = 1$, but more systems successfully eject the shared envelope. This leads to a greater number of mergers in general, as we discussed in Sec. 4.3.2.

The behavior for lower-mass BHs is similar to $\alpha = 0.5$, with the CE channel being dominant for $M_{\rm BH} \lesssim 12\,{\rm M}_\odot$ and remaining relevant up to $\sim 14\,{\rm M}_\odot$. Furthermore, the number of mergers with primary BHs in the $32 - 37\,{\rm M}_\odot$ mass interval is increased by $\sim 7\%$, with the CE channel again being the dominant contributor, constituting 57% of the systems in the bump. Nonetheless, as we found for $\alpha = 0.5$, the two channels are degenerate in the mass interval $32 - 34.5\,{\rm M}_\odot$, while the CE channel produces more BHs for $M_{BH} \in [35, 37.5]$.

On the other hand, the population of primary BHs produced through the SMT channel does not depend on the efficiency of CE, since these systems do not undergo CE phases. Therefore, we retrieve the same properties we found for $\alpha = 0.5$.

For $\alpha = 3$ (upper right panel), we fint the maximum number of most merging BBHs, as discussed in Sec. 4.3.2. However, in the primary BH masses produced by binaries experiencing at least on CE event, we see a shift toward lower BH masses. The CE remains the dominant channel up to $M_{\rm BH} \sim 16\,{\rm M}_\odot$. Furthermore, in this scenario the $32 - 37\,{\rm M}_\odot$ bump is primarily populated by BHs produced in systems that evolve through the SMT channel. Such systems now account for 54% of the BHs in the $32 - 37\,{\rm M}_\odot$ mass interval, with both channels contributing similarly in the $35 - 37\,{\rm M}_\odot$ mass range.

In the lower left panel, we show the primary BH distribution for $\alpha = 5$. In this scenario, the CE ejection is highly efficient, leading to a reduced efficiency in shrinking binaries. Therefore, there are fewer BBH mergers compared to previous cases (see also Section 2.2.2).

The CE channel remains the primary contributor for BBH mergers with primary BH masses $\leq 14\,{\rm M}_\odot$. On the other hand, the SMT channel produces BHs dominates the $16 - 22\,{\rm M}_\odot$ and $32 - 34.5\,{\rm M}_\odot$ mass intervals. In this latter, we find that 65% of the systems have evolved without experiencing a CE phase, i.e. are produced by SMT-binaries. In turn, the system that populated this mass interval which evolved through CE are decreasing. This is because they not able to merge within a Hubble time since the CE is promptly ejected, and thus the system's semi-major axis remain too big to allow for a BBH merger.

In the lower central panel, we show the results for $\alpha = 10$. CE-binaries mainly produce primary BHs with mass $\leq 15\,{\rm M}_\odot$, while SMT-binaries dominate the at higher mass range, shaping the primary BH mass distribution. Furthermore, we find that 83% of the systems never triggered a CE episode. Additionally, the shape of the primary BH mass distribution is very close to the scenario with $\alpha = 0.5$, with also a similar number of BBH mergers. The main difference is the broadness of the primary BH mass peak, that for higher α is concentrated between $32\,{\rm M}_\odot$ and $34.5\,{\rm M}_\odot$, while for lower α extends up to $37\,{\rm M}_\odot$.

Finally, in the lower right panel we present the scenario where mass transfer is always assumed to be stable. As discussed in Sec. 4.3.2 this assumption does not entirely prevent CE phases, which may still occur if both stars overfill their RL. When a CE phase is triggered it is treated with the usual energy formalism, with an efficiency value $\alpha = 3$. In this scenario, the CE channel becomes a secondary contributor, with even the least massive BHs now being formed through SMT. Interestingly, the CE channel still plays a role in forming the most massive BHs, contributing 38% of the primary BHs in the bump mass interval.

Therefore, our analysis indicates that the CE and SMT channels play distinct but complementary roles in shaping the primary BH mass distribution. The CE channel is most effective for forming lower-mass BHs, while the SMT channel dominates at higher masses, particularly

in the 32–37 $M_\odot$ peak region. These findings highlight the complex interplay between different binary evolutionary processes in determining the characteristics of the BH mass spectrum.

4.4.3 Progenitors of the systems in the peak

In the previous section, we showed the role that CE efficiency plays in shaping the primary BH mass distribution. In this section, we will study the properties of the systems that contribute to the bump in the 32–37 $M_\odot$ mass range.

In Figure 4.6 and Figure 4.7, we show the distribution of the evolutionary phases of the two stars of the binary at the onset of the first SMT (blue bars) and of the first CE (purple bars) event. Figure 4.6 shows the results for the metal-poor population ($Z \leq 5 \times 10^{-4}$). We find that the first SMT episode typically occurs when the primary star is a core-helium burning (CHeB) star and the secondary is still on the main sequence (MS). A secondary, less common channel occurs when both stars are on the MS at the onset of SMT, accounting for $\lesssim 30\%$ of bump-BHs formed through SMT.

On the other hand, the bump-BHs produced through CE experience such a phase mainly when both stars of the binary are in the CHeB stage. However, as illustrated in the various panels of Figure 4.6, other combinations of evolutionary phases are also present, even though they are not significantly influenced by CE efficiency, apart from the number of events (see Section 4.4.2 for more details). For the various CE efficiencies (upper-row panels and left and middle panels of the bottom row of Figure 4.6), a fraction of the CE events takes place for different evolutionary stages of the stars. The most common of these is the combination of a black hole (BH) and a CHeB star, indicating that the primary has already collapsed into a BH before the first CE episode which accounts for $\gtrsim 50\%$ of the non CHeB + CHeB events for $\alpha \leq 5$.

Other, less frequent scenarios include, in order of occurrence, terminal core-helium burning (TCHeB, where the star has begun forming a CO core) + CHeB, CHeB + MS, and TCHeB + MS. The latter two combinations typically result from stellar collisions, where the stars' radii overlap at periastron (see Iorio et al., 2023 for more details). Furthermore, we find that the CHeB + MS scenario becomes the second most efficient combination for $\alpha = 10$, instead of the BH + CHeB scenario.

In the scenario where MT is assumed to be always stable (bottom right panel of Figure 4.6), we retrieve features similar to the case for $\alpha = 10$, although the number of events is higher. This is because, even for systems that only experience SMT, a CE event can still be triggered if both stars fill their Roche lobe (RL), which occurs mainly for CHeB + CHeB binaries. Figure 4.7 presents the combination of evolutionary stages for the bump-binaries, now accounting for all simulated metallicities (see Table 4.1).

Comparing Figures 4.6 and 4.7, it is apparent—as previously shown in Figure 4.5—that systems evolving only through SMT and forming primary BHs in the bump mass range are primarily produced by metal-poor binaries. On the other hand, bump-primaries formed through CE events exhibit a metallicity dependence that is coupled with CE efficiency. We find that for $\alpha = 0.5,\ 1$ a significant fraction of the total BHs in the $32 - 37\,\mathrm{M}_\odot$ mass interval are produced by systems with $Z \geq 5 \times 10^{-4}$. However, for higher values of the CE efficiency ($\alpha = 3,\ 5,\ 10$) the bump-primary BHs formed through CE episodes are formed mainly by metal-poor stellar progenitors, a result similar to the scenario where MT is always stable. This tendency is primarily due to the effect of stellar winds, which influence both the semi-major axis of the binary's orbit (see Section 1.2.2) and the stripping of hydrogen envelopes. Together, these effects prevent both stars from simultaneously filling their RL.

We also studied the mass distribution of the bump-binaries. In Figure 4.8, Figure 4.9, and Figure 4.10, we show both the primary (solid lines) and the secondary (dashed lines) masses, both at the ZAMS (first row of each Figure) and at the occurrence of the first event (second row

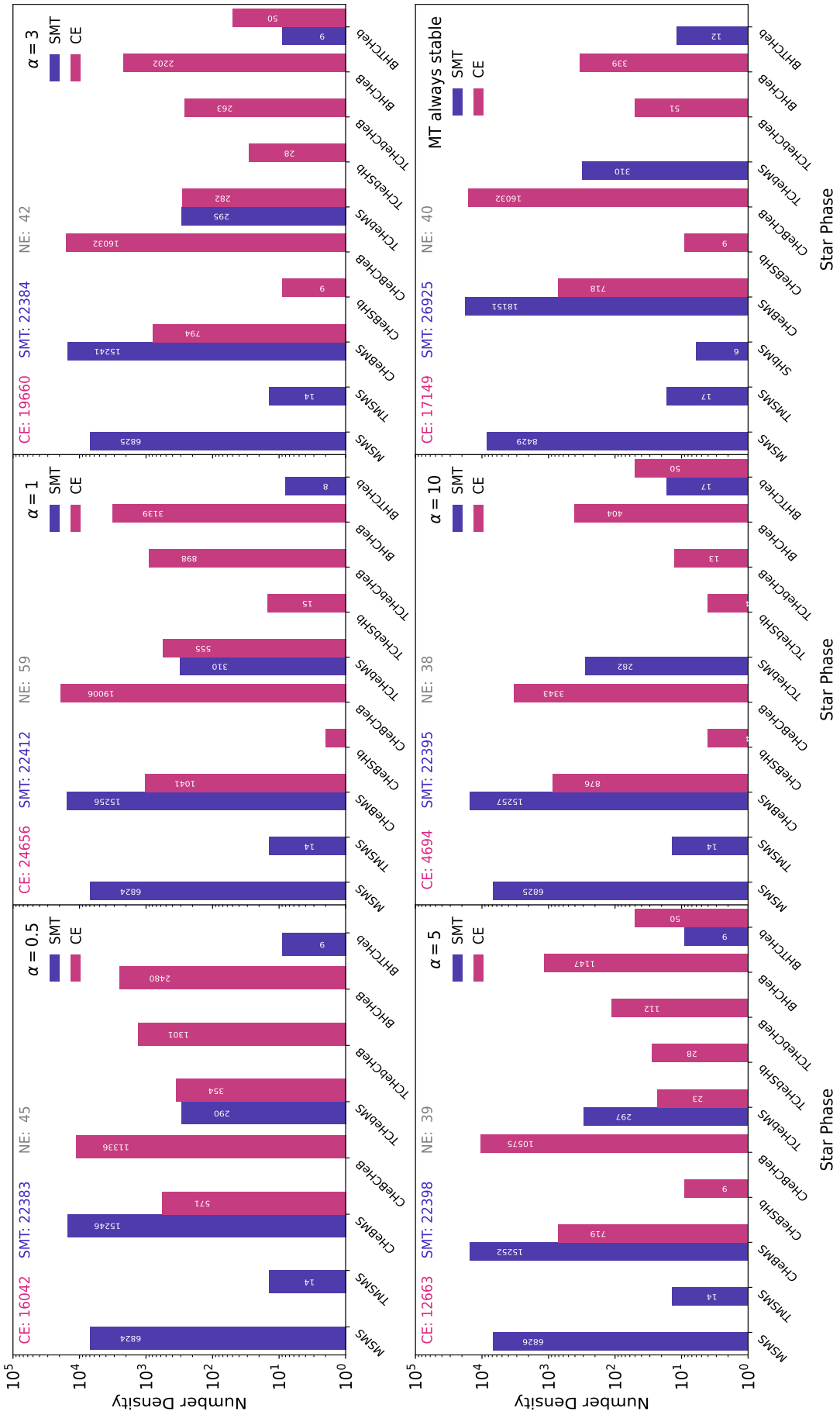

FIGURE 4.6: Distribution of phases of primary and secondary stars at the onset of the first SMT (blue bars, we show in white the number of events) or CE (purple bars, we show in white the number of events) event, for the metal-poor binary systems ($Z \leq 0.0005$). Each panel shows results for a different CE efficiency, α, and in the top left corner of each panel are shown the number of systems in the bump per channel (CE in purple, SMT in blue). Upper panels, from left to right: $\alpha = 0.5$, 1, and 3. Lower panels, from left to right: $\alpha = 5$, 10, and the scenario where mass transfer is always stable.

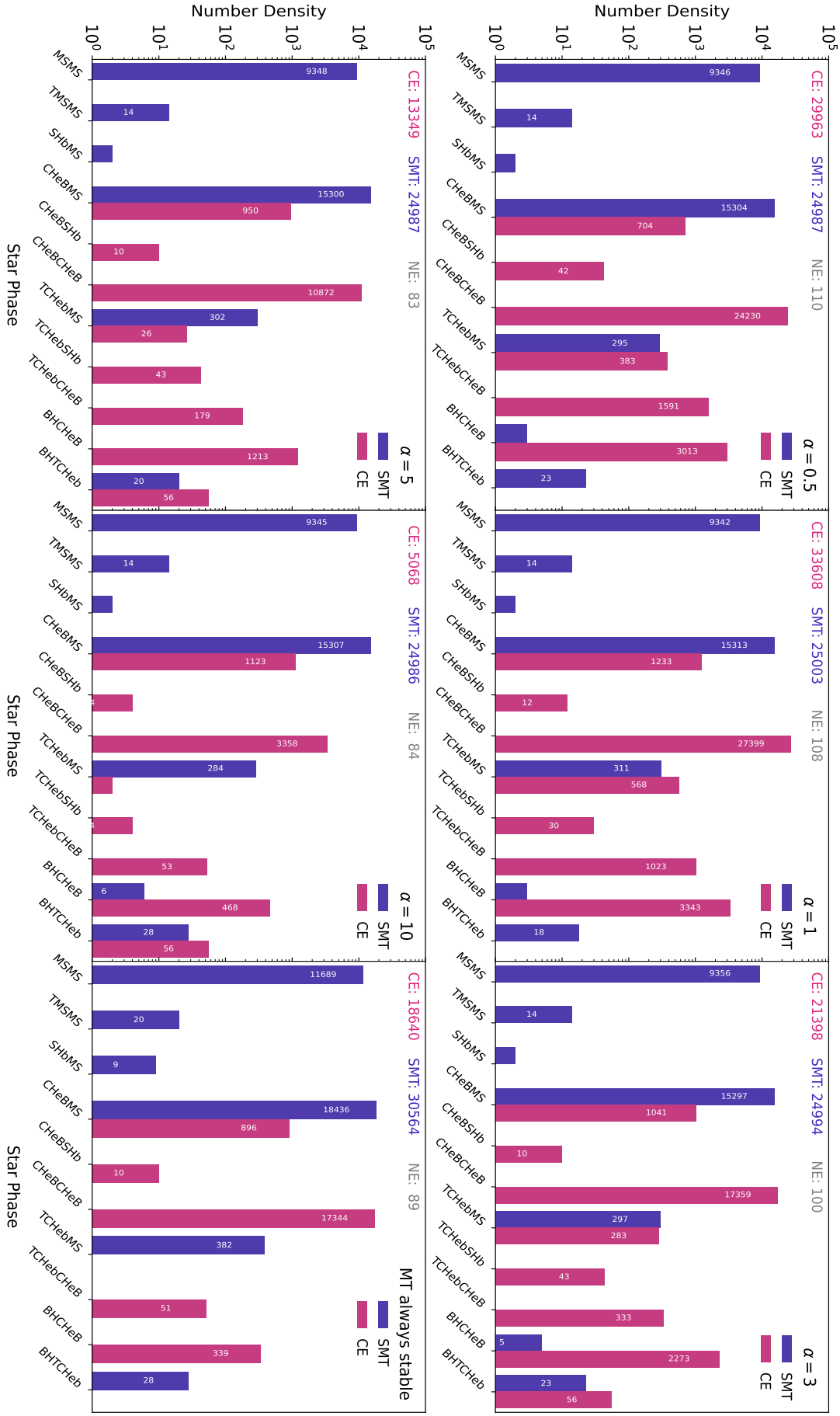

FIGURE 4.7: Same as Figure 4.6 but aggregated for all the metallicities range, see Table 4.1.

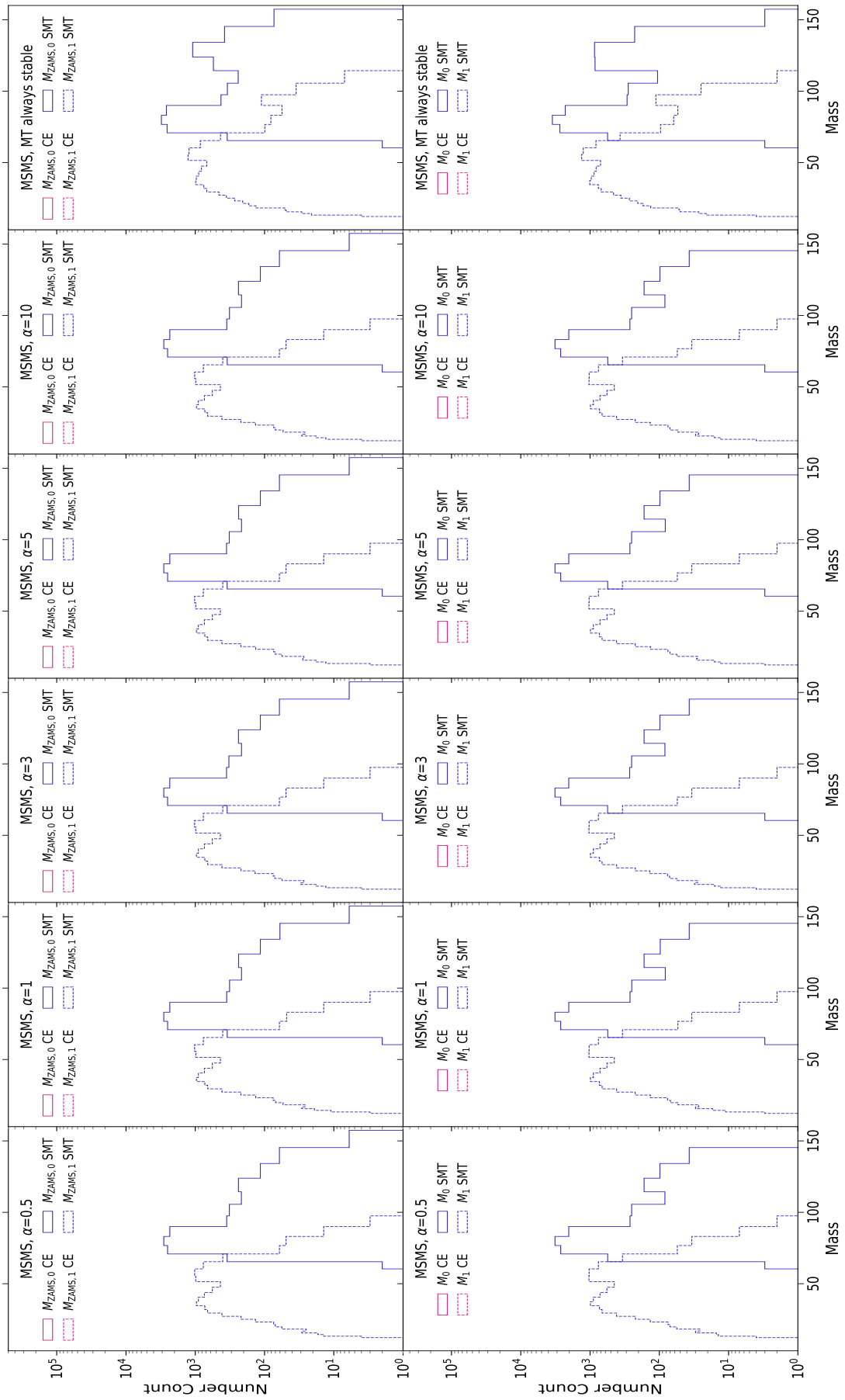

FIGURE 4.8: Distribution of masses of primary and secondary stars at the onset of the first SMT (blue) or CE (purple) event (first row), and at the ZAMS for different phases (bottom rows). In this Figure we show the one three most populated configurations: MSMS in the first (masses at the ZAMS) and second (masses at the onset of SMT or CE) rows. Each panel shows results for a different CE efficiency, α. From left to right: $\alpha = 0.5$, 1, 3, 5, 10, and the scenario where mass transfer is always stable.

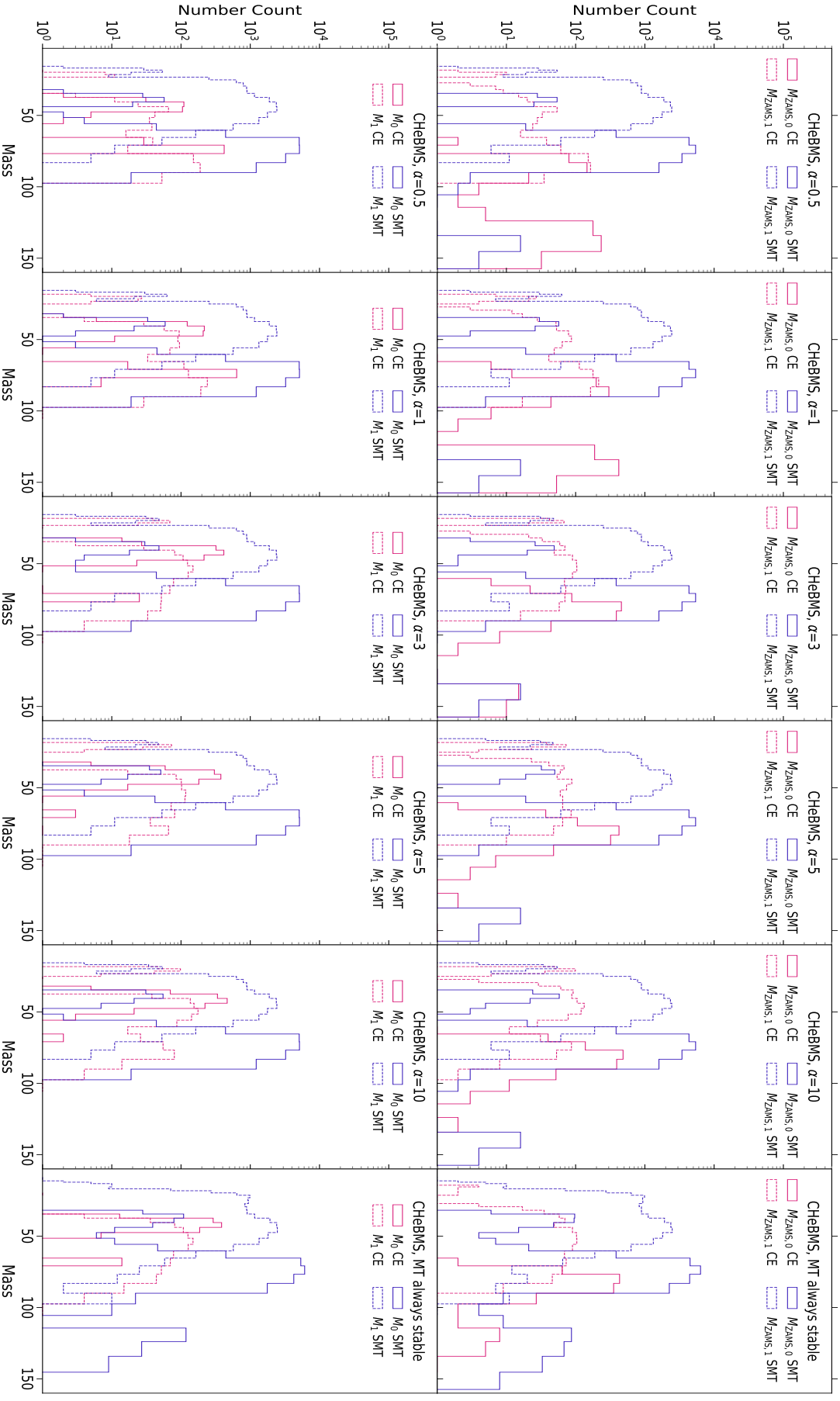

FIGURE 4.9: Same as Figure 4.8 but for systems in the CHeBMS configuration.

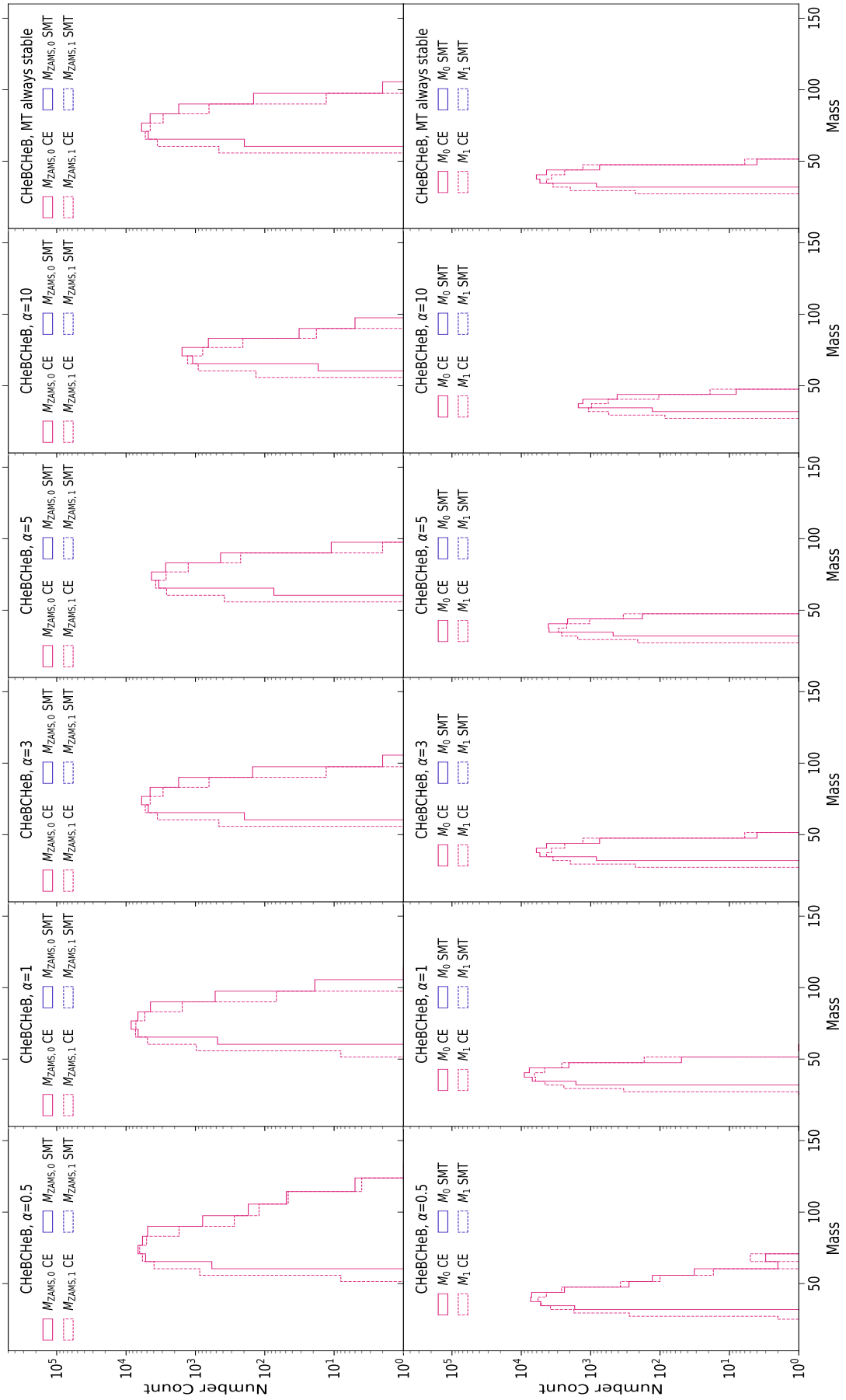

FIGURE 4.10: Same as Figure 4.9 but for progenitors in the CHeBCHeB configuration.

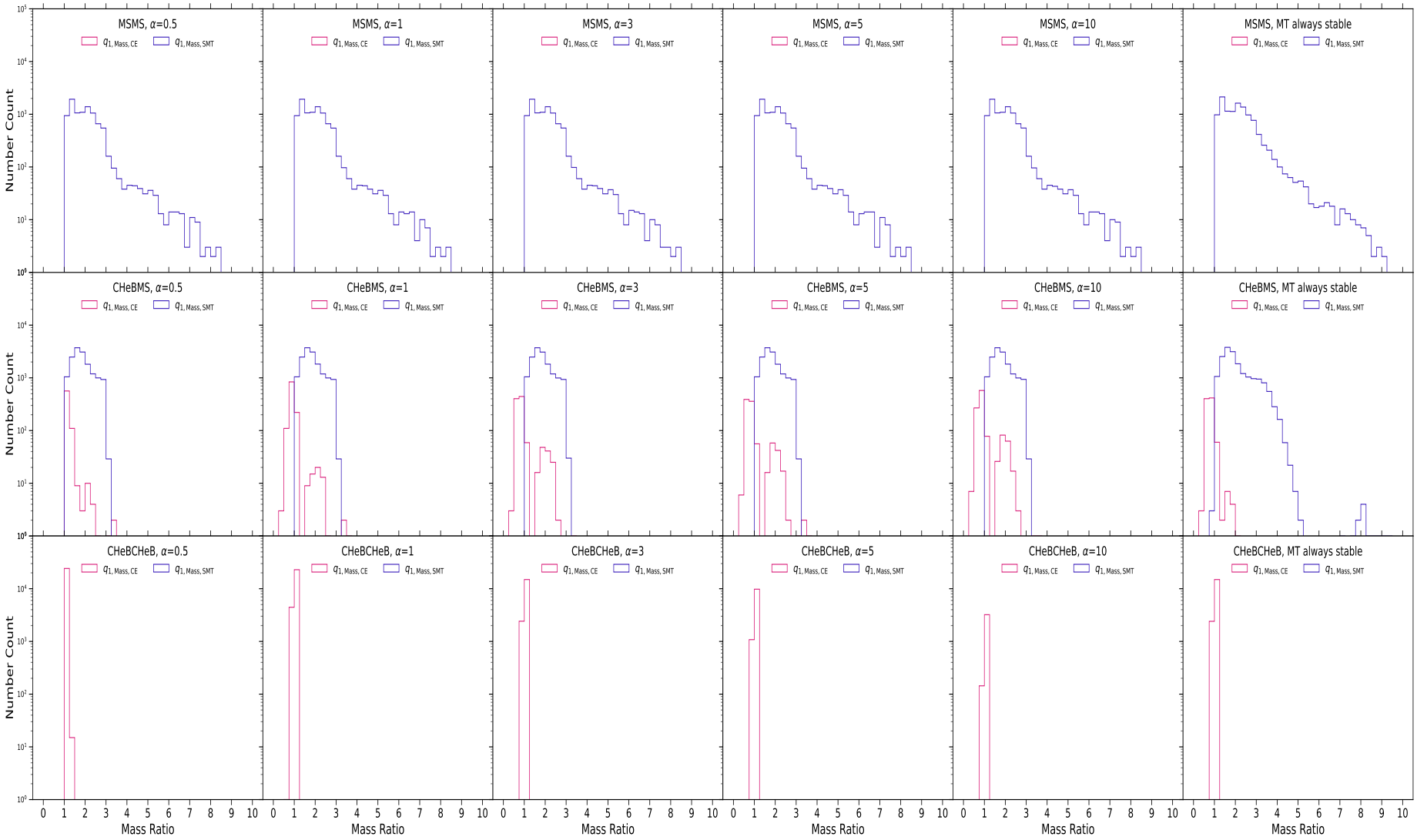

FIGURE 4.11: Distribution of mass ratios (computed as $q = M_{\mathrm{ZAMS},0} / M_{\mathrm{ZAMS},1}$) at the onset of the first SMT (blue) or CE (purple) event (even rows), and at the ZAMS for different phases (odd rows). We show the three most populated configurations: MSMS in the first row, CHeBMS in the second row, and CHeBCHeB in the third row. Each panel shows results for a different CE efficiency, α. From left to right: $\alpha = 0.5$, 1, 3, 5, 10, and the scenario where mass transfer is always stable.

of each Figure). The figures show combinations of evolutionary stages that mainly contribute to the two evolutionary paths: MS + MS in Figure 4.8, and CHeB + MS in Figure 4.9 for SMT binaries, and CHeB + CHeB in Figure 4.10 for CE binaries. We distinguish also the evolution channel (either CE or SMT, in purple and blue lines, respectively). Furthermore, each column shows results for a different CE efficiency $\alpha = 0.5,\ 1,\ 3,\ 5,\ 10,$ and the scenario where the MT is assumed to be always stable.

In Figure 4.8, we show the mass distribution of the primary and secondary stars of the bump-binaries undergoing SMT when both stars are on the MS. For this stars the mass distribution does not vary significantly, between the ZAMS and the first SMT episode. We find that the primaries have masses mainly in the $70 - 90\,M_\odot$ mass interval, with the the secondary stars having masses in the $30 - 50\,M_\odot$ mass interval. Furthermore, primary stars show a tail towards higher masses, with a non-negligible number of binaries having $M_{\mathrm{ZAMS},0} \geq 100\,M_\odot$. A similar trend is observed for secondary masses, with a tail extending to $M_{\mathrm{ZAMS},1} \geq 70\,M_\odot$.

In Figure 4.9 we show the mass distributions for CHeB + MS binaries, the most common bump-producing combination for SMT. These results are similar to the MS + MS scenario, though the tail towards higher masses is less populated. This is the most populated combination of bump-binaries that evolve through SMT.

We find that the results for the SMT binaries are close to the MS + MS scenario. The primary masses at the ZAMS are clustered between $70 - 90\,M_\odot$, while secondary stars have masses in the interval $30 - 60\,M_\odot$ with a tail that extends to $M_{\mathrm{ZAMS},1} \sim 90$. However, at the onset of the SMT the tail of the primary stars disappears, and all the masses are concentrated in the $70 - 90\,M_\odot$ mass interval.

The CE systems, though few in number, show a bimodal distribution both at ZAMS and at the onset of CE events. For $\alpha \leq 1$, primary star masses at ZAMS are concentrated in the intervals $60 - 90\,M_\odot$ and $120 - 140\,M_\odot$, with the secondary masses are distributed roughly uniformly between $40\,M_\odot$ and $90\,M_\odot$. At the onset of CE, primary mass distributions show again bimodality, with most masses in the intervals $40 - 60\,M_\odot$ and $70 - 90\,M_\odot$ for $\alpha = 0.5$ and $40 - 50\,M_\odot$ and $70 - 80\,M_\odot$ for $\alpha = 1$. The mass distribution of secondary stars exhibits a similar behavior, with a bimodality around the mass intervals $30 - 50\,M_\odot$ and $70 - 80\,M_\odot$ for $\alpha = 0.5$ and $30 - 60\,M_\odot$ and $70 - 100\,M_\odot$ for $\alpha = 1$. On the other hand, for $\alpha \geq 3$, the mass of the primary stars at the onset of the CE is clustered in the interval $30 - 50\,M_\odot$. We find the same result for the scenario with the MT always stable. Furthermore, for the high CE efficiencies, we find that the secondary stars are either rather light, clustered around masses of $\sim 20\,M_\odot$ with a secondary peak between $40\,M_\odot$ and $60\,M_\odot$.

In Figure 4.10, we show the mass distributions for CHeB + CHeB bump-binaries. In this scenario, CE events are always triggered. We find that the mass distributions do not depend on CE efficiency, either at ZAMS or at the onset of CE.

In Figure 4.10, we show the primary and secondary mass distributions at the ZAMS and at the onset of the first event for CHeB + CHeB bump-binaries. For this configuration of evolutionary stages of the two stars, see also Figure 4.6 and Figure 4.7, we have only binaries that trigger at least one CE episode. We find that mass distributions do not depend on the CE efficiency, both at the ZAMS and at the onset of the CE. Therefore, we find that to produce primary BHs in the bump mass interval, both stars must have formed at ZAMS with a mass ratio close to 1 (see Figure 4.11) and masses in the range $60 - 100\,M_\odot$, primarily clustered between $70 - 90\,M_\odot$. At the onset of the CE event, the star masses are concentrated between $30 - 50\,M_\odot$, again with mass ratio ~ 1.

Finally, we studied the mass ratios between primary and secondary stars at the onset of the first event. In Figure 4.11 we illustrate the results. The mass ratio q is computed as

$$q = \frac{M_0}{M_1} \tag{4.7}$$

where M_0 and M_1 are the primary and the secondary masses, respectively.

We show the mass ratios at the onset of the first SMT (in blue) or CE(in purple) event, for the same evolutionary stages (MS + MS, CHeB + MS, and CHeB + CHeB) discussed in Figure 4.6 and 4.7. The various columns in Figure 4.11 show the results for different CE efficiencies: $\alpha = 0.5,\ 1,\ 3,\ 5,\ 10,$ and the stable MT scenario.

In the first row of Figure 4.11, we show the mass ratio distribution for the bump-binaries that have the first SMT episode at the MS + MS evolutionary stage of the binaries. We find that mass ratios are clustered in the interval $1 - 2.5$, consistent with the mass distribution of primary and secondary stars (see second row of 4.8), including for the tail towards more extreme mass ratios.

In the second row of Figure 4.11, we present the mass ratio distribution of SMT and CE binaries that have the first event as CHeB + Ms. For binaries that undergo SMT, we find that mass ratios are clustered in the interval $1.5 - 2$, without the extreme tails observed in the MS + MS scenario. This result matches the mass distributions shown in the second row of Figure 4.9, with primary stars concentrated in the $70 - 90\,M_\odot$ mass interval and secondaries stars between $30\,M_\odot$ and $50\,M_\odot$. For CE binaries, we find a bimodal mass ratio distribution, with a primary peak centered at $q \sim 1$, and a less populated second bump ($\sim 10\%$ of CE binaries) at $q \sim 2$. However, this latter peak depends on CE efficiency and is more prominent for $\alpha \geq 3$. Furthermore, some binaries have an inverted initial mass ratio $q \sim 0.5$ at the onset of the CE, indicating a previous SMT episode where the primary was the donor. In the scenario where MT is always stable, we find a tail towards extreme mass ratios for SMT binaries, while the second peak in the CE mass ratio distribution is suppressed.

In the third row of Figure 4.11, we show the mass ratio distribution for bump-binaries that trigger undergo CE as CHeB + CHeB stars. We find that most of the binaries($\sim 85\%$ of the CHeB+ CHeB binaries in the bump) have q in the interval $1 - 1.25$. The secondary component of the mass ratio distribution correspond to $0.75 \leq q \leq 1$. These latter are the system that underwent SMT before the onset of the CE episode.

4.4.4 Effect of a top-heavy IMF

In the previous section, we presented the initial mass distribution of the bump-binaries, both at the ZAMS and at the onset of the first SMT or CE event. We found that the progenitors of these systems are massive, with the primary stars having $M_{\rm ZAMS} \geq 70\,M_\odot$. Therefore, the choice of IMF used to generate the initial conditions plays a significant role in determining the number of primary BHs produced in the $32 - 37\,M_\odot$ mass interval.

In this section, we present the results obtained by generating the stellar population using a top-heavy IMF. While we chose a Larson IMF (see Larson, 1998), it is worth mentioning that this IMF is generally used for Population III stars, and applying it across all metallicities in our simulations may be an extreme assumption. Nevertheless, the Larson IMF allows us to explore the effects of favoring the formation of massive stars. In this case, Equation 4.1 takes the form:

$$\mathrm{pdf}(M_{\rm ZAMS,1}) \propto M_{\rm ZAMS,1}^{-2.3} e^{-M_c / M_{\rm ZAMS,1}} \quad \text{with} \quad M_{\rm ZAMS,1} \in [8, 150] \tag{4.8}$$

where M_c is the mass cut in the exponential termset to $M_c = 30\,M_\odot$. This IMF favors the formation of more massive stars, resulting in more BBH mergers overall, and significantly more primary BHs in the bump mass interval. Other initial conditions are drawn according to the fiducial set of parameters (see Section 4.2.1).

In Figure 4.12, we show the primary BH mass distribution of simulations using the Larson IMF for various CE efficiency, $\alpha = 3,\ 5,\ 10$. We distinguish systems that undergo at least on CE event (purple lines) from those that only experience SMT (blue lines). We also display the

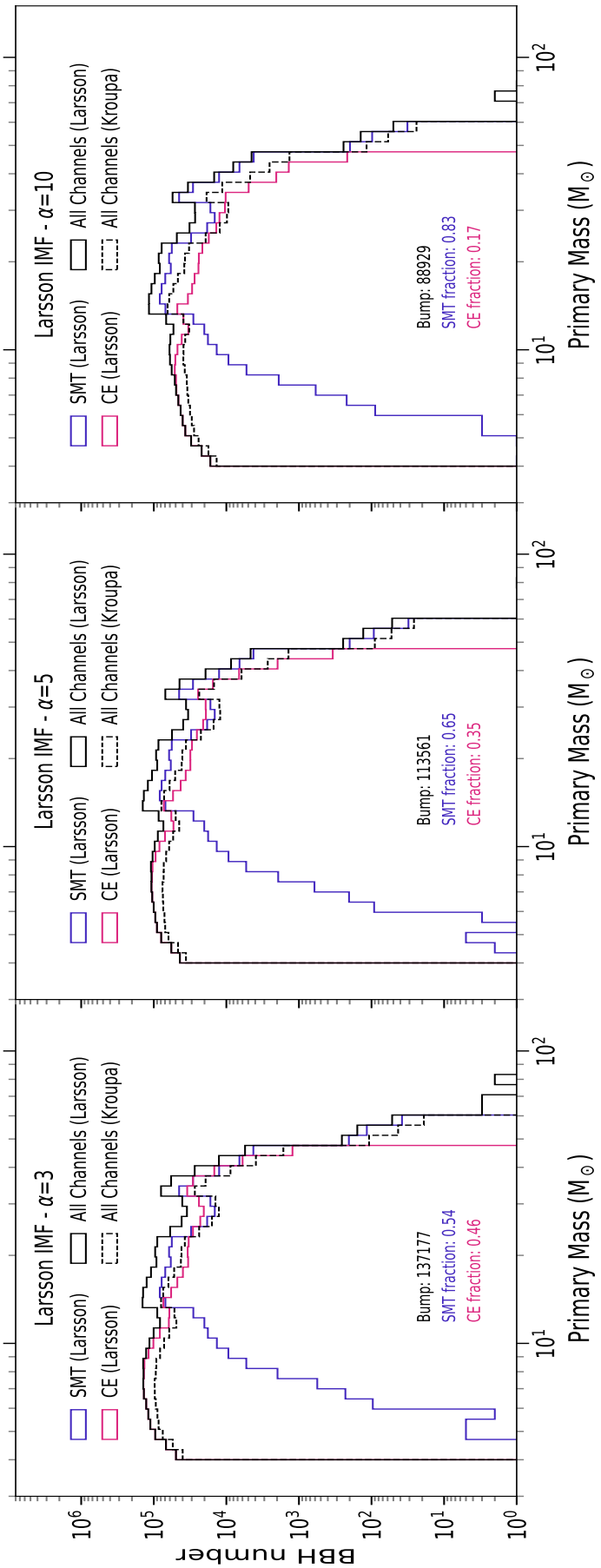

FIGURE 4.12: Primary BH mass distribution of BBH merging system in our simulations for a Larson initial mass functions. Each plot shows the results we obtain for a different CE efficiency α, from left to right: $\alpha = 3$, 5, 10. In each panel, we show the primary BH mass distribution depending on the evolutionary channel leading to the BBH merger such as the SMT (blue lines) and the CE (purple lines). Finally, we show also the total primary BH mass distribution, built considering all the possible BSE processes for the Larson-IMF (black solid line) and for the Kroupa-IMF (black dashed line).

aggregated primary BHs population of BBH mergers both for the fiducial Kroupa IMF (black dashed line) and for the Larson IMF (black solid lines).

In the left panel, we show the results for $\alpha = 3$. Similar to the Kroupa IMF scenario (see 4.3.2), primary BHs from SMT-binaries accounts for 54% of the bump population, while those formed through at least one CE phase make up 46% of the BHs in the bump. Furthermore, we find that the Larson IMF produces significantly more BBH mergers overall - approximately 67% more - particularly in the bump mass interval, where we observe ~ 3 times as many mergers. On the other hand, with a Larson IMF the number of low-mass primary BHs produced does not increase significantly.

In the central panel, we present the primary BHs mass distribution for $\alpha = 5$. For this CE efficiency, the evolution of systems contributing to the bump is similar to that of a population generated using a Kroupa IMF (see Section 4.3.2). Thus, 65% of the primary BHs in the $32 - 37\,M_\odot$ mass interval are formed in binaries that experience only SMT during their evolution making them the dominant contributor to the bump. On the other hand, primary BHs from CE binaries account for 35% of the bump population. However, with a Larson IMF the absolute number of primary BHs in the $32 - 37\,M_\odot$ mass interval increases significantly. Similarly to the $\alpha = 3$ scenario, also for $\alpha = 5$ we find ~ 3 times more BHs in the bump-mass interval, while the total number of mergers increases by 68%.

In the right panel, we show the primary BH mass distribution for $\alpha = 10$. As found for the Kroupa IMF (see Section 4.3.2), the $32 - 37\,M_\odot$ mass interval is dominated by the primary BHs produced in binaries that never undergo a CE phase, experiencing only SMT throughout their life, and they constitute 83% of the primary BHs in the bump-mass interval. Once again, as for $\alpha = 3,\ 5$, we find that the sheer number of primary black holes (BHs) in the $32 - 37\,M_\odot$ mass interval is approximately three times the number obtained with a Kroupa IMF, while the total number of BBH mergers is increased by $\sim 80\%$.

Therefore, we find that the net effect of a top-heavy IMF, such as the Larson IMF, is to increase the total number of BBH merger. This effect is particularly pronounced for BHs in the $32 - 37\,M_\odot$ mass interval. With a Larson IMF, we find roughly three times as many BHs in this interval compared to a population generated using a Kroupa IMF, while the total number of mergers increases by $67 - 80\%$ depending on α.

4.4.5 A possible metric to estimate astrophysical processes from the primary BH distribution

In the previous section, we presented the results obtained using a top-heavy IMF. In this section, we introduce a potential metric that may help in breaking some of the degeneracies identified in our analysis.

In Figures 2.2.2 and 4.12, we showed the effects of different BSE prescriptions and of the use of a top-heavy IMF on the primary BH mass distribution. We found that high CE efficiencies ($\alpha \geq 5$) suppress the formation of primary BHs in the bump-mass interval through CE, leaving only BHs formed by binaries that evolve exclusively through SMT. Moreover, for $\alpha \leq 1 \vee \alpha > 5$, we observed that the formation of low-mass primary BHs is also suppressed, either due to stellar mergers during the CE phase in the former case, or due to insufficient orbital shrinking during the CE phase in the latter. When using a top-heavy IMF, we observed similar effects linked to CE efficiency, which partially suppresses the formation of low-mass BHs (see Section 4.3.2 and 4.4.2).

Furthermore, for a top-heavy IMF the production of BHs in the $32 - 37\,M_\odot$ mass interval is enhanced, leading to ~ 3 times more BHs with respect to the fiducial IMF scenario (see Section 4.4.4).

Therefore, to break the degeneracies between CE efficiency and the IMF, we propose a metric that combines the total number of BBH mergers with the relative number count of

TABLE 4.2: Results of the simulations for various IMF. Column 1: CE efficiency α, Column 2: total number of BBH mergers, Column 3: number of primary BH in the $5-10\,M_\odot$ compared with those in the $32-37\,M_\odot$ mass interval, computed as in eq. 4.9, Column 4: fraction of SMT binaries producing bump-primary BHs, Column 5: fraction of CE binaries producing bump-primary BHs.

α	N_{BBH}	δN	$\delta N_{bump,\,\mathrm{SMT}}$	$\delta N_{bump,\,\mathrm{CE}}$
Kroupa IMF				
3	1703979	21.72	0.071	0.016
5	1472677	20.92	0.071	0.012
10	913100	12.10	0.071	0.009
Larson IMF				
3	2854895	10.31	0.098	0.030
5	2486064	9.844	0.098	0.023
10	1647830	5.75	0.098	0.017

BHs in the first and second peaks of the observed BBH population (see Abbott et al. 2023). Specifically, we compute this value as:

$$\delta N = \frac{N_{BH}(5 \leq M_{BH} \leq 10)}{N_{BH}(32 \leq M_{BH} \leq 37)} \tag{4.9}$$

where $N_{BH}(5 \leq M_{BH} \leq 10)$ represents the number of primary BHs with mass in the $5-10\,M_\odot$ range, and $N_{BH}(32 \leq M_{BH} \leq 37)$ is the number of primary BHs with mass in the $32-37\,M_\odot$ interval.

We summarize the results of our simulations as function of α (Column 1) and in terms of number of merging BBH N_{BBH} (column 2) and δN (Column 3) in Table 4.2. In the Table, we also present the relative abundance, with respect to the number of mergers per channel, of the SMT and CE-BHs in the $32-37\,M_\odot$ mass interval.

From Figure 4.12, and as summarized in Table 4.2, it is apparent that the relative height of the two peaks is much more pronounced in the Kroupa IMF scenario. On the other hand, for a Larson IMF we find that δN is approximately half that of the Kroupa IMF ($\delta N_{Larson} \sim 0.5\delta N_{Kroupa}$). This difference arises because a top-heavy IMF is much more efficient at producing bump-primary BHs compared to the Kroupa IMF. Furthermore, although a Larson IMF produce generally more BHs, they are tends to be more massive. Thus, the production of low-mass primary BHs does not experience the same increase as the bump-primary BHs. This leads to lower values of δN for the same CE efficiencies.

Therefore, δN provides a metric for distinguishing between different values of α, particularly when used alongside the total number of detected BBH mergers, which serves as a proxy for the underlying IMF.

4.5 Summary and conclusions

In this Chapter, we have analyzed the features of the primary black hole (BH) mass distribution for binary black hole (BBH) systems using extensive population synthesis simulations. Our primary focus was the so-called *bump* in the primary BH mass spectrum observed at approximately 32–37, $M_\odot$, a prominent feature in the inferred population of gravitational-wave (GW) detections. Here, we summarize the main findings of our work:

- **Role of PPISNe in Shaping the Bump**: We found that pulsational pair-instability supernovae (PPISNe) are not the sole contributors to the 32–37, $M_\odot$ bump. While PPISNe contribute by imposing sharp cutoffs at the upper end of the BH mass spectrum,

their influence accounts for approximately 30% of the primary BHs in this mass range, depending on the specific prescription used (e.g., `M20`, `F19`, or `U24`). The remaining BHs in the bump are produced through binary evolution processes, particularly through binaries that experience either stable mass transfer (SMT) or common envelope (CE) events.

- **Binary Evolution Channels and CE Efficiency**: The 32–37, $M_\odot$ mass interval is shaped by distinct contributions from binaries that experience at least one CE event and those evolving only through SMT:
  - **CE Channel**: Binaries that evolve through CE events dominate the formation of primary BHs below 15, $M_\odot$. For $\alpha \leq 1$, the CE channel remains a significant contributor to the bump but primarily for metal-rich progenitors. Higher CE efficiencies ($\alpha \geq 3$) lead to a preference for metal-poor progenitors, as CE ejections become too efficient, preventing sufficient orbital shrinking for higher-metallicity systems to merge within a Hubble time.
  - **SMT Channel**: SMT is the dominant evolutionary channel for producing primary BHs in the bump range when $\alpha \geq 3$. For high CE efficiencies ($\alpha = 5, 10$), 65% to 83% of bump-primary BHs are formed through SMT, indicating the critical role of this channel in shaping the upper BH mass distribution.
- **Progenitor Properties**: The progenitors of bump-primary BHs are predominantly massive stars:
  - For binaries evolving through SMT, primary stars typically have zero-age main sequence (ZAMS) masses in the 70–90, $M_\odot$ range, with mass ratios ($q = M_1 / M_2$) between 1 and 2.5.
  - For CE binaries, the progenitor stars generally exhibit mass ratios close to unity and masses clustered in the 60–90, $M_\odot$ range at ZAMS.
- **Impact of Initial Mass Function (IMF)**: A top-heavy initial mass function (IMF), such as a Larson IMF, significantly enhances the production of primary BHs in the bump mass interval. Simulations using the Larson IMF yielded approximately three times more BHs in the 32–37, $M_\odot$ range compared to a Kroupa IMF. However, the relative abundance of low-mass BHs (5–10, $M_\odot$) to bump-primary BHs was notably lower, suggesting that the IMF strongly influences the shape of the mass distribution.
- **Proposed Metric for Degeneracy Breaking**: To distinguish between different CE efficiencies and IMFs, we introduced a metric, δN, defined as the ratio of primary BHs in the 5–10, $M_\odot$ mass range to those in the 32–37, $M_\odot$ range. This metric:
  - Decreases with higher CE efficiencies, as low-mass BHs are suppressed.
  - Is sensitive to the choice of IMF, with top-heavy IMFs producing significantly lower δN values due to the enhanced production of bump-primary BHs.
- **Implications for Astrophysical Modeling**: Our results emphasize the complex interplay between binary evolution processes, progenitor metallicity, and the initial mass function in shaping the BBH mass distribution. Specifically:
  - The observed 32–37, $M_\odot$ bump likely arises from a combination of PPISNe and binary evolutionary processes, with SMT playing a critical role for higher CE efficiencies.

- The efficiency of CE ejection and the IMF both significantly impact the relative abundance of low-mass and high-mass BHs, offering potential pathways to constrain these parameters through GW observations.
- The proposed δN metric, combined with the total number of detected BBH mergers, could serve as a powerful diagnostic tool to disentangle degeneracies between CE efficiency and IMF.

In conclusion, this Chapter demonstrates the power of population synthesis simulations in uncovering the underlying astrophysical processes shaping the BBH mass distribution. By combining theoretical predictions with observational data, we can better constrain key parameters, such as CE efficiency and the IMF, and gain deeper insights into the evolutionary pathways leading to BBH mergers.

Chapter 5

Conclusions

5.1 Results summary

In this Thesis, I explored the formation and evolution of massive BHs from both single and binary star systems, addressing some critical uncertainties in stellar evolution and compact object formation.

I employed advanced numerical tools such as the HYPERION code for core collapse supernova simulations and the SEVN code for population synthesis.

5.1.1 Final fate of massive stars

In the first part of my work, I performed simulations of ccSN explosion starting from a grid of evolved massive stars, simulated with the FRANEC stellar evolution code (see Chieffi and Limongi, 2013; Limongi and Chieffi, 2018; Roberti, Limongi, and Chieffi, 2024). The stellar progenitor had various initial masses, ranging between 13 $M_\odot$ and 120 $M_\odot$, initial metallicities $\left[\mathrm{Fe/H}\right] = 0, -1, -2, -3$, and initial angular velocities $v = 0, 300\,\mathrm{kms}^{-}1$. I found that both metallicity and angular rotation play a major role in determining the final fate of the explosion and the final mass of the compact remnant. At higher metallicity ($\left[\mathrm{Fe/H}\right] = 0$ and $\left[\mathrm{Fe/H}\right] = -1$), both for non-rotating and rotating stellar progenitors, stellar winds were strong enough to completely remove the hydrogen envelope of the star, preventing the formation of BHs more massive than $\sim 40\,M_\odot$. On the other hand, lower metallicity stars ($\left[\mathrm{Fe/H}\right] = -2$ and $\left[\mathrm{Fe/H}\right] = -3$) present very different behaviors depending if they are or not rotating. Rotating progenitors, however, experienced severe mass loss due to rotation-enhanced stellar winds, entering the PPISN regime at lower initial masses, thus preventing the formation of massive BHs. On the other hand, non-rotating stellar progenitors are able to form BHs well within the upper-mass gap, as the FRANEC code predicts PPISN to appears for CO core masses $\geq 33\,M_\odot$.

I compared the BH mass results I obtained with predictions from other authors (see Woosley, 2017; Spera and Mapelli, 2017; Farmer et al., 2019). We found that the lower edge of the upper-mass gap can vary significantly depending on the chosen criterion for the onset of PPISNe. While Spera and Mapelli, 2017 suggested that the most massive BHs formed by an isolated massive star are around 60, $M_\odot$, our method yielded approximately 87, $M_\odot$. Applying the criterion of Farmer et al., 2019 to stars with a hydrogen envelope, which they originally applied to naked helium stars, suggested that isolated massive stars could form intermediate-mass BHs, shifting the lower edge of the upper-mass gap to around 110, $M_\odot$. Furthermore, I discussed the several factors that have an impact on the onset of PPISNe, such as different $^{12}C(\alpha,\gamma)^{16}O$ reactions rate (see Farmer et al., 2019; Costa et al., 2021) or different overshooting prescriptions (see Vink, de Koter, and Lamers, 2018).

Next, I studied the compact-object mass distribution by applying the results for ccSNe and PPISNe to a population of 10^6 massive stars with $M_{\mathrm{ZAMS}} \in [15\,Ms,\ 150\,Ms]$, distributed according to a Kroupa IMF (Kroupa, 2001). I showed that the features emerging in the BH

mass distribution depend significantly on the adopted stellar models and show significant degeneracies.

Finally, I provided fitting formulas to predict the final remnant mass from a ccSN based on the stellar progenitor properties at the preSN stage. In the case of non-rotating progenitors, some monotonic linear relationships were identified, though a few stars deviated from the fit. In contrast, rotating progenitors did not exhibit any linear relationship.

5.1.2 Features of the BBH mass distribution

In the second part of my work, I implemented my findings on ccsNe in the SEVN code (Spera and Mapelli, 2017; Spera et al., 2019; Iorio et al., 2023) for population synthesis. I simulated the evolution of 9.6×10^9 binary systems assuming various prescriptions for the IMF, the initial metallicity, the SN models, both ccSN and PPISN, and for the CE efficiency and mass transfer stability.

The goal was to address the effects causing a piling up of primary BHs at $32 - 37\,M_\odot$ in the LVK data (see Abbott et al., 2021; Abbott et al., 2023). Initially, this peak was attributed to PPISNe, which were thought to cause an accumulation of BHs in this mass range. I explored this by assuming various ccSN models (`delayed_Gauss`, `rapid_Gauss`, `SN_U24`) and PPISNe models (`noPPISN`, `F19`, `M20`, `U24`), for a fiducial CE efficiency $\alpha = 3$. I found that the contribution of PPISNe to the peak is highly model-dependent and it strongly depends on the criterion for the onset of PPISNe. The bump is present even in the extreme `noPPISN` scenario, where all the massive stars end their life as ccSN, and only with the `M20` criterion it was found to be more prominent, but still contributing $\sim$ 30% to the bump-population. This is because such a criterion predicts a transition He-core mass of $\sim 32\,M_\odot$, that indeed causes an accumulation of BHs, while other criteria based on the CO core mass allow for the formation of more massive BHs having threshold masses of $\sim 35\,M_\odot$ and $\sim 38\,M_\odot$, `U24` and `F19`, respectively.

However, since the peak is present even in a scenario where PPISNe are disabled, we I inferred that an astrophysical phenomenon linked to the binary systems themselves must be at play. Recent works by van Son et al., 2022; Briel, Stevance, and Eldridge, 2023, suggests that the interplay between binaries undergoing CE or SMT may play a role in the accumulation of BHs in the bump-mass interval. Therefore, we investigated various CE efficiency $\alpha = 0.5,\ 1.0,\ 3.0,\ 5.0,\ 10$ and a scenario assuming always-stable mass transfer. I found that, depending on the binary processes in place, the channel through which bump-BH were produced varies. For $\alpha \leq 1$, the bump is dominated by binaries that evolve through at least one CE event, that on turn becomes a subdominant factor for higher CE efficiencies ($\alpha \geq 3$), where most of the bump-BHs are produced by binaries that evolves only through SMT, without ever triggering a CE phase.

I also analyzed the properties of stellar progenitors contributing to the bump systems. SMT binaries predominantly have primary star ZAMS masses of $70 - 90, M_\odot$ with mass ratios in the $1.5 - 2$ range, while CE binaries have $M_{\rm ZAMS} \sim 60 - 90, M_\odot$ with mass ratios close to unity.

I explored different IMFs, particularly top-heavy IMFs favoring massive stars. Using the Larson IMF in simulations for a fiducial parameter set (`delayed_Gauss` + `M20`), I found approximately three times more BHs in the 32–37, $M_\odot$ range compared to a Kroupa IMF. However, the relative abundance of low-mass BHs (5–10, $M_\odot$) to bump-primary BHs was notably lower. To disentangle degeneracies from various CE efficiencies and IMFs, I proposed a metric, δN, defined as the ratio of primary BHs in the 5–10, $M_\odot$ range to those in the 32–37, $M_\odot$ range. Increasing α suppresses low-mass BH formation, decreasing δN. A top-heavy IMF also reduces δN but produces more BBH mergers.

By combining these quantities, we can deduce the astrophysical properties of BBH progenitors, using GW merger populations detected by LVK as a tool to study astrophysics rather than to fine-tune population synthesis codes.

5.2 Follow-up works and perspectives

The research presented in this Thesis is relevant to the astrophysical interpretation of gravitational wave signals detected by both current and forthcoming generations of gravitational wave observatories.

We are on the brink of the data release from the fourth observative run performed by the LVK collaboration, which will greatly extend the currently known populations of massive BHs. In this framework, to use these data to infer the astrophysical processes in place and the possible environments that host GW events, we need the astrophysical model to be as accurate as possible. Furthermore, in the next decade we expect the third generation GW detectors to start searching for signals. Einstein Telescope, Cosmic Explorer and LISA will open a new window on the universe, extending our grasp to an early stage of the universe and to new kind of processes, from white dwarf binaries to the coalescence of extremely massive BHs. Therefore, we need to be prepared.

In this Thesis, I presented our instruments and the first results we obtained. However, we are far from a definitive stage and many improvements are possible, with some of them hopefully on the way.

5.2.1 ccSN- Future perspective

In Chapter 3, we used the HYPERION code to simulate ccSNe by artificially inducing shockwave formation. This was achieved by injecting a fixed amount of thermal energy well within the iron core of massive stars of our grid. This method relies on several calibrated parameters, which we tuned based on SN 1987A, a well-studied event with reliable estimates of explosion parameters such as ejecta kinetic energy and ^{56}Ni production. However, there is debate in literature on the evolution SN 1987A stellar progenitor. However, debates remain regarding the evolutionary history of SN 1987A's progenitor. Expanding the calibration set to include other supernova events, particularly by reproducing their lightcurves, would enhance HYPERION's predictive accuracy.

Another approach, that would bring to self-consistently achieved explosion, would be to change HYPERION paradigm. We are currently investigating the possibility to interface HYPERION with GR1D (Boccioli, Mathews, and O'Connor, 2021), a 1D hydrodynamics code that incorporates GR-effects and neutrino energy transport. GR1D operates in the STIR approximation (see Couch, Warren, and O'Connor, 2020), overcoming traditional limitations of 1D models by projecting 3D turbulence effects into 1D. By using GR1D's shockwave velocity profiles at late explosion times (in its time domain, i.e., few seconds after the core bounce) as input for HYPERION, we could replace the artificial energy injection paradigm. This would allow us to distinguish between *successful SNe* and *failed SNe* more robustly and to produce reliable estimates of NS and BH mass distributions alongside their progenitors. When integrated into population synthesis codes, these estimates will provide more accurate compact object distributions, aiding in modeling kilonova rates from BNS mergers and the BBH mass distribution.

5.2.2 Improving the CE formalism

My analysis of primary BH mass distributions shows how BBH population data can be exploited to infer the properties of binary progenitors and the efficiency of the CE process.

However, even if this approach seems promising, orthogonal strategies are needed to validate our results are not artifacts of a specific combinations of parameters in population synthesis simulations.

With this goal in mind, one should look to the effects of the CE phase on the stellar binaries. CE outcomes lead either to partial/full ejections of the shared envelope or to a stellar mergers, after which the previously shared envelope is completely ejected. Therefore, after a CE we will always expect an envelope ejection.

Furthermore, envelope ejections produce a particular kind of electromagnetic transients, known as Luminous Red Novas (LRNs, see Pastorello et al., 2019; Pastorello et al., 2021a; Pastorello et al., 2021b).

The properties of LRN lightcurves—linked to the ejected envelope's mass and velocity—offer a theoretically robust method for constraining CE efficiency (see MacLeod et al., 2017; Metzger and Pejcha, 2017; Matsumoto and Metzger, 2022). However, as emphasized by Pastorello et al., 2021b, a population-level study is essential. Generating synthetic LRN lightcurves and their rates across cosmic time would provide a means to cross-validate CE models. This effort would benefit from the forthcoming LSST campaign by the Vera Rubin Observatory, offering an extensive dataset for comparison. Improved CE formalism informed by LRN observations would refine our understanding of binary evolution, directly linking CE efficiency to GW event modeling.

5.2.3 The role of dynamic

In Chapter 4, I presented results for the $32 - 37, M_\odot$ bump in the primary BH mass distribution observed in GW detections.

I showed how our result could help constraining the properties of the stellar progenitors of the BBH, and a possible metric to interpret our detections. However, this work has been performed under a very strong hypothesis: that all the merging BBH are the results the isolated binary formation pathway for GW merger.

In Chapter 1, I showed the effects that dynamical interaction have on a population of massive stars. Furthermore, we know that in dense environments stellar dynamics produce more massive binaries, both via stellar merger and through dynamical exchanges.

To reproduce the bump, I found that massive systems ZAMS masses $\gtrsim 70\,M_\odot$, and mass ratios in the range $1 \sim 2$ are required. These systems are challenging to form in isolation but could arise more naturally in dense environments due to dynamical interactions.

By integrating the catalogs of massive binaries produced in this work into the semi-analytical code `BPOP` (see Arca Sedda et al., 2023), I aim to estimate BBH merger rates self-consistently. This approach will allow us to distinguish between formation pathways and assess the role of stellar dynamics in producing BHs within the bump-mass interval.

Appendix A

Appendix A

A.1 Calibration parameters

In Section 3.2.1 we present the calibration of our parameters and the final set we choose to stimulate the SN explosion in our simulations. In this Appendix we will discuss further the contribution of the different parameters $E_{\rm inj}$, $dm_{\rm inj}$ and $dt_{\rm inj}$.

A.1.1 Calibration of $E_{\rm inj}$

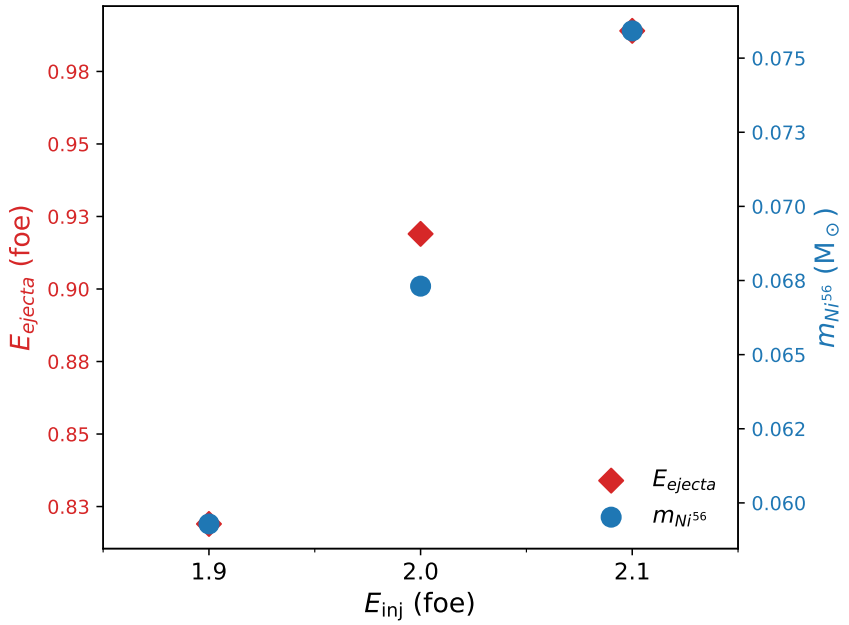

FIGURE A.1: The Figure shows the values of $E_{\rm ejecta}$ (red diamonds, whose scale is on the left-hand y-axes) and $m_{^{56}\rm Ni}$ (blue points, whose scale is on the right-hand y-axis) as function of $E_{\rm inj}$.

Figure A.1 shows the values that we find for $E_{\rm ejecta}$ and $m_{^{56}\rm Ni}$ for different values of $E_{\rm inj}$. We studied the variation of the outcomes of the explosion assuming $dt_{\rm inj} = 10^{-9} s$ and $dm_{\rm inj} = 0.1 M_\odot$, and by injecting the thermal energy at the arbitrary mass coordinate of $0.8 M_\odot$. The values we find for $E_{\rm ejecta}$ and $m_{^{56}\rm Ni}$ are also reported in Table A.4.

We find that increasing the value of thermal energy inducing the explosion, $E_{\rm ejecta}$ and $m_{^{56}\rm Ni}$ increases as well. This is because the SN is stronger, thus the explosive nucleosynthesis reaches outer layers of the star, i.e. producing more ^{56}Ni.

We chose $E_{\rm inj} = 2.0$ foe because above this values we find an overproduction of ^{56}Ni, while the energy of the explosion is compatible with the value usually assumed in literature

(see Arnett et al. 1989; Shigeyama and Nomoto 1990; Utrobin 1993; Utrobin 2006; Blinnikov et al. 2000).

A.1.2 Calibration of $dm_{\rm inj}$

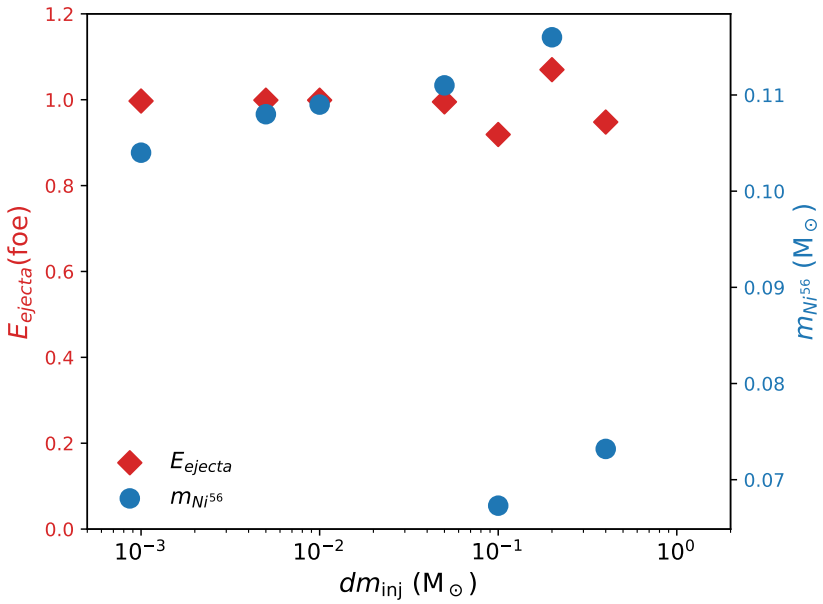

FIGURE A.2: The Figure shows the values of $E_{\rm ejecta}$ (red diamonds, whose scale is on the left-hand y-axes) and $m_{^{56}\rm Ni}$ (blue points, whose scale is on the right-hand y-axis) as function of $dm_{\rm inj}$.

Figure A.2 shows the values that we find for $E_{\rm ejecta}$ and $m_{^{56}\rm Ni}$ for different values of $dm_{\rm inj}$. We studied the variation of the outcomes of the explosion assuming $dt_{\rm inj} = 10^{-9} s$ and $dE_{\rm inj} = 2.0$foe, and by injecting the thermal energy at the arbitrary mass coordinate of $0.8 M_\odot$. The values we find for $E_{\rm ejecta}$ and $m_{^{56}\rm Ni}$ are also reported in Table A.5.

We find that if we choose to inject the energy in thinner layers, the explosion is more energetic, and because of this when the shock reaches the silicon shell, the explosive Si-burning is more efficient, with respect to scenarios with larger $dm_{\rm inj}$. Thus, in these cases we have an overproduction of ^{56}Ni and the outcome of the explosion do not match the observations of SN1987A.

Our simulations are in agreement with the observations for $dm_{\rm inj} = 0.1 M_\odot$ and $dm_{\rm inj} = 0.4 M_\odot$. We chose $dm_{\rm inj} = 0.1 M_\odot$, since our goal was to obtain a parameter set in good agreement with the observation of SN1987A, not the best parameter set because such analysis would have required a more sophisticated approach, and to calibrate on multiple SN sources. We will explore this aspect in an upcoming work.

A.1.3 Calibration of $dt_{\rm inj}$

Figure A.3 shows the values that we find for $E_{\rm ejecta}$ and $m_{^{56}\rm Ni}$ for different values of $dm_{\rm inj}$. We studied the variation of the outcomes of the explosion assuming $dt_{\rm inj} = 10^{-9} s$ and $dE_{\rm inj} = 2.0$foe, and by injecting the thermal energy at the arbitrary mass coordinate of $0.8 M_\odot$. The values we find for $E_{\rm ejecta}$ and $m_{^{56}\rm Ni}$ are also reported in Table A.6.

we find that the $E_{\rm ejecta}$ is roughly independent on the timescale over which we inject the energy. On the other hand, the amount of ^{56}Ni produced (i.e. the efficiency of the explosive Si-burning) is strongly dependent on $dt_{\rm inj}$. From Figure A.3 we see that $m_{^{56}\rm Ni}$ is constant

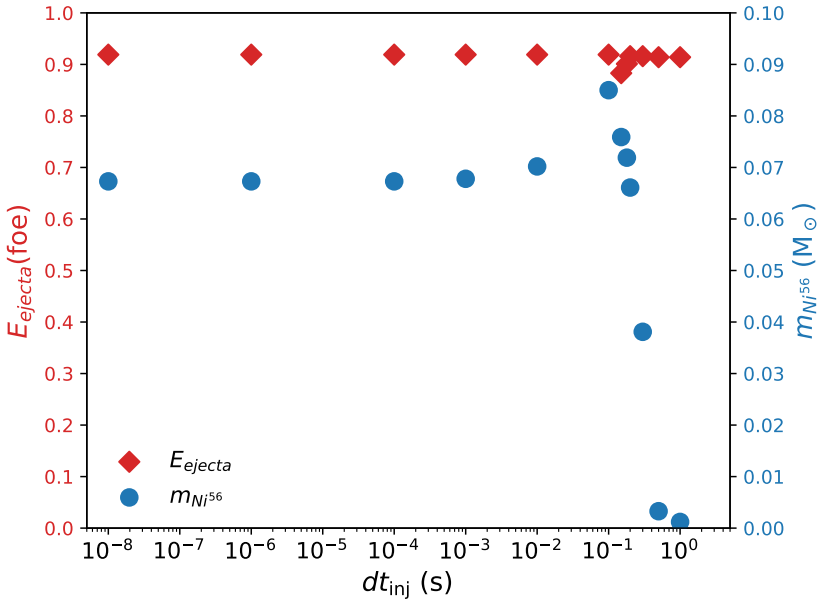

FIGURE A.3: The Figure shows the values of $E_{\rm ejecta}$ (red diamonds, whose scale is on the left-hand y-axes) and $m_{^{56}\rm Ni}$ (blue points, whose scale is on the right-hand y-axis) as function of $dt_{\rm inj}$.

for $dt_{\rm inj} \leq 10^{-3} s$, while for longer timescales the efficiency of the explosive nucleosynthesis increases, resulting in an overproduction of ^{56}Ni with respect to SN1987A. The value of $m_{^{56}\rm Ni}$ reaches its maximum for $dt_{\rm inj} = 0.1 s$, with $m_{^{56}\rm Ni} \sim 0.085 M_\odot$, while on longer timescales it start decreasing. This is because the shockwave reaches the Si shell, where the production of ^{56}Ni takes place, at $\sim 0.2 s$, thus if the thermal energy is not completely injected before this moment the shockwave will not have enough energy to trigger the complete explosive Si-burning. This is apparent from Figure A.3 because for $dt_{\rm inj} \geq 0.2 s$ the amount of ^{56}Ni produced is about an order of magnitude lower than what we obtain for lower $dt_{\rm inj}$. Finally, the values of $dt_{\rm inj}$ that is closer to the observative properties of SN1987A is $dt_{\rm inj} = 0.01 s$, for which we obtain exactly $m_{^{56}\rm Ni} = 0.07 M_\odot$, which is the value one usually can find in the literature (e.g. Arnett et al. 1989; Shigeyama and Nomoto 1990; Utrobin 1993; Utrobin 2006; Blinnikov et al. 2000).

A.2 Tables

A.3 Calibration Tables

TABLE A.1: Results of the interpolation described in Sec. 3.2.2. Column 1: Metallicity, Column 2: $M_{\rm ZAMS}$ of the first progenitor undergoing PPISN, Column 3: Mass Pre-SN of the first progenitor undergoing PPISN. If the most massive progenitor of our grid is stable against PPISN we cannot obtain such information, thus we labeled it as Not Available (NA), Column 4: slope of Eq. 3.1, Column 5: intercept of Eq. 3.1, Column 6: slope of Eq. 3.2, Column 7: intercept of Eq. 3.2.

$[Fe/H]$	$M_{\rm ZAMS}^{\rm PPISN}(M_\odot)$	$M_{\rm preSN}^{\rm PPISN}(M_\odot)$	k_1	$q_1(M_\odot)$	k_2	$q_2(M_\odot)$
v=0 km/s						
0	N.A.	N.A.	N.A.	N.A.	N.A.	N.A.
-1	87.43	41.91	0.28	8.3	0.27	18.3
-2	87.66	83.27	0.53	-13.9	0.61	29.8
-3	87.01	87.01	0.48	-9.2	1.0	0.0
v=300 km/s						
0	N.A.	N.A.	N.A.	N.A.	N.A.	N.A.
-1	120.0	40.5	0.18	11.1	0.21	15.3
-2	65.19	39.89	0.39	7.9	0.48	8.6
-3	64.8	41.63	0.37	-0.6	0.37	8.7

TABLE A.2: Final properties of stars with various initial metallicities and initial masses for the non-rotating stellar progenitors. Column 1: $M_{\rm ZAMS}$, Column 2: Pre-SN helium core mass, Column 3: Pre-SN CO core mass, Column 4: Pre-SN mass, Column 5: Pre-SN binding energy, Column 6: Pre-SN total energy, Column 7: Final mass of the compact remnant, Column 8: Fraction of mass expelled during the explosion.

$M_{\rm ZAMS}(\rm M_\odot)$	$M_{\rm He}(\rm M_\odot)$	$M_{\rm CO}(\rm M_\odot)$	$M_{\rm preSN}(\rm M_\odot)$	$E_{\rm bind}$(foe)	$E_{\rm tot}$(foe)	$M_{\rm rem}(\rm M_\odot)$	dM/M
			[Fe/H]=-0 v=0 km/s				
13	4.08	2.03	11.9	2.02	-0.93	0.81	0.93
15	4.95	2.78	13.2	2.47	-1.07	0.81	0.94
20	7.29	3.86	7.54	2.59	-1.05	2.21	0.71
25	8.54	6.21	8.54	3.58	-1.35	3.69	0.57
30	10.8	7.91	10.8	6.39	-2.13	8.7	0.19
40	14.1	10.6	14.1	7.60	-2.31	12.3	0.13
60	16.9	13.0	16.9	10.6	-3.04	16.2	0.04
80	22.7	18.0	22.7	17.3	-4.52	22.7	0.00
120	27.9	22.0	27.9	24.4	-6.07	27.9	0.00
			[Fe/H]=-1 v=0 km/s				
13	4.26	2.13	12.5	1.95	-0.89	0.81	0.94
15	5.22	3.01	14.2	2.73	-1.15	1.66	0.88
20	7.52	4.21	18.3	3.19	-1.26	3.31	0.82
25	10.2	6.82	20.6	5.52	-1.91	7.49	0.64
30	11.9	7.22	28.3	5.95	-1.99	11.8	0.58
40	16.7	10.9	28.7	8.03	-2.39	16.7	0.42
60	26.8	19.6	42.0	19.5	-4.94	36.7	0.13
80	39.2	30.9	39.9	40.0	-9.27	39.9	0.00
			[Fe/H]=-2 v=0 km/s				
13	4.34	2.14	13	2.25	-1.01	0.81	0.94
15	5.21	2.72	14.8	2.25	-0.95	0.82	0.94
20	7.49	4.23	19.7	3.26	-1.28	3.44	0.83
25	9.87	5.93	24.7	4.05	-1.47	5.77	0.77
30	11.7	6.98	29.9	5.46	-1.84	12.7	0.58
40	16.7	11.2	39.7	8.78	-2.57	25.8	0.35
60	27.2	20.0	59.4	20.7	-5.16	59.4	0.00
80	38.3	28.9	78.6	36.1	-8.18	78.6	0.00
			[Fe/H]=-3 v=0 km/s				
13	4.22	2.15	13	2.03	-0.92	0.81	0.94
15	5.22	3.09	15	2.92	-1.20	1.85	0.88
20	7.42	4.35	20	3.29	-1.29	3.37	0.83
25	9.84	6.29	25	4.39	-1.56	6.30	0.75
30	12.3	8.08	30	5.71	-1.87	12.7	0.58
40	17.5	12.2	40	10.3	-2.99	32.9	0.18
60	28.5	21.7	60	23.6	-5.80	60	0.00
80	38.9	29.6	80	37.9	-8.56	80	0.00

TABLE A.3: Final properties of stars with various initial metallicities and initial masses for the non-rotating stellar progenitors. Column 1: $M_{\rm ZAMS}$, Column 2: Pre-SN helium core mass, Column 3: Pre-SN CO core mass, Column 4: Pre-SN mass, Column 5: Pre-SN binding energy, Column 6: Pre-SN total energy, Column 7: Final mass of the compact remnant, Column 8: Fraction of mass expelled during the explosion.

$M_{\rm ZAMS}(\rm M_\odot)$	$M_{\rm He}(\rm M_\odot)$	$M_{\rm CO}(\rm M_\odot)$	$M_{\rm preSN}(\rm M_\odot)$	$E_{\rm bind}$(foe)	$E_{\rm tot}$(foe)	$M_{\rm rem}(\rm M_\odot)$	dM/M
			[Fe/H]=-0 v=300 km/s				
15	6.23	4.31	6.23	3.95	-1.65	4.29	0.31
20	8.18	5.92	8.18	7.61	-3.16	8.18	0.00
25	9.48	7.16	9.48	6.30	-2.39	8.45	0.11
30	11.2	8.46	11.2	7.07	-2.69	11.2	0.00
40	13.8	10.6	13.8	9.14	-3.06	13.8	0.00
60	16.6	13.0	16.6	11.0	-3.19	16.6	0.00
80	17.5	13.7	17.5	11.6	-3.29	17.5	0.00
120	18.6	14.6	18.6	13.1	-3.63	18.6	0.00
			[Fe/H]=-1 v=300 km/s				
15	6.50	4.89	11.6	5.85	-2.77	11.6	0.00
20	8.12	6.16	17.1	7.21	-3.21	17.1	0.00
25	12.2	9.73	18.5	8.52	-3.07	12.6	0.32
30	16.0	12.3	16.0	11.9	-3.85	16.0	0.00
40	20.7	16.2	20.7	16.3	-4.7	20.7	0.00
60	27.5	21.4	27.5	23.7	-6.21	27.5	0.00
80	32.1	25.7	32.1	29.8	-7.25	32.1	0.00
120	40.5	33.0	40.5	41.8	-9.33	40.5	0.00
			[Fe/H]=-2 v=300 km/s				
15	6.47	4.72	13.75	5.85	-2.8	13.75	0.00
20	9.85	6.77	16.8	8.83	-3.45	15.3	0.09
25	13.2	10.4	13.2	9.37	-3.28	13.2	0.00
30	15.1	11.7	15.6	10.5	-3.35	15.6	0.00
40	17.6	18.5	22.9	22.9	-5.24	22.9	0.00
60	37.4	31.0	37.4	42.7	-11.0	37.4	0.00
			[Fe/H]=-3 v=300 km/s				
15	6.09	4.16	13.8	4.23	-1.81	4.38	0.68
20	7.89	5.29	20	7.28	-3.1	20.0	0.00
25	13.0	10.5	13.3	9.41	-3.22	13.3	0.00
30	16.9	13.1	17.1	11.2	-3.68	17.1	0.00
40	24.5	19.1	24.5	20.1	-5.72	24.5	0.00
60	38.1	29.4	38.1	37.1	-9.24	38.1	0.00

TABLE A.4: Calibration on $E_{\rm inj}$. Column 1: $E_{\rm inj}$, Column 2: $E_{\rm ejecta}$ of the explosion, Column 3: $m_{^{56}\rm Ni}$ produced in the explosive nucleosynthesis, Column 4: M_{rem} we find for the explosion.

$E_{\rm inj}$(foe)	$E_{\rm ejecta}$(foe)	$m_{^{56}\rm Ni}(\rm M_\odot)$	$M_{rem}(\rm M_\odot)$
1.9	0.82	0.059	0.835
2.0	0.92	0.067	0.829
2.1	0.99	0.076	0.822

TABLE A.5: Calibration on $dm_{\rm inj}$. Column 1: $dm_{\rm inj}$, Column 2: $E_{\rm ejecta}$ of the explosion, Column 3: $m_{^{56}\rm Ni}$ produced in the explosive nucleosynthesis, Column 4: M_{rem} we find for the explosion.

$E_{\rm inj}$(foe)	$E_{\rm ejecta}$(foe)	$m_{^{56}\rm Ni}(\rm M_\odot)$	$M_{rem}(\rm M_\odot)$
0.400	0.948	0.073	1.148
0.200	1.070	0.116	0.923
0.100	0.919	0.067	0.829
0.050	0.995	0.111	0.858
0.010	0.999	0.109	0.879
0.005	0.999	0.108	0.897
0.001	0.997	0.104	0.905

TABLE A.6: Calibration on $dt_{\rm inj}$. Column 1: $dt_{\rm inj}$, Column 2: $E_{\rm ejecta}$ of the explosion, Column 3: $m_{^{56}\rm Ni}$ produced in the explosive nucleosynthesis, Column 4: M_{rem} we find for the explosion.

$dt_{\rm inj}(\rm M_\odot)$	$E_{\rm ejecta}$(foe)	$m_{^{56}\rm Ni}(\rm M_\odot)$	$M_{rem}(\rm M_\odot)$
1×10^{0}	0.914	0.001	0.801
5×10^{-1}	0.914	0.003	0.801
3×10^{-1}	0.916	0.004	0.815
2×10^{-1}	0.916	0.066	0.801
1.8×10^{-1}	0.901	0.072	0.808
1.5×10^{-1}	0.883	0.076	0.822
1×10^{-1}	0.919	0.085	0.822
1×10^{-2}	0.919	0.070	0.822
1×10^{-3}	0.919	0.068	0.829
1×10^{-4}	0.919	0.067	0.829
1×10^{-6}	0.919	0.067	0.829
1×10^{-8}	0.919	0.067	0.822

Appendix B

Appendix B

In Section 4.3.1, we discuss the impact of various SSE prescriptions on the primary BH mass distribution, presenting results for different ccSN and PPISN prescriptions across all the metallicities simulated, with a fixed CE efficiency of $\alpha = 3$. Furthermore, in Section 4.3.2, we examine the effect of CE efficiency on the primary BH mass distribution, also showing results for all the simulated metallicities, for the fiducial treatment for SNe.

In this Appendix, we present the results for different ccSN and PPISN prescriptions for the various CE efficiencies, across all the metallicities simulated.

B.1 Effect of SSE prescriptions for different α

Figure B.1, Figure B.2, Figure B.3, and Figure B.4 show the results for all the possible combinations of ccSN and PPISN models across all the simulated metallicities for $\alpha =$ 0.5, 1, 5, and 10, respectively. In all the Figures, each row represents a different prescription for core-collapse supernovae (ccSNe): `delayed_Gauss` (top row), `rapid_Gauss` (central row), and `SN_U24` (bottom row). Correspondingly, each column shows different criteria for the onset of PPISNe: `noPPISN` (first column), `M20` (second column), `F19` (third column), and `U24` (fourth column), as outlined in Table 4.1. The color variations in each panel reflect different progenitor metallicities.

In all Figures, we observe the trends discussed in Section 4.3.1 for different SSE prescriptions. Similarly, the effects of varying CE efficiencies align with the discussion in Section 4.3.2. For $\alpha \leq 1$, low-mass BHs predominantly originate from metal-rich systems, while for $\alpha = 3$ and $\alpha = 5$, their progenitors are evenly distributed across all metallicities. At $\alpha = 10$, low-mass BHs primarily form in metal-poor systems. Across all CE efficiencies, the most massive BHs are consistently produced by metal-poor progenitors.

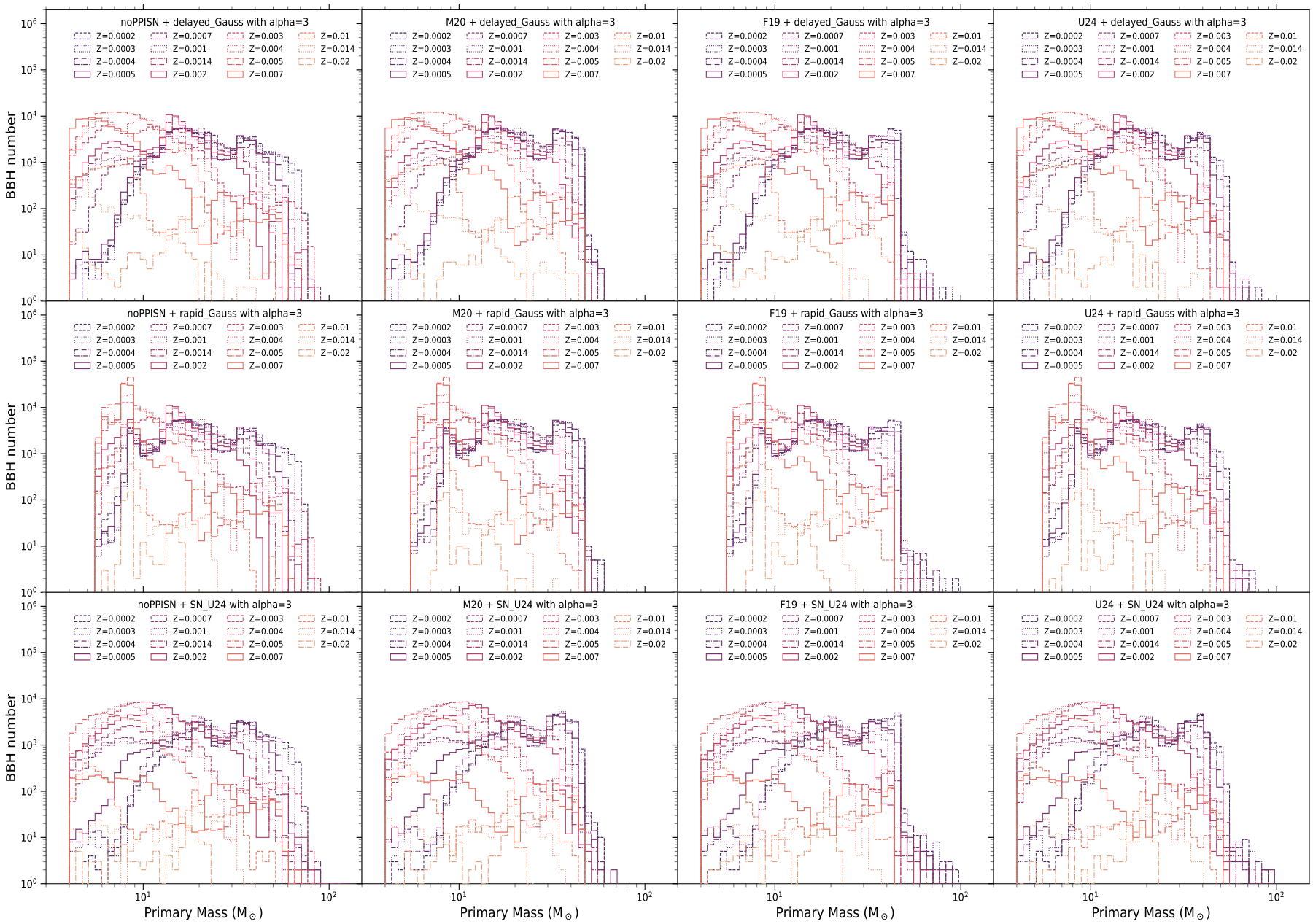

FIGURE B.1: Primary BH mass distribution of BBH merging system in our simulation with CE efficiency $\alpha = 0.5$. From left to right: each row shows a different prescription for ccSNe (`delayed_Gauss` on the top row, `rapid_Gauss` on the central row, and `SN_U24`) on the bottom row), while each column shows a different treatment PPISNe (`noPPISN` on the first column, `M20` on the second column, `F19` on the third column, and `U24` on the fourth column). The color map refers to the metallicity of the progenitors ($Z = 2\times10^{-4}, 3\times10^{-4}, 4\times10^{-4}, 5\times10^{-4}, 7\times10^{-4}, 1\times10^{-3}, 1.4\times10^{-3}, 2\times10^{-3}, 3\times10^{-3}, 4\times10^{-3}, 5\times10^{-3}, 7\times10^{-3}, 1\times10^{-2}, 1.4\times10^{-2}, 2\times10^{-2}$).

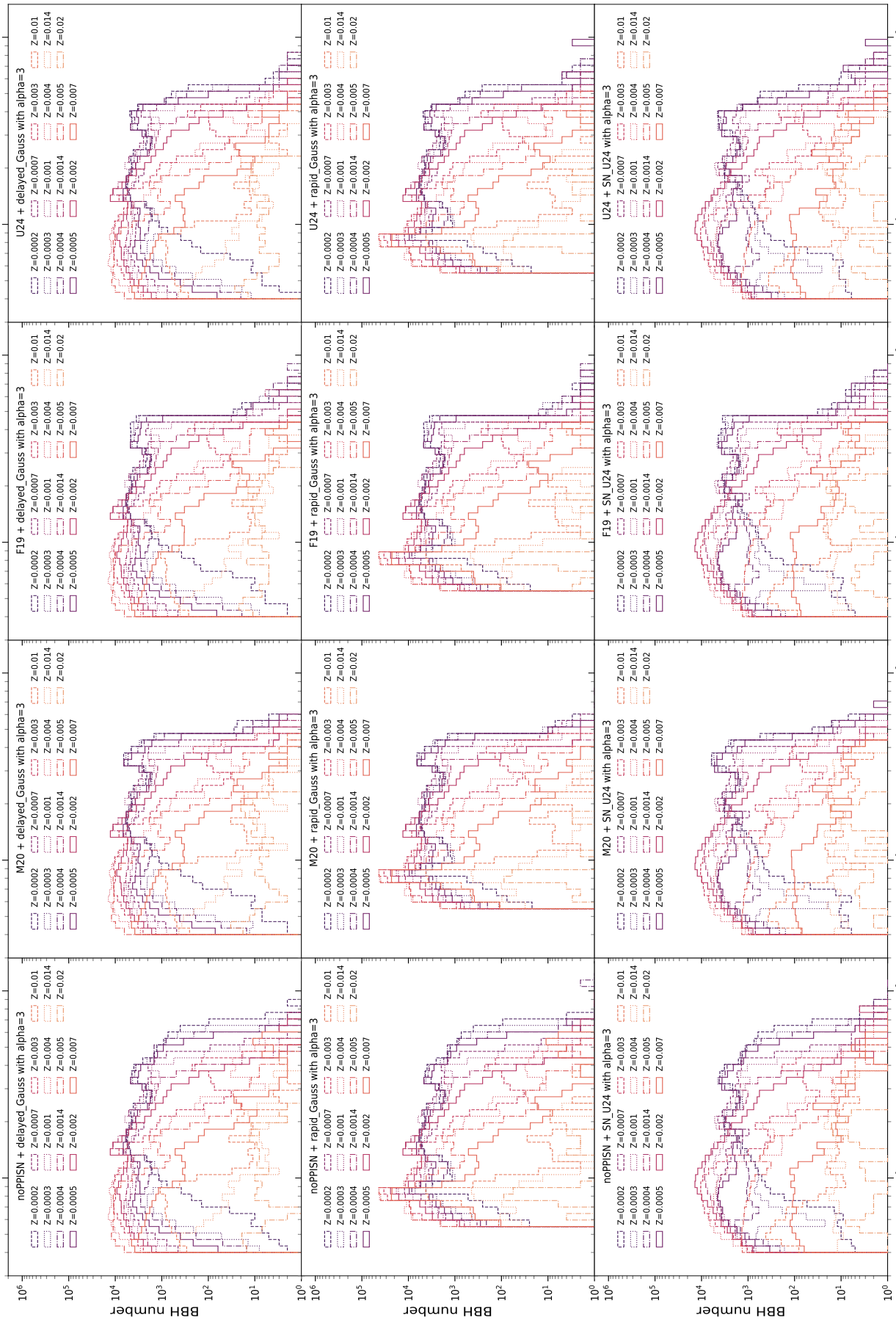

FIGURE B.2: Same as Figure B.1 but with CE efficiency $\alpha = 1$.

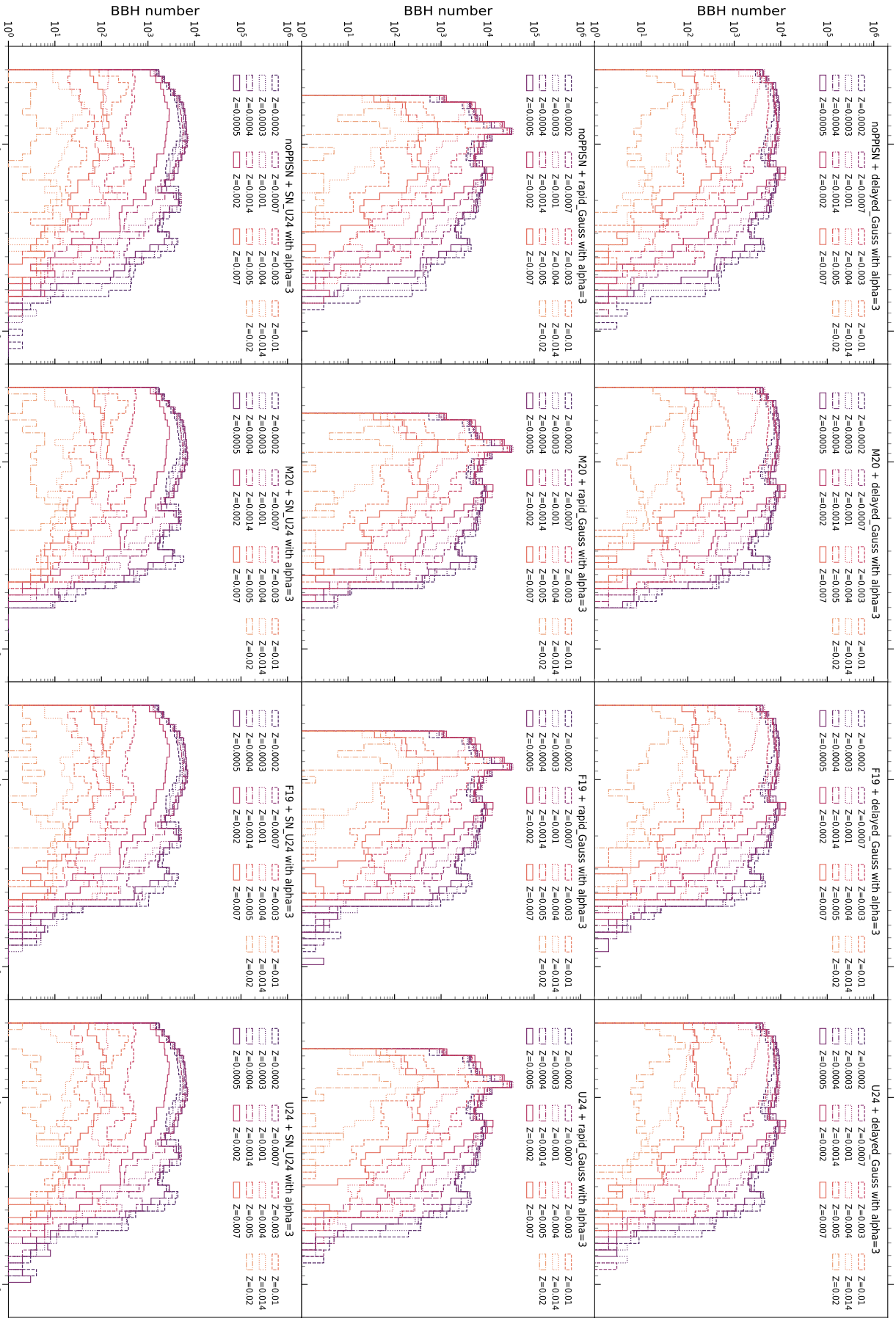

FIGURE B.3: Same as Figure B.1 but with CE efficiency $\alpha = 5$.

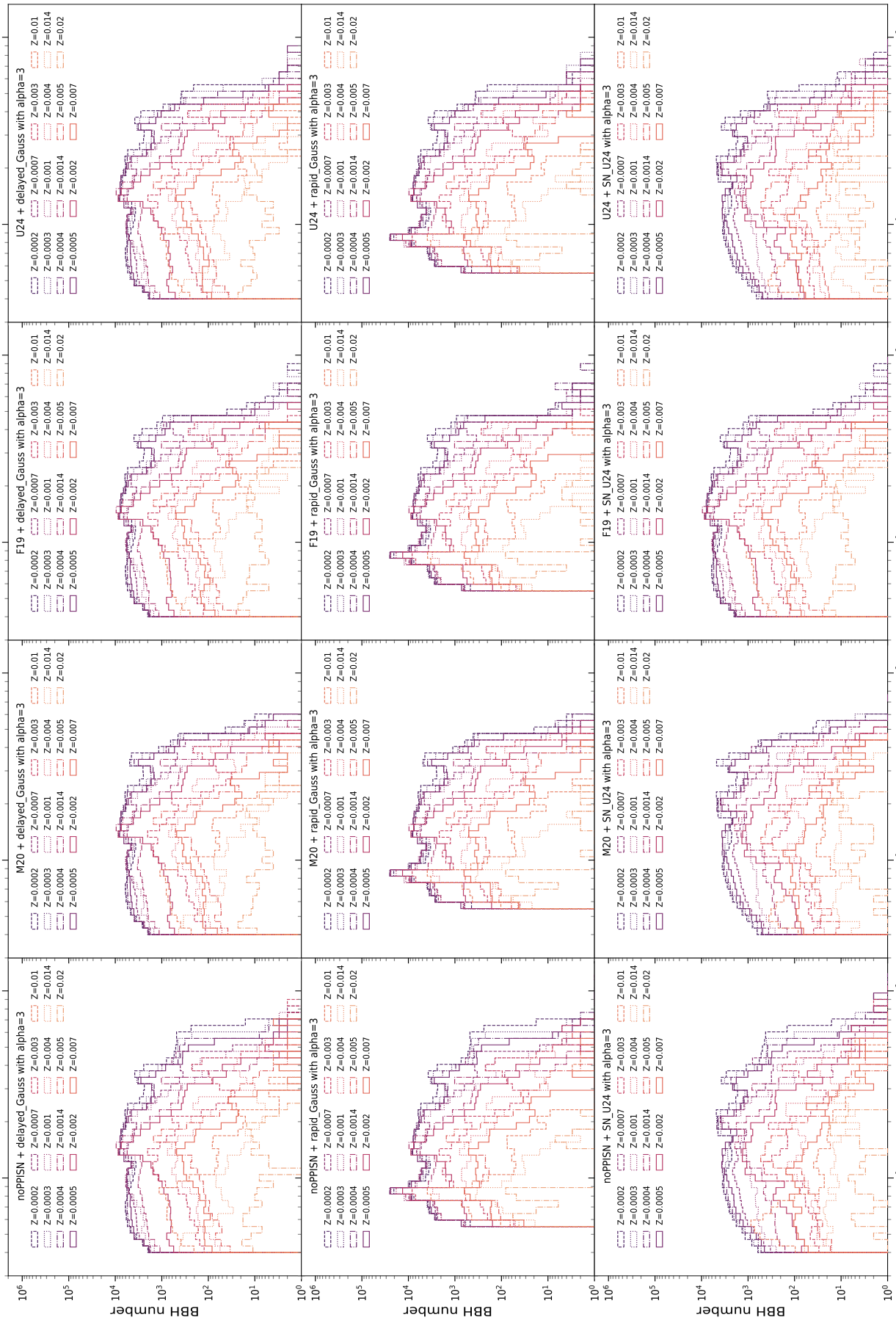

FIGURE B.4: Same as Figure B.1 but with CE efficiency $\alpha = 10$.

Bibliography

Abbott, B. P. et al. (Feb. 2016a). "Astrophysical Implications of the Binary Black-hole Merger GW150914". In: *The Astrophysical Journall* 818.2, p. L22. DOI: 10.3847/2041-8205/818/2/L22.

Abbott, B. P. et al. (2016b). "Binary Black Hole Mergers in the First Advanced LIGO Observing Run". In: *Phys. Rev. X*.

Abbott, B. P. et al. (2016c). "GW150914: First Results from the Search for Binary Black Hole Coalescence with Advanced LIGO". In: *Physical Review D* 93, p. 122003. ISSN: 1550-79980556-2821. DOI: 10.1103/PhysRevD.93.122003.

Abbott, B. P. et al. (Sept. 2019). "Binary Black Hole Population Properties Inferred from the First and Second Observing Runs of Advanced LIGO and Advanced Virgo". In: *The Astrophysical Journall* 882.2, p. L24. DOI: 10.3847/2041-8213/ab3800.

Abbott, D. C. and L. B. Lucy (Jan. 1985). "Multiline transfer and the dynamics of stellar winds." In: *The Astrophysical Journal* 288, pp. 679–693. DOI: 10.1086/162834.

Abbott, R. et al. (May 2021). "Population Properties of Compact Objects from the Second LIGO-Virgo Gravitational-Wave Transient Catalog". In: *The Astrophysical Journall* 913.1, L7, p. L7. DOI: 10.3847/2041-8213/abe949. arXiv: 2010.14533 [astro-ph.HE].

Abbott, R. et al. (Dec. 2023). "GWTC-3: Compact Binary Coalescences Observed by LIGO and Virgo during the Second Part of the Third Observing Run". In: *Physical Review X* 13.4. ISSN: 2160-3308. DOI: 10.1103/physrevx.13.041039.

Abbott, R. et al. (Jan. 2023). "Population of Merging Compact Binaries Inferred Using Gravitational Waves through GWTC-3". In: *Physical Review X* 13.1, 011048, p. 011048. DOI: 10.1103/PhysRevX.13.011048. arXiv: 2111.03634 [astro-ph.HE].

Agrawal, Poojan et al. (Oct. 2020). "The Fates of Massive Stars: Exploring Uncertainties in Stellar Evolution with METISSE". In: *Monthly Notices of the Royal Astronomical Society* 497, pp. 4549–4564. ISSN: 0035-8711. DOI: 10.1093/mnras/staa2264.

Aguilera-Dena, David R. et al. (Mar. 2022). *Stripped-Envelope Stars in Different Metallicity Environments. II. Type I Supernovae and Compact Remnants*. DOI: 10.48550/arXiv.2204.00025.

Antonini, Fabio and Frederic A. Rasio (Nov. 2016). "MERGING BLACK HOLE BINARIES IN GALACTIC NUCLEI: IMPLICATIONS FOR ADVANCED-LIGO DETECTIONS". In: *The Astrophysical Journal* 831.2, p. 187. ISSN: 1538-4357. DOI: 10.3847/0004-637x/831/2/187.

Arca Sedda, Manuel (Mar. 2020). "Birth, Life, and Death of Black Hole Binaries around Supermassive Black Holes: Dynamical Evolution of Gravitational Wave Sources". In: *The Astrophysical Journal* 891.1, p. 47. DOI: 10.3847/1538-4357/ab723b.

Arca Sedda, Manuel, Abbas Askar, and Mirek Giersz (Oct. 2018). "MOCCA-Survey Database - I. Unravelling black hole subsystems in globular clusters". In: *Monthly Notices of the Royal Astronomical Society* 479.4, pp. 4652–4664. DOI: 10.1093/mnras/sty1859. arXiv: 1801.00795 [astro-ph.GA].

Arca Sedda, Manuel et al. (Jan. 2023). "Isolated and dynamical black hole mergers with<tt>B-POP</tt>: the role of star formation and dynamics, star cluster evolution, natal kicks, mass and spins, and hierarchical mergers". In: *Monthly Notices of the Royal Astronomical Society* 520.4, 5259–5282. ISSN: 1365-2966. DOI: 10.1093/mnras/stad331.

Arnett, David (1996). *Supernovae and Nucleosynthesis: An Investigation of the History of Matter from the Big Bang to the Present*.

Arnett, W. David et al. (Sept. 1989). "Supernova 1987A". In: *Annual Review of Astronomy and Astrophysics* 27.1, pp. 629–700. DOI: 10.1146/annurev.aa.27.090189.003213.

Askar, Abbas et al. (Jan. 2017). "MOCCA-SURVEY Database - I. Coalescing binary black holes originating from globular clusters". In: *Monthly Notices of the Royal Astronomical Society* 464.1, pp. L36–L40. DOI: 10.1093/mnrasl/slw177. arXiv: 1608.02520 [astro-ph.HE].

Banerjee, Sambaran (May 2017). "Stellar-Mass Black Holes in Young Massive and Open Stellar Clusters and Their Role in Gravitational-Wave Generation". In: *Monthly Notices of the Royal Astronomical Society* 467, pp. 524–539. ISSN: 0035-8711. DOI: 10.1093/mnras/stw3392.

— (Sept. 2022). "Binary Black Hole Mergers from Young Massive Clusters in the Pair-Instability Supernova Mass Gap". In: *A&A* 665, A20. ISSN: 0004-6361, 1432-0746. DOI: 10.1051/0004-6361/202142331. arXiv: 2109.14612 [astro-ph].

Banerjee, Sambaran, Holger Baumgardt, and Pavel Kroupa (Feb. 2010). "Stellar-Mass Black Holes in Star Clusters: Implications for Gravitational Wave Radiation". In: *Monthly Notices of the Royal Astronomical Society* 402, pp. 371–380. ISSN: 0035-8711. DOI: 10.1111/j.1365-2966.2009.15880.x.

Barkat, Z., G. Rakavy, and N. Sack (1967). "Dynamics of Supernova Explosion Resulting from Pair Formation". In: *prl* 18.10, pp. 379–381. DOI: 10.1103/PhysRevLett.18.379.

Bartos, Imre et al. (Jan. 2017). "Rapid and Bright Stellar-mass Binary Black Hole Mergers in Active Galactic Nuclei". In: *The Astrophysical Journal* 835.2, p. 165. DOI: 10.3847/1538-4357/835/2/165.

Belczynski, K. et al. (Oct. 2016). "The Effect of Pair-Instability Mass Loss on Black-Hole Mergers". In: *A&A* 594, A97. ISSN: 0004-6361, 1432-0746. DOI: 10.1051/0004-6361/201628980.

Belczynski, K. et al. (Apr. 2020). "Evolutionary Roads Leading to Low Effective Spins, High Black Hole Masses, and O1/O2 Rates for LIGO/Virgo Binary Black Holes". In: *Astronomy & Astrophysics* 636, A104. DOI: 10.1051/0004-6361/201936528.

Bellovary, Jillian M. et al. (Mar. 2016). "MIGRATION TRAPS IN DISKS AROUND SUPERMASSIVE BLACK HOLES". In: *The Astrophysical Journal Letters* 819.2, p. L17. DOI: 10.3847/2041-8205/819/2/L17.

Bethe, H. A. and J. R. Wilson (Aug. 1985). "Revival of a Stalled Supernova Shock by Neutrino Heating". In: *The Astrophysical Journal* 295, pp. 14–23. DOI: 10.1086/163343.

Bethe, Hans A. and G. E. Brown (Oct. 1998). "Evolution of Binary Compact Objects That Merge". In: *The Astrophysical Journal* 506, pp. 780–789. ISSN: 0004-637X. DOI: 10.1086/306265.

Bird, Simeon et al. (May 2016). "Did LIGO Detect Dark Matter?" In: *Physical Review Letters* 116.20. ISSN: 1079-7114. DOI: 10.1103/physrevlett.116.201301.

Blinnikov, Sergei et al. (2000). "Radiation Hydrodynamics of SN 1987A. I. Global Analysis of the Light Curve for the First 4 Months". In: *The Astrophysical Journal* 532.2, pp. 1132–1149. DOI: 10.1086/308588. arXiv: astro-ph/9911205.

Boccioli, Luca, Grant J. Mathews, and Evan P. O'Connor (May 2021). "General Relativistic Neutrino-driven Turbulence in One-dimensional Core-collapse Supernovae". In: *The Astrophysical Journal* 912, p. 29. ISSN: 0004-637X. DOI: 10.3847/1538-4357/abe767.

Bollig, Robert et al. (June 2021). "Self-Consistent 3D Supernova Models From -7 Minutes to $\mathplus$7 s: A 1-Bethe Explosion of a $\sim$19 M $ødot$ Progenitor". In: *The Astrophysical Journal* 915.1, p. 28. DOI: 10.3847/1538-4357/abf82e.

Bond, J. R., W. D. Arnett, and B. J. Carr (May 1984). "The evolution and fate of Very Massive Objects". In: *The Astrophysical Journal* 280, pp. 825–847. DOI: 10.1086/162057.

Bondi, H. and F. Hoyle (Jan. 1944). "On the mechanism of accretion by stars". In: *Monthly Notices of the Royal Astronomical Society* 104, p. 273. DOI: 10.1093/mnras/104.5.273.

Bowman, Dominic M. (Oct. 2020). "Asteroseismology of high-mass stars: new insights of stellar interiors with space telescopes". In: *Frontiers in Astronomy and Space Sciences* 7, 70, p. 70. DOI: 10.3389/fspas.2020.578584. arXiv: 2008.11162 [astro-ph.SR].

Bressan, Alessandro et al. (2012). "PARSEC Stellar Tracks and Isochrones with the PAdova and TRieste Stellar Evolution Code". In: *Monthly Notices of the Royal Astronomical Society*.

Briel, M M, H F Stevance, and J J Eldridge (Apr. 2023). "Understanding the High-Mass Binary Black Hole Population from Stable Mass Transfer and Super-Eddington Accretion in Bpass". In: *Monthly Notices of the Royal Astronomical Society* 520.4, pp. 5724–5745. ISSN: 0035-8711. DOI: 10.1093/mnras/stad399.

Briel, Max M. et al. (July 2022). "Estimating transient rates from cosmological simulations and BPASS". In: *Monthly Notices of the Royal Astronomical Society* 514.1, pp. 1315–1334. DOI: 10.1093/mnras/stac1100. arXiv: 2111.08124 [astro-ph.CO].

Broekgaarden, Floor S. et al. (Dec. 2021). "Impact of Massive Binary Star and Cosmic Evolution on Gravitational Wave Observations I: Black Hole-Neutron Star Mergers". In: *Monthly Notices of the Royal Astronomical Society* 508, pp. 5028–5063. ISSN: 0035-8711. DOI: 10.1093/mnras/stab2716.

Brott, I. et al. (June 2011). "Rotating Massive Main-Sequence Stars - I. Grids of Evolutionary Models and Isochrones". In: *A&A* 530, A115. ISSN: 0004-6361, 1432-0746. DOI: 10.1051/0004-6361/201016113.

Brown, G. E. (Feb. 1995). "Neutron Star Accretion and Binary Pulsar Formation". In: *The Astrophysical Journal* 440, p. 270. ISSN: 0004-637X. DOI: 10.1086/175268.

Burrows, Adam, John Hayes, and Bruce A. Fryxell (Sept. 1995). "On the Nature of Core-Collapse Supernova Explosions". In: *The Astrophysical Journal* 450, p. 830. DOI: 10.1086/176188.

Burrows, Adam, David Radice, and David Vartanyan (May 2019). "Three-Dimensional Supernova Explosion Simulations of 9-, 10-, 11-, 12-, and 13-M$_\ensuremathødot$ Stars". In: *Monthly Notices of the Royal Astronomical Society* 485.3, pp. 3153–3168. DOI: 10.1093/mnras/stz543.

Burrows, Adam et al. (Jan. 2020). "The Overarching Framework of Core-Collapse Supernova Explosions as Revealed by 3D FORNAX Simulations". In: *Monthly Notices of the Royal Astronomical Society* 491.2, pp. 2715–2735. DOI: 10.1093/mnras/stz3223.

Burrows, Adam et al. (2024). *A Theory for Neutron Star and Black Hole Kicks and Induced Spins*. arXiv: 2311.12109 [astro-ph.HE].

Böker, Torsten et al. (Mar. 2002). "A Hubble Space Telescope Census of Nuclear Star Clusters in Late-Type Spiral Galaxies. I. Observations and Image Analysis*". In: *The Astronomical Journal* 123.3, p. 1389. DOI: 10.1086/339025.

Callister, Thomas A. and Will M. Farr (Nov. 2023). *A Parameter-Free Tour of the Binary Black Hole Population*. arXiv: 2302.07289 [astro-ph, physics:gr-qc].

Carr, B. J. and S. W. Hawking (Aug. 1974). "Black holes in the early Universe". In: *Monthly Notices of the Royal Astronomical Society* 168, pp. 399–416. DOI: 10.1093/mnras/168.2.399.

Carr, Bernard, Florian Kühnel, and Marit Sandstad (Oct. 2016). "Primordial black holes as dark matter". In: *Physical Review D* 94.8. ISSN: 2470-0029. DOI: 10.1103/physrevd.94.083504.

Castor, J. I., D. C. Abbott, and R. I. Klein (Jan. 1975). "Radiation-driven winds in Of stars." In: *The Astrophysical Journa* 195, pp. 157–174. DOI: 10.1086/153315.

Chaboyer, B. and J. P. Zahn (Jan. 1992). "Effect of horizontal turbulent diffusion on transport by meridional circulation." In: *Astronomy & Astrophysics* 253, pp. 173–177.

Chatzopoulos, E. and J. Craig Wheeler (Mar. 2012). "Effects of Rotation on the Minimum Mass of Primordial Progenitors of Pair-instability Supernovae". In: *The Astrophysical Journal* 748.1, p. 42. DOI: 10.1088/0004-637X/748/1/42.

Chen, Yang et al. (Sept. 2015). "PARSEC evolutionary tracks of massive stars up to 350 $M_{\odot}$ at metallicities $0.0001 \leq Z \leq 0.04$". In: *Monthly Notices of the Royal Astronomical Society* 452.1, pp. 1068–1080. DOI: 10.1093/mnras/stv1281. arXiv: 1506.01681 [astro-ph.SR].

Chieffi, Alessandro and Marco Limongi (June 2004). "Explosive Yields of Massive Stars from $Z = 0$ to $Z = Z_{solar}$". In: *The Astrophysical Journal* 608.1, pp. 405–410. DOI: 10.1086/392523.

— (Feb. 2013). "Pre-Supernova Evolution of Rotating Solar Metallicity Stars in the Mass Range 13-120 M ⊙ and Their Explosive Yields". In: *The Astrophysical Journal* 764, p. 21. ISSN: 0004-637X. DOI: 10.1088/0004-637X/764/1/21.

— (Feb. 2020). "The Presupernova Core Mass-Radius Relation of Massive Stars: Understanding Its Formation and Evolution". In: *The Astrophysical Journal* 890.1, p. 43. DOI: 10.3847/1538-4357/ab6739.

Claeys, J. S. W. et al. (Mar. 2014). "Theoretical uncertainties of the Type Ia supernova rate". In: *Astronomy & Astrophysics* 563, A83, A83. DOI: 10.1051/0004-6361/201322714. arXiv: 1401.2895 [astro-ph.SR].

Colella, Phillip and Paul W. Woodward (1984). "The Piecewise Parabolic Method (PPM) for Gas-Dynamical Simulations". In: *Journal of Computational Physics*.

Colgate, Stirling A. and Richard H. White (Mar. 1966). "The Hydrodynamic Behavior of Supernovae Explosions". In: *The Astrophysical Journal* 143, p. 626. DOI: 10.1086/148549.

Costa, Guglielmo et al. (June 2019). "Mixing by overshooting and rotation in intermediate-mass stars". In: *Monthly Notices of the Royal Astronomical Society* 485.4, pp. 4641–4657. DOI: 10.1093/mnras/stz728. arXiv: 1903.04368 [astro-ph.SR].

Costa, Guglielmo et al. (Mar. 2021). "Formation of GW190521 from Stellar Evolution: The Impact of the Hydrogen-Rich Envelope, Dredge-up, and $^{12}C(\alpha, \gamma)^{16}O$ Rate on the Pair-Instability Black Hole Mass Gap". In: *Monthly Notices of the Royal Astronomical Society* 501, pp. 4514–4533. ISSN: 0035-8711. DOI: 10.1093/mnras/staa3916.

Couch, Sean M., MacKenzie L. Warren, and Evan P. O'Connor (Feb. 2020). "Simulating Turbulence-aided Neutrino-driven Core-collapse Supernova Explosions in One Dimension". In: *The Astrophysical Journal* 890, p. 127. ISSN: 0004-637X. DOI: 10.3847/1538-4357/ab609e.

Davies, Ben, René D. Oudmaijer, and Jorick S. Vink (Sept. 2005). "Asphericity and clumpiness in the winds of Luminous Blue Variables". In: *Astronomy & Astrophysics* 439.3, pp. 1107–1125. DOI: 10.1051/0004-6361:20052781. arXiv: astro-ph/0505344 [astro-ph].

de Kool, M. (July 1990). "Common Envelope Evolution and Double Cores of Planetary Nebulae". In: *Astrophysical Journal* 358, p. 189. DOI: 10.1086/168974.

Dewi, J. D. M., Ph. Podsiadlowski, and A. Sena (June 2006). "Double-Core Evolution and the Formation of Neutron Star Binaries with Compact Companions". In: *Monthly Notices of the Royal Astronomical Society* 368, pp. 1742–1748. ISSN: 0035-8711. DOI: 10.1111/j.1365-2966.2006.10233.x.

Di Carlo, Ugo N. et al. (2019). "Merging Black Holes in Young Star Clusters". In: *Monthly Notices of the Royal Astronomical Society* 487.2, pp. 2947–2960. DOI: 10.1093/mnras/stz1453. arXiv: 1901.00863.

Di Carlo, Ugo N. et al. (2020a). "Binary Black Holes in the Pair Instability Mass Gap". In: *Monthly Notices of the Royal Astronomical Society* 497.1, pp. 1043–1049. DOI: 10.1093/mnras/staa1997. arXiv: 1911.01434.

Di Carlo, Ugo N. et al. (Oct. 2020b). "Binary Black Holes in Young Star Clusters: The Impact of Metallicity". In: *Monthly Notices of the Royal Astronomical Society* 498.1, pp. 495–506. DOI: 10.1093/mnras/staa2286.

Di Carlo, Ugo N. et al. (Nov. 2021). "Intermediate-mass black holes from stellar mergers in young star clusters". In: *Monthly Notices of the Royal Astronomical Society* 507.4, pp. 5132–5143. DOI: 10.1093/mnras/stab2390. arXiv: 2105.01085 [astro-ph.GA].

Dominik, Michal et al. (Nov. 2012). "Double Compact Objects. I. The Significance of the Common Envelope on Merger Rates". In: *The Astrophysical Journal* 759.1, p. 52. DOI: 10.1088/0004-637X/759/1/52.

Dominik, Michal et al. (June 2015). "Double Compact Objects III: Gravitational-wave Detection Rates". In: *The Astrophysical Journal* 806.2, p. 263. DOI: 10.1088/0004-637X/806/2/263. arXiv: 1405.7016.

Dosopoulou, Fani and Vicky Kalogera (June 2016a). "ORBITAL EVOLUTION OF MASS-TRANSFERRING ECCENTRIC BINARY SYSTEMS. I. PHASE-DEPENDENT EVOLUTION". In: *The Astrophysical Journal* 825.1, p. 70. DOI: 10.3847/0004-637X/825/1/70.

— (June 2016b). "ORBITAL EVOLUTION OF MASS-TRANSFERRING ECCENTRIC BINARY SYSTEMS. II. SECULAR EVOLUTION". In: *The Astrophysical Journal* 825.1, p. 71. DOI: 10.3847/0004-637X/825/1/71.

Downing, J. M. B. et al. (Sept. 2011). "Compact Binaries in Star Clusters - II. Escapers and Detection Rates". In: *Monthly Notices of the Royal Astronomical Society* 416.1, pp. 133–147. DOI: 10.1111/j.1365-2966.2011.19023.x.

Eggleton, P. P. (May 1983). "Aproximations to the Radii of Roche Lobes." In: *The Astrophysical Journal* 268, pp. 368–369. ISSN: 0004-637X. DOI: 10.1086/160960.

Eggleton, Peter (2006). *Evolutionary Processes in Binary and Multiple Stars*.

Eggleton, Peter P., Ludmila G. Kiseleva, and Piet Hut (June 1998). "The Equilibrium Tide Model for Tidal Friction". In: *The Astrophysical Journal* 499.2, p. 853. DOI: 10.1086/305670.

Eldridge, John J., Robert G. Izzard, and Christopher A. Tout (Mar. 2008). "The Effect of Massive Binaries on Stellar Populations and Supernova Progenitors". In: *Monthly Notices of the Royal Astronomical Society* 384, pp. 1109–1118. ISSN: 0035-8711. DOI: 10.1111/j.1365-2966.2007.12738.x.

Endal, A. S. and S. Sofia (Nov. 1976). "The evolution of rotating stars. I. Method and exploratory calculations for a 7 M sun star." In: *The Astrophysical Journal* 210, pp. 184–198. DOI: 10.1086/154817.

Ertl, T. et al. (Feb. 2016). "A Two-parameter Criterion for Classifying the Explodability of Massive Stars by the Neutrino-driven Mechanism". In: *The Astrophysical Journal* 818, p. 124. ISSN: 0004-637X. DOI: 10.3847/0004-637X/818/2/124.

Farag, Ebraheem et al. (Oct. 2022). "Resolving the Peak of the Black Hole Mass Spectrum". In: *The Astrophysical Journal* 937.2, 112, p. 112. DOI: 10.3847/1538-4357/ac8b83. arXiv: 2208.09624 [astro-ph.HE].

Farah, Amanda M., Maya Fishbach, and Daniel E. Holz (Feb. 2024). "Two of a Kind: Comparing Big and Small Black Holes in Binaries with Gravitational Waves". In: *ApJ* 962.1, p. 69. ISSN: 0004-637X. DOI: 10.3847/1538-4357/ad0558.

Farmer, R. et al. (Dec. 2019). "Mind the Gap: The Location of the Lower Edge of the Pair Instability Supernovae Black Hole Mass Gap". In: *ApJ* 887.1, p. 53. ISSN: 0004-637X, 1538-4357. DOI: 10.3847/1538-4357/ab518b. arXiv: 1910.12874 [astro-ph].

Farr, Ben, Daniel E. Holz, and Will M. Farr (Feb. 2018). "Using Spin to Understand the Formation of LIGO and Virgo's Black Holes". In: *The Astrophysical Journal Letters* 854.1, p. L9. ISSN: 2041-8213. DOI: 10.3847/2041-8213/aaaa64.

Farr, Will M. et al. (Aug. 2017). "Distinguishing spin-aligned and isotropic black hole populations with gravitational waves". In: *Nature* 548.7668, 426–429. ISSN: 1476-4687. DOI: 10.1038/nature23453.

Farrah, Duncan et al. (Feb. 2023). "A Preferential Growth Channel for Supermassive Black Holes in Elliptical Galaxies at z ≤ 2". In: *ApJ* 943.2, p. 133. ISSN: 0004-637X, 1538-4357. DOI: 10.3847/1538-4357/acac2e.

Farrell, Eoin et al. (Mar. 2021). "Is GW190521 the merger of black holes from the first stellar generations?" In: *Monthly Notices of the Royal Astronomical Society* 502.1, pp. L40–L44. DOI: 10.1093/mnrasl/slaa196. arXiv: 2009.06585 [astro-ph.SR].

Ferguson, Jason W. et al. (Apr. 2005). "Low-Temperature Opacities". In: *The Astrophysical Journal* 623.1, pp. 585–596. DOI: 10.1086/428642.

Foglizzo, T., L. Scheck, and H.-Th Janka (Dec. 2006). "Neutrino-Driven Convection versus Advection in Core-Collapse Supernovae". In: *The Astrophysical Journal* 652.2, pp. 1436–1450. DOI: 10.1086/508443.

Fowler, William A. and F. Hoyle (1964). "Neutrino Processes and Pair Formation in Massive Stars and Supernovae." In: *The Astrophysical Journals* 9, p. 201. DOI: 10.1086/190103.

Fragos, Tassos et al. (Oct. 2019). "The Complete Evolution of a Neutron-star Binary through a Common Envelope Phase Using 1D Hydrodynamic Simulations". In: *The Astrophysical Journal Letters* 883.2, p. L45. DOI: 10.3847/2041-8213/ab40d1.

Fragos, Tassos et al. (Feb. 2023). "POSYDON: A General-purpose Population Synthesis Code with Detailed Binary-evolution Simulations". In: *The Astrophysical Journal Supplement Series* 264, p. 45. ISSN: 0067-0049. DOI: 10.3847/1538-4365/ac90c1.

Fraley, Gary S. (Aug. 1968). "Supernovae Explosions Induced by Pair-Production Instability". In: *Astrophysics and Space Science* 2.1, pp. 96–114. DOI: 10.1007/BF00651498.

Fryer, C. L., S. E. Woosley, and A. Heger (Mar. 2001). "Pair-Instability Supernovae, Gravity Waves, and Gamma-Ray Transients". In: *ApJ* 550.1, p. 372. ISSN: 0004-637X. DOI: 10.1086/319719.

Fryer, Chris L. et al. (2012). "COMPACT REMNANT MASS FUNCTION: DEPENDENCE ON THE EXPLOSION MECHANISM AND METALLICITY". In: *The Astrophysical Journal*.

Gabrielli, Francesco et al. (Oct. 2024). "The cosmic rate of pair-instability supernovae". In: *Monthly Notices of the Royal Astronomical Society* 534.1, pp. 151–172. DOI: 10.1093/mnras/stae2048. arXiv: 2408.16823 [astro-ph.HE].

Gallegos-Garcia, Monica et al. (Dec. 2021). "Binary Black Hole Formation with Detailed Modeling: Stable Mass Transfer Leads to Lower Merger Rates". In: *The Astrophysical Journal* 922, p. 110. ISSN: 0004-637X. DOI: 10.3847/1538-4357/ac2610.

Ge, Hongwei et al. (June 2010). "ADIABATIC MASS LOSS IN BINARY STARS. I. COMPUTATIONAL METHOD". In: *The Astrophysical Journal* 717.2, p. 724. DOI: 10.1088/0004-637X/717/2/724.

Giacobbo, Nicola and Michela Mapelli (Oct. 2018). "The progenitors of compact-object binaries: impact of metallicity, common envelope and natal kicks". In: *Monthly Notices of the Royal Astronomical Society* 480.2, pp. 2011–2030. DOI: 10.1093/mnras/sty1999. arXiv: 1806.00001 [astro-ph.HE].

— (Mar. 2020). "Revising Natal Kick Prescriptions in Population Synthesis Simulations". In: *The Astrophysical Journal* 891.2, 141, p. 141. DOI: 10.3847/1538-4357/ab7335. arXiv: 1909.06385 [astro-ph.HE].

Gräfener, G. and W. R. Hamann (May 2008). "Mass loss from late-type WN stars and its Z-dependence. Very massive stars approaching the Eddington limit". In: *Astronomy & Astrophysics* 482.3, pp. 945–960. DOI: 10.1051/0004-6361:20066176. arXiv: 0803.0866 [astro-ph].

Gräfener, G. et al. (Nov. 2011). "The Eddington factor as the key to understand the winds of the most massive stars. Evidence for a Γ-dependence of Wolf-Rayet type mass loss". In: *Astronomy & Astrophysics* 535, A56, A56. DOI: 10.1051/0004-6361/201116701. arXiv: 1106.5361 [astro-ph.SR].

Graham, Alister W. and Lee R. Spitler (Aug. 2009). "Quantifying the coexistence of massive black holes and dense nuclear star clusters". In: *Monthly Notices of the Royal Astronomical Society* 397.4, pp. 2148–2162. DOI: 10.1111/j.1365-2966.2009.15118.x. arXiv: 0907.5250 [astro-ph.CO].

Graziani, L. et al. (June 2020). "Cosmic archaeology with massive stellar black hole binaries". In: *Monthly Notices of the Royal Astronomical Society* 495.1, pp. L81–L85. DOI: 10.1093/mnrasl/slaa063. arXiv: 2004.03603 [astro-ph.GA].

Hadjidemetriou, John D. (Jan. 1963). "Two-body problem with variable mass: A new approach". In: *Icarus* 2, pp. 440–451. DOI: 10.1016/0019-1035(63)90072-1.

Hamers, Adrian S. and Fani Dosopoulou (Feb. 2019). "An Analytic Model for Mass Transfer in Binaries with Arbitrary Eccentricity, with Applications to Triple-star Systems". In: *The Astrophysical Journal* 872.2, p. 119. DOI: 10.3847/1538-4357/ab001d.

Heger, A. and S. E. Woosley (2002). "The Nucleosynthetic Signature of Population III". In: *The Astrophysical Journal* 567.1, pp. 532–543. DOI: 10.1086/338487.

Heger, A. et al. (July 2003). "How Massive Single Stars End Their Life". In: *The Astrophysical Journal* 591.1, 288–300. ISSN: 1538-4357. DOI: 10.1086/375341.

Heggie, D. C. (Dec. 1975). "Binary Evolution in Stellar Dynamics." In: *Monthly Notices of the Royal Astronomical Society* 173, pp. 729–787. DOI: 10.1093/mnras/173.3.729.

Hendriks, D. D. et al. (Sept. 2023). *Pulsational Pair-Instability Supernovae in Gravitational-Wave and Electromagnetic Transients*. arXiv: 2309.09339 [astro-ph].

Herant, Marc et al. (Nov. 1994). "Inside the Supernova: A Powerful Convective Engine". In: *The Astrophysical Journal* 435, p. 339. ISSN: 0004-637X. DOI: 10.1086/174817.

Higgins, Erin R. and Jorick S. Vink (Feb. 2019). "Massive Star Evolution: Rotation, Winds, and Overshooting Vectors in the Mass-Luminosity Plane - I. A Calibrated Grid of Rotating Single Star Models". In: *A&A* 622, A50. ISSN: 0004-6361, 1432-0746. DOI: 10.1051/0004-6361/201834123.

Hills, J. G. (Aug. 1983). "The effect of low-velocity, low-mass intruders (collisionless gas) on the dynamical evolution of a binary system". In: *Astronomical Journal* 88, pp. 1269–1283. DOI: 10.1086/113418.

Hills, J. G. and L. W. Fullerton (Sept. 1980). "Computer simulations of close encounters between single stars and hard binaries". In: *Astronomical Journal* 85, pp. 1281–1291. DOI: 10.1086/112798.

Hobbs, G. et al. (July 2005). "A statistical study of 233 pulsar proper motions". In: *Monthly Notices of the Royal Astronomical Society* 360.3, pp. 974–992. DOI: 10.1111/j.1365-2966.2005.09087.x. arXiv: astro-ph/0504584 [astro-ph].

Horiuchi, S. et al. (Nov. 2014). "The Red Supergiant and Supernova Rate Problems: Implications for Core-Collapse Supernova Physics." In: *Monthly Notices of the Royal Astronomical Society* 445, pp. L99–L103. DOI: 10.1093/mnrasl/slu146.

Hurley, Jarrod R., Onno R. Pols, and Christopher A. Tout (July 2000). "Comprehensive Analytic Formulae for Stellar Evolution as a Function of Mass and Metallicity". In: *Monthly Notices of the Royal Astronomical Society* 315, pp. 543–569. ISSN: 0035-8711. DOI: 10.1046/j.1365-8711.2000.03426.x.

Hurley, Jarrod R., Christopher A. Tout, and Onno R. Pols (Feb. 2002). "Evolution of binary stars and the effect of tides on binary populations". In: *Monthly Notices of the Royal Astronomical Society* 329.4, pp. 897–928. DOI: 10.1046/j.1365-8711.2002.05038.x. arXiv: astro-ph/0201220 [astro-ph].

Iglesias, Carlos A. and Forrest J. Rogers (June 1996). "Updated Opal Opacities". In: *The Astrophysical Journal* 464, p. 943. DOI: 10.1086/177381.

Inomata, Keisuke et al. (June 2017). "Inflationary primordial black holes for the LIGO gravitational wave events and pulsar timing array experiments". In: *Physical Review D* 95.12. ISSN: 2470-0029. DOI: 10.1103/physrevd.95.123510.

Iorio, Giuliano et al. (Sept. 2023). "Compact Object Mergers: Exploring Uncertainties from Stellar and Binary Evolution with SEVN". In: *Monthly Notices of the Royal Astronomical Society* 524, pp. 426–470. ISSN: 0035-8711. DOI: 10.1093/mnras/stad1630.

Ivanova, N., S. Justham, and Ph. Podsiadlowski (Mar. 2015). "On the Role of Recombination in Common-Envelope Ejections". In: *Monthly Notices of the Royal Astronomical Society* 447, pp. 2181–2197. ISSN: 0035-8711. DOI: 10.1093/mnras/stu2582.

Ivanova, N. et al. (Feb. 2013). "Common Envelope Evolution: Where We Stand and How We Can Move Forward". In: *Astron Astrophys Rev* 21.1, p. 59. ISSN: 1432-0754. DOI: 10.1007/s00159-013-0059-2.

Ivanova, Natalia (May 2018). "On the Use of Hydrogen Recombination Energy during Common Envelope Events". In: *The Astrophysical Journal* 858, p. L24. ISSN: 0004-637X. DOI: 10.3847/2041-8213/aac101.

Janka, H. T. and E. Mueller (Feb. 1996). "Neutrino Heating, Convection, and the Mechanism of Type-II Supernova Explosions." In: *Astronomy & Astrophysics* 306, p. 167.

Janka, Hans-Thomas (2017). "Neutrino-Driven Explosions". In: *Handbook of Supernovae*. Springer International Publishing, pp. 1095–1150. DOI: 10.1007/978-3-319-21846-5_109.

Janka, Hans-Thomas, Tobias Melson, and Alexander Summa (2016). "Physics of Core-Collapse Supernovae in Three Dimensions: A Sneak Preview". In: *Annual Review of Nuclear and Particle Science* 66.1, pp. 341–375. DOI: 10.1146/annurev-nucl-102115-044747.

Justham, Stephen, Philipp Podsiadlowski, and Zhanwen Han (Jan. 2011). "On the formation of single and binary helium-rich subdwarf O stars". In: *Monthly Notices of the Royal Astronomical Society* 410.2, pp. 984–993. DOI: 10.1111/j.1365-2966.2010.17497.x. arXiv: 1008.1584 [astro-ph.SR].

Karathanasis, Christos, Suvodip Mukherjee, and Simone Mastrogiovanni (Aug. 2023). "Binary black holes population and cosmology in new lights: signature of PISN mass and formation channel in GWTC-3". In: *Monthly Notices of the Royal Astronomical Society* 523.3, pp. 4539–4555. DOI: 10.1093/mnras/stad1373. arXiv: 2204.13495 [astro-ph.CO].

Kimpson, Thomas O. et al. (Dec. 2016). "Hierarchical black hole triples in young star clusters: impact of Kozai-Lidov resonance on mergers". In: *Monthly Notices of the Royal Astronomical Society* 463.3, pp. 2443–2452. DOI: 10.1093/mnras/stw2085. arXiv: 1608.05422 [astro-ph.GA].

Kippenhahn, R. and H. C. Thomas (Jan. 1970). "A Simple Method for the Solution of the Stellar Structure Equations Including Rotation and Tidal Forces". In: *IAU Colloq. 4: Stellar Rotation*. Ed. by Arne Slettebak, p. 20.

Kotake, Kei, Katsuhiko Sato, and Keitaro Takahashi (Apr. 2006). "Explosion Mechanism, Neutrino Burst and Gravitational Wave in Core-Collapse Supernovae". In: *Rep. Prog. Phys.* 69.4, pp. 971–1143. ISSN: 0034-4885, 1361-6633. DOI: 10.1088/0034-4885/69/4/R03.

Kremer, Kyle et al. (Nov. 2020). "Populating the Upper Black Hole Mass Gap through Stellar Collisions in Young Star Clusters". In: *The Astrophysical Journal* 903.1, 45, p. 45. DOI: 10.3847/1538-4357/abb945. arXiv: 2006.10771 [astro-ph.HE].

Kroupa, Pavel (Apr. 2001). "On the Variation of the Initial Mass Function". In: *Monthly Notices of the Royal Astronomical Society* 322, pp. 231–246. ISSN: 0035-8711. DOI: 10.1046/j.1365-8711.2001.04022.x.

Kruckow, Matthias U. et al. (Dec. 2018). "Progenitors of Gravitational Wave Mergers: Binary Evolution with the Stellar Grid-Based Code COMBINE". In: *Monthly Notices of the Royal Astronomical Society* 481, pp. 1908–1949. ISSN: 0035-8711. DOI: 10.1093/mnras/sty2190.

Lada, Charles J. and Elizabeth A. Lada (Sept. 2003). "Embedded Clusters in Molecular Clouds". In: *Annual Review of Astronomy and Astrophysics* 41.1, 57–115. ISSN: 1545-4282. DOI: 10.1146/annurev.astro.41.011802.094844.

Langer, N., M. F. El Eid, and K. J. Fricke (Apr. 1985). "Evolution of massive stars with semiconvective diffusion". In: *Astronomy & Astrophysics* 145.1, pp. 179–191.

Larson, Richard B. (Dec. 1998). "Early star formation and the evolution of the stellar initial mass function in galaxies". In: *Monthly Notices of the Royal Astronomical Society* 301.2, pp. 569–581. DOI: 10.1046/j.1365-8711.1998.02045.x. arXiv: astro-ph/9808145 [astro-ph].

Leigh, N. W. C. et al. (Mar. 2018). "On the rate of black hole binary mergers in galactic nuclei due to dynamical hardening". In: *Monthly Notices of the Royal Astronomical Society* 474.4, pp. 5672–5683. DOI: 10.1093/mnras/stx3134. arXiv: 1711.10494 [astro-ph.GA].

Levermore, C. D. and G. C. Pomraning (Aug. 1981). "A Flux-Limited Diffusion Theory". In: *The Astrophysical Journal* 248, p. 321. DOI: 10.1086/159157.

LIGO Scientific Collaboration and Virgo Collaboration et al. (Sept. 2020). "GW190521: A Binary Black Hole Merger with a Total Mass of $150\text{ }\text{ }{M}_{\ensuremath{\bigodot}}$". In: *Phys. Rev. Lett.* 125.10, p. 101102. DOI: 10.1103/PhysRevLett.125.101102.

Limongi, M. and A. Chieffi (Nov. 2008). "Final stages of massive stars. SN explosion and explosive nucleosynthesis". In: *EAS Publications Series*. Ed. by C. Charbonnel and J. P. Zahn. Vol. 32. EAS Publications Series, pp. 233–281. DOI: 10.1051/eas:0832007.

Limongi, Marco (Jan. 2017). *Supernovae from Massive Stars*, p. 513. DOI: 10.1007/978-3-319-21846-5_119.

Limongi, Marco and Alessandro Chieffi (July 2003). "Evolution, Explosion, and Nucleosynthesis of Core-Collapse Supernovae". In: *The Astrophysical Journal* 592.1, pp. 404–433. DOI: 10.1086/375703.

— (July 2018). "Presupernova Evolution and Explosive Nucleosynthesis of Rotating Massive Stars in the Metallicity Range -3 \ensuremath\leq [Fe/H] \ensuremath\leq 0". In: *The Astrophysical Journals* 237.1, p. 13. DOI: 10.3847/1538-4365/aacb24.

— (Oct. 2020). "Hydrodynamical Modeling of the Light Curves of Core-collapse Supernovae with HYPERION. I. The Mass Range 13–25 M $ødot$, the Metallicities -3 $\leq$ [Fe/H] $\leq$ 0, and the Case of SN 1999em". In: *ApJ* 902.2, p. 95. ISSN: 0004-637X. DOI: 10.3847/1538-4357/abb4e8.

Limongi, Marco, Oscar Straniero, and Alessandro Chieffi (Aug. 2000). "Massive Stars in the Range 13-25 M_{solar}: Evolution and Nucleosynthesis. II. The Solar Metallicity Models". In: *The Astrophysical Journals* 129.2, pp. 625–664. DOI: 10.1086/313424.

Limongi, Marco et al. (Nov. 2023). *Evolution and Final Fate of Solar Metallicity Stars in the Mass Range 7-15 Msun. I. The Transition from AGB to SAGB Stars, Electron Capture and Core Collapse Supernovae Progenitors*. arXiv: 2312.00107 [astro-ph].

Liu, Boyuan and Volker Bromm (Nov. 2020). "The Population III Origin of GW190521". In: *The Astrophysical Journal Letters* 903.2, p. L40. DOI: 10.3847/2041-8213/abc552.

Loon, J. Th. van et al. (July 2005). "An empirical formula for the mass-loss rates of dust-enshrouded red supergiants and oxygen-rich Asymptotic Giant Branch stars". In: *Astronomy & Astrophysics* 438.1, 273–289. ISSN: 1432-0746. DOI: 10.1051/0004-6361:20042555.

MacLeod, Morgan et al. (Feb. 2017). "Lessons from the Onset of a Common Envelope Episode: The Remarkable M31 2015 Luminous Red Nova Outburst". In: *ApJ* 835.2, p. 282. ISSN: 0004-637X. DOI: 10.3847/1538-4357/835/2/282.

Maeder, A. (Feb. 2003). "Stellar rotation: Evidence for a large horizontal turbulence and its effects on evolution". In: *Astronomy & Astrophysics* 399, pp. 263–269. DOI: 10.1051/0004-6361:20021731. arXiv: astro-ph/0301258 [astro-ph].

Mandel, Ilya and Alison Farmer (Apr. 2022). "Merging Stellar-Mass Binary Black Holes". In: *Physics Reports* 955, pp. 1–24. ISSN: 0370-1573. DOI: 10.1016/j.physrep.2022.01.003.

Mandel, Ilya and Tassos Fragos (June 2020). "An Alternative Interpretation of GW190412 as a Binary Black Hole Merger with a Rapidly Spinning Secondary". In: *The Astrophysical Journal* 895, p. L28. ISSN: 0004-637X. DOI: 10.3847/2041-8213/ab8e41.

Mapelli, M. et al. (Dec. 2005). "The fingerprint of binary intermediate-mass black holes in globular clusters: suprathermal stars and angular momentum alignment". In: *Monthly Notices of the Royal Astronomical Society* 364.4, pp. 1315–1326. DOI: 10.1111/j.1365-2966.2005.09653.x. arXiv: astro-ph/0506405 [astro-ph].

Mapelli, M. et al. (Mar. 2013). "Dynamics of Stellar Black Holes in Young Star Clusters with Different Metallicities - I. Implications for X-ray Binaries". In: *Monthly Notices of the Royal Astronomical Society* 429, pp. 2298–2314. ISSN: 0035-8711. DOI: 10.1093/mnras/sts500.

Mapelli, Michela (2016). "Massive Black Hole Binaries from Runaway Collisions: The Impact of Metallicity". In: *Monthly Notices of the Royal Astronomical Society* 459.4, pp. 3432–3446. DOI: 10.1093/mnras/stw869.

— (2018). *Astrophysics of Stellar Black Holes*.

— (2021). "Formation Channels of Single and Binary Stellar-Mass Black Holes". In: *Handbook of Gravitational Wave Astronomy*, p. 16. DOI: 10.1007/978-981-15-4702-7_16-1.

Mapelli, Michela and Nicola Giacobbo (Oct. 2018). "The Cosmic Merger Rate of Neutron Stars and Black Holes". In: *Monthly Notices of the Royal Astronomical Society* 479.4, pp. 4391–4398. DOI: 10.1093/mnras/sty1613.

Mapelli, Michela and Nicola Giacobbo (Oct. 2018). "The cosmic merger rate of neutron stars and black holes". In: *Monthly Notices of the Royal Astronomical Society* 479.4, pp. 4391–4398. DOI: 10.1093/mnras/sty1613. arXiv: 1806.04866 [astro-ph.HE].

Mapelli, Michela et al. (2020). "Impact of the Rotation and Compactness of Progenitors on the Mass of Black Holes". In: *The Astrophysical Journal*.

Marassi, S et al. (2019). "Evolution of Dwarf Galaxies Hosting GW150914-like Events". In: *Monthly Notices of the Royal Astronomical Society*.

Marchant, Pablo et al. (Sept. 2019). "Pulsational Pair-instability Supernovae in Very Close Binaries". In: *ApJ* 882.1, p. 36. ISSN: 0004-637X, 1538-4357. DOI: 10.3847/1538-4357/ab3426.

Marchant, Pablo et al. (June 2021). "The Role of Mass Transfer and Common Envelope Evolution in the Formation of Merging Binary Black Holes". In: *Astronomy and Astrophysics* 650, A107. ISSN: 0004-6361. DOI: 10.1051/0004-6361/202039992.

Mathis, S., A. Palacios, and J. P. Zahn (Oct. 2004). "On shear-induced turbulence in rotating stars". In: *Astronomy & Astrophysics* 425, pp. 243–247. DOI: 10.1051/0004-6361:20040279. arXiv: astro-ph/0403580 [astro-ph].

Matsumoto, Tatsuya and Brian D. Metzger (Oct. 2022). "Light-Curve Model for Luminous Red Novae and Inferences about the Ejecta of Stellar Mergers". In: *The Astrophysical Journal* 938, p. 5. ISSN: 0004-637X. DOI: 10.3847/1538-4357/ac6269.

McKernan, B., K. E. S. Ford, and R. O'Shaughnessy (Nov. 2020). "Black hole, neutron star, and white dwarf merger rates in AGN discs". In: *Monthly Notices of the Royal Astronomical Society* 498.3, pp. 4088–4094. DOI: 10.1093/mnras/staa2681. arXiv: 2002.00046 [astro-ph.HE].

McKernan, B. et al. (Sept. 2012). "Intermediate mass black holes in AGN discs - I. Production and growth". In: *Monthly Notices of the Royal Astronomical Society* 425.1, pp. 460–469. DOI: 10.1111/j.1365-2966.2012.21486.x. arXiv: 1206.2309 [astro-ph.GA].

McKernan, B. et al. (June 2014). "Intermediate-mass black holes in AGN discs - II. Model predictions and observational constraints". In: *Monthly Notices of the Royal Astronomical Society* 441.1, pp. 900–909. DOI: 10.1093/mnras/stu553. arXiv: 1403.6433 [astro-ph.GA].

McKernan, B. et al. (May 2020). "Monte Carlo simulations of black hole mergers in AGN discs: Low χ_{eff} mergers and predictions for LIGO". In: *Monthly Notices of the Royal Astronomical Society* 494.1, pp. 1203–1216. DOI: 10.1093/mnras/staa740. arXiv: 1907.04356 [astro-ph.HE].

McKernan, Barry et al. (Oct. 2018). "Constraining Stellar-mass Black Hole Mergers in AGN Disks Detectable with LIGO". In: *The Astrophysical Journal* 866.1, p. 66. DOI: 10.3847/1538-4357/aadae5.

Mehta, Ajit Kumar et al. (Jan. 2022). "Observing Intermediate-mass Black Holes and the Upper Stellar-mass gap with LIGO and Virgo". In: *The Astrophysical Journal* 924.1, 39, p. 39. DOI: 10.3847/1538-4357/ac3130. arXiv: 2105.06366 [gr-qc].

Metzger, Brian D. and Ondřej Pejcha (Nov. 2017). "Shock-Powered Light Curves of Luminous Red Novae as Signatures of Pre-Dynamical Mass-Loss in Stellar Mergers". In: *Monthly Notices of the Royal Astronomical Society* 471.3, pp. 3200–3211. ISSN: 0035-8711. DOI: 10.1093/mnras/stx1768.

Meynet, G., S. Ekström, and A. Maeder (Feb. 2006). "The early star generations: the dominant effect of rotation on the CNO yields". In: *Astronomy & Astrophysics* 447.2, pp. 623–639. DOI: 10.1051/0004-6361:20053070. arXiv: astro-ph/0510560 [astro-ph].

Meynet, G. and A. Maeder (May 1997). "Stellar evolution with rotation. I. The computational method and the inhibiting effect of the μ-gradient." In: *Astronomy & Astrophysics* 321, pp. 465–476.

Miller-Jones, James C. A. et al. (Mar. 2021). "Cygnus X-1 contains a 21–solar mass black hole—Implications for massive star winds". In: *Science* 371.6533, 1046–1049. ISSN: 1095-9203. DOI: 10.1126/science.abb3363.

Moe, Maxwell and Rosanne Di Stefano (June 2017). "Mind Your Ps and Qs: The Interrelation between Period (P) and Mass-ratio (Q) Distributions of Binary Stars". In: *The Astrophysical Journal Supplement Series* 230.2, p. 15. DOI: 10.3847/1538-4365/aa6fb6.

Moody, Kenneth and Steinn Sigurdsson (Dec. 2008). "MODELING THE RETENTION PROBABILITY OF BLACK HOLES IN GLOBULAR CLUSTERS: KICKS AND RATES". In: *The Astrophysical Journal* 690.2, p. 1370. DOI: 10.1088/0004-637X/690/2/1370.

Moriya, Takashi et al. (Aug. 2010). "Fallback Supernovae: A Possible Origin of Peculiar Supernovae with Extremely Low Explosion Energies". In: *The Astrophysical Journal* 719, pp. 1445–1453. ISSN: 0004-637X. DOI: 10.1088/0004-637X/719/2/1445.

Morozova, Viktoriya et al. (2015). "Light Curves of Core-collapse Supernovae with Substantial Mass Loss Using the New Open-source SuperNova Explosion Code (SNEC)". In: *Astrophysical Journal*.

Muijres, L. E. et al. (Feb. 2011). "Predictions of the effect of clumping on the wind properties of O-type stars". In: *Astronomy & Astrophysics* 526, A32, A32. DOI: 10.1051/0004-6361/201014290.

Nakamura, Takayoshi et al. (July 2001). "Explosive Nucleosynthesis in Hypernovae". In: *The Astrophysical Journal* 555, pp. 880–899. ISSN: 0004-637X. DOI: 10.1086/321495.

Neijssel, Coenraad J. et al. (Dec. 2019). "The Effect of the Metallicity-Specific Star Formation History on Double Compact Object Mergers". In: *Monthly Notices of the Royal Astronomical Society* 490, pp. 3740–3759. ISSN: 0035-8711. DOI: 10.1093/mnras/stz2840.

Nelemans, Gijs et al. (2000). *Reconstructing the evolution of double helium white dwarfs: envelope loss without spiral-in*. arXiv: astro-ph/0006216 [astro-ph].

Nguyen, C. T. et al. (Sept. 2022). "PARSEC V2.0: Stellar tracks and isochrones of low- and intermediate-mass stars with rotation". In: *Astronomy & Astrophysics* 665, A126, A126. DOI: 10.1051/0004-6361/202244166. arXiv: 2207.08642 [astro-ph.SR].

Nomoto, Ken'ichi et al. (Oct. 2006). "Nucleosynthesis Yields of Core-Collapse Supernovae and Hypernovae, and Galactic Chemical Evolution". In: *Nuclear Physics A* 777, pp. 424–458. ISSN: 0375-9474. DOI: 10.1016/j.nuclphysa.2006.05.008.

O'Connor, Evan and Christian D. Ott (2011). "Black Hole Formation in Failing Core-Collapse Supernovae". In: *The Astrophysical Journal*.

Orosz, Jerome A. (2003). *Inventory of Black Hole Binaries*.

Özel, Feryal et al. (Sept. 2012). "On the Mass Distribution and Birth Masses of Neutron Stars". In: *The Astrophysical Journal* 757.1, 55, p. 55. DOI: 10.1088/0004-637X/757/1/55. arXiv: 1201.1006 [astro-ph.HE].

Özel, Feryal et al. (Mar. 2016). "The Dense Matter Equation of State from Neutron Star Radius and Mass Measurements". In: *The Astrophysical Journal* 820.1, 28, p. 28. DOI: 10.3847/0004-637X/820/1/28. arXiv: 1505.05155 [astro-ph.HE].

Pastorello, A. et al. (Oct. 2019). "Luminous Red Novae: Stellar Mergers or Giant Eruptions?" In: *A&A* 630, A75. ISSN: 0004-6361, 1432-0746. DOI: 10.1051/0004-6361/201935999.

Pastorello, A. et al. (Feb. 2021a). "Forbidden Hugs in Pandemic Times - I. Luminous Red Nova AT 2019zhd, a New Merger in M 31". In: *A&A* 646, A119. ISSN: 0004-6361, 1432-0746. DOI: 10.1051/0004-6361/202039952.

Pastorello, A. et al. (Mar. 2021b). "Forbidden Hugs in Pandemic Times - II. The Luminous Red Nova Variety: AT 2020hat and AT 2020kog". In: *A&A* 647, A93. ISSN: 0004-6361, 1432-0746. DOI: 10.1051/0004-6361/202039953.

Patton, Rachel A. and Tuguldur Sukhbold (Dec. 2020). "Towards a realistic explosion landscape for binary population synthesis". In: *Monthly Notices of the Royal Astronomical Society* 499.2, pp. 2803–2816. DOI: 10.1093/mnras/staa3029. arXiv: 2005.03055 [astro-ph.SR].

Patton, Rachel A, Tuguldur Sukhbold, and J J Eldridge (Feb. 2022). "Comparing Compact Object Distributions from Mass- and Presupernova Core Structure-Based Prescriptions". In: *Monthly Notices of the Royal Astronomical Society* 511.1, pp. 903–913. ISSN: 0035-8711, 1365-2966. DOI: 10.1093/mnras/stab3797.

Pavlovskii, K. et al. (Feb. 2017). "Stability of Mass Transfer from Massive Giants: Double Black Hole Binary Formation and Ultraluminous X-ray Sources". In: *Monthly Notices of the Royal Astronomical Society* 465, pp. 2092–2100. ISSN: 0035-8711. DOI: 10.1093/mnras/stw2786.

Peters, P. C. (Nov. 1964). "Gravitational Radiation and the Motion of Two Point Masses". In: *Phys. Rev.* 136 (4B), B1224–B1232. DOI: 10.1103/PhysRev.136.B1224.

Portegies Zwart, S. F. and F. Verbunt (May 1996). "Population synthesis of high-mass binaries." In: *Astronomy & Astrophysics* 309, pp. 179–196.

Portegies Zwart, Simon F., Stephen L.W. McMillan, and Mark Gieles (Aug. 2010). "Young Massive Star Clusters". In: *Annual Review of Astronomy and Astrophysics* 48.1, 431–493. ISSN: 1545-4282. DOI: 10.1146/annurev-astro-081309-130834.

Puls, J. et al. (Aug. 2006). "Bright OB stars in the Galaxy. III. Constraints on the radial stratification of the clumping factor in hot star winds from a combined H_α, IR and radio analysis". In: *Astronomy & Astrophysics* 454.2, pp. 625–651. DOI: 10.1051/0004-6361:20065073. arXiv: astro-ph/0604372 [astro-ph].

Quinlan, Gerald D. (July 1996). "The dynamical evolution of massive black hole binaries I. Hardening in a fixed stellar background". In: *New Astronomy* 1.1, 35–56. ISSN: 1384-1076. DOI: 10.1016/s1384-1076(96)00003-6.

Rakavy, G. and G. Shaviv (June 1967). "Instabilities in Highly Evolved Stellar Models". In: *The Astrophysical Journal* 148, p. 803. DOI: 10.1086/149204.

Rastello, S. et al. (Feb. 2019). "Stellar black hole binary mergers in open clusters". In: *Monthly Notices of the Royal Astronomical Society* 483.1, pp. 1233–1246. DOI: 10.1093/mnras/sty3193. arXiv: 1811.10628 [astro-ph.GA].

Rastello, Sara et al. (Sept. 2020). "Dynamics of Black Hole-Neutron Star Binaries in Young Star Clusters". In: *Monthly Notices of the Royal Astronomical Society* 497, pp. 1563–1570. ISSN: 0035-8711. DOI: 10.1093/mnras/staa2018.

Rastello, Sara et al. (Aug. 2021). "Dynamics of binary black holes in low-mass young star clusters". In: *Monthly Notices of the Royal Astronomical Society* 507.3, 3612–3625. ISSN: 1365-2966. DOI: 10.1093/mnras/stab2355.

Renzo, M. and N. Smith (Aug. 2024). *Pair-Instability Evolution and Explosions in Massive Stars*. arXiv: 2407.16113 [astro-ph].

Renzo, M. et al. (Aug. 2020). "Predictions for the Hydrogen-Free Ejecta of Pulsational Pair-Instability Supernovae". In: *Astronomy and Astrophysics* 640, A56. ISSN: 0004-6361. DOI: 10.1051/0004-6361/202037710.

Ricker, Paul M. and Ronald E. Taam (Jan. 2012). "AN AMR STUDY OF THE COMMON-ENVELOPE PHASE OF BINARY EVOLUTION". In: *ApJ* 746.1, p. 74. ISSN: 0004-637X. DOI: 10.1088/0004-637X/746/1/74.

Roberti, Lorenzo, Marco Limongi, and Alessandro Chieffi (Feb. 2024). "Zero and Extremely Low-metallicity Rotating Massive Stars: Evolution, Explosion, and Nucleosynthesis Up to the Heaviest Nuclei". In: *The Astrophysical Journal Supplement Series, Volume 270, Issue 2, id.28, 41 pp.* 270.2, p. 28. ISSN: 0067-0049. DOI: 10.3847/1538-4365/ad1686.

Rodriguez, Carl L., Sourav Chatterjee, and Frederic A. Rasio (Apr. 2016). "Binary Black Hole Mergers from Globular Clusters: Masses, Merger Rates, and the Impact of Stellar Evolution". In: *Phys. Rev. D* 93.8, p. 084029. DOI: 10.1103/PhysRevD.93.084029.

Rodriguez, Carl L. et al. (2015). "Binary Black Hole Mergers from Globular Clusters: Implications for Advanced LIGO". In: *Physical Review Letters* 115.5, p. 051101. DOI: 10.1103/physrevlett.115.051101.

Rodriguez, Carl L. et al. (2019). "Black Holes: The next Generation—Repeated Mergers in Dense Star Clusters and Their Gravitational-Wave Properties". In: *Phys. Rev. D* 100.4, p. 043027. DOI: 10.1103/PhysRevD.100.043027.

Röpke, Friedrich K. and Orsola De Marco (Dec. 2023). "Simulations of common-envelope evolution in binary stellar systems: physical models and numerical techniques". In: *Living Reviews in Computational Astrophysics* 9.1, 2, p. 2. DOI: 10.1007/s41115-023-00017-x. arXiv: 2212.07308 [astro-ph.SR].

Roupas, Zacharias and Demosthenes Kazanas (Dec. 2019). "Generation of massive stellar black holes by rapid gas accretion in primordial dense clusters". In: *Astronomy & Astrophysics* 632, L8, p. L8. DOI: 10.1051/0004-6361/201937002. arXiv: 1911.03915 [astro-ph.GA].

Rudolf Kippenhahn Alfred Weigert, Achim Weiss (2012). *Stellar Structure and Evolution*. Ed. by 2012 Springer-Verlag Berlin Heidelberg. Second.

Sabhahit, Gautham N. et al. (Sept. 2023). "Very massive stars and pair-instability supernovae: mass-loss framework for low metallicity". In: *Monthly Notices of the Royal Astronomical Society* 524.1, pp. 1529–1546. DOI: 10.1093/mnras/stad1888. arXiv: 2306.11785 [astro-ph.SR].

Sadiq, Jam, Thomas Dent, and Daniel Wysocki (June 2022). "Flexible and fast estimation of binary merger population distributions with an adaptive kernel density estimator". In: *Phys. Rev. D* 105 (12), p. 123014. DOI: 10.1103/PhysRevD.105.123014.

Safarzadeh, Mohammadtaher and Zoltán Haiman (Nov. 2020). "Formation of GW190521 via Gas Accretion onto Population III Stellar Black Hole Remnants Born in High-redshift

Minihalos". In: *The Astrophysical Journal Letters* 903.1, p. L21. DOI: 10.3847/2041-8213/abc253.

Saha, Megh Nad (Oct. 1919). "On Radiation-Pressure and the Quantum Theory". In: *The Astrophysical Journal* 50, p. 220. DOI: 10.1086/142497.

Sana, H. et al. (July 2012). "Binary Interaction Dominates the Evolution of Massive Stars". In: *Science* 337, p. 444. ISSN: 0036-8075. DOI: 10.1126/science.1223344.

Sandquist, Eric L. et al. (June 1998). "Double Core Evolution. X. Through the Envelope Ejection Phase". In: *The Astrophysical Journal* 500.2, pp. 909–922. DOI: 10.1086/305778.

Schneider, F. R. N. et al. (May 2015). "Evolution of Mass Functions of Coeval Stars through Wind Mass Loss and Binary Interactions". In: *The Astrophysical Journal* 805, p. 20. ISSN: 0004-637X. DOI: 10.1088/0004-637X/805/1/20.

Schwarzschild, M. and R. Härm (1958). "Evolution of Very Massive Stars." In: *Astrophysical Journal*.

Secunda, Amy et al. (June 2019). "Orbital Migration of Interacting Stellar Mass Black Holes in Disks around Supermassive Black Holes". In: *The Astrophysical Journal* 878.2, p. 85. DOI: 10.3847/1538-4357/ab20ca.

Shen, Yangping et al. (Mar. 2023). "New Determination of the $12^C(\alpha,\gamma)^{16}O$ Reaction Rate and Its Impact on the Black-hole Mass Gap". In: *The Astrophysical Journal* 945.1, p. 41. DOI: 10.3847/1538-4357/acb7de.

Shigeyama, Toshikazu and Ken'ichi Nomoto (Sept. 1990). "Theoretical Light Curve of SN 1987A and Mixing of Hydrogen and Nickel in the Ejecta". In: *The Astrophysical Journal* 360, p. 242. DOI: 10.1086/169114.

Sigurdsson, Steinn and Lars Hernquist (July 1993). "Primordial black holes in globular clusters". In: *Nature* 364.6436, pp. 423–425. DOI: 10.1038/364423a0.

Sigurdsson, Steinn and E. S. Phinney (Aug. 1995). "Dynamics and Interactions of Binaries and Neutron Stars in Globular Clusters". In: *Astrophysical Journal Supplement* 99, p. 609. DOI: 10.1086/192199. arXiv: astro-ph/9412078 [astro-ph].

Sobolev, V. V. (1960). *Moving Envelopes of Stars*. DOI: 10.4159/harvard.9780674864658.

Spera, M. and M. Mapelli (2017). "Very Massive Stars, Pair-Instability Supernovae and Intermediate-Mass Black Holes with the Sevn Code". In: *Monthly Notices of the Royal Astronomical Society*.

Spera, Mario, Michela Mapelli, and Alessandro Bressan (Aug. 2015). "The Mass Spectrum of Compact Remnants from the PARSEC Stellar Evolution Tracks". In: *Monthly Notices of the Royal Astronomical Society* 451.4, pp. 4086–4103. DOI: 10.1093/mnras/stv1161.

Spera, Mario, Alessandro Alberto Trani, and Mattia Mencagli (June 2022). "Compact Binary Coalescences: Astrophysical Processes and Lessons Learned". In: *Galaxies* 10.4, p. 76. DOI: 10.3390/galaxies10040076.

Spera, Mario et al. (May 2019). "Merging Black Hole Binaries with the SEVN Code". In: *Monthly Notices of the Royal Astronomical Society* 485.1, pp. 889–907. DOI: 10.1093/mnras/stz359.

Stevenson, Simon et al. (Sept. 2019). "The Impact of Pair-instability Mass Loss on the Binary Black Hole Mass Distribution". In: *The Astrophysical Journal* 882, p. 121. ISSN: 0004-637X. DOI: 10.3847/1538-4357/ab3981.

Stothers, R. (1970). "Internal Structure of Upper Main-Sequence Stars". In: *Monthly Notices of the Royal Astronomical Society*.

Sukhbold, Tuguldur, S. E. Woosley, and Alexander Heger (June 2018). "A High-resolution Study of Presupernova Core Structure". In: *ApJ* 860.2, p. 93. ISSN: 0004-637X. DOI: 10.3847/1538-4357/aac2da.

Sukhbold, Tuguldur et al. (2016). "CORE-COLLAPSE SUPERNOVAE FROM 9 TO 120 SOLAR MASSES BASED ON NEUTRINO-POWERED EXPLOSIONS". In: *The Astrophysical Journal*.

Takahashi, Koh (Aug. 2018). "The Low Detection Rate of Pair-instability Supernovae and the Effect of the Core Carbon Fraction". In: *The Astrophysical Journal* 863.2, 153, p. 153. DOI: 10.3847/1538-4357/aad2d2. arXiv: 1807.05373 [astro-ph.HE].

Talbot, Colm and Eric Thrane (Apr. 2018). "Measuring the Binary Black Hole Mass Spectrum with an Astrophysically Motivated Parameterization". In: *The Astrophysical Journal* 856.2, p. 173. DOI: 10.3847/1538-4357/aab34c.

Talon, S. and J. P. Zahn (Feb. 1997). "Anisotropic diffusion and shear instabilities." In: *Astronomy & Astrophysics* 317, pp. 749–751. DOI: 10.48550/arXiv.astro-ph/9609010. arXiv: astro-ph/9609010 [astro-ph].

Tang, Jing et al. (Dec. 2014). "New PARSEC evolutionary tracks of massive stars at low metallicity: testing canonical stellar evolution in nearby star-forming dwarf galaxies". In: *Monthly Notices of the Royal Astronomical Society* 445.4, pp. 4287–4305. DOI: 10.1093/mnras/stu2029. arXiv: 1410.1745 [astro-ph.SR].

Tanikawa, Ataru et al. (Mar. 2021). "Merger Rate Density of Population III Binary Black Holes Below, Above, and in the Pair-instability Mass Gap". In: *The Astrophysical Journal* 910.1, p. 30. DOI: 10.3847/1538-4357/abe40d.

Tauris, T. M. et al. (Sept. 2017). "Formation of Double Neutron Star Systems". In: *The Astrophysical Journal* 846.2, 170, p. 170. DOI: 10.3847/1538-4357/aa7e89. arXiv: 1706.09438 [astro-ph.HE].

Tauris, Thomas M., Norbert Langer, and Philipp Podsiadlowski (Aug. 2015). "Ultra-stripped supernovae: progenitors and fate". In: *Monthly Notices of the Royal Astronomical Society* 451.2, pp. 2123–2144. DOI: 10.1093/mnras/stv990. arXiv: 1505.00270 [astro-ph.SR].

Thielemann, Friedrich-Karl, Masa-Aki Hashimoto, and Ken'ichi Nomoto (Jan. 1990). "Explosive Nucleosynthesis in SN 1987A. II. Composition, Radioactivities, and the Neutron Star Mass". In: *The Astrophysical Journal* 349, p. 222. ISSN: 0004-637X. DOI: 10.1086/168308.

Thielemann, Friedrich-Karl, Ken'ichi Nomoto, and Masa-Aki Hashimoto (Mar. 1996). "Core-Collapse Supernovae and Their Ejecta". In: *The Astrophysical Journal* 460, p. 408. DOI: 10.1086/176980.

Tout, Christopher A. et al. (Nov. 1997). "Rapid binary star evolution for N-body simulations and population synthesis". In: *Monthly Notices of the Royal Astronomical Society* 291.4, pp. 732–748. DOI: 10.1093/mnras/291.4.732.

Trani, A. A. et al. (June 2021). "Spin misalignment of black hole binaries from young star clusters: implications for the origin of gravitational waves events". In: *Monthly Notices of the Royal Astronomical Society* 504.1, pp. 910–919. DOI: 10.1093/mnras/stab967. arXiv: 2102.01689 [astro-ph.HE].

Trani, Alessandro A., Michiko S. Fujii, and Mario Spera (Apr. 2019). "The Keplerian Three-body Encounter. I. Insights on the Origin of the S-stars and the G-objects in the Galactic Center". In: *The Astrophysical Journal* 875.1, 42, p. 42. DOI: 10.3847/1538-4357/ab0e70. arXiv: 1809.07339 [astro-ph.GA].

Trani, Alessandro A. and Mario Spera (Jan. 2023). "Modeling gravitational few-body problems with tsunami and okinami". In: *The Predictive Power of Computational Astrophysics as a Discover Tool*. Ed. by Dmitry Bisikalo, Dmitri Wiebe, and Christian Boily. Vol. 362. IAU Symposium, pp. 404–409. DOI: 10.1017/S1743921322001818. arXiv: 2206.10583 [astro-ph.HE].

Tutukov, A. V. and L. R. Yungelson (Feb. 1993). "The merger rate of neutron star and black hole binaries." In: *Monthly Notices of the Royal Astronomical Society* 260, pp. 675–678. DOI: 10.1093/mnras/260.3.675.

Ugliano, Marcella et al. (Sept. 2012). "Progenitor-Explosion Connection and Remnant Birth Masses for Neutrino-driven Supernovae of Iron-core Progenitors". In: *The Astrophysical Journal* 757.1, p. 69. DOI: 10.1088/0004-637X/757/1/69.

Ugolini, Cristiano et al. (2024). "The initial mass-remnant mass relation from core collapse supernovae [in press.]" In: *Astronomy & Astrophysics*.

Ugolini, Cristiano et al. (in prep). "Constraining the features of the BBH mass distribution through population synthesis simulation [in prep.]" In: *Astronomy & Astrophysics*.

Umeda, Hideyuki and Ken'ichi Nomoto (Jan. 2002). "Nucleosynthesis of Zinc and Iron Peak Elements in Population III Type II Supernovae: Comparison with Abundances of Very Metal Poor Halo Stars". In: *The Astrophysical Journal* 565.1, pp. 385–404. DOI: 10.1086/323946.

Utrobin, V. (Mar. 1993). "Hydrodynamic Study of Supernova 1987A: Near the Peak Luminosity." In: *Astronomy & Astrophysics* 270, pp. 249–258.

Utrobin, V. P. (Sept. 2006). "An Optimal Hydrodynamic Model for the Normal Type IIP Supernova 1999em". In: *Astronomy & Astrophysics* 461.1, pp. 233–251. DOI: 10.1051/0004-6361:20066078.

Utrobin, Victor P., Stefan Immler, and Kurt Weiler (2007). "Supernova 1987A: The Ejecta Mass and the Explosion Energy". In: *AIP Conference Proceedings*.

van den Heuvel, E. P. J. and C. De Loore (June 1973). "The Nature of X-ray Binaries III. Evolution of Massive Close Binaries with One Collapsed Component - with a Possible Application to Cygnus X-3." In: *Astronomy and Astrophysics* 25, p. 387. ISSN: 0004-6361.

van den Heuvel, E. P. J., S. F. Portegies Zwart, and S. E. de Mink (Nov. 2017). "Forming Short-Period Wolf-Rayet X-ray Binaries and Double Black Holes through Stable Mass Transfer". In: *Monthly Notices of the Royal Astronomical Society* 471, pp. 4256–4264. ISSN: 0035-8711. DOI: 10.1093/mnras/stx1430.

van Son, L. A. C. et al. (Dec. 2022). "No Peaks without Valleys: The Stable Mass Transfer Channel for Gravitational-wave Sources in Light of the Neutron Star-Black Hole Mass Gap". In: *The Astrophysical Journal* 940, p. 184. ISSN: 0004-637X. DOI: 10.3847/1538-4357/ac9b0a.

van Son, Lieke, Stephen Justham, and Selma De Mink (Jan. 2021). "Filling the Gap: Possible Pathways to Get a BBH Merger in the PISN Mass Gap". In: 43, p. 2124.

Vigna-Gómez, Alejandro et al. (Dec. 2018). "On the Formation History of Galactic Double Neutron Stars". In: *Monthly Notices of the Royal Astronomical Society* 481, pp. 4009–4029. ISSN: 0035-8711. DOI: 10.1093/mnras/sty2463.

Vink, Jorick et al. (Mar. 2021). "Maximum Black Hole Mass across Cosmic Time". In: *Monthly Notices of the Royal Astronomical Society* 504. DOI: 10.1093/mnras/stab842.

Vink, Jorick S. (Aug. 2022). "Theory and Diagnostics of Hot Star Mass Loss". In: *Annual Review of Astronomy and Astrophysics* 60, pp. 203–246. ISSN: 0066-4146. DOI: 10.1146/annurev-astro-052920-094949.

Vink, Jorick S. and A. de Koter (Oct. 2002). "Predictions of variable mass loss for Luminous Blue Variables". In: *Astronomy & Astrophysics* 393, pp. 543–553. DOI: 10.1051/0004-6361:20021009. arXiv: astro-ph/0207170 [astro-ph].

Vink, Jorick S., A. de Koter, and H. J. G. L. M. Lamers (2001). "Mass-Loss Predictions for O and B Stars as a Function of Metallicity". In: *Astronomy and Astrophysics*.

— (July 2018). "Presupernova Evolution and Explosive Nucleosynthesis of Rotating Massive Stars in the Metallicity Range -3 ≤ [Fe/H] ≤ 0". In: *The Astrophysical Journal Supplement Series* 237.1, p. 13. ISSN: 0067-0049. DOI: 10.3847/1538-4365/aacb24.

Vink, Jorick S. and A. de Koter (Oct. 2005). "On the metallicity dependence of Wolf-Rayet winds". In: *Astronomy & Astrophysics* 442.2, 587–596. ISSN: 1432-0746. DOI: 10.1051/0004-6361:20052862.

Vink, Jorick S. et al. (Mar. 2010). "The nature of B supergiants: clues from a steep drop in rotation rates at 22 000 K. The possibility of Bi-stability braking". In: *Astronomy & Astrophysics* 512, L7, p. L7. DOI: 10.1051/0004-6361/201014205. arXiv: 1003.1280 [astro-ph.SR].

Wang, Long (Jan. 2020). "The Survival of Star Clusters with Black Hole Subsystems". In: *Monthly Notices of the Royal Astronomical Society* 491, pp. 2413–2423. ISSN: 0035-8711. DOI: 10.1093/mnras/stz3179.

Wang, Long, Ataru Tanikawa, and Michiko Fujii (Oct. 2022). "Gravitational Wave of Intermediate-Mass Black Holes in Population III Star Clusters". In: *Monthly Notices of the Royal Astronomical Society* 515, pp. 5106–5120. ISSN: 0035-8711. DOI: 10.1093/mnras/stac2043.

Wang, Tianshu and Adam Burrows (2024). *Supernova Explosions of the Lowest-Mass Massive Star Progenitors*. arXiv: 2405.06024 [astro-ph.HE].

Wang, Yuan-Zhu et al. (May 2021). "Black Hole Mass Function of Coalescing Binary Black Hole Systems: Is There a Pulsational Pair-instability Mass Cutoff?" In: *ApJ* 913.1, p. 42. ISSN: 0004-637X. DOI: 10.3847/1538-4357/abf5df.

Webbink, R. F. (Jan. 1985). *Stellar Evolution and Binaries*, p. 39.

Webbink, R. F. (1985). "Stellar evolution and binaries". In: *Interacting Binary Stars*. Ed. by J. E. Pringle and R. A. Wade, p. 39.

— (Jan. 1988). "The Formation and Evolution of Symbiotic Stars". In: *IAU Colloq. 103: The Symbiotic Phenomenon*. Ed. by Joanna Mikolajewska et al. Vol. 145. Astrophysics and Space Science Library, p. 311. DOI: 10.1007/978-94-009-2969-2_69.

Winch, Ethan R. J. et al. (Feb. 2024). *Predicting the Heaviest Black Holes below the Pair Instability Gap*. arXiv: 2401.17327 [astro-ph].

Woosley, S. E. (1988). "SN 1987A - After the Peak". In: *The Astrophysical Journal* 330, p. 218. DOI: 10.1086/166468.

Woosley, S. E. (2017). "Pulsational Pair-instability Supernovae". In: *The Astrophysical Journal* 836.2, p. 244. DOI: 10.3847/1538-4357/836/2/244.

Woosley, S. E. (June 2019). "The Evolution of Massive Helium Stars, Including Mass Loss". In: *The Astrophysical Journal* 878.1, 49, p. 49. DOI: 10.3847/1538-4357/ab1b41. arXiv: 1901.00215 [astro-ph.SR].

Woosley, S. E. and Thomas A. Weaver (Nov. 1995). "The Evolution and Explosion of Massive Stars. II. Explosive Hydrodynamics and Nucleosynthesis". In: *The Astrophysical Journal Supplement Series* 101, p. 181. DOI: 10.1086/192237.

Wysocki, Daniel et al. (Feb. 2018). "Explaining LIGO's Observations via Isolated Binary Evolution with Natal Kicks". In: *prd* 97.4, p. 043014. DOI: 10.1103/PhysRevD.97.043014.

Yang, Y. et al. (Nov. 2019). "Hierarchical Black Hole Mergers in Active Galactic Nuclei". In: *Phys. Rev. Lett.* 123 (18), p. 181101. DOI: 10.1103/PhysRevLett.123.181101.

Ye, Claire S. et al. (June 2022). "Compact Object Modeling in the Globular Cluster 47 Tucanae". In: *The Astrophysical Journal* 931, p. 84. ISSN: 0004-637X. DOI: 10.3847/1538-4357/ac5b0b.

Yoon, Sung-Chul and Matteo Cantiello (July 2010). "Evolution of Massive Stars with Pulsation-driven Superwinds During the Red Supergiant Phase". In: *The Astrophysical Journal* 717.1, pp. L62–L65. DOI: 10.1088/2041-8205/717/1/L62. arXiv: 1005.4925 [astro-ph.SR].

Zahn, J. P. (May 1977). "Tidal friction in close binary systems." In: *Astronomy & Astrophysics* 57, pp. 383–394.

Zahn, J. P. (Nov. 1992). "Circulation and turbulence in rotating stars." In: *Astronomy & Astrophysics* 265, pp. 115–132.

Zapartas, E. et al. (Dec. 2021). "Revisiting the explodability of single massive star progenitors of stripped-envelope supernovae". In: *Astronomy & Astrophysics* 656, L19, p. L19. DOI: 10.1051/0004-6361/202141506. arXiv: 2106.05228 [astro-ph.HE].

Zevin, Michael et al. (Apr. 2021). "One Channel to Rule Them All? Constraining the Origins of Binary Black Holes Using Multiple Formation Pathways". In: *The Astrophysical Journal* 910.2, p. 152. DOI: 10.3847/1538-4357/abe40e.

Ziosi, B. M. et al. (June 2014). "Dynamics of stellar black holes in young star clusters with different metallicities - II. Black hole-black hole binaries". In: *Monthly Notices of the Royal Astronomical Society* 441.4, 3703–3717. ISSN: 1365-2966. DOI: 10.1093/mnras/stu824.

Zwart, Simon F. Portegies and Stephen L. W. McMillan (Dec. 1999). "Black Hole Mergers in the Universe". In: *The Astrophysical Journal* 528.1, p. L17. DOI: 10.1086/312422.

Özel, Feryal et al. (Dec. 2010). "THE BLACK HOLE MASS DISTRIBUTION IN THE GALAXY". In: *The Astrophysical Journal* 725.2, p. 1918. DOI: 10.1088/0004-637X/725/2/1918.